EFFECTS OF INFLOW BOUNDARY LAYER ON THE WAKE CHARACTERISTICS OF A RADIALLY NON-UNIFORM POROUS DISC

A THESIS SUBMITTED TO
THE GRADUATE SCHOOL OF NATURAL AND APPLIED SCIENCES
OF
MIDDLE EAST TECHNICAL UNIVERSITY

BY

ANAS ABDULRAHİM

IN PARTIAL FULFILLMENT OF THE REQUIREMENTS
FOR
THE DEGREE OF DOCTOR OF PHILOSOPHY
IN
AEROSPACE ENGINEERING

JANUARY 2022

Approval of the thesis:

EFFECTS OF INFLOW BOUNDARY LAYER ON THE WAKE CHARACTERISTICS OF A RADIALLY NON-UNIFORM POROUS DISC

submitted by **ANAS ABDULRAHİM** in partial fulfillment of the requirements for the degree of **Doctor of Philosophy** i**n Aerospace Engineering, Middle East Technical University** by,

Prof. Dr. Halil Kalıpçılar
Dean, Graduate School of **Natural and Applied Sciences** _____

Prof. Dr. Serkan Özgen
Head of the Department, **Aerospace Eng.** _____

Prof. Dr. Oğuz Uzol
Supervisor, **Aerospace Eng., METU** _____

Asst. Prof. Dr. Mustafa Perçin
Co-Supervisor, **Aerospace Eng., METU** _____

Examining Committee Members:

Prof. Dr. Serkan Özgen
Aerosapce Eng, METU _____

Prof. Dr. Oğuz Uzol
Aerospace Eng., METU _____

Prof. Dr. Özgür Kurç
Civil Eng., METU _____

Assoc. Prof. Dr. Munir ElFarra
Aerospace Eng., Ankara YBU _____

Prof. Dr. Nuriye Leman Okşan Çetiner-Yıldırım
Astronautical Eng., ITU _____

Date: 03.01.2022

I hereby declare that all information in this document has been obtained and presented in accordance with academic rules and ethical conduct. I also declare that, as required by these rules and conduct, I have fully cited and referenced all material and results that are not original to this work.

Name, Last name : Anas Abdulrahim

Signature :

ABSTRACT

EFFECTS OF INFLOW BOUNDARY LAYER ON THE WAKE CHARACTERISTICS OF A RADIALLY NON-UNIFORM POROUS DISC

Abdulrahim, Anas
Doctor of Philosophy, Aerospace Engineering
Supervisor: Prof. Dr. Oğuz Uzol
Co-Supervisor: Asst. Prof. Dr. Mustafa Perçin

January 2022, 210 pages

This thesis study presents the results of an experimental investigation focusing on the effects of inflow boundary layer on the wake characteristics of a porous disc (disc diameter-to-boundary layer height is 0.2) with radially non-uniform porosity in terms of mean flow, turbulence, wake scaling, and proper orthogonal decomposition. Two-dimensional two-component particle image velocimetry measurements within the wake are performed up to 7.5 diameters downstream as the disc is lowered deeper in to a boundary layer that is representative of a neutral atmospheric boundary layer over a flat terrain (corresponds to 435 scale factor compared to field length scale). Results show that otherwise symmetrical wake velocity profiles that exist outside the boundary layer get skewed and sheared around the disc centerline in the boundary layer due to the inflow wind shear. The turbulent kinetic energy, its production and Reynolds shear stress levels in the wake get asymmetrical around the centerline of the disc such that the production of turbulent kinetic energy is observed to be higher above centerline. Due to the inflow shear, the wake centerline gets shifted downwards (i.e., towards the wind tunnel wall), which is in contrast to the

observations on real wind turbine wakes in the literature where the wake actually lifts up. The asymmetrical and skewed velocity profiles both in the streamwise and cross-stream directions can be collapsed onto a single function by using proper wake scaling parameters based on the ratio of local strain to average strain within the velocity profile calculated separately for either side of the wake. Proper orthogonal decomposition reveals that the most energetic modes are the first and second modes. The differences in the modes are significant when the disc is at different positions within the boundary layer. Finally, the wake velocity profiles of the porous disc are compared against model predictions from the Bastankhah and Porté-Agel wake model and the Ishihara and Qian wake model under different inflow conditions. A method is proposed as an extension to the wake models to generate asymmetric wake velocity profiles. The comparison illustrates the deviation due to the wake growth rate and initial wake width estimation. The wake growth rate of the porous disc can be significantly higher than field turbines as well as those estimated through empirical relations suggested in the literature in the context of engineering wake models, particularly at low ambient turbulence conditions. This suggests caution in the use of porous discs to simulate wind turbine wakes and wind farms in wind tunnel studies. Results show that the when using the estimated wake growth rate and initial wake width of the porous disc, the wake models show better predictions overall for all the test cases considered.

Keywords: Atmospheric Boundary Layer, Porous Disc, Wind Turbine, Wake Model, Wake Turbulence, Wake Growth Rate, Proper Orthogonal Decomposition

ÖZ

RADYAL OLARAK DEĞİŞKEN GÖZENEKLİLİĞE SAHİP BİR GÖZENEKLİ DİSKE GİRİŞ AKIŞ SINIR TABAKASININ ETKİLERİ

Abdulrahim, Anas
Doktora, Havacılık ve Uzay Mühendisliği
Tez Yöneticisi: Prof. Dr. Oğuz Uzol
Ortak Tez Yöneticisi: Yrd. Doç. Dr. Mustafa Perçin

Ocak 2022, 210 sayfa

Bu tez çalışmasında radyal olarak değişken gözenekliliğe sahip bir gözenekli diskin giriş sınır tabaka akış etkisi altındaki iz bölgesi karakteristikleri ortalama akış, türbülans ve iz bölgesi ölçeklendirme yönlerinden deneysel olarak incelenmiştir. Gözenekli disk, düz bir arazi üzerindeki nötr atmosferik sınır tabakayı temsil eden bir sınır tabakanın içine çeşitli konumlarda yerleştirilmiş ve bu konumlarda gözenekli diskin iz bölgesinde 7.5 çap akışaltı uzaklığa kadar iki-boyutlu, iki-bileşenli parçacık görüntülemeli hız ölçümü tekniği kullanılarak deneysel ölçümler gerçekleştirilmiştir. Sonuçlar normal şartlar altında simetrik olan iz bölgesi hız profillerinin sınır tabakanın içindeyken disk önündeki hız profili nedeniyle disk orta çizgisi etrafında eğildiğini ve kırıldığını göstermektedir. Türbülans kinetik enerjisi, türbülans kinetik enerjisi üretimi ve Reynolds kayma gerilmesi seviyelerinin iz bölgesinde orta çizgi etrafında asimetrik olduğu görülmüştür. Türbülans kinetik enerji üretimi orta çizgi üzerinde daha yüksektir. Disk önündeki hız profili nedeniyle iz bölgesi orta noktası aşağı doğru (rüzgar tüneli alt duvarına doğru) kaymaktadır. Bu durum, literatürdeki gerçek boyutlu rüzgar türbini üzerinde yapılan gözlemlere

ters düşmektedir. İz bölgesinin her iki tarafı için ayrı ayrı hesaplanan, hız profilinin yerel gerilmesinin ortalama gerilmesine oranına dayalı belirlenmiş uygun ölçeklendirme parametreleri kullanılarak hem akış yönündeki hem de akışa dik yönderki asimetrik ve çarpık hız profillerinin sabit bir dağılıma indirgenmesi mümkün olmaktadır. Rüzgar türbini iz bölgelerinin analitik modeller kullanılarak doğru bir şekilde öngörülebilmesi için iz bölgesi büyüme oranının doğru değerlendirilebilmesi kritik öneme sahiptir. Rüzgar tünellerinde rüzgar türbinlerinin iz bölgelerini benzeştirebilmek amacıyla kullanılan gözenekli disklerin iz bölgesi büyüme oranı parametreleri özellikle düşük ortam türbülans yoğunluğunda rüzgar türbinlerine göre çoğunlukla daha yüksektir. Bir gözenekli diskin ve bir rüzgar türbini tarafından akışa eklenen türbülansın farklılıkları da farklı ortam türbülans yoğunluğu koşullarında araştırılmıştır. Disk ve rotor iz bölgesi türbülansı ile birlikte eksenel indükleme faktörünü de hesaba katan yeni bir denklem önerilmiştir. Buna ek olarak, gözenekli diskler ve rüzgar türbinlerine ait deneysel veri Bastankhah ve Porté-Agel ve Ishihara ve Qian iz bölgesi modelleri ile yapılan tahminler ile karşılaştırılmıştır. Sonuçlar yeni önerilen iz bölgesi büyüme oranı denkleminin genel olarak daha iyi çalıştığını ve iz bölgesi modellerine eklenerek gerçek boyutlu rüzgar türbinlerinin iz bölgelerinin tahmininde kullanılabilme potansiyelinin olduğunu göstermektedir.

Anahtar Kelimeler: Atmosferik Sınır Tabaka, Gözenekli Disk, Rüzgar Türbini, İz Bölgesi Modeli, İz Bölgesi Türbülansı, İz Bölgesi Büyüme Oranı

"*If you want to go fast, go alone.*

If you want to go far, go together"

-African Proverb-

ACKNOWLEDGMENTS

Firstly, I wish to express my deepest gratitude to my supervisor Prof. Dr. Oğuz Uzol and co-supervisor Asst. Prof. Dr. Mustafa Perçin for their valuable support and patience through all these years. Without their enthusiasm, energy, and the late-night meetings, I could not be able to complete this study.

Also I would like to express gratitude to the jury members Prof. Dr. Serkan Özgen, Prof. Dr. Özgür Kurç, Prof. Dr. Okşan Çetiner-Yıldırım, and Assoc. Prof. Dr. Munir Elfarra for their valuable comments and discussions.

I would like to thank METU Center for Wind Energy (RÜZGEM) for supporting this thesis study and allocating the necessary time to carry out my experiments. Also acknowledgment goes to Ankara Yıldırım Beyazıt Üniversitesi for allowing me to use their NUMECA FINE/OPEN software to carry out the CFD simulations.

I have been working with lots of graduate and undergraduate students in the Aerodynamics lab, for which I am very grateful. I have enjoyed working and studying with you all, İmge Yiğili, Burcu Erol, Mert Ali Andirin, Buğrahan Öztürk, Mahdi Yazdanpanah, and Yusufcan Taşmaz. Big thanks go to my friends M. Tuğrul Akpolat and Abdelrahman Hassanein for spending long time with me while performing the PIV measurements and the data analysis. I would like to thank my colleague Emre Karabakla for his help in the wind tunnel control system and various related tasks. Special thanks goes to my friend Dr. Human Amiri for his help in the early stages of this thesis study and all the discussions we had.

I would like to thank, Mohammed Salman, Anas Abdel-Hadi, and Dr. Muhanned Gilani for their long-time friendship and support.

Lastly, but most importantly, I would like to express my eternal gratitude to my family and wife for their never ending prayers, love and support throughout my life.

TABLE OF CONTENTS

ABSTRACT v

ÖZ… vii

ACKNOWLEDGMENTS x

TABLE OF CONTENTS xi

LIST OF TABLES xv

LIST OF FIGURES xvii

LIST OF ABBREVIATIONS xxvii

LIST OF SYMBOLS xxviii

1 INTRODUCTION 1

1.1 Motivation 1

1.2 Overview of Wind Shear, Atmospheric Turbulence and Wake Effects 3

1.3 Literature Review 5

1.3.1 Field Measurement Studies 6

1.3.2 Numerical Studies 10

1.3.3 Wind Tunnel Studies 12

1.3.4 Analytical Wake Models 18

1.4 Objectives and Scope 21

1.5 Thesis Outline 22

2 ATMOSPHERIC BOUNDARY LAYER 23

2.1 Overview of the Atmospheric Boundary Layer 23

2.2 Structure of the Atmospheric Boundary Layer 24

2.3 Characteristics of the Atmospheric Boundary Layer 26

2.3.1 Atmospheric Boundary Layer Stability 26
2.3.2 Mean Velocity Profiles 27
2.3.3 Turbulence Intensity 28
2.3.4 Turbulence Length and Time Scales 29
2.3.5 Power Spectrum of Turbulence 31
2.4 Simulation of the Atmospheric Boundary Layer 32
3 NUMERICAL SIMULATION OF THE ATMOSPHERIC BOUNDARY LAYER IN WIND TUNNELS 37
3.1 Validation Study 38
3.1.1 Wind Tunnel Facility 38
3.1.2 Numerical Methodology 38
3.1.3 Grid Independence Study 39
3.1.4 Results of the Validation Study 40
3.2 RÜZGEM Large-Scale Boundary Layer Wind Tunnel (BLWT) 46
3.2.1 Wind Tunnel Facility 46
3.2.2 Design Methodology for Spires and Roughness Elements 47
3.2.2.1 Design Methodology for Spires 47
3.2.2.2 Design Methodology for Roughness Elements 51
3.2.3 Numerical Methodology 53
3.2.3.1 Comparison between the ½ -Model and 1/7th–Model Approach 53
3.2.3.2 Grid Independence Study 56
3.2.3.3 Empty Boundary Layer Wind Tunnel Test Section 58
3.2.4 Effect of Spires and Roughness Elements 59
3.2.4.1 Effect of Spires 60
3.2.4.2 Effect of Roughness Element Height, Spacing and Layout 62

3.2.4.3 Effect of Spires and Roughness Elements 67
3.2.4.4 Selection and Summary of Test Cases 70
3.3 RÜZGEM C3 Boundary Layer Wind Tunnel 72
3.3.1 Wind tunnel Facility 72
3.3.2 Experimental Characterization of the Wind Tunnel Facility 73
3.3.3 Numerical Methodology 76
3.3.4 Results of RÜZGEM C3 Boundary Layer Wind Tunnel 77
3.3.4.1 Empty Wind Tunnel 78
3.3.4.2 Wind Tunnel Equipped with Spires 85
3.3.4.3 Wind Tunnel Equipped with Spires and Roughness Elements.. 90
3.3.4.4 Comparison with International Standards 95
3.4 Upgrade of RÜZGEM C3 Boundary Layer Wind Tunnel 96
4 POROUS DISC EXPERIMENTAL SETUP AND MEASUREMENT DETAILS 99
4.1 Upgraded Wind Tunnel Facility 99
4.1.1 Wind Tunnel Control System 100
4.2 Porous Disc 102
4.3 Boundary Layer Generation and Disc Inflow Conditions 103
4.4 Measurements Details 106
4.5 Particle Image Velocimetry 108
4.6 Uncertainty Analysis 112
5 EFFECTS OF INFLOW WIND SHEAR AND TURBULENCE ON THE WAKE CHARACTERISTICS OF A RADIALLY NON-UNIFORM POROUS DISC 115
5.1 Effects on Mean Wake Flow Field 116
5.2 Effects on Wake Turbulence 121

5.3 Wake Scaling Under the Effect of Inflow Shear 128

5.4 Proper Orthogonal Decomposition 135

5.4.1 Theory..... 136

5.4.2 Snapshot Proper Orthogonal Decomposition 138

6 ON THE WAKE GROWTH RATE OF A POROUS DISC IMMERSED IN A BOUNDARY LAYER 149

6.1 Comparison of Wake Models Predictions with Porous Disc Data 149

6.1.1 Wake Growth Rate and Initial Wake Width Models..... 150

6.1.2 Modeling Wake Asymmetry 151

6.1.3 Results 153

6.2 Porous Disc Wake Growth Rate 158

6.2.1 Estimation of Wake Growth Rate and Initial Wake Width 158

6.3 Wake Turbulence and Disc Added Turbulence 163

6.4 Wake Model Predictions Based on the Estimated k^* and ϵ..... 170

6.5 Concluding Remarks..... 174

7 CONCLUSIONS AND FUTURE WORKS 175

REFERENCES 177

CURRICULUM VITAE 207

LIST OF TABLES

TABLES

Table 1.1 Length, velocity, and time scale requirements in wind turbine aerodynamics [2] 4
Table 3.1 Summary of the atmospheric boundary layer properties 43
Table 3.2 Design parameters for spires and roughness elements..... 51
Table 3.3 Comparison of boundary layer properties between the 1/2-model and 1/7th-model approach 56
Table 3.4 Grid independence study for 1/7th-model approach (spires only)..... 57
Table 3.5 Grid independence study for the empty BLWT test section..... 58
Table 3.6 Comparison of boundary layer properties between the theoretical and CFD results for empty BLWT test section 59
Table 3.7 Design parameters of spires for each terrain exposure (or category) 60
Table 3.8 Summary of the atmospheric boundary layer properties 61
Table 3.9 Summary of atmospheric boundary layer properties for the cases of roughness elements 66
Table 3.10 Summary of the atmospheric boundary layer properties for the cases of spires with roughness elements..... 68
Table 3.11 Summary of the atmospheric boundary layer properties for each terrain exposure (or category)..... 71
Table 3.12 Summary of atmospheric boundary layer properties for the empty wind tunnel..... 84
Table 3.13 Design parameters of spires for terrain exposure B..... 85
Table 3.14 Summary of atmospheric boundary layer properties for the wind tunnel equipped with spires..... 89
Table 3.15 Summary of atmospheric boundary layer properties for the wind tunnel equipped with spires and roughness elements 94
Table 3.16 Comparison of aerodynamic roughness height with empirical formulas from literature..... 95

Table 4.1 Porous disc properties 102
Table 4.2 Boundary layer properties at the streamwise positions of ($x/D = -8.5$) and ($x/D = 0$) 105
Table 4.3 Inflow conditions for porous disc wake measurements 107
Table 4.4 2D2C-PIV experimental parameters 110
Table 4.5 The normalized mean statistical uncertainty estimates for the mean flow, Reynolds stresses and turbulent kinetic energy 112
Table 5.1 Power law fits for the decay of normalized turbulent kinetic energy of the upper and lower halves of the wake 127
Table 5.2 Power law fit coefficients for the streamwise variations of the velocity scale (top) and length scale (bottom) distributions in the upper and lower halves of the wake for all z/δ locations 134
Table 5.3 Percentage of TKE contribution from each mode 140
Table 6.1 $k^*$and ϵ for the selected boundary positions of the porous disc 161

LIST OF FIGURES

FIGURES

Figure 1.1 *Horns Rev* offshore wind farm [54] 3
Figure 1.2 Schematic figure of the wake flow field downstream of a wind turbine immersed in an ABL [54] 5
Figure 2.1 Typical development of the atmospheric boundary layer (ABL) during the course of the day [166] 24
Figure 2.2 Schematic layout of the structure of the atmospheric boundary layer (ABL) [170] 25
Figure 2.3 Variation of the Reynolds stress within the atmospheric boundary layer [171] 26
Figure 2.4 Dependency of the turbulence intensity on wind speed and atmospheric stability [12] 29
Figure 2.5 Energy spectrum of turbulence [170] 31
Figure 2.6 Schematic layout of the grid of parallel rods inside the wind tunnel test section [173] 33
Figure 2.7 Vortex generators used by Counihan [176] 34
Figure 2.8 Geometry of Spires used by Standen [180] 34
Figure 2.9 Triangular spire with splitter plate used by Irwin [182] 35
Figure 2.10 Schematic layout of the array of differentially-spaced flat plates in wind tunnel test section [190] 36
Figure 3.1 Open-loop boundary layer wind tunnel facility at the University of Windsor [216] 38
Figure 3.2 (a) Computational domain, (b) Unstructured hexahedral mesh with a close-up view of the mesh around the spires and roughness elements 39
Figure 3.3 Grid independence study: (a) 3-spire case, (b) 3-spire with roughness elements case 40
Figure 3.4 Velocity magnitude profiles: (a) 3-spire case, (b) 5-spire case, and (c) roughness elements (20 x 10 array) case 42

Figure 3.5 Normalized velocity profiles: (a) 3-spire case, (b) 5-spire case, (c) roughness elements (20 x 10 array) case, and (d) 3-spire with roughness elements case 42
Figure 3.6 Velocity magnitude contours at the mid-plane: (a) 3-spire case, (b) 5-spire case, (c) Roughness elements (20 x 10 array) case, and (d) 3-spire with roughness elements case 44
Figure 3.7 Velocity magnitude contours: (a) 3-spire case, (b) 5-spire case, (c) Roughness elements (20 x 10 array) case, and (d) 3-spire with roughness elements case 45
Figure 3.8 RÜZGEM large scale multi-purpose wind tunnel 47
Figure 3.9 Relationship between δ/h and α at $X_0 \approx 6h$ [182] 48
Figure 3.10 (a) Schematic layout of the test section control volume [182], and (b) triangular spire with a splitter plate [182] 49
Figure 3.11 Surface roughness dimensions and layouts [222] 52
Figure 3.12 Terminology for spires and roughness elements 53
Figure 3.13 (a) unstructured hexahedral mesh for the ½-model approach, (b) close-up view of the spires and mesh around the spires 54
Figure 3.14 (a) Computational domain highlighting the 1/7th-model, (b) unstructured hexahedral mesh around the spires and roughness elements 55
Figure 3.15 Normalized velocity profiles: (a) Terrain A spires only, (b) Terrain B spires only, (c) Terrain A spires with roughness element 56
Figure 3.16 Grid independence study for 1/7th-model approach (spires only) 57
Figure 3.17 (a) Grid independent study for empty BLWT, (b) normalized velocity profile at 10 m/s, and (c) normalized velocity profile at 20 m/s. 59
Figure 3.18 Normalized velocity profiles for different terrain exposures: (a) Terrain Exposure A, (b) Terrain Exposure B, (c) Terrain Exposure C, and (d) Terrain Exposure D 61
Figure 3.19 (a) Normalized velocity profiles, and (b) turbulent kinetic energy profiles for different terrain exposures. Solid lines represent the power law curve fits 62
Figure 3.20 (a-h) Roughness element layouts and configurations. x-axis is along the wind direction, y-axis is along the transverse direction 64

Figure 3.21 (a-h) Normalized velocity profiles for different roughness element layouts and configurations 65
Figure 3.22 (a) Normalized velocity profiles, and (b) turbulent kinetic energy profiles for different roughness element cases 67
Figure 3.23 (a-h) Normalized velocity profiles for the cases of spires with roughness elements..... 69
Figure 3.24 (a) Normalized velocity profiles, and (b) turbulent kinetic energy profiles for different spires and roughness elements cases 70
Figure 3.25 Normalized velocity profiles: (a) Terrain exposure A, (b) Terrain exposure B, (c) Terrain exposure C, and (d) Terrain exposure D..... 72
Figure 3.26 METUWIND C3 boundary layer wind tunnel: (a) inlet of the wind tunnel, (b) test section with spires and roughness elements, and (c) sketch of the wind tunnel..... 73
Figure 3.27 Horizontal measurements at the inlet of the test section: (a) streamwise velocity, (b) normalized streamwise velocity, (c) streamwise turbulence intensity. Dashed blue line marks the tunnel centerline 75
Figure 3.28 Vertical measurements at the inlet of the test section: (a) streamwise velocity, (b) normalized streamwise velocity, (c) streamwise turbulence intensity. Dashed blue line marks the tunnel centerline 76
Figure 3.29 (a) Computational domain, (b) unstructured hexahedral mesh with close-up view of the mesh around the spires and roughness elements..... 77
Figure 3.30 Contour plots of: (a) streamwise velocity, and (b) turbulent kinetic energy for the empty wind tunnel. Velocity profiles represented as vectors are shown at different streamwise positions..... 78
Figure 3.31 Contour plots of: (a) streamwise velocity, and (b) turbulent kinetic energy for the empty wind tunnel 79
Figure 3.32 Horizontal profiles at the inlet of the test section: (a) streamwise velocity, (b) normalized streamwise velocity, (c) streamwise turbulence intensity, and (d) turbulent kinetic energy. Dashed blue line marks the tunnel centerline 80

Figure 3.33 Vertical profiles at the inlet of the test section: (a) streamwise velocity, (b) normalized streamwise velocity, (c) streamwise turbulence intensity, and (d) turbulent kinetic energy. Dashed blue line marks the tunnel centerline 81
Figure 3.34 Horizontal profiles 6 m dowstream of the test section inlet: (a) streamwise velocity, (b) normalized streamwise velocity, (c) streamwise turbulence intensity, and (d) turbulent kinetic energy. Dashed blue line marks the tunnel centerline 82
Figure 3.35 Horizontal profiles 7 m dowstream of the test section inlet: (a) streamwise velocity, (b) normalized streamwise velocity, (c) streamwise turbulence intensity, and (d) turbulent kinetic energy. Dashed blue line marks the tunnel centerline 83
Figure 3.36 Vertical profiles 7 m dowstream of the test section inlet: (a) streamwise velocity, (b) normalized streamwise velocity, (c) streamwise turbulence intensity, and (d) turbulent kinetic energy. Dashed blue line marks the tunnel centerline 84
Figure 3.37 (a) streamwise velocity distribution with power law curve fit, and (b) log-law with logarithmic curve fit 85
Figure 3.38 Contour plots of: (a) streamwise velocity, and (b) turbulent kinetic energy for the empty wind tunnel equipped with spires. Velocity profiles represented as vectors are shown at different streamwise positions 86
Figure 3.39 Contour plots of: (a) streamwise velocity, and (b) turbulent kinetic energy for the empty wind tunnel equipped with spires. Velocity profiles represented as vectors are shown at different streamwise positions 87
Figure 3.40 Horizontal profiles 7 m dowstream of the test section inlet: (a) streamwise velocity, (b) normalized streamwise velocity, (c) streamwise turbulence intensity, and (d) turbulent kinetic energy. Dashed blue line marks the tunnel centerline 88
Figure 3.41 Vertical profiles 7 m dowstream of the test section inlet: (a) streamwise velocity, (b) normalized streamwise velocity, (c) streamwise turbulence intensity, and (d) turbulent kinetic energy. Dashed blue line marks the tunnel centerline 89
Figure 3.42 (a) streamwise velocity distribution with power law curve fit, and (b) log-law with logarithmic curve fit 90

Figure 3.43 Contour plots of: (a) streamwise velocity, and (b) turbulent kinetic energy for the empty wind tunnel equipped with spires and roughness elements. Velocity profiles represented as vectors are shown at different streamwise positions 91
Figure 3.44 Contour plots of: (a) streamwise velocity, and (b) turbulent kinetic energy for the empty wind tunnel equipped with spires and roughness elements. Velocity profiles represented as vectors are shown at different streamwise positions 92
Figure 3.45 Vertical profiles 7 m dowstream of the test section inlet: (a) streamwise velocity, (b) normalized streamwise velocity, (c) streamwise turbulence intensity, and (d) turbulent kinetic energy. Dashed blue line marks the tunnel centerline..... 93
Figure 3.46 (a) streamwise velocity distribution with power law curve fit, and (b) log-law with logarithmic curve fit..... 94
Figure 3.47 Comparison of the ABL turbulence intensity profiles at full scale with international standards 96
Figure 3.48 Horizontal profiles of: (a) normalized streamwise velocity, and (b) streamwise turbulence intensity of the old and new configuration of the wind tunnel facility. Dashed blue line marks the tunnel centerline 97
Figure 3.49 Vertical profiles of: (a) normalized streamwise velocity, and (b) streamwise turbulence intensity of the old and new configuration of the wind tunnel facility. Dashed blue line marks the tunnel centerline 98
Figure 4.1 Open return boundary layer wind tunnel facility at Center for Wind Energy Research (RÜZGEM) at the Middle East Technical University (METU) 100
Figure 4.2 User interface of the closed-loop control system for the wind tunnel facility 100
Figure 4.3 Sketch of the wind tunnel facility with the instruments and sensors locations for the closed-loop control system..... 101
Figure 4.4 (a) Schematic of the porous disc, 120 mm diameter and non-uniform porosity [230], (b) a picture of the porous disc used in the current experiments attached to the support 103

Figure 4.5 Schematic layout of the wind tunnel test section and porous disc measurement setup 104
Figure 4.6 Vertical profiles of: (a) normalized mean streamwise velocity, and (b) streamwise turbulence intensity. Dashed red lines mark the disc positions used during wake measurements 105
Figure 4.7 Thrust coefficient variation with Reynolds number for the porous disc 108
Figure 4.8 PIV measurement setup for porous disc wake measurements 109
Figure 4.9 PIV measurement domain showing the windows with the overlap region and the field of view dimensions. The porous disc is marked as a solid blue rectangle and is located between: $-0.5 \leq z'/D \leq 0.5$ 110
Figure 5.1 Mean streamwise velocity normalized with the velocity at hub height (left) and Normalized mean out-of-plane vorticity (right) at different disc positions. *1st row*: $z/\delta = 1.17$, *2nd row*: $z/\delta = 0.71$, *3rd row*: $z/\delta = 0.56$, *4th row*: $z/\delta = 0.32$. Porous disc is marked as a solid blue rectangle and is located between: $-0.5 \leq z'/D \leq 0.5$. The dashed black line passes through the center of the disc $z'/D = 0$. The solid grey line represents the wake centerline 118
Figure 5.2 Normalized streamwise velocity distributions for all z/δ locations along the streamwise direction from (a-e): $x'/D = 3$ to $x'/D = 7$ downstream of the disc. Porous disc is located between: $-0.5 \leq z'/D \leq 0.5$ 120
Figure 5.3 Velocity defect ($1-U_{min} / U_{hub}$) along the streamwise distance for the selected disc positions 121
Figure 5.4 Mean turbulent kinetic energy normalized with the velocity at hub height (left), and mean Reynolds shear stress normalized with the velocity at hub height (right) at different disc positions. *1st row:* $z/\delta = 1.17$, *2nd row:* $z/\delta = 0.71$, *3rd row:* $z/\delta = 0.56$, *4th row:* $z/\delta = 0.32$. Porous disc is marked as a solid blue rectangle and is located between: $-0.5 \leq z'/D \leq 0.5$. The dashed black line passes through the center of the disc $z'/D = 0$ 123
Figure 5.5 Production of turbulent kinetic energy (P_{12}) normalized with hub velocity and disc diameter at different disc positions. (a) $z/\delta = 1.17$, (b) $z/\delta = 0.71$, (c) $z/\delta = 0.56$, (d) $z/\delta = 0.32$. Porous disc is marked as a solid blue rectangle and is

located between: $-0.5 \leq z'/D \leq 0.5$. The dashed black line passes through the center of the disc $z'/D = 0$ 125
Figure 5.6 Normalized turbulent kinetic energy distributions for all z/δ locations along the streamwise direction from (a-e): $x'/D = 3$ to $x'/D = 7$ downstream of the disc. Porous disc is located between: $-0.5 \leq z'/D \leq 0.5$ 126
Figure 5.7 Decay of normalized turbulent kinetic energy. (a) wake upper half, and (b) wake lower half along the streamwise distance for the selected disc positions. Solid black lines represent the power law fits (note that the legends are the same for both plots) 128
Figure 5.8 Wake scaling schematic and nomenclature 129
Figure 5.9 Scaled wake velocity profiles using $\beta = 0.5$ (as suggested by Chow et al. [258]) for the wake velocity profiles along the streamwise direction from (a-e): $x'/D = 3$ to $x'/D = 7$ downstream of the disc at different z/δ locations within the boundary layer (see Figure 5.2). Here u and l denote upper and lower halves of the wake, respectively 131
Figure 5.10 Scaled wake velocity profiles using $\beta = 0.5$ (as suggested by Chow et al. [258]) for the wake velocity profiles at different z/δ locations within the boundary layer along the streamwise direction from $x'/D = 3$ to $x'/D = 7$ downstream of the disc (see Figure 5.2). (a) at $z/\delta = 1.17$, (b) at $z/\delta = 0.71$, (c) at $z/\delta = 0.56$, and (d) at $z/\delta = 0.32$. Here u and l denote upper and lower halves of the wake, respectively 132
Figure 5.11 Scaled wake velocity profiles for all the wake velocity profiles at different z/δ locations within the boundary layer along the streamwise direction from $x'/D = 3$ to $x'/D = 7$ downstream of the disc. Here u and l denote upper and lower halves of the wake, respectively 133
Figure 5.12 Variations of: (a) $(U_\beta - U_0)/U_{hub}$, and (b) δ_β/D along the streamwise direction for the upper and lower halves of the wake for all z/δ locations (note that the legends are the same for both plots) 134
Figure 5.13 Eigenvalues for the snapshot POD in the near wake of the porous disc at different positions in the boundary layer. (a) $z/\delta = 1.17$, (b) $z/\delta = 0.71$, (c) $z/\delta = 0.56$, and (d) $z/\delta = 0.32$. Subgraphs shows only the first 15 modes 139

Figure 5.14 Percentage of TKE contribution from each eigenvalue in the near wake of the porous disc at different positions in the boundary layer. (a) $z/\delta = 1.17$, (b) $z/\delta = 0.71$, (c) $z/\delta = 0.56$, and (d) $z/\delta = 0.32$. Subgraphs shows only the first 15 modes 141
Figure 5.15 Components of the first spatial POD mode. Streamwise component $\phi U1$ (left), vertical component $\phi W1$ (right). *1st row:* $z/\delta = 1.17$, *2nd row*: $z/\delta = 0.71$, *3rd row*: $z/\delta = 0.56$, and *4th row:*$z/\delta = 0.32$. Porous disc is marked as a solid blue rectangle and is located between: $-0.5 \leq z'/D \leq 0.5$ 143
Figure 5.16 Components of the second spatial POD mode. Streamwise component $\phi U2$ (left), vertical component $\phi W2$ (right). *1st row:* $z/\delta = 1.17$, *2nd row*: $z/\delta = 0.71$, *3rd row*: $z/\delta = 0.56$, and *4th row:*$z/\delta = 0.32$. Porous disc is marked as a solid blue rectangle and is located between: $-0.5 \leq z'/D \leq 0.5$ 145
Figure 5.17 Components of the third spatial POD mode. Streamwise component $\phi U3$ (left), vertical component $\phi W3$ (right). *1st row:* $z/\delta = 1.17$, *2nd row*: $z/\delta = 0.71$, *3rd row*: $z/\delta = 0.56$, and *4th row:*$z/\delta = 0.32$. Porous disc is marked as a solid blue rectangle and is located between: $-0.5 \leq z'/D \leq 0.5$ 147
Figure 5.18 Components of the fourth spatial POD mode. Streamwise component $\phi U4$ (left), vertical component $\phi W4$ (right). *1st row:* $z/\delta = 1.17$, *2nd row*: $z/\delta = 0.71$, *3rd row*: $z/\delta = 0.56$, and *4th row:*$z/\delta = 0.32$. Porous disc is marked as a solid blue rectangle and is located between: $-0.5 \leq z'/D \leq 0.5$ 148
Figure 6.1 Conceptual sketch showing the proposed methodology for generating asymmetric wake profiles: (a) symmetric wakes under uniform inflow, and (b) asymmetric wake under non-uniform inflow. The turbine rotor is represented as a solid black rectangle 152
Figure 6.2 Comparison between the experimental data and the predictions of the wake models at $z/\delta = 1.17$ along the streamwise direction from (a-d): $x'/D = 4$ to $x'/D = 7$. Porous disc is located between: $-0.5 \leq z'/D \leq 0.5$ 154
Figure 6.3 Comparison between the experimental data and the predictions of the wake models at $z/\delta = 0.71$ along the streamwise direction from (a-d): $x'/D = 4$ to $x'/D = 7$. Porous disc is located between: $-0.5 \leq z'/D \leq 0.5$ 155

Figure 6.4 Comparison between the experimental data and the predictions of the wake models at $z/\delta = 0.56$ along the streamwise direction from (a-d): $x'/D = 4$ to $x'/D = 7$. Porous disc is located between: $-0.5 \leq z'/D \leq 0.5$ 156
Figure 6.5 Comparison between the experimental data and the predictions of the wake models at $z/\delta = 0.32$ along the streamwise direction from (a-d): $x'/D = 4$ to $x'/D = 7$. Porous disc is located between: $-0.5 \leq z'/D \leq 0.5$. 157
Figure 6.6 Normalized wake velocity profiles for all z/δ locations along the streamwise direction from (a-e): $x'/D = 3$ to $x'/D = 7$ downstream of the disc. Porous disc is located between: $-0.5 \leq z'/D \leq 0.5$..... 160
Figure 6.7 Variation of the normalized standard deviation (i.e. wake width) of the velocity deficit profiles for all z/δ locations along the streamwise direction with curve fits to obtain k^* and ϵ. 161
Figure 6.8 Variation of wake growth rate with ambient turbulence intensity for the porous disc as well as the values predicted by the wake models. Field data reported in Fuertes et al. [265] are included for comparison 163
Figure 6.9 Variation of initial wake width with ambient turbulence intensity for the porous disc as well as the values predicted by the wake models. 163
Figure 6.10 Streamwise turbulence intensity at different disc positions: (a) $z/\delta = 1.17$, (b) $z/\delta = 0.71$, (c) $z/\delta = 0.56$, and (d) $z/\delta = 0.32$. Porous disc is marked as a solid blue rectangle and is located between: $-0.5 \leq z'/D \leq 0.5$. The dashed black line represents the geometric centerline and passes through the center of the disc $z'/\mathrm{D} = 0$..... 164
Figure 6.11 Turbulence intensity distributions for all z/δ locations along the streamwise direction from (a-e): $x'/D = 3$ to $x'/D = 7$ downstream of the disc. Porous disc is located between: $-0.5 \leq z'/D \leq 0.5$..... 166
Figure 6.12 Wake turbulence intensity (I_{wake}) and disc added turbulence intensity (I_{+}) variations with streamwise distance along the geometric centerline of the disc (i.e. $z'/D = 0$) for different z/δ positions. (a) $z/\delta = 1.17$, (b) $z/\delta = 0.71$, (c) $z/\delta = 0.56$, and (d) $z/\delta = 0.32$..... 168
Figure 6.13 Rotor/Disc added turbulence intensity variations with streamwise distance along the centerline of the rotor/disc (i.e. $z'/D = 0$) at different ambient

turbulence intensity levels for porous disc and model wind. This figure is prepared using the data presented in Neunaber et al. [262]. 169
Figure 6.14 Comparison between the porous disc data of the current experiments and the Crespo and Hernandez model at different positions within the boundary layer. 170
Figure 6.15 Comparison between the experimental data and the predictions of the wake models using the estimated k^* and ϵ at $z/\delta = 1.17$ along the streamwise direction from (a-d): $x'/D = 4$ to $x'/D = 7$. Porous disc is located between: $-0.5 \leq z'/D \leq 0.5$ 171
Figure 6.16 Comparison between the experimental data and the predictions of the wake models using the estimated k^* and ϵ at $z/\delta = 0.71$ along the streamwise direction from (a-d): $x'/D = 4$ to $x'/D = 7$. Porous disc is located between: $-0.5 \leq z'/D \leq 0.5$ 172
Figure 6.17 Comparison between the experimental data and the predictions of the wake models using the estimated k^* and ϵ at $z/\delta = 0.56$ along the streamwise direction from (a-d): $x'/D = 4$ to $x'/D = 7$. Porous disc is located between: $-0.5 \leq z'/D \leq 0.5$ 173
Figure 6.18 Comparison between the experimental data and the predictions of the wake models using the estimated k^* and ϵ at $z/\delta = 0.32$ along the streamwise direction from (a-d): $x'/D = 4$ to $x'/D = 7$. Porous disc is located between: $-0.5 \leq z'/D \leq 0.5$ 174

LIST OF ABBREVIATIONS

ABBREVIATIONS

2D2C PIV	Two-dimensional Two-component Particle Image Velocimetry
ABL	Atmospheric Boundary Layer
ADM	Actuator Disk Model
AEP	Annual Energy Production
ASCE	American Society of Civil Engineers
BLWT	Boundary Layer Wind Tunnel
CBL	Convective Boundary Layer
CFD	Computational Fluid Dynamics
CMOS	Complementary Metal-Oxide-Semiconductor
DES	Delayed-Detached-Eddy Simulations
EAWE	European Academy of Wind Energy
FOV	Field of View
HWA	Hotwire Anemometry
IA	Interrogation Area
LES	Large Eddy Simulations
LIDAR	Light Detection and Ranging
NBL	Nocturnal Boundary Layer
Nd:YAG	Neodymium-Doped Yttrium Aluminum Garnet ($Nd:Y_3Al_5O_{12}$)
PIV	Particle Image Velocimetry
POD	Proper Orthogonal Decomposition
RANS	Reynolds Average Naiver-Stokes
SAR	Satellite Synthetic Aperture Radar
SST	Shear Stress Transport
TI	Turbulence Intensity
TKE	Turbulent Kinetic Energy

LIST OF SYMBOLS

SYMBOLS

a	Power law coefficient, axial induction factor
b	Power law exponent
D	disc diameter (m)
h	Spire height (m)
H	Test section height (m)
I_u	Streamwise turbulence intensity
$I_{ambient}$	Ambient turbulence intensity
I_{wake}	Disc/rotor wake turbulence intensity
I_+	Disc/rotor added turbulence intensity
k	Turbulent kinetic energy (m^2/s^2)
k^*	Wake growth rate parameter
L	Test section length (m)
N	Number of vector field images
P_{12}	Production of turbulent kinetic energy: $P_{12} = -\overline{u'w'}(dU/dz)$ (m^2/s^3)
R^2	Goodness of fit
Re_D	Reynolds number based on disc diameter and hub velocity
S_A	Average shear strain
S_L	Local shear strain
$\overline{u'w'}$	Reynolds shear stress (m^2/s^2)
U	Mean streamwise velocity (m/s)
U_∞	Freestream velocity (m/s)
U_{hub}	Hub velocity (m/s)
U_{min}	Minimum velocity (m/s)
U_0	Wake center velocity (m/s)
U_β	Velocity scale at δ_β (m/s)
x', y', z'	Local coordinate system used for wake measurements (m)

x, y, z	Coordinate system used to refer to disc position in the test section (m)
Δz	Relative distance from the wake center (m)
Δ_U , Δ_W	Uncertainty of the mean flow velocity components
$\Delta_{\overline{u'^2}}$, $\Delta_{\overline{w'^2}}$, $\Delta_{\overline{u'w'}}$	Uncertainty of the Reynolds stresses
Δ_k	Uncertainty of the turbulent kinetic energy
α	Power law exponent
β	Scaling parameter
δ	Boundary layer thickness (m)
δ^*	Displacement thickness (m)
δ_β	Length scale (m)
θ	Momentum thickness (m)
δ^*/θ	Shape factor
σ	Standard deviation of the Gaussian velocity profile
ϵ	The value of σ at rotor plane (initial wake width)
Ω	Out-of-plane vorticity (s^{-1})

CHAPTER 1

INTRODUCTION

1.1 Motivation

Increasing demand for renewable energy stimulates design efforts to achieve more efficient wind turbine systems. The performance and structural integrity of a wind turbine, in addition to numerious other parameters, are affected by the presence of other turbines nearby, espcially in wind farms where a cluster of turbines are sited at the same location in order to produce vast amount of electricity.

One of the key factors for higher production capacity is the need for larger wind turbine rotors. However, there are constraints associated with large-diameter rotors, mainly structural constraints. In addition, larger rotors require larger areas for wind farm installation due to the wake interaction of the wind turbines. The velocity deficit in the wake of a wind turbine generally causes downstream wind turbines to extract less power from the wind, and the relatively high turbulence levels of the wake flow result in high dynamic loading on the downstream turbines [1]. These two effects reduce the energy production and the efficiency of wind farms significantly. In this respect, a comprehensive understanding of the physical phenomena associated with the wind turbine wake flow is required to overcome the aforementioned issues.

In addition to wake interactions occurring in wind farms, the impact of incoming atmospheric boundary layer (ABL) on turbine wakes and performance is also significant. Wind turbines naturally operate within the ABL; hence, they get subjected to atmospheric turbulence, wind shear, and wind direction changes both in time and space. Predicting and characterizing wind turbine operating conditions require detailed knowledge of the atmospheric wind fields as well as wind turbine aerodynamics sometimes down to millimeter scale [2].

Previous studies have been conducted in order to simulate the atmospheric boundary layer (ABL) and investigate its effects on wind turbine rotor/blade performance and wake characteristics both on single and multiple turbine arrangements. Studies have focused on effects of turbulence intensity, wind shear, and atmospheric stability using wind tunnel experiments, numerical studies as well as field measurements which will be discussed in the following sections. However, in terms of wind tunnel studies there still exists a difficulty of correctly simulating the ABL, basically achieving the same turbulence intensities and same turbulent length scales. Although studies have provided a vital contribution on the necessity of investigating this area of research, still there is a demand to better understand the physical aspects of the ABL and its impact on wind turbine performance and wake characteristics.

Porous discs are frequently used to simulate wind turbine far wake characteristics due to their design simplicity. Many studies have been conducted using porous discs, however, most studies are conducted under low turbulence uniform inflow or decaying isotropic turbulence generated by means of grids. In terms of ABL inflow effects, most measurements are limited in the near wake region or taken on horizontal planes (parallel to the ground). However, no study have shown measurements conducted across the vertical plane (i.e. along the shear flow) as well as cover the near and far wake regions. In addition, effects of various wind velocity gradients and turbulence intensity gradients on the wake charactersitcs were not tested before. Therefore, the main motivation in this study is to investigate the effects of inflow boundary on the wake characteristics of a porous disc by successively exposing the disc to different inflow velocity gradients and turbulence intensity gradients. In addition, comparison of the porous disc wake velocity profiles with analytical models is conducted to highlight the deviations in the wake spreading charactersitics, which is not conducted before and it reveals important differences in the wake spreading characteristics of porous disc compared to wind turbines.

1.2 Overview of Wind Shear, Atmospheric Turbulence and Wake Effects

As mentioned previously, wind turbines naturally operate within the atmospheric boundary layer, hence they get subjected to atmospheric turbulence, wind shear, as well as wind directional changes both in time and space [2]. These factors combined represent the normal operating conditions experienced by the wind turbine. In addition, wind turbine placement within wind farms requires comprehensive understanding of the wind conditions for a certain terrain or space such as offshore and onshore conditions [2]. Figure 1.1 shows a typical offshore wind farm *(Horns Rev)* located in the Danish North Sea where turbulence is present in the flow field surrounding the wind turbines.

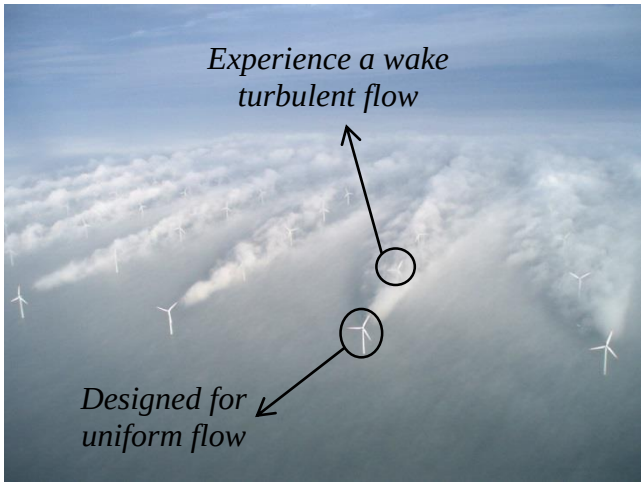

Figure 1.1 *Horns Rev* offshore wind farm [54]

Wind turbines operating within the ABL are subjected to different length, velocity and time scales, making it difficult to analyze their impact on wind turbines or wind farms. These scales range from the millimeter-thin boundary layer on the blade surface to the length of modern turbines, which are approaching 90-100 m [2]. For wind farms these length scales can reach up to hundreds of kilometers in size [2]. Table 1.1 shows typical estimated length, velocity and time scales in wind turbine aerodynamics.

Table 1.1 Length, velocity, and time scale requirements in wind turbine aerodynamics [2]

	Length Scale (m)	Velocity Scale (m/s)	Time Scale (s)
Airfoil boundary layer	0.001	100	0.00001
Airfoil	1	100	0.01
Rotor	100	10	10
Cluster	1000	10	100
Wind farm	10 000	10	1000
Cluster of wind farms	100 000	10	10 000

According to several wind energy communities, turbulence and wind shear present in the atmosphere are important challenges affecting the aerodynamics of wind turbines and wind farms. Therefore, a thorough understanding of the physical phenomena associated with the ABL plays a key role in improving the design and performance of wind turbines. Due to this fact, research is conducted in order to understand the effects of the ABL using numerical and experimental studies as well as field studies.

Wind turbines are installed in wind farms with different layouts or configurations and they are exposed to different wind directions. They are also exposed to wind shear and turbulence from the atmosphere (i.e. ABL). Power losses and dynamic loading are important issues that wind turbines experience in wind farms mainly due to wakes generated from upstream turbines. The wakes coming from upstream turbines have two distinct features, velocity deficits which are responsible for power losses and added turbulence which results in increased fatigue loading on the blades of downstream turbines which compromises their structural integrity.

The structure of the wind turbine wake is very complex where many phenomena are present. To illustrate, the characteristics of the freestream flow, the aerodynamic design and the swirl generated due to blade rotation, the shear layer generated by the tip vortices, the root vortices and the turbine tower, hub as well as the nacelle affect the mean flow field and turbulence structures in the wake [54].

Figure 1.2 shows a schematic figure of the wake region downstream of a typical wind turbine immersed in an ABL. As illustrated in the figure the upstream region is called the induction region, where the velocity drops in proximity of the turbine [54]. The existence of the wind turbine influences both the upstream and downstream (called the near wake) regions of the wind turbine. The region from the turbine rotor to approximately 2-4 rotor diameters downstream is considered as the near wake. In this region the geometry of the wind turbine determines the shape of the wake flow field. This region is dominated by the tip and root vortices shedding from the wind turbine. Moreover, the axial pressure gradient across the rotor plane is responsible for the wake deficit [54]. On the other hand, the far wake is the region where the effect of the turbine rotor is insignificant. In the far wake the focus lies on the modelling of the wake, wake-wake interaction, turbulence modeling and terrain effects [54]. The wake velocity profile in the far wake is axisymmetric, self-similar with a Gaussian distribution [54].

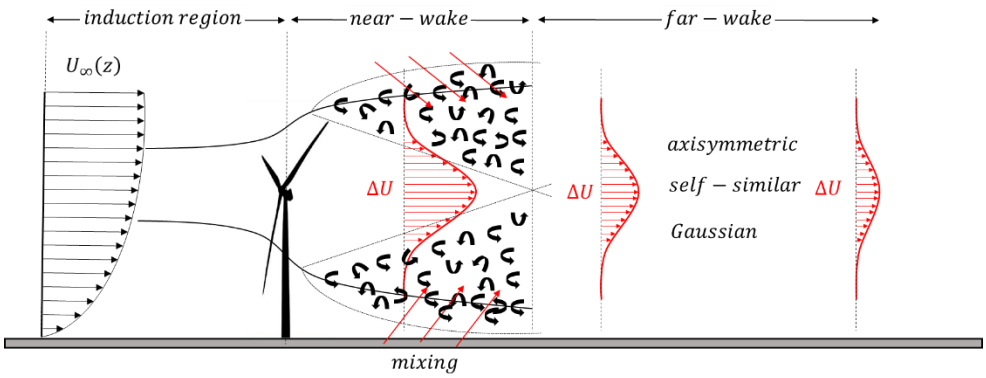

Figure 1.2 Schematic figure of the wake flow field downstream of a wind turbine immersed in an ABL [54]

1.3 Literature Review

Several studies have been conducted in order to investigate the impact of turbulence and wind shear for wind farm control and optimization. These studies range from field measurements for both onshore and offshore wind farms, to wind tunnel studies of scaled-down model wind turbines and wind farms, as well as numerical studies

and comparisons of state-of-art simulations such as large eddy simulation (LES). These studies have shed light into the importance of turbulence and wind shear and their impact on wind farm performance.

1.3.1 Field Measurement Studies

Field measurement studies have been conducted in order to understand the impact of meteorological conditions and atmospheric boundary layer (ABL) properties such as wind shear, turbulence intensity as well as atmospheric stability on the performance, efficiency, and annual energy production of existing wind farms located in different parts of the world. Wake losses and their effects on power deficits of wind farms are also investigated under different atmospheric conditions. Other studies have been used to improve numerical simulations and develop analytical models in order to improve wind farm design and optimization.

For instance, Barthelmie et al. [3-5] investigated the effects of meteorological conditions on the *Vindeby* offshore wind farm in Denmark. Factors such as wind speed variability from land to sea, wind shear, diurnal variability, turbulence intensity as well as atmospheric stability have been investigated to understand their impact on losses due to wakes, energy production as well as turbine loading. Results from these measurements have been also used for engineering wake model validation. Another study conducted by Jensen et al. [6] regarding wake measurements at the *Horns Rev* offshore wind farm situated in Denmark. The study investigated wind speed and turbulence in the wakes of multiple wind turbines both in aligned and diagonal arrangements. They also investigated the wake downstream of the entire wind farm. Their results show that there is large velocity deficit from first row to the second row of turbines, however, wind speed variation is undetectable from the second to the tenth row. The influence of the wind farm wake is still persistent 6 km downstream on wind speed and turbulence measurements.

Christiansen and Hasager [7], and Hasager et al. [8] carried out measurements using Satellite Synthetic Aperture Radar (SAR) to investigate the wake effects from two large offshore wind farms namely *Horns Rev* and *Nysted* in the North Sea. Their

observations show around 8-9% of velocity deficit downstream of the wind turbine arrays, and the wind speed recovery is around 2% over a distance of 5-20 km combined with added turbulence intensity. Similarly, Méchali et al. [9], carried out measurements at *Horns Rev* wind farm to understand the impact of wake effects and wind direction changes on the power production of the wind farm. The results were also used for wake-model validation proposed by Frandsen et al. [10]. Authors show that large power deficits exist where the wind is along the turbine rows. They also show that the wake development and wind direction are strongly affected by atmospheric stability. Finally, the wake model was able to predict the power deficits associated with wake losses for the first two rows. However, towards the end of the wind farm the model seems to over-predict the energy production as compared with the measurements.

Additional studies regarding the impact of wind shear, turbulence intensity, wind direction changes as well as atmospheric stability on power losses due to wind turbine wakes at *Horns Rev* and *Nysted* wind farms in Denmark were conducted by Barthelmie et al. [11,12] and Hansen et al. [13,14]. Results show that turbulence intensity and atmospheric stability have strong influence on the power deficit. They concluded that in stable conditions the power deficits are significant, however, the higher the turbulence intensity the lower the power deficits.

Bardal et al. [15] and Bardal and Saetran [16] investigated the effects of turbulence intensity and wind shear on wind turbine power output and Annual Energy Production (AEP) for a 3MW wind turbine, which was a part of a wind farm located in Mid-Norway (*Valsneset test site*). Results show that low-shear and low-turbulence conditions result in an increase in the AEP. Furthermore, they observed that the largest impact of turbulence on the power appears to be around the rated wind speed. Stival et al. [17] conducted another study using LiDAR measurements at a North American wind farm in the United States of America (USA). They claim that high turbulence intensity associated with high wind shear diminishes wind turbine power production significantly. Sakagami et al. [18] performed measurements in the *Pedra Do Sal* wind farm located in the northwest coast of Brazil. The objective of that study was to investigate the effects of inflow turbulence intensity, wind shear, and

atmospheric stability on the power performance. Their results showed that the inflow turbulence intensity affects the performance of the wind turbines significantly by up to 2.4% of the rated power output at turbulence intensity levels larger than 7% and 3.5% at turbulence intensity levels smaller than 5%.

Wharton and Lundquist [19] presented field measurements of a wind farm located in the West Coast of North America focusing on the impact of atmospheric stability wind turbine power output. They claim that atmospheric stability is related to the wind generated shear, consequently affecting the wind turbine power output. Their results show that the power generated is higher under stable conditions compared to convective conditions with almost 15% difference. Kumer et al. [20], investigated the impact of different stability conditions on wind turbine wakes at ECN's wind turbine test site, *Wieringermeer* in the Netherlands. They showed that the performance of the wind turbine is greatly affected by the wake during stable conditions. Westerhellweg et al. [21] observed the effects of turbulence intensity and stability at *Alpha Ventus* wind farm on the power deficits due to wake losses. Results show that wake effects are significant under stable conditions. The wake width was broader and the power deficits are around 4% larger compared to unstable conditions.

These studies strongly suggest that understanding ABL effects such as inflow wind shear and turbulence is crucial in order to improve the performance and efficiency of wind turbines and wind farms. On the other hand, other studies have focused on modelling the power losses of existing wind farms due to wake effects in order to improve the numerical simulations and analytical models, by integrating the effects of wind shear, turbulence, wind direction, as well as stability. In addition, comparisons were made with field measurements to assess the performance of existing wake models.

For instance, Barthelmie et al. [22-25] collected data from *Middelgrunden* offshore wind farm in order to analyze the wake losses as well as the wind turbine induced turbulence under a variety of wind speed conditions. Results were also compared with state-of-the-art models (such as *WAsP* [26,27] wind farm model, and Frandsen and Madsen [28] model) for predicting power losses and turbulence induced by wind turbine due to wakes. Results show that wake losses are reasonably predicted by

WAsP model, which are largest at low wind speeds and decrease as wind speed increases. Moreover, turbulence intensity shows strong dependency on wind speed and direction, and the added turbulence models seem to generate comparable prediction of the turbulence increase due to wakes. Additional measurements were conducted to evaluate the performance of several other wake models such as *WindFarmer from GH* [29,30], *WAKEFARM from ECN* [31], *CRES-flowNS from CRES* [32], and *NTUA* [33,34]. Analysis showed that wind farm based models under-predict wake losses, whereas CFD based models over-predict the wake losses.

Riedel and Neumann [35] also developed a CFD model to predict the wind and turbulence conditions in large offshore wind farms including the effects of wind shear and turbulence for fatigue analysis. Schlez and Neubert [36] presented an extension to the standard wake and wind flow models *HG WindFarmer* with additional empirical corrections for disturbances coming from the wind farm. Results from validation cases for two large wind farms show that the model accurately represents the losses in those wind farms. Frandsen et al. [37] developed and modified various existing models for wind farm efficiency and for intermediate scale models and validation results were used against data collected from *Horns Rev* wind farm.

Cleve et al. [38] conducted validation for the *Jensen* wake model [39,40] with wake flow data collected from *the Nysted* offshore wind farm. Results show that the *Jensen* model agrees with the power losses between the first and second rows of turbines. Emeis [41] integrated atmospheric stability on the existing wind park model developed by Emeis and Frandsen [42]. The model could be used for first order estimations of wind farm efficiency and its wake effects for different roughness and stability conditions. Gaumond et al. [43,44] made comparisons between the predictions of three wake models against data from *Horns Rev* and *Lillgrund* offshore wind farms. The results show that when the simulations are averaged over wind direction sectors of 30^0, the power production is accurately predicted by the models. On the other hand, within narrow sectors, the wake models under predict the power outputs.

There have been many experimental and numerical works on the wake of a wind turbine and its interaction with the downstream turbines. In these studies, in general, wind turbines are either subjected to uniform low-turbulence free-stream conditions or to inflow conditions with different wind shear and turbulence levels simulating different ABL profiles. Some of the numerical and experimental studies are explained in the following sections.

1.3.2 Numerical Studies

Some of the numerical approaches include the implementation of the actuator disc concept, where the wind turbine is modeled as a solid disc by introducing a force component in the streamwise direction (viz., drag) at the grid points corresponding to the area swept by the turbine rotor [76-81]. Other methods take into account the aerodynamic properties of the blades as well as the rotation effects on the wake, such as the actuator line-based simulations [82-87]. Moreover, numerical investigations on fully resolved geometries combined with the Reynolds-Averaged Navier-Stokes (RANS) equations or more recently by using the Large Eddy Simulations (LES) have also been conducted [88-91]. The former lacks accuracy since it only computes the mean flow and parameterizes the effects of all scales of turbulence. On the other hand, LES show superiority over RANS by computing explicitly the large scales of turbulence and modelling the smaller ones; however, it is still computationally expensive [92].

For instance, Troldborg et al. [82, 93-95] used LES coupled with actuator line technique to simulate the wake interactions of multiple wind turbine operating in uniform and turbulent inflow conditions. Results show that the power deficits, mean wake deficit, and added turbulence intensity at different downstream positions are comparable with field measurements. Furthermore, in the case of turbulent flow as compared to uniform flow the wake characteristics are significantly changed, in the sense that, root and tip vortices sustain to shorter distances downstream of the turbine in the turbulent case. Moreover, the swirl in the wake decays rapidly in the turbulent

case. Finally, results show that ambient turbulence results in faster wake recovery and increased blade loading on downstream turbine.

Calaf et al. [79] employed LES to investigate the vertical transport of momentum and kinetic energy in a wind farm immersed in an ABL. They claim that the fluxes of kinetic energy in the vertical direction associated with turbulence have the same order of magnitude as the power extracted by the forces modeling the wind turbines. Churchfield et al. [96] used LES to investigate the effects of atmospheric and wake turbulence on wind turbine dynamics. Results show that under unstable conditions the downstream turbine performance has improved significantly compared to neutral conditions.

Wu and Porté-Agel [60,80], and Porté-Agel et al. [86,99] employed LES coupled with an actuator disk model (ADM) with and without rotation to investigate the wake downstream of model wind turbine in a neutrally stratified ABL. Results show that the characteristics of the far-wake downstream of the wind turbine are in agreement with the experiments. However, in terms of the near wake characteristics the ADM with rotation shows better predictions compared to the one without rotation. Moreover, the spatial distribution of the mean velocity deficit, turbulence intensity, and turbulent shear stress in the wake are dependent on the ambient turbulence. Wu and Porté-Agel [100-102] also used a similar approach to study the flow within wind farms with different configurations and their effects on power losses. Results show that wind farm layout has a significant influence on wake flow field and the performance of the wind turbine. For instance, in staggered layout the lateral interaction between the wakes is stronger resulting in a more homogenous wind farm wake along the spanwise direction and faster wake recovery. Lu and Porté-Agel [103] investigated the wake interactions within wind farms under stable conditions. Results show non-axisymmetric wind turbine wakes compared with non-uniform conditions.

Ivanell et al. [104] used LES coupled with the actuator disk model to simulate the wakes generated by the *Horns Rev* offshore wind farm. Results show that this approach could capture the main production within the wind farm as compared with the measurements. Furthermore, wind measurements downstream of the wind farm

show that LES slightly over predicts the wake recovery downstream of the wind farm. Politis et al. [105] used RANS based models coupled with actuator disk methods to predict the power production for wind farms in complex terrain. Wang et al. [106] performed experimental and numerical (LES) investigations on wake redirection techniques in a boundary layer wind tunnel. Dörenkämper et al. [107] studied the impact of stable ABL on the wakes and performance of offshore wind turbines using LES. Results show that the wake effects are stronger in stable conditions compared to neutral and unstable situations. In addition, they claim that the distance of the wind farm to the coast has a major influence on the power output. Schulz et al. [108] used Delayed-Detached-Eddy Simulations (DES) to investigate the effects of atmospheric turbulence on wind turbine wake in complex terrain. Results show that the complex terrain leads to deflection of the wake.

1.3.3 Wind Tunnel Studies

Wind tunnel studies of the effect of turbulence and wind shear on wind turbines and wind farms are very extensive in the literature. Studies have focused on investigating the effects of turbulence intensity and wind shear on the performance of single turbine, tandem turbines, as well as wind turbine arrays. Research has focused on load measurements, wake characteristics as well as tip vortex characteristics. Additional work in terms of wind farm control strategies such as the effect of yaw misalignment on wind turbine wakes and wind farm performance has been reported as well.

For instance, Sicot et al. [109] performed measurements on 2-bladed rotor under different inflow turbulence intensities with integral length scales of the order of the chord length of the blade by utilizing a regular grid. They claim that the power and thrust are slightly affected by turbulence levels.

Chamorro and Porté-Agel [55,56] and Zhang et al. [58] performed a series of experiments investigating the effect of ABL under different thermal stratification and turbulence structures, on the wake characteristics and performance of model wind turbines. Results show that until 20 rotor diameters downstream of the wind turbine

the impact of the wake on turbulence fields is still present. In addition, under stable conditions the velocity deficit represented as power-law decay is faster compared to neutral conditions. The experiments were extended to wind farm study to better understand the turbulent flow inside and above the wind farm and its impact on the power output as reported in Chamorro and Porté-Agel [113]. Chamorro et al. [114] investigated the flow within aligned and staggered wind farm placed in a thermally neutral ABL. They claim that the staggered layout is more efficient in transferring momentum from the ABL when compared with aligned layout having the same streamwise and spanwise spacing, resulting in better overall wind farm power output of around 10%.

Another wind tunnel study was performed by Cal et al. [115] on a 3 x 3 array of model wind turbines using PIV under atmospheric boundary layer conditions in order to investigate the vertical transport of momentum and kinetic energy across the wind turbine array. Their results show that the vertical transport of kinetic energy associated with the Reynolds shear stresses have the same order of magnitude as the power extracted by the wind turbines. Maeda et al. [116,117] performed a wind tunnel study of the effects of inflow turbulence intensity generated by grids of different blockage ratios on the wake and power output of a model wind turbine. Their results show that the turbulence of main flow affects the wind turbine wake profile, i.e. high turbulence intensities enhance entrainment of the main flow and the wake, as well as faster recovery of the wake. In addition, they found out that the tip vortex structure is diffused due to higher turbulence levels. Mahmoodilari [118] also performed wind tunnel measurements both on wind turbine blade as well as model wind turbine. Results show that the lift-to-drag ratio of the wind turbine blade increases significantly which resulted in higher power coefficient of the model turbine. His arguments were based on the fact that high turbulence intensity associated with smaller turbulent length scale produced this effect. This had also an impact on the performance of a model wind turbine operating under the same freestream condition where the results show an increase in power coefficient.

Hu et al. [119] performed an extensive experimental study to characterize the dynamic wind loads and evolution of unsteady vortex in the near wake of a HAWT

operating within the ABL. Results show that the higher turbulence levels caused wandering of the tip vortices as well as wake meandering. Similar studies were reported by Zhang et al. [120]. Ozbay [121,122] and Tian et al. [123-125] investigated the effects of the ABL on the performance and wake interference of individual and multiple wind turbines. They reported that for wind turbines located over the hilltop, the effect of the wake is limited by the elevation of the hill. However, downstream of the hill, the wake effects are more drastic resulting in a drop in the power outputs of the wind turbines situated in this region.

Mikkelsen [126] performed experiments of the effect of freestream turbulence using a turbulence generating grid and her results show that the power coefficient drops by 2.4% which is not expected since turbulence intensity results in better performance. She argued that the reason behind this reduction was due to drag. In addition, she also performed wake measurements using hot-wire anemometry, and the results show that the velocity gradients and turbulent kinetic energy in the tip vortices were diffused and due to freestream turbulence. Moreover, faster wake recovery in the velocity profiles due to increased turbulence levels were also observed. Al-Abadi [127] and Al-Abadi et al. [128] performed wind tunnel tests using two turbulence generating grids (fine and coarse) and the results show that the higher the turbulence level the higher the power coefficient. Their arguments were based on the fact that higher turbulence leads to suppressing the boundary layer separation and delaying the onset of stall. In addition, higher turbulence levels lead to damping out the tip vortices, hence reducing tip losses and leading to faster recovery of the wake flow region. Bastankhah [129] and Bastankhah and Porté-Agel [130-132] performed a series of wind tunnel studies to investigate the interaction of the ABL with wind turbine wakes under different yaw conditions. Results show the wake velocity fields are skewed with respect to the wake centerline. The presence of counter-rotating vortex pair in the wake as well as vertical displacement of the wake center under highly yawed conditions were also reported.

Bartl and Saetran [133] performed wind tunnel experiments on the effect of different turbulent inflow conditions on the performance and wake measurements of two in-line model wind turbines. Their results show that for the case of high turbulence

uniform flow the power coefficient of both the upstream and downstream (positioned at 5.18D downstream of upstream turbine) turbines increased by 1.3% and 29.65% respectively. However, for the case of high turbulence non-uniform flow (i.e. wind shear) the power coefficient of the upstream turbine decreased by 1.95% and that of the downstream turbine increased by 26.9%. In addition, Bartl et al. [134] and Schottler et al. [135] performed wind tunnel tests of the effect of wind shear on wind turbine performance under different yaw conditions. Results were used for numerical validation and the tests focused on the wake characteristics behind a yawed wind turbine. For instance, asymmetric wake velocity fields were observed when the yaw angle is changed. Double Gaussian velocity deficit distribution was also observed for all inflow conditions due to the detection of counter-rotating vortex pair. In addition, they found out that inflow turbulence has significant effect on the wake flow.

Jin et al. [136] studied the effect of freestream turbulence on the wake structure of a model wind turbine. The study focused on the integral length scale evolution as well as the impact of the large-scale motion coming from the inflow. They reported that the inflow turbulence results in faster wake recovery and that the integral scale evolves linearly along the axis of the rotor. The growth rate of the integral scale was 5 times larger in the high turbulence case than that with low turbulence. Coudou et al. [137] also performed an experimental study on wind turbine wake meandering inside wind turbine array immersed in the ABL. In addition, Wind-tunnel measurements using particle image velocimetry (PIV) of the influence of turbulence on two in-line model wind turbines were conducted by Talavera and Shu [138] using an active grid system as a turbulence generator. They claim that by using turbulent inflow the efficiency of both the upstream and downstream turbines was highly improved. Moreover, the performance of a single turbine improved significantly almost three times in the turbulent case as compared to the laminar one. The reason for this improvement is due to suppressing of the flow separation around wind turbine blades.

Studies have also been conducted on wind turbine rotor blades in order to investigate the effects of freestream turbulence on the lift and drag characteristics as well as

boundary layer separations [139-145]. Most of the results show similar outcomes, that the lift-to-drag ratio has increased and that boundary layer separation on the turbine blade is delayed to higher angles of attack.

As mentioned previously, experimental studies attempt to investigate the aerodynamics of wind turbines by reproducing them at small scales in wind tunnels. However, these scaled wind turbine models suffer from several physical and operational limitations, especially when the wind tunnel test section is relatively small. For instance, low Reynolds numbers due to smaller blade chord lengths may lead to degraded aerodynamic performance for wind tunnel models when compared to the life-size wind turbines. In addition, since the wake of the wind turbine strongly depends on the thrust realized by the rotor disc, a wind turbine model has to be designed to produce the same thrust coefficient [59,146]. Neff et al. [147] claimed that the wake behaviour is strongly dependent on the tip speed ratio, Reynolds number, thrust coefficient and power coefficient.

As an alternative to small wind turbine models, the porous disc model has been introduced for wind turbine wake research in wind tunnels [148], which is the experimental counterpart of the actuator disc model used in numerical applications. This concept has been widely used in previous studies to model the wake of the wind turbines [149-159]. Porous disc models are easy to produce since they do not consider the exact geometry and details of the wind turbine rotor. In addition, since many numerical models are based on the actuator disc concept, comparisons can be made relatively easily. In other words, using a porous disc for model validation offers great simplifications and requires less computational time. However, porous discs still suffer from some limitations. For instance, they can only be used to model the far-wake characteristics of actual wind turbines, whereas the near-wake characteristics cannot be captured because the effect of the rotating blades is inherently excluded. Furthermore, one needs to know the wake characteristics of the actual wind turbine in order to produce a representative porous disc which is not possible before it is built [160].

Porous discs were utilized by Aubrun [149] to model wind turbine wake characteristics [149-152]. The study was inspired by the work of Vermeulen and Builtjes [148]. The porous discs were made of metallic mesh with different porosity levels, disc sizes, and mesh sizes in order to parametrize the wind turbine wake characteristics. In an experimental study conducted by Aubrun et al. [149-151], the wake characteristics of a three-bladed wind turbine model and a porous disc of the same diameter in two different inflow conditions (ABL and decaying isotropic turbulence) were compared. Hot-wire measurements were carried out at two downstream locations (0.5 and 3 diameters downstream) and the results include comparisons of mean velocity, turbulence intensity, flatness, skewness, integral length scale and power spectra. The results show that around 3 diameters downstream the above mentioned quantities could be modeled using a porous disc with good agreement, especially under turbulent atmospheric boundary layer inflow condition where the turbulence intensity is sufficiently high. Furthermore, wind farm simulations were carried out using a 3 x 3 wind turbine and porous disc arrays. Their results show good agreement in terms of thrust and power coefficients, as well as the distribution of mean velocity, velocity deficit, and turbulence intensity. Furthermore, these studies have also been extended to investigate the wake meandering phenomenon as well as the displacements of wake centerline downstream of porous discs (e.g. Aubrun et al. [153] and España et al. [154]).

Lignarolo et al. [155,156] and Camp and Cal [157,158] investigated the wake of a porous disc and a model wind turbine with similar thrust coefficient using particle image velocimetry (PIV). Lignarolo et al. [155,156] used laminar inflow conditions in order to eliminate the effect of ambient turbulence so that the wake-induced mixing characteristics of the model wind turbine and the porous disc could be compared directly. They showed that the magnitude of the spanwise velocity component and the turbulence intensity levels are higher in the wake of the wind turbine due to rotation of the blades and the presence of the tip vortices, respectively. Their comparative analysis revealed a different turbulent mixing between the porous disc and wind turbine. Camp and Cal [157] investigated the wake of the center model in the last row of a 3 x 3 model array. They found that the mean kinetic energy

transport in the far wake could be represented by the porous disc; however, in the near wake significant differences occur in the areas where rotation is dominant. Furthermore, Camp and Cal [158] also conducted comparisons between the porous disc and model wind turbine based on proper orthogonal decomposition by looking at the energy modes and showed that the first mode for the longitudinal velocity is similar for both the disc and turbine.

Neunaber [159] conducted a comparison between a porous disc and a model wind turbine under different inflow conditions (laminar inflow, regular grid inflow and active grid inflow) up to 4 diameters downstream. Results show that the porous disc and wind turbine have similar wake characteristics and the influence of inflow conditions are minimal in the far wake unlike the near wake region due to different mixing mechanisms between the turbine and disc. Similar observations were found by Bossuyt [161] and Helvig et al. [162].

Finally, porous disc studies have also been performed for wind farm control, such as different yaw conditions as well as investigating the impact of unsteady loading on the wake of porous discs (e.g. Howland et al. [163] and Yu et al. [164]). These studies strongly suggest that porous discs could be used to model the far-wake characteristics of wind turbines if specific conditions are met.

1.3.4 Analytical Wake Models

In terms of simulating wind turbine wakes, analytical wake models are frequently used due to their reasonably accurate prediction capability at low computational cost [45]. Several analytical models were proposed in the literature, some of which are discussed hereafter. One of the most commonly used wake models in the industry is the one developed by N.O. Jensen [39] in 1983 and later improved by Katic et al. [40]. The Jensen model assumes a top-hat distribution for the velocity deficit and was claimed to be based on the conservation of momentum. However, it was later shown by Bastankhah and Porté-Agel [53] that this model was derived by use of only the mass conservation. Furthermore, the Jensen assumes that the wake grows linearly with distance downstream and therefore the wake decay coefficient is assumed to be

constant. Jensen suggested that the wake decay coefficient is 0.1, whereas values of 0.04 [38,46] or 0.05 [23,47] for offshore conditions and 0.075 [48] for onshore ones were reported in the literature. This model has been extensively used in commercial software such as WAsP [47], WindPRO [48], WindSim [49], WindFarmer [50], and OpenWind [51]. Frandsen et al. [10] proposed a wake model based on both mass and momentum conservation with the same top-hat assumption. Larsen [52] developed a semi-analytical wake model based on Prandtl's turbulent boundary layer equations. The Larsen model assumes a self-similar axisymmetric velocity profile.

Studies have shown that the top-hat distribution is an unrealistic representation of the velocity deficit in the wake and results in several errors [53]. For instance, these wake models tend to underestimate the velocity deficit at the wake center and overestimate it at the edges of the wake [54]. Furthermore, Bastankhah and Porté-Agel [53] showed that these models result in significant errors in the power estimation of a wind farm with varying wind directions.

Several studies reported that the velocity deficit in the wake of a wind turbine has a self-similar Gaussian axisymmetric shape. This particular velocity deficit shape in turbine wakes has been observed in wind-tunnel measurements [55-59], numerical simulations [60], and field measurements [44,61]. Consequently, many Gaussian-based analytical models have been proposed such as Ishihara wake model [62] and Jensen-Gaussian wake model [63]. In addition, Bastankhah and Porté-Agel [53] proposed an analytical model with a Gaussian shape profile for the velocity deficit by employing both the mass and momentum conservation. The model also assumes a linear expansion of the wake similar to the Jensen model. Subsequently, Ishihara and Qian [64] proposed a modified Gaussian wake model based on Bastankhah and Porté-Agel model which improves the predictions of velocity deficit in the near wake region. In addition, they proposed a new formula for the wake growth rate taking into account the ambient turbulence intensity and thrust coefficient. Finally, instead of using a Gaussian shape for the velocity deficit, others have suggested the use of a cosine function to represent the velocity deficit (e.g. Tian et al. [65] and Zhang et al. [66]).

The aforementioned wake models have been developed to predict the optimal layout and performance of future wind farms, which minimizes wake losses and therefore increases the power production. Therefore, several studies ranging from field measurements [5,25,67-70] to wind tunnel experiments [71-75] have been used to assess the performance of these models in predicting the wind turbine wake.

For instance, Sorensen and Nielsen [67] conducted a comparison between three wake models (Jensen, Larsen, and CFD-based eddy viscosity model) at the *Horns Rev 1* offshore wind farm. Their results show that the Jensen wake model performed better than the other wake models. Barthelmie et al. [5] compared several wake models with data obtained from *Vindeby* offshore wind farm for single wakes. The models seem to predict the wake profile shapes qualitatively but not quantitatively as reported by the authors. However, due to the fact that there is a large uncertainty in the wind speed measurements, it was difficult to determine which model performed the best. Barthelmie et al. [25] compared data from two offshore wind farms (*Nysted* and *Horns Rev 1*) with the Jensen wake model and two CFD-based wake models. They stated that the Jensen model performs worse than the other two models and significantly underpredicts the power deficit. Shakoor et al. [68] made comparisons between Jensen, Larsen, Frandsen, and eddy viscosity model and observed that the Jensen wake model is better for wind farm layout optimization. Göçmen et al. [69] conducted comparisons among six wake models using data from the *Sexbierum* onshore wind farm and *Lillgrund* offshore wind farm. Their conclusions were different for the two wind farms. At *Lillgrund*, Larsen and FUGA performed worse than the others, whereas at *Sexbierum*, FUGA, Larsen, and a standard RANS model underestimate the velocity deficit, while Jensen performs better than the others. Archer et al. [70] performed comparisons between six analytical wake models with data from three wind farms. They showed that the Jensen model and Xie and Archer model perform better than the others for all wind farms under all wind directions.

In terms of wind tunnel studies, Renkema [71] compared the outcomes of the wind turbine wake models (namely, Jensen, Larsen and Frandsen) with wind tunnel measurements. Results revealed that the Larsen wake model shows significantly better performance than the other models. Polster [72] made a similar comparison

among six different wake models including the newly-developed Gaussian-based models. It was shown that the Jensen-Gaussian wake model gives the best overall performance for all of the test cases. Stein et al. [73] compared the Bastankhah and Porté-Agel and the Jiménez & Crespo wake models with wind tunnel measurements. They reported that both models are capable of reproducing the general trends regarding the wake growth and the decay of the centerline velocity deficit. Campagnolo et al. [74] compared six analytical wake models with wind tunnel measurements under different conditions and concluded that the Bastankhah and Porté-Agel model seems to provide the best results for a wide range of inflow and wind turbine operating conditions. Amiri et al. [75] compared the predictions obtained by some of the analytical wake models with the measured wakes of uniform and non-uniform porous discs at 4 diameters downstream. They showed that the predicted wakes by the Ishihara model fairly agrees with the measured porous disc wakes unlike the Jensen and Larsen models.

These studies that stem from field measurements and wind tunnel measurements show that analytical models are very efficient in predicting the wake characteristics downstream of wind turbines or within wind farms. However, no model shows superiority over the others due to the approach and assumptions involved in deriving these wake models [70]. Therefore, it is vital to know under which conditions these wake models would perform best and be utilized for future wind farm design and optimization. In addition, improvements to these wake models in order to cover wider range of inflow and operating conditions are necessary.

1.4 Objectives and Scope

The main objective of this thesis study is to investigate the effects of the inflow boundary layer, which is representative of a neutral ABL, on the wake development characteristics in terms of mean flow, turbulence, wake scaling as well as proper orthogonal decomposition in the wake of an isolated porous disc with radially non-uniform porosity. This is achieved by exposing the disc to different velocity and turbulence intensity gradients as it is lowered deeper inside the boundary layer. Two-

dimensional two-component particle image velocimetry (2D2C PIV) measurements are performed in the wake of a 0.12 m diameter disc in an open-return suction type boundary layer wind tunnel. In addition, comparisons of the porous disc wake velocity fields against analytical models are presented by focusing on the wake growth rate characteristics of porous discs immersed in a boundary layer.

1.5 Thesis Outline

The present thesis is structured as follows. Chapter 1 presents the introduction with a detailed literature review of the effects of wind shear and turbulence by means of field studies, numerical studies, as well as wind tunnel studies. In addition, analytical wake models used in the literature are also summarized. Chapter 2 describes the structure and characteristics of the ABL with a literature review on the simulation of the ABL inside wind tunnels. Chapter 3 presents the experimental and numerical simulation of the ABL inside RÜZGEM large scale wind tunnel and METUWIND C3 boundary layer wind tunnel. Chapter 4 talks about the porous disc experimental setup, measurement details and PIV measurements. Chapters 5 and 6 present the results and discussions of the main study. Conclusions and future works are presented in chapter 7.

CHAPTER 2

ATMOSPHERIC BOUNDARY LAYER

This section presents a brief description of the basic phenomena and characteristics of the atmospheric boundary layer.

2.1 Overview of the Atmospheric Boundary Layer

The atmospheric boundary layer (ABL) is considered as the lowest part of the atmosphere where many physical phenomena are considered to be present such as mass, momentum and heat interaction between the air and the ground. Therefore, the physical quantities such as velocity, temperature, density, pressure and relative humidity can vary significantly in space and time. For instance, variation in the horizontal speed with height above the surface within the atmospheric boundary layer is called the vertical profile of the wind speed or vertical wind shear [165].

The complex nature of the atmospheric boundary layer is due to many factors. For instance, the diurnal effects which means convection during the day and stratification at night. Complex terrain such as buildings, forests, hills and mountains. Large weather events, such as the replacement of air masses by prevailing winds, clouds and precipitation [166].

The ABL thickness ranges from 100 m to 3 km depending on the time of day and the physical phenomena present. Two primary factors are present when there is interaction between the surface and the air. These two effects are classified as mechanical and thermal effects. The mechanical effect results from the friction exerted by the air against the ground, also this friction creates wind shear and turbulence. The thermal effect arises because of diurnal intermittency, the sun shines during the day (*convection*) and absent at night (*stratification*). The convection

causes mixing motions to be present which typically results in a thick ABL [166]. Figure 2.1 shows typical development of the ABL over the course of the day. During sunrise heating from the surface results in a convective boundary layer (CBL), however, at sunset cooling from below creates a thin nocturnal boundary layer (NBL).

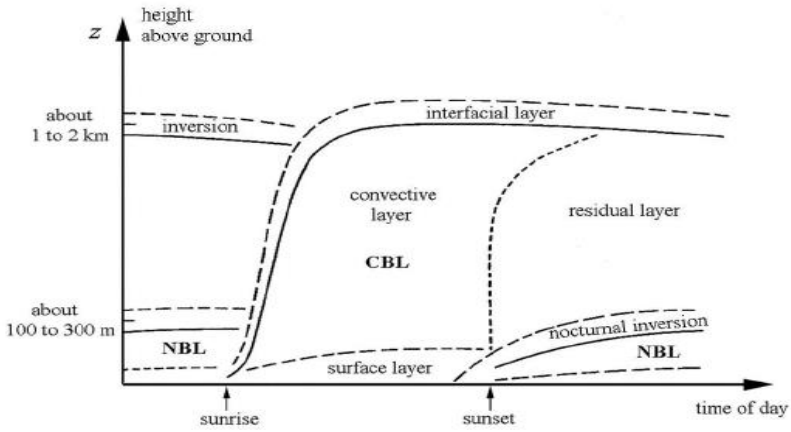

Figure 2.1 Typical development of the atmospheric boundary layer (ABL) during the course of the day [166]

2.2 Structure of the Atmospheric Boundary Layer

The ABL is influenced by many phenomena such as convection and stratification as stated earlier. This section describes the structure of the ABL under neutral conditions.

The ABL can be divided into two main regions, an inner region and an outer (*Ekman layer*) region. The inner region is divided into two more layers, an interfacial (*roughness*) sublayer and an inertial (*logarithmic*) sublayer. Figure 2.2 shows a schematic representation of the structure of the ABL.

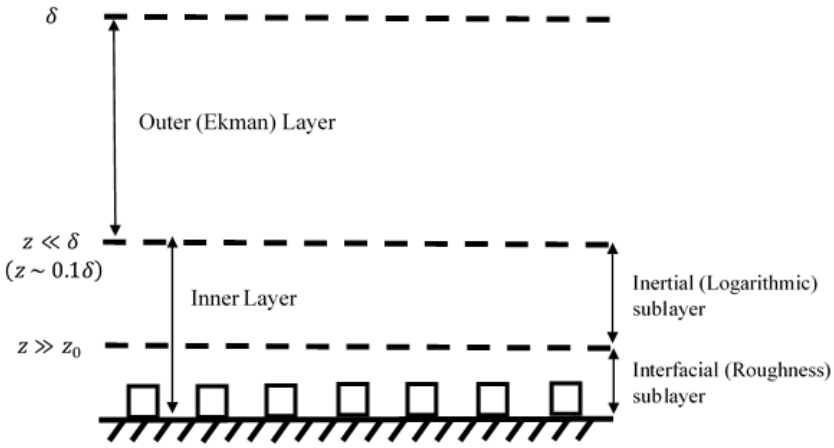

Figure 2.2 Schematic layout of the structure of the atmospheric boundary layer (ABL) [170]

The region occupied by the surface roughness features is considered as the interfacial (or roughness) sublayer. In this region, the Reynolds stress $(-\rho\overline{u'w'})$ reaches a maximum value at the edge of the surface roughness and then decreases to zero at the ground [192]. This is due to the pressure forces acting on the individual roughness elements resulting in momentum loss [192]. The thickness of the interfacial sublayer is called the zero-plane displacement, z_d, where the Reynolds stress is maximum [192]. When the surface roughness is small or insignificant, e.g., in open terrain, the zero-plane displacement can be assumed zero [171]. The inertial (logarithmic) sublayer is the region which is directly affected by the surface characteristics or terrain exposure. The surface characteristics can be divided into four distinct terrain types, urban, suburban, rural and flat. These terrain exposures are described in details in the following sections [192]. Beyond this region is the outer region, i.e., the Ekman layer, where the surface roughness characteristics have minimal effects [192]. The Reynolds stress decreases from a maximum in the inner region to zero at the maximum height. Variation of th Reynolds stress within the ABL is illustrated in Figure 2.3.

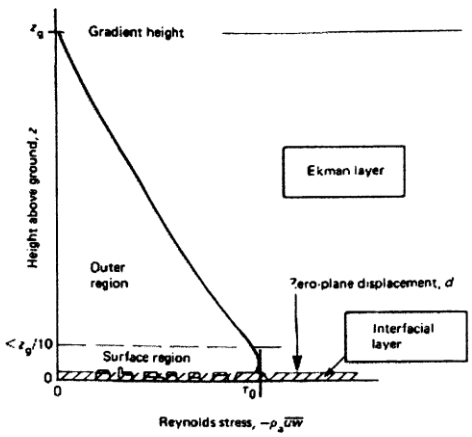

Figure 2.3 Variation of the Reynolds stress within the atmospheric boundary layer [171]

2.3 Characteristics of the Atmospheric Boundary Layer

2.3.1 Atmospheric Boundary Layer Stability

Atmospheric stability is defined as the tendency to resist vertical motions (fluxes) or to suppress existing turbulence. The stability of the ABL is also important for wind speed gradients that are encountered in the first layers above the ground [165].

Due to the significant changes occurring within the ABL, the boundary layer stability is classified into three types: *stable*, *unstable* and *neutral*. Large surface heating causes hot air close to the surface to rise and due to pressure reduction will cool down adiabatically, this is known as unstable stratification (*associated with it high turbulence intensity, develops during the day*). However, if the cooling is not sufficient to maintain thermal equilibrium with the surrounding, large convective cells will be present resulting in a thick boundary layer with large-scale turbulent eddies. Stable stratification (*associated with it low turbulence intensity, develops during night)* occurs when the rising air becomes colder than the surrounding, which results in suppressing its vertical motion. When the thermal processes are absent, i.e., the rising air is in thermal equilibrium with the surroundings, neutral stratification occurs where the mechanical effects are dominant because of the friction exerted by

the wind against the ground surface, resulting in the wind to be sheared and turbulence to be present [167]. Studies have shown that the ABL stability is one the key factors affecting wind farm performance since it is directly related to turbulence intensity and wind speed as mentioned previously in Chapter 1.

2.3.2 Mean Velocity Profiles

The variation of the horizontal velocity from zero at the surface (*no-slip condition*) and increasing with height results in the distribution of velocity within the ABL called vertical profile of wind speed or vertical wind shear [165]. Wind resource assessment and the design of wind turbines are directly affected by the vertical wind profile, hence, it is vital to define this profile correctly [165]. The two widely used mathematical models for vertical wind profile are the Log-law and the Power-law models. These models are defined for homogenous, flat terrain as follows:

- Logarithmic wind profile is defined as:

$$U(z) = \frac{u^*}{k} ln\left(\frac{z}{z_0}\right), \qquad [2.1]$$

where z is the height above the ground, z_0 is the aerodynamic surface roughness length and $k = 0.4$ is the von Karman's constant [165]. $u^* = \sqrt{\frac{\tau_0}{\rho}}$ is defined as the friction velocity, where ρ is the density of the air and τ_0 is the surface shear stress or wall shear stress defined as $\tau_0 = \mu\left(\frac{d\bar{u}}{dy}\right)_{y=0}$. Another definition of the friction velocity in terms of the Reynolds stress is defined as: $u^* = \sqrt{-(\overline{u'w'})}$. The roughness length z_0 represents the roughness of the surface, ground or terrain. Typical values of the roughness length for different types of terrain exposures can be found in Burton et al. [167].

- Power law profile is defined as:

$$\frac{U(z)}{U(z_{ref})} = \left(\frac{z}{z_{ref}}\right)^{\alpha}, \qquad [2.2]$$

where $U(z)$ is the wind speed at height z, $U(z_{ref})$ is the reference wind speed at reference height z_{ref} and α is the power law exponent, where α depends on the surface roughness and the atmospheric stability [168]. ASCE 7-16 [169] defines four different exposure types and describes the associated terrain conditions based on the power law exponent.

2.3.3 Turbulence Intensity

Another important characteristic of the ABL is the turbulence intensity. The turbulence intensity is defined as the ratio of standard deviation (σ) of the wind speed to the mean wind speed (U). The length of the time period used for the calculation of the mean wind speed and standard deviation in wind energy engineering is normally around 10 minutes and the sampling rate is at least 1 Hz [165]. Equations 2.3-2.5 show the turbulence intensities along the longitudinal, lateral and vertical directions. The value of the turbulence intensity is the greatest along the longitudinal direction and the smallest along the vertical direction.

$Longitudinal\ turbulence\ intensity$:

$$I_u = \frac{\sigma_u}{U} = \frac{\sqrt{\overline{u'^2(z)}}}{U} \qquad [2.3]$$

$Lateral\ turbulence\ intensity$:

$$I_v = \frac{\sigma_v}{U} = \frac{\sqrt{\overline{v'^2(z)}}}{U} \qquad [2.4]$$

$Vertical\ turbulence\ intensity$:

$$I_w = \frac{\sigma_w}{U} = \frac{\sqrt{\overline{w'^2(z)}}}{U} \qquad [2.5]$$

The turbulence intensity is normally in the range of 0.1 to 0.4 inside the ABL [165]. Studies have shown that the highest levels of turbulence intensity are associated with the lowest wind speeds. Another important feature of the turbulence intensity is its dependence on atmospheric stability. Figure 2.5 shows the relationship between the turbulence intensity and wind speed with atmospheric stability. As one can observe

the lower levels of turbulence intensity are associated with high wind speeds and stable conditions, whereas higher levels of turbulence intensity are associated with low wind speeds and unstable conditions. In addition, higher wind speeds associated with low turbulence intensities are significant in the neutral conditions [12].

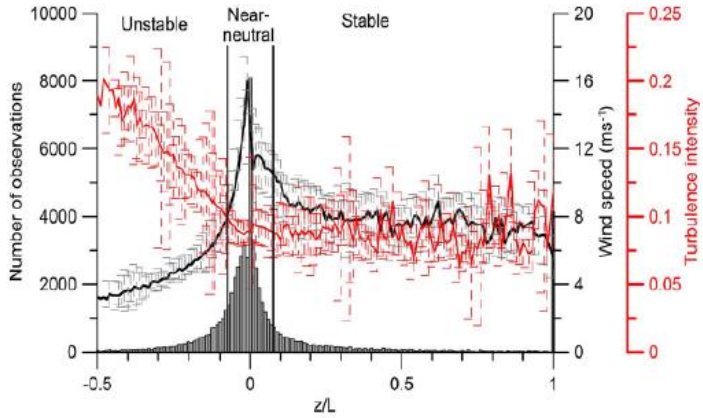

Figure 2.4 Dependency of the turbulence intensity on wind speed and atmospheric stability [12]

Moreover, turbulence intensity is also affected by other factors such as the surface roughness, the height above the ground, as well as the topographical features such as hills or mountains, as well as trees and buildings [167]. Barthelmie et al. [4] argued that in offshore conditions the ambient turbulence levels are lower than the ones over onshore conditions. They measured values around 6-8% offshore and 10-12% onshore.

2.3.4 Turbulence Length and Time Scales

The integral time scale of turbulence is a measure of the average time over which wind speed fluctuations are correlated with each other. This is found by integrating the autocorrelation function from the zero lag to the first zero crossing [165]. Typical values of the integral time scale are less than 10 seconds. In the ABL the integral time scale is dependent on many factors such as location, atmospheric stability and terrain type, which results in larger values of integral time scales than 10 seconds [165].

The integral length scale is found by multiplying the integral time scale by the mean wind velocity. The integral length scale is a measure of the largest separation distance over which components of the velocity for a certain eddy are correlated at two distinct points. The spectrum of energy for large and small scale eddies is characterized by the integral length scale [165]. In addition, in the ABL the integral length scales depend on the height above the ground as well as on the terrain exposure. There are 9 integral turbulent length scales shown as follows:

L_u^x, L_u^y, L_u^z $length\ scales\ for\ the\ u$
$- component\ along\ the\ longitudinal\ direction$

L_v^x, L_v^y, L_v^z $length\ scales\ for\ the\ v - component\ along\ the\ lateral\ direction$

L_w^x, L_w^y, L_w^z $length\ scales\ for\ the\ w$
$- component\ along\ the\ vertical\ direction$

The most important integral length scale is L_u^x which defines the size of eddies along the longitudinal direction due to velocity fluctuation in the longitudinal direction expressed as shown in equation 2.6 using Taylor's hypothesis of frozen turbulence.

$$L_u^x = \int_0^\infty R_u^x(\Delta x) d\Delta x \,, \qquad [2.6]$$

where R_u^x shown in equation 2.7 is the cross-covariance of the fluctuating longitudinal velocity components separated at a spatial distance.

$$R_u^x(\Delta x) = \frac{\overline{u_1'(t) \cdot u_1'(t - \Delta t)}}{\overline{u'^2_1}} = R_u^x(\Delta t) \,;\ \Delta t = \frac{\Delta x}{2} \qquad [2.7]$$

If the velocity fluctuations are assumed to be traveling with the mean velocity $\bar{u}(\vec{r}, t)$, then the longitudinal integral length scale can be written as follows:

$$L_u^x = \bar{u} \cdot \int_0^\infty R(\tau) d\tau \,, \qquad [2.8]$$

where $R(\tau)$ is the autocorrelation function of the fluctuating longitudinal velocity, and τ is the time lag between the measured fluctuating velocities.

2.3.5 Power Spectrum of Turbulence

Power spectra of velocity describes the frequency content of the wind-speed fluctuations. Kolmogorov, 1941 presented a clear description of the small-scale structure of turbulence and the energy transfer process (i.e. energy cascade) from larger eddies to smaller ones [170]. Kolmogorov stated that small-scale turbulent eddies are associated with high frequency end of the spectrum, which have independent properties and are considered isotropic [170]. On the other hand, large-scale turbulent eddies are associated with low frequency end of the spectrum [170]. This energy spectrum of turbulence is shown in Figure 2.6.

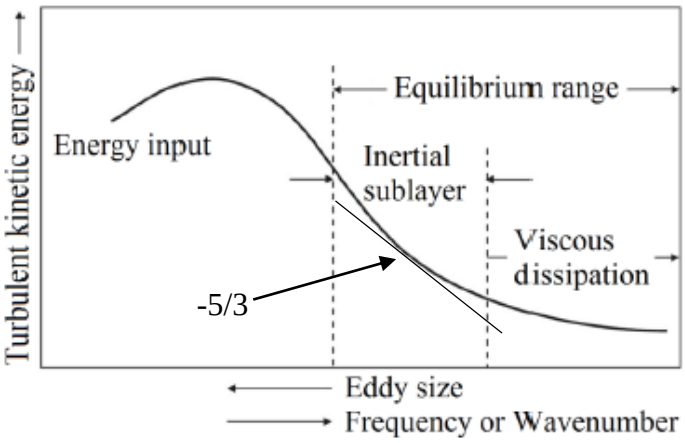

Figure 2.5 Energy spectrum of turbulence [170]

This spectrum is divided into three regions [192]:

- The energy-containing range: corresponds to low frequency range, which contains most of the turbulent energy. This energy is then transferred to the higher frequency region by means of inertial forces.
- The inertial subrange: considered as an intermediate range, which follows Kolmogorov's -5/3 law. In this region the energy is neither created nor dissipated, but transferred to smaller eddies.

- The dissipation range: corresponds to the high frequency range associated with smaller eddies, where viscous forces are dominated and cause the kinetic energy to dissipate into heat energy.

2.4 Simulation of the Atmospheric Boundary Layer

Wind tunnel simulation of the atmospheric boundary layer could be achieved by implementing passive techniques such as the use of spires or vortex generators, barrier walls, roughness elements, grids as well as a combination of these devices. Alternatively, active techniques such as the use of active grids, jets, multiple fans have been utilized as well.

In order to correctly simulate the ABL inside wind tunnel, certain conditions need to be met such as the velocity profile, turbulence intensity as well as turbulent length scales and power spectrum. As mentioned previously wind turbines operate within the ABL, therefore it is vital that the natural ABL is correctly simulated in order to better predict the performance and wake development of the wind turbines. Such wind tunnel that are used for ABL studies are called Boundary Layer Wind Tunnel (BLWT). These wind tunnels normally have long test sections around 15-20 meters, and are specifically designed to produce thick boundary layer [172]. However, not all wind tunnels are BLWTs, certain wind tunnels have short test sections (i.e. aeronautical test sections) which require the design of specific devices to be integrated at the inlet of the test section in order to produce the desired characteristics of the ABL [172].

Simulation of the atmospheric boundary layer started several decades ago. For instance, Owen and Zienkiewicz [173] utilized a grid of parallel rods with varying spacing from bottom to top of the tunnel in order to generate a shear flow represented by a linear or logarithmic velocity profile as show in Figure 2.7.

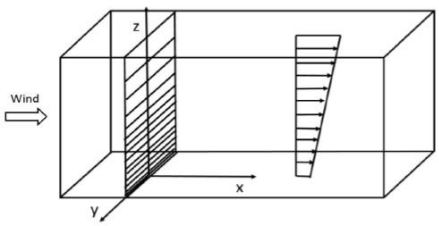

Figure 2.6 Schematic layout of the grid of parallel rods inside the wind tunnel test section [173]

Armitt and Counihan [174] developed methods for simulating the ABL for rural terrain inside a wind tunnel. They claim that a working section length of 4-5 boundary layer thickness is required to model the desired atmospheric flow. Furthermore, Counihan [175-177], designed four different types of vortex generators as shown in Figure 2.8, i.e. triangular, cranked triangular, plane elliptic and the wedge elliptic, in order to simulate the ABL of rural terrain. Counihan found out that the characteristics of the wakes behind the triangular and elliptic were different. To illustrate, for triangular generator significant momentum loss in the inner region of the boundary layer was observed, however; in the outer region the momentum loss was insufficient. The elliptic generator on the other hand was suitable to represent the atmospheric flow for rural terrain. Moreover, Counihan [178] claims that in order to represent urban wind conditions, the magnitude of the roughness length and zero-plane displacement are significant in reproducing the desired characteristics of this type of terrain. Therefore, he developed an empirical formula using “LEGO” elements based on wind tunnel measurements to relate the aerodynamic roughness length to the planar density distribution of the roughness elements. Later on, Counihan [179] modified his rural simulation technique for an urban terrain by introducing a fetch of roughness elements covering the entire length of the test section floor. The results show that the simulation was an adequate representation of the atmospheric conditions of an urban environment.

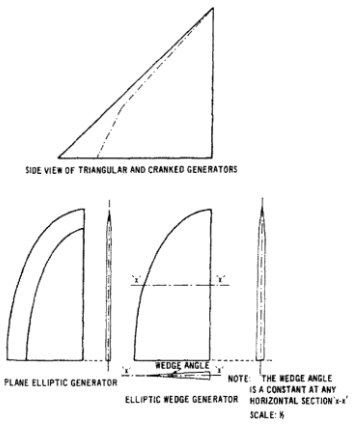

Figure 2.7 Vortex generators used by Counihan [176]

Standen [180] designed different triangular shapes called spires to generate a thick shear layer as shown in Figure 2.9. He stated that the ABL can be well simulated up to 450 m.

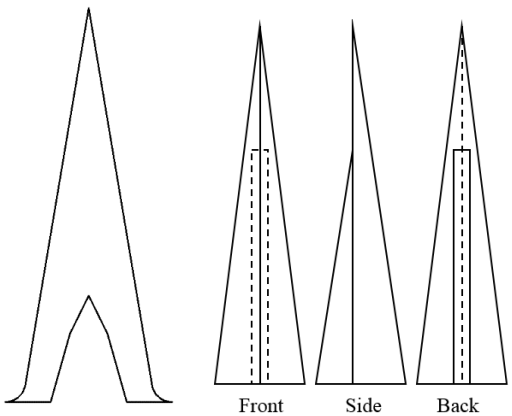

Figure 2.8 Geometry of Spires used by Standen [180]

Irwin [181,182] argued that Standen's approach might result in very high spire drag as well as high power law exponent. Therefore, he improved Standen's method and pointed out that the spire geometric features were not that critical. Irwin developed a new approach to design spires with a triangular shape as presented in Figure 2.10. His results show a good match between the simulated ABL and the full-scale measurements in terms of the vertical velocity profile, turbulence intensity, integral length scale and power spectrum. These results were obtained by installing triangular shaped spires at the inlet of the wind tunnel test section followed by a fetch of roughness elements. The significance of the design approach for spires allowed measurements to be conducted in different wind tunnels by changing only the size

of the spires. A description of the design methodology will be presented in Chapter 3.

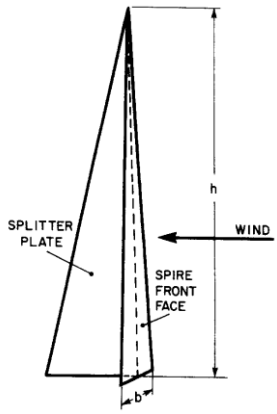

Figure 2.9 Triangular spire with splitter plate used by Irwin [182]

Peterka and Cermak [183] used spires extending the full height of the test section followed by an appropriate fetch of roughness elements to generate a 52″-thick boundary layer and with power law exponents ranging from 0.14-0.3. Cook [184-186] used a barrier downstream of a grid to simulate the lower one-third of the ABL with a realistic integral length scale. However, the roughness element fetch used was spaced so closely that a large effective wall displacement occurred. Raine [187] simulated a neutrally stable ABL using a combination of a non-uniform bi-plane lattice grid, trip fences of various height and “Torro” baseboard floor roughness. Results show that the wind speed profile and the turbulence characteristics are in agreement with the real ABL for rural conditions.

Tieleman and Reinhold [188] used the spire-roughness technique consisting of three spires followed by a staggered fetch of roughness elements to simulate rural and suburban terrains. Farell and Iyengar [189] reproduced the ABL using a quarter-elliptic, constant- wedge-angle spires or triangular flat spires together with a barrier wall in order to produce the initial momentum deficit followed by a staggered set of cubic roughness elements in order to simulate the terrain conditions. Their work was based on Counihan [176]. Their results show that the thickness of the ABL amounts to 80 % of the height of the spires using triangular spires. Whereas, the boundary layer thickness has the same height if quarter-elliptic spires were used. The wind

velocity profile of the simulated ABL fits well with the power law model having a power law exponent of 0.28. In addition, the turbulence intensity showed that this technique could be implemented to simulate the terrain conditions of urban cities.

Phillips et al. [190] implemented an array of non-uniformly spaced flat plates as shown in Figure 2.11 to generate shear flow with zero pressure gradient. The fully developed flow could be adjusted by changing the length of the plate and the spacing between two the plates.

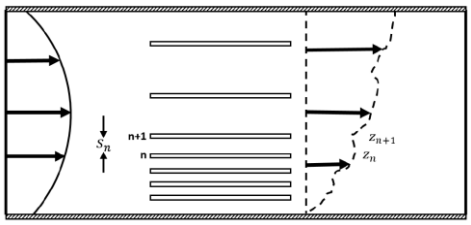

Figure 2.10 Schematic layout of the array of differentially-spaced flat plates in wind tunnel test section [190]

Wittwer and Moller [191] and Balendera et al. [193] reproduced the ABL for urban terrain using five quarter-elliptic wedge spires, a castellated barrier and many roughness elements were used. Results show that the power law exponent was about 0.29 which is within the range for urban terrains. Burton [192] attempted to simulate the ABL for rural terrain exposure by using triangular-shaped spires, two fence barriers and a carpet, whereas, for the suburban terrain exposure he utilized spires combined with fence barriers and roughness elements. Results show that ABL could be simulated at a model scale of 1:350 for rural and 1:300 for the suburban exposures respectively. Finally, recent studies have been conducted based on previously used passive devices to artificially simulate the ABL inside the wind tunnel [194-216].

Therefore, based on this literature survey of the methods used to simulate the ABL inside wind tunnels, the Irwin's approach [182] for spire-roughness element technique will be adopted in this thesis study due to its design simplicity, design approach and wide applications, in order to generate the ABL inside RÜZGEM Large Scale Boundary Layer Wind Tunnel and RÜZGEM C3 Boundary Layer Wind Tunnel using experimental and numerical approaches.

CHAPTER 3

NUMERICAL SIMULATION OF THE ATMOSPHERIC BOUNDARY LAYER IN WIND TUNNELS

A new large scale wind tunnel is under development at METU Center for Wind Energy (RÜZGEM). This wind tunnel is a closed-loop multi-purpose wind tunnel with a $3\,m \times 7\,m \times 20\,m$ boundary layer test section. Inside this test section the atmospheric boundary layer (ABL) will be simulated using the spire-roughness element technique in order to represent different terrain exposures (or categories) as defined by American Society of Civil Engineers (ASCE 7-16). Since no experimental data are available yet, Computational Fluid Dynamics (CFD) will be implemented as a tool in order to provide an initial assessment for the simulation of the ABL. However, in order to validate the CFD approach, another wind tunnel test case from literature will be used for comparison. This wind tunnel has $1.82\,m \times 1.82\,m \times 9.8\,m$ test section. Four different test cases have been simulated and the results show reasonable agreement between the experiments and numerical results. For RÜZGEM wind tunnel different configurations of spires, roughness elements and spires with roughness elements have been simulated in order to find the best combination for a certain terrain exposure. Results show that CFD can provide an initial assessment of the ABL inside the RÜZGEM Large-scale Boundary Layer Wind Tunnel (BLWT) test section. For instance, terrain exposures A and B require both spires combined with roughness elements, on the other hand, for terrain exposures C and D spires alone will be sufficient to achieve the target velocity profiles. Finally, another numerical simulation of the ABL was conducted inside RÜZGEM C3 boundary layer wind tunnel at the aerodynamics laboratory and validated with experimental data. This wind tunnel has a $1\,m \times 1\,m \times 8\,m$ test section length. Results show reasonable agreement between the experiments and numerical results for the test cases considered.

3.1 Validation Study

3.1.1 Wind Tunnel Facility

The wind tunnel used in this study is an open-loop suction type boundary layer wind tunnel located at the University of Windsor Ontario, Canada as shown in Figure 3.1. The wind tunnel has a total length of 17.6 meters. It consists of an inlet contraction, a development section of 7.35 meters long, and a test section of 2.45 meters long with a cross sectional area of 1.82 m x 1.82 m. For more information regarding this wind tunnel refer to Song [216].

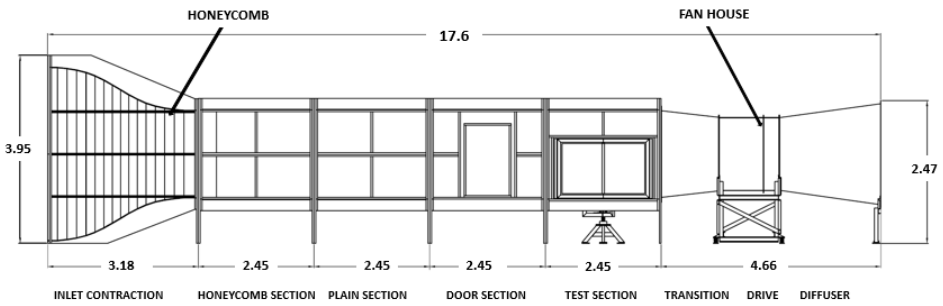

Figure 3.1 Open-loop boundary layer wind tunnel facility at the University of Windsor [216]

3.1.2 Numerical Methodology

All CFD simulations in this study are conducted using the commercial CFD package FINE/Open developed by NUMECA International [217]. The FINE/Open solver is a 3-dimensional, unstructured, multi-block and multi-grid finite volume code. A sample computational domain and grid for the validation study are shown in Figure 3.2. The grid is an unstructured hexahedral mesh with nearly 1-5 million cells depending on the test case considered. Half-models have been considered in order to reduce the domain size and computational time with symmetry imposed as shown in Figure 3.2a for the small wind tunnel. 3D steady-state compressible RANS equations with *k-ω M-SST* (Shear Stress Transport) turbulence model [218], have been solved with 2nd-order central numerical schemes and *Merkle* preconditioning to account for

the very low speed condition [219]. The working fluid (air) is treated as an ideal gas with viscosity obtained from the *Sutherland* law. Convergence criteria have been considered based on the outlet mass flow rate, where after sufficient number of computations the outlet mass flow rate remains steady.

Figure 3.2 shows the computational domain with the boundary conditions as well as the unstructured hexahedral mesh for spires with roughness elements case with a closed-up view of the boundary layer resolved around the spires and roughness elements. As mentioned previously half-models have been used for the test cases in order to reduce the computational size and time.

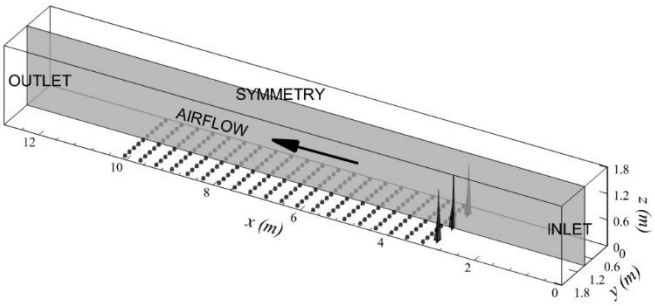

(a)

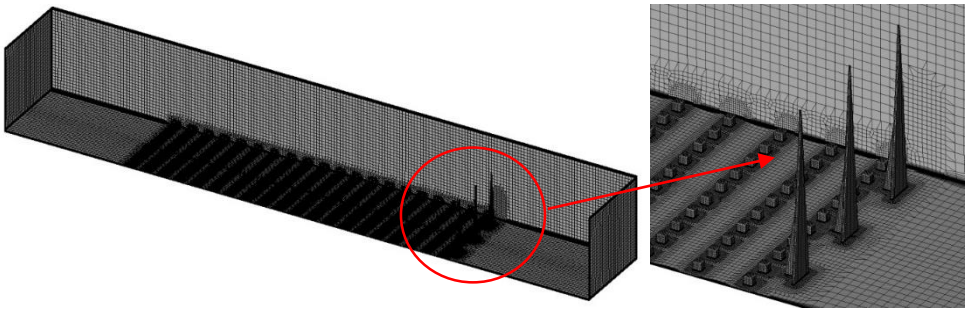

(b)

Figure 3.2 (a) Computational domain, (b) Unstructured hexahedral mesh with a close-up view of the mesh around the spires and roughness elements

3.1.3 Grid Independence Study

The results of a numerical simulation are generally dependent on the size of the mesh being used. A too coarse mesh will result in a significant error, and as the mesh size

gets finer this error should reduce as a consequence [220]. However, if the size of the mesh elements is small enough that the numerical results are close to the experimental data, a further decrease in cell size should not affect the solution significantly. Therefore, in here we present a grid independence study in order to identify how coarse the grid can be without having significant errors. Figure 3.3 shows the velocity magnitude profiles for 3 refinement levels conducted for the 3-spire case, and the 3-spire with roughness elements case. Results show that there is no significant difference between the grid sizes used, and this has proved that using a coarser mesh will suffice for the test cases considered. This analysis has limited the number of elements between 1-5 million depending on the test case considered.

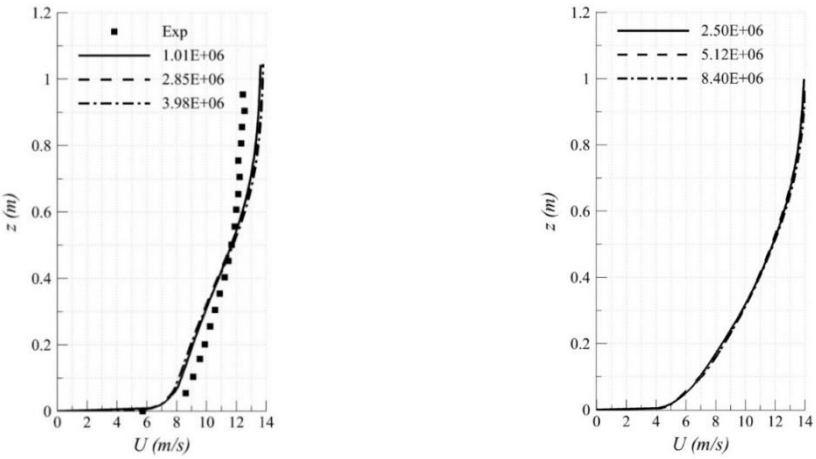

(a) (b)

Figure 3.3 Grid independence study: (a) 3-spire case, (b) 3-spire with roughness elements case

3.1.4 Results of the Validation Study

The validation study is based on the study of Song [216] where experiments are conducted inside a low-speed open return wind tunnel with cross-sectional area of 1.82 m x 1.82 m as shown in Figure 3.1 previously. The length of the boundary layer development section and the working test section is 9.8 m. Spires and roughness elements are located at the beginning of the development section. Different cases have been tested inside the wind tunnel for spires and roughness elements as well as combinations of both. It should be noted here that an additional 3 m straight section

was added upstream of the spires and roughness elements in order to compensate for the inlet contraction. Previous studies show that adding an extension will have no effect on the results as long as the distance between spires and measurement locations is kept the same [221]. An additional reason is to allow the flow to initially develop before encountering the spires and cubes [211]. However, care should be taken not to make this section too long otherwise a boundary layer will develop upstream of the spires and roughness elements and this could affect the expected results.

The CFD simulations for the cases considered have been compared with the experimental results from Song [216]. The velocity used for the test cases is 12 m/s as measured from the inlet of the boundary layer development section. Four test cases have been considered in the analysis, namely, 3 spires, 5 spires, roughness elements (20 x 10 array-aligned), and 3 spires with roughness elements.

Figures 3.4 and 3.5 show the comparison of the streamwise velocity profiles obtained with CFD and the experimental results. The measurements were taken at the center of the turntable of the wind tunnel test section. As one could observe there is a reasonable agreement between the CFD and experiments. The velocity profiles show similar trends as well as comparable boundary layer thicknesses. Unlike the 5-spire case the 3-spire case seems to slightly under predicts the velocity values in the lower part of the boundary layer, whereas, the roughness element case over predicts the velocity values. This has been reflected in the quantitative results of the power law exponents and boundary layer properties.

Table 3.1 shows a quantitative comparison of the CFD results with the experimental data using the boundary layer properties such as displacement thickness, momentum thickness and the shape factor. The boundary layer thickness is measured using the $U_\delta = 0.99U_{max}$ (U_δ: velocity at the edge of the boundary layer) rule. Moreover, using the velocity profiles the displacement thickness and momentum thickness have been calculated using the *Trapezoidal* rule for definite integrals.

Results show that the boundary layer properties are in general comparable in predictions with the experimental data, though there are differences. Nevertheless,

one can conclude that CFD simulations could give a reasonable assessment of the effects of spires and roughness elements to be used in the RÜZGEM Large-Scale BLWT test section.

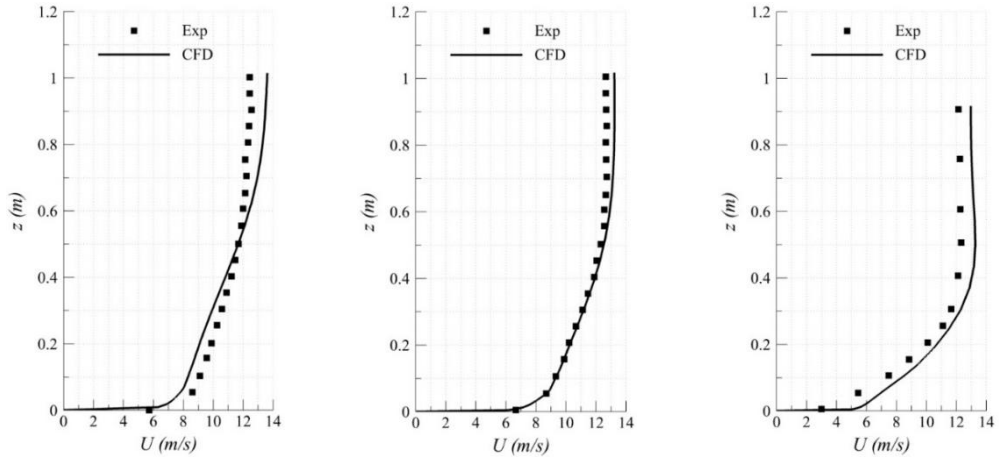

(a) (b) (c)

Figure 3.4 Velocity magnitude profiles: (a) 3-spire case, (b) 5-spire case, and (c) roughness elements (20 x 10 array) case

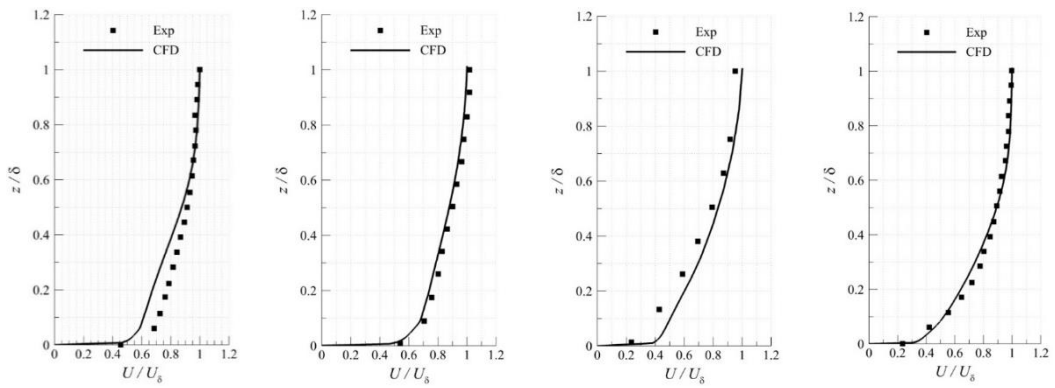

(a) (b) (c) (d)

Figure 3.5 Normalized velocity profiles: (a) 3-spire case, (b) 5-spire case, (c) roughness elements (20 x 10 array) case, and (d) 3-spire with roughness elements case

Table 3.1 Summary of the atmospheric boundary layer properties

Test Cases	Properties	α	$\delta\ (m)$	$\delta^*\ (m)$	$\theta\ (m)$	H
3-spire case	*Exp.*	*0.15*	*0.95*	*0.12*	*0.09*	*1.28*
	CFD	*0.19*	*1.07*	*0.17*	*0.12*	*1.40*
	Error (%)	26.67	12.63	41.67	33.33	9.4
5-spire case	*Exp.*	*0.14*	*0.61*	*0.07*	*0.06*	*1.27*
	CFD	*0.17*	*0.69*	*0.10*	*0.08*	*1.33*
	Error (%)	21.43	13.11	42.86	33.33	4.72
Roughness elements case	*Exp.*	*0.36*	*0.41*	*0.11*	*0.06*	*1.71*
	CFD	*0.28*	*0.43*	*0.09*	*0.06*	*1.56*
	Error (%)	22.22	4.88	18.18	0	8.77
3-spire with roughness elements	*Exp.*	*0.27*	*0.96*	*0.16*	*0.10*	*1.54*
	CFD	*0.29*	*1.19*	*0.21*	*0.13*	*1.59*
	Error (%)	7.40	23.96	31.25	30	3.25

Figure 3.6 shows the velocity magnitude contours at the mid-plane section of the wind tunnel for the test cases considered. As expected the effect of spires is significant in the boundary layer and is felt all the way until the exit of the test section especially within the wake of the spires. Moreover, one can observe that as we move downstream and away from the spires the flow starts to recover to the freestream flow. The case of 3-spire shows significant effect than the 5-spire case since it has larger spire size. Similarly, roughness elements also affect the boundary layer by adding more energy and momentum to the flow. For this reason, a combination of spires and roughness element could produce the desired boundary layer and power law exponent. As mentioned previously, the spires dictate the thickness of the ABL and the roughness element improves the lower part of the ABL in order to represent a certain terrain category.

Figure 3.7 also shows the velocity contours on the downstream planes of the spires and roughness elements. Mirror planes have been generated in order to show the

complete flow field for better visualization. Results show that after a certain distance downstream of the spires the flow becomes developed and no significant changes occur in the velocity profiles and boundary layer thickness. In addition, the effect of the spires diffuses in the freestream flow as one would expect. However, the larger the spire height the more significant the effect will be on the flow field and the longer it takes for the spire effects to disappear.

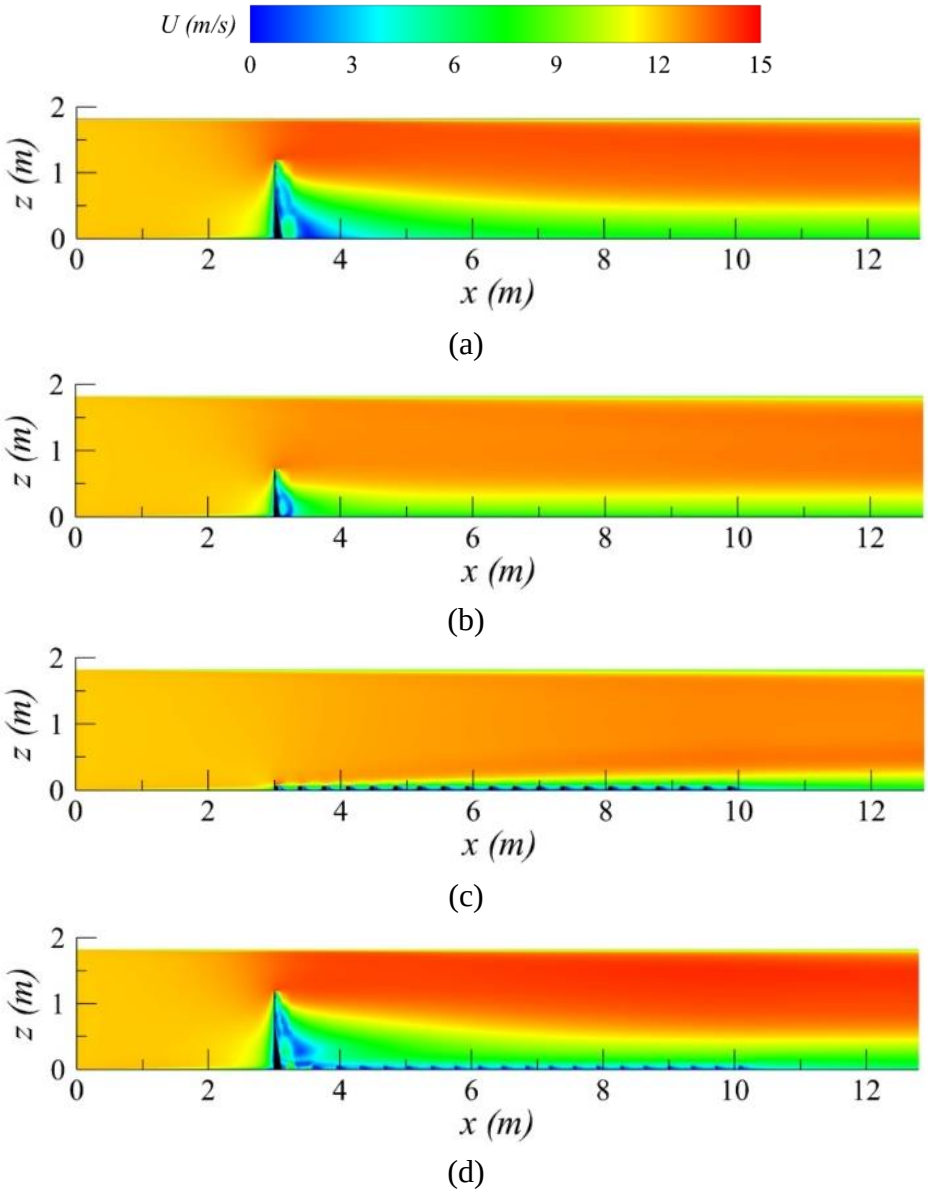

Figure 3.6 Velocity magnitude contours at the mid-plane: (a) 3-spire case, (b) 5-spire case, (c) Roughness elements (20 x 10 array) case, and (d) 3-spire with roughness elements case

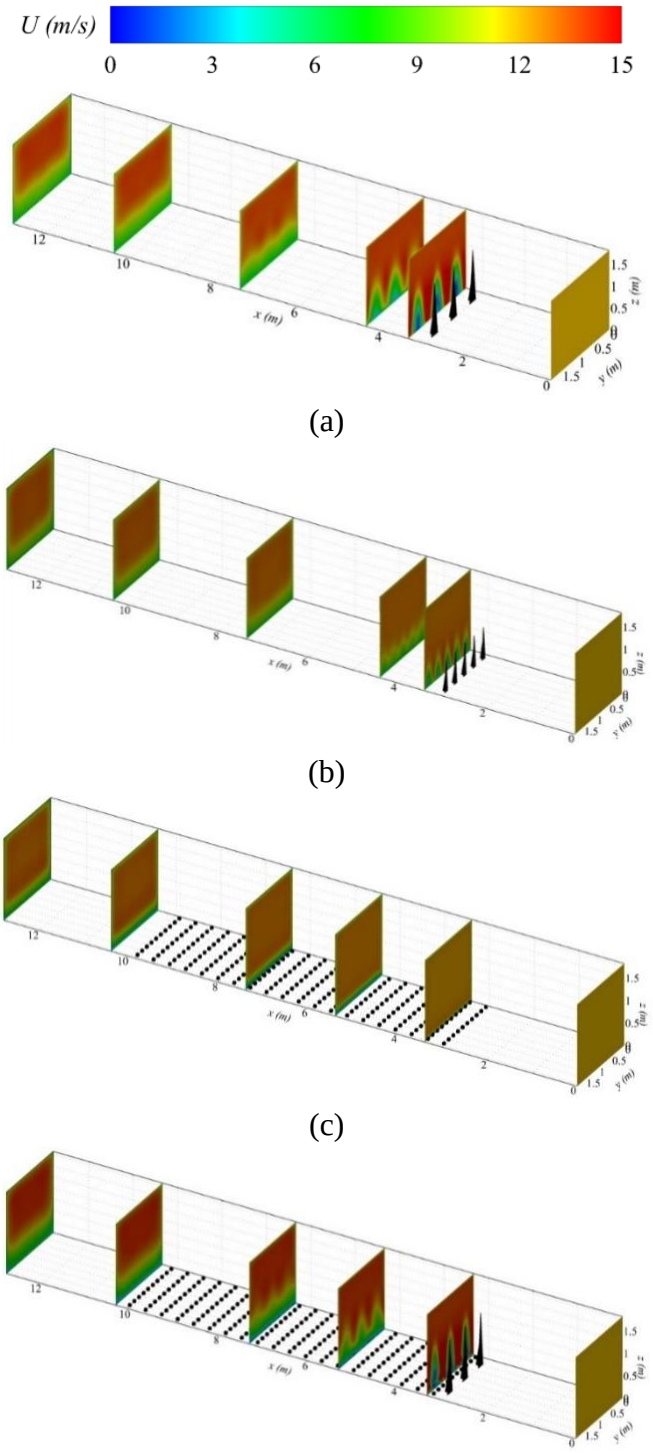

Figure 3.7 Velocity magnitude contours: (a) 3-spire case, (b) 5-spire case, (c) Roughness elements (20 x 10 array) case, and (d) 3-spire with roughness elements case

3.2 RÜZGEM Large-Scale Boundary Layer Wind Tunnel (BLWT)

In this section we will present the preliminary CFD simulations of the ABL inside RÜZGEM large-scale boundary layer test section in order to provide an initial assessment of the boundary layer characteristics. The aim is to represent different terrain exposures with different power law exponents as defined by ASCE 7-16 [169]. Four different terrain exposures namely A, B, C and D will be simulated inside the wind tunnel boundary layer test section. The spire-roughness element technique developed by Irwin [182] will be implemented for the simulation of the ABL.

3.2.1 Wind Tunnel Facility

RÜZGEM Large Scale Multi-Purpose Wind Tunnel is a closed loop atmospheric wind tunnel facility with interchangeable test sections as shown in Figure 3.8. The high speed test section is located on one side of the loop, which has a $2.5\,m \times 2.5\,m$ cross-section and is $10\,m$ long and the wind speeds can reach up to $100\ m/s$. On the other side of the loop there is the low-speed boundary layer test section with a $3\,m \times 7\,m$ cross-section and is $20\,m$ long, and can reach wind speeds up to $30\ m/s$. Both test sections have turntables for model installations and the one in the boundary layer test section has a diameter of $6.4\,m$.

The high-speed test section sits on an air-bearing/guide rail system, which is used to move the test section in and out of the plenum room. When the test section is moved out a $3\,m$ diameter open-jet is created, which is designed to be used for aerodynamic measurements of rotating systems such as model wind turbines and helicopter rotors as well as propellers. The tunnel is of steel construction with multiple honeycombs and screens for high flow quality. It is driven by a 2×3 axial fan array of $2.4\,MW$ power in total. Its temperature control is achieved by a $750\,kW$ heat exchanger that is connected to a cooling tower outside the building. The entire tunnel structure is situated in a large hall of a new building. The tunnel sits on concrete columns above the floor in the hallway, which is equipped with a 10-ton overhead crane.

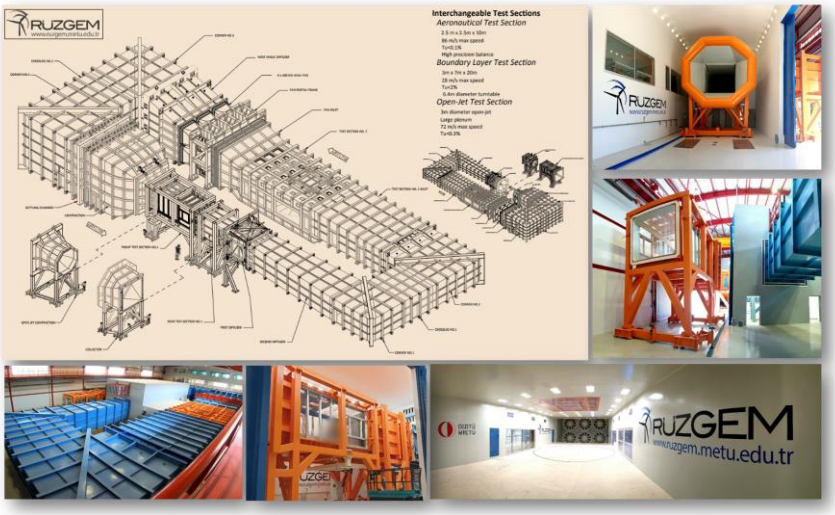

Figure 3.8 RÜZGEM large scale multi-purpose wind tunnel

3.2.2 Design Methodology for Spires and Roughness Elements

3.2.2.1 Design Methodology for Spires

The geometry of the spire should be designed in order to achieve a specific atmospheric boundary layer depth that corresponds to a particular value of the power law exponent in the velocity profile which represents a specific terrain (or exposure) type. To achieve lateral uniformity and homogeneity in the mean velocity, the spires should be arranged symmetrically at the inlet of the test section. This uniformity is expected to be at approximately 6-spire heights downstream of the spire location. Irwin [182] suggested that the spires are spaced laterally at an interval of approximately half the spire height ($s = h/2$).

The spire lateral spacing, s is related to the test section width (W) and the number of spires (N) by the following formula:

$$Spire\ Lateral\ Spacing: s = \frac{W}{N}, \qquad [3.1]$$

The spire height, h should be two times of the spires lateral spacing (s), i.e.

$$h = \frac{2W}{N} \qquad [3.2]$$

Irwin [182] provided a relationship between the boundary layer thickness-to-spire height ratio, δ/h and power law exponent, α using several wind tunnel simulations, as shown in Figure 3.9.

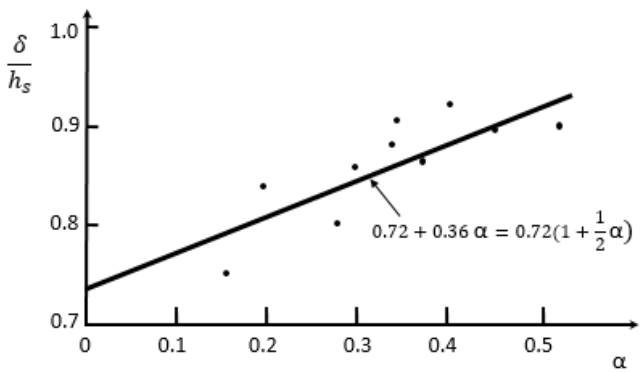

Figure 3.9 Relationship between δ/h and α at $X_0 \approx 6h$ [182]

The relationship between the spire height h, boundary layer thickness δ and power law exponent α is as follows:

$$\delta = 0.72h\left(1 + \frac{1}{2}\alpha\right) \qquad [3.3]$$

The test section of the wind tunnel is considered as a control volume as reported in Irwin's method. A schematic layout of the wind tunnel test section is shown in Figure 3.10. At a distance approximately 6-spire heights downstream of the spires, the desired wind velocity profile is assumed to have the form of:

$$\frac{U(z)}{U_\delta} = \left(\frac{z}{\delta}\right)^\alpha, \qquad [3.4]$$

where $U(z)$ is the wind speed at a height z, U_δ is the wind speed at the edge of the boundary layer δ, z is the height above the wind tunnel floor, and δ is the boundary layer thickness.

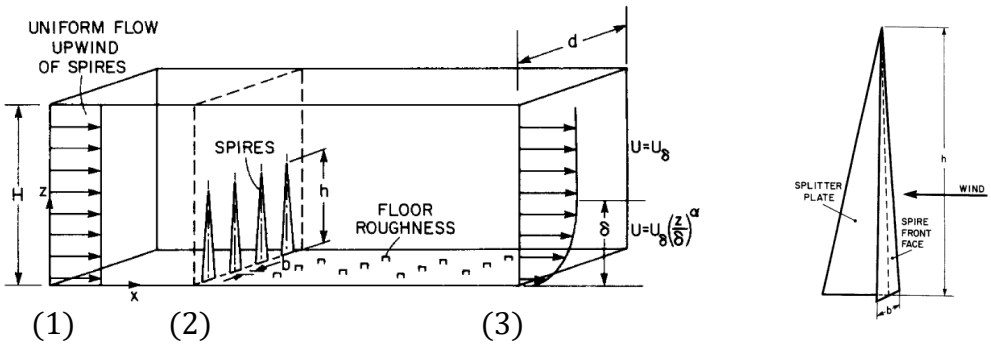

(a) (b)

Figure 3.10 (a) Schematic layout of the test section control volume [182], and (b) triangular spire with a splitter plate [182]

As one can observe from Figure 3.10a, the inlet of the wind tunnel test section is defined as station 1, station 2 refers to the location of the spires, and station 3 refers to the location downstream of the development region. [216]. Irwin in his approach considered the control volume to be the working section between stations 1 and 3. Based on the Conservation of Momentum applied across the control volume the design formulae for spire shape are derived [216]. The derivation is based on the excess of momentum flux at station 3 over that at station 1 which is equal to the force due to pressure drop from station 1 to station 3 minus the sum of the reaction force of the spires and frictional forces of the ceiling, walls and floor on the air.

Which can also be written as:

$$\rho W \int_0^H U_3^2 dz - \rho U_1^2 HW = (p_1 - p_2)HW - \frac{1}{2}\rho U_2^2 C_{D_0} A_s - \frac{1}{2}\rho U_e^2 C_f X_0 W, \quad [3.5]$$

where 1, 2 and 3 refer to stations; ρ is the density of the air, p is the static pressure, H and W are the height and width of the test section, respectively. C_f is the effective surface friction coefficient, and C_{D_0} is the drag coefficient including aerodynamic interference from adjacent spires. U_δ is the wind velocity above the boundary layer at station 3, A_s is the total frontal area of all the spires.

Substituting the wind velocity profile, Equation 3.4, and Equations 3.1 and 3.2 into Equation 3.5, yields:

$$A_s = \frac{\psi HW}{(1+\psi\theta)C_{D_0}}, \qquad [3.6]$$

where θ is the blockage factor and C_{D_0} is the true drag coefficient including aerodynamic interference from adjacent spires. According to the results of Irwin [182], $\theta = 1.7$ and $C_{D_0} = 1.45$ for spires with shapes in the range $0.02 < \frac{b}{h} < 0.2$. W is the width of the test section, and ψ is the coefficient introduced to calculate the required total frontal area of the spires, which is given in Equation 3.7 as:

$$\psi = \beta\left(\frac{2}{1+2\alpha} + \beta - C_f\frac{X_0}{\delta}\frac{1+\alpha}{\alpha}\right)/(1-\beta)^2, \qquad [3.7]$$

where $\beta = (\delta/H)[\alpha/(1+\alpha)]$ and H is the height of the wind tunnel test section. X_0 is the distance downstream of the spires, which equals to about 6-spire heights and C_f is the floor friction coefficient, shown in Equation 3.8 as:

$$Cf = 0.136\,[\alpha/(1+\alpha)] \qquad [3.8]$$

Substituting Equation 3.8 into Equation 3.7, yields,

$$\psi = \beta\left[\frac{2}{1+2\alpha} + \beta - \frac{X_0}{\delta}\cdot\frac{0.136\alpha}{1+\alpha}\right]/(1-\beta)^2 \qquad [3.9]$$

Substituting Equation 3.9 into Equation 3.6, the total frontal area (A_s) of the spires can be calculated. Based on the total frontal area, the height and the number of spires, the base of the spires can be computed using Equation 3.10 as follows:

$$b = \frac{2A_s}{Nh} \qquad [3.10]$$

Accordingly, the spire dimensions can be obtained using the previous formulae based on the criterion that $0.02 < b/h < 0.2$.

Table 3.2 shows a sample procedure to obtain a boundary layer of 1-meter thickness inside RÜZGEM boundary layer test section for each terrain exposure or category. As one could observe it requires 12 spires of around 1.17 m to generate the target boundary layer thickness. Keeping the number of spires and spire height fixed, the spire base width will change causing a reduction in the boundary layer thickness as one changes the terrain exposure.

Table 3.2 Design parameters for spires and roughness elements

Terrain Exposure	N	$h\ (m)$	δ (m)	$X_0\ (m)$	$b\ (m)$	$s\ (m)$	$w\ (m)^*$	$D\ (m)$	$k\ (m)$
A	12	1.17	1.01	7.0	0.19	0.58	0.29	0.32	0.15
B	12	1.17	0.95	7.0	0.15	0.58	0.29	0.32	0.07
C	12	1.17	0.90	7.0	0.11	0.58	0.29	0.32	~ 0
D	12	1.17	0.88	7.0	0.09	0.58	0.29	0.32	~ 0

**w=h/4: splitter width*

3.2.2.2 Design Methodology for Roughness Elements

The roughness elements are considered as passive devices and are usually integrated together with spires to make adjustments for the wind velocity profile generated by the spires to satisfy the atmospheric boundary layer simulation requirement associated with a certain type of terrain condition in the wind tunnel. Additional advantage of the use of roughness elements in the increase in turbulence levels especially in the lower part of the ABL. Irwin [182] suggested that to specify the roughness size that will produce the desired value of skin-friction coefficient C_f, by using empirical relations relating the roughness height k to boundary layer thickness δ as shown in Equation 3.11.

$$\frac{k}{\delta} = exp\left\{(2/3)ln(D/\delta) - 0.1161\left[\left(2/C_f\right) + 2.05\right]^{1/2}\right\}, \qquad [3.11]$$

where D is the spacing of the roughness elements. Equation 3.11 is valid in the range $30 < \delta D^2/k^3 < 2000$. Another criterion is based on the density area of the

cubes (roughness elements) that represents a certain terrain category as shown in Figure 3.11.

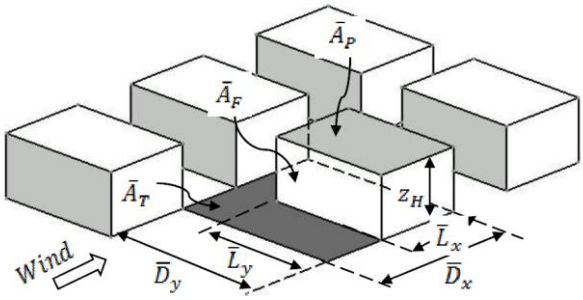

Figure 3.11 Surface roughness dimensions and layouts [222]

- The roughness plan area density $\overline{\lambda_p}$ is defined as the ratio between the block top surface area $\overline{A_p}$ and the block floor area $\overline{A_T}$, i.e.

$$\overline{\lambda_p} = \frac{\overline{A_p}}{\overline{A_T}} = \frac{\overline{L_x}\ \overline{L_y}}{\overline{D_x}\ \overline{D_y}}, \qquad [3.12]$$

where $\overline{L_x}$ is the length of the block (along the wind direction), $\overline{L_y}$ is the width of the block (transverse to the wind direction), $\overline{D_x}$ is the length of the influence area of a block (along the wind direction), $\overline{D_y}$ is the width of the influence area of a block (transverse to the wind direction).

- The roughness element frontal area density $\overline{\lambda_f}$ is defined as:

$$\overline{\lambda_f} = \frac{\overline{A_F}}{\overline{A_T}} = \frac{\overline{z_H}\ \overline{L_y}}{\overline{D_x}\ \overline{D_y}}, \qquad [3.13]$$

where $\overline{z_H}$ is the height of the block. Table 3.2 shows the roughness height and spacing for each terrain category based on Equation 3.11. Based on design formulae it appears that only terrain exposures A and B require the installation of roughness elements.

Although Table 3.2 shows a sample design methodology for the spires and roughness elements more test cases will be investigated in order to understand better the effect

of these passive devices especially roughness element height, spacing and layout. Therefore, in order to avoid confusion among the test cases considered, a new terminology will be followed so we can distinguish between the different cases as shown below in Figure 3.12.

Figure 3.12 Terminology for spires and roughness elements

3.2.3 Numerical Methodology

The CFD simulations of the RÜZGEM Large-Scale Boundary Layer Wind Tunnel test section have been conducted using the same numerical approach of the validation study. However, due to the large size of the wind tunnel especially with the roughness elements and spires included the computational grid is expected to be large even with the $1/2-$model approach. Since we are only interested in the boundary layer developing on the bottom and top walls [211], $1/7^{\text{th}}$ of the test section's width has been considered while imposing symmetry boundary conditions on the side walls as shown on Figure 3.14a. In this approach at least 2 spires are included with several roughness elements. In addition, to be sure that $1/7^{\text{th}}-$model gives acceptable results comparisons with the $1/2-$model approach have been conducted in the next section.

3.2.3.1 Comparison between the ½ -Model and 1/7th–Model Approach

As mentioned previously, $1/2-$model approach although seems applicable for small wind tunnels, on large wind tunnel test sections, this poses a large obstacle of

computational size and time which is restricted by the capability of the computer. Alternatively, $1/7^{\text{th}} - \text{model}$ approach will be used instead to reduce the computational size and time. However, to check the reliability of the $1/7^{\text{th}} - \text{model}$ approach comparisons with $1/2 - \text{model}$ approach are conducted. Different cases have been tested to in order to increase the confidence of the $1/7^{\text{th}} - \text{model}$ approach. The velocity used for the simulation is $10\ \text{m/s}$ as measured from the inlet of the boundary layer test section.

Figure 3.13 and 3.14 show the unstructured hexahedral mesh around the $1/2 - \text{model}$ and $1/7^{\text{th}} - \text{model}$ as well as the geometry and domain respectively. Results include the boundary layer properties as well as the normalized velocity profiles extracted at $15\ \text{m}$ downstream of wind tunnel test section inlet (i.e. center of the turntable). The spires are located 2.5 meters downstream from the test section inlet.

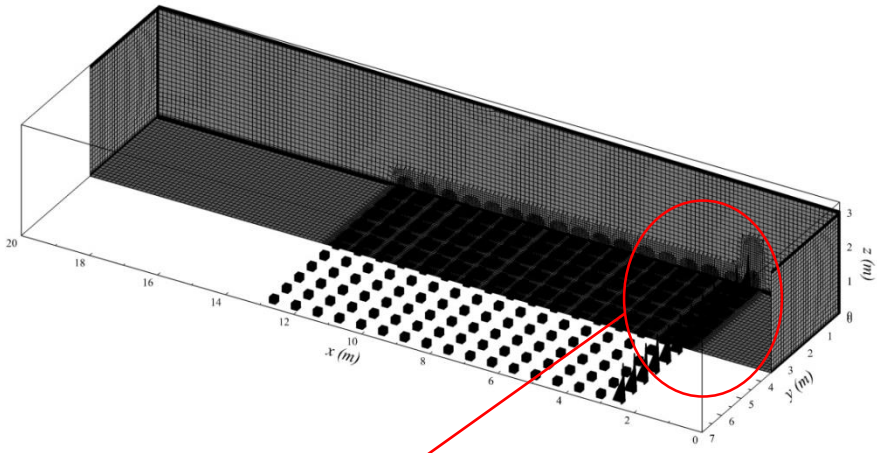

(a)

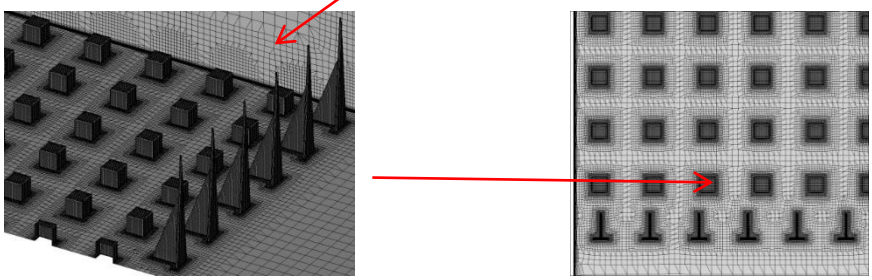

(b)

Figure 3.13 (a) unstructured hexahedral mesh for the ½-model approach, (b) close-up view of the spires and mesh around the spires

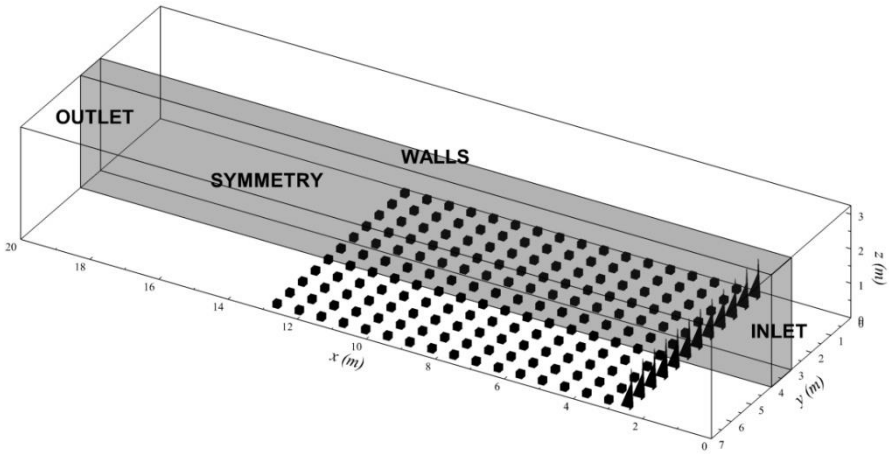

(a)

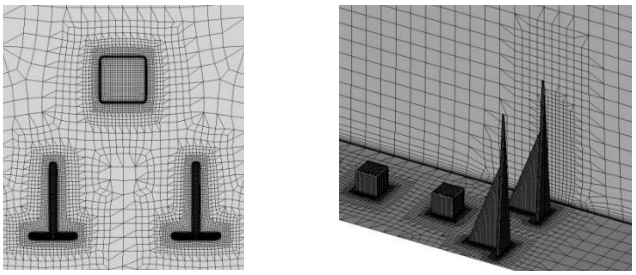

(b)

Figure 3.14 (a) Computational domain highlighting the 1/7th-model, (b) unstructured hexahedral mesh around the spires and roughness elements

Figure 3.15 and Table 3.3 shows the normalized velocity profiles and boundary layer properties for the test cases considered. As can be seen from the results, the $1/2-$ model and $1/7^{\mathrm{th}}-$ model show similar trends and comparable boundary layer thicknesses, though there are differences. The maximum error observed in the boundary layer thickness is $4.50\,\%$ for terrain B. However, there are some differences in the results and this is attributed to the choice of the boundary conditions imposed on the side walls. The $1/7^{\mathrm{th}}-$ model approach seems to over predict the boundary layer properties slightly. The maximum error observed is in the displacement and momentum thicknesses. Since no experimental data are available yet for the large wind tunnel to validate the results, the $1/7^{\mathrm{th}}-$ model will be used for further analysis in order to provide a preliminary assessment of ABL inside RÜZGEM large-scale BLWT test section.

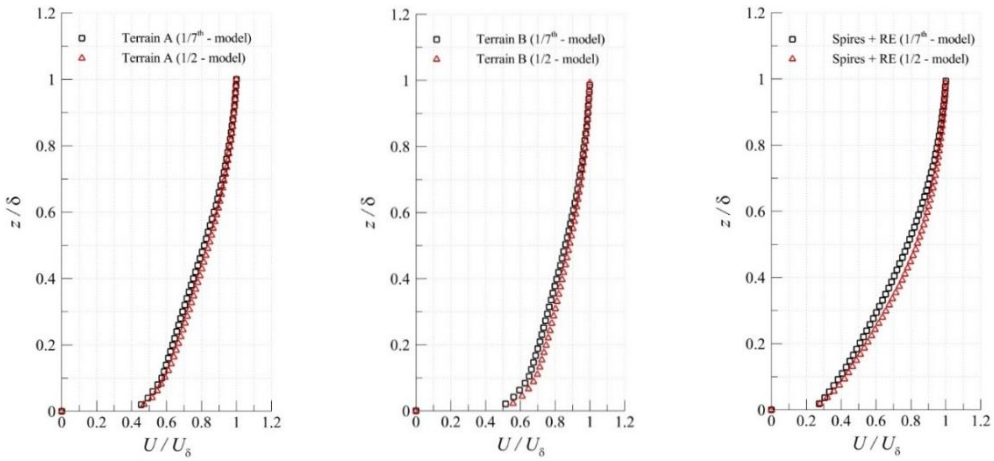

(a) (b) (c)

Figure 3.15 Normalized velocity profiles: (a) Terrain A spires only, (b) Terrain B spires only, (c) Terrain A spires with roughness element

Table 3.3 Comparison of boundary layer properties between the 1/2-model and 1/7th-model approach

Test Cases		α	$\delta\ (m)$	$\delta^*\ (m)$	$\theta\ (m)$	H
Terrain A (spires only)	$1/2-\text{model}$	0.23	1.20	0.22	0.15	1.45
	$1/7^{\text{th}}-\text{model}$	0.26	1.22	0.25	0.17	1.49
	Error (%)	13.04	1.67	13.64	13.33	2.76
Terrain B (spires only)	$1/2-\text{model}$	0.17	1.11	0.16	0.12	1.32
	$1/7^{\text{th}}-\text{model}$	0.20	1.16	0.19	0.14	1.38
	Error (%)	17.65	4.50	18.75	16.67	3.43
Terrain A (spires + roughness elements)	$1/2-\text{model}$	0.38	1.31	0.31	0.17	1.75
	$1/7^{\text{th}}-\text{model}$	0.40	1.33	0.35	0.20	1.81
	Error (%)	5.26	1.53	12.90	17.65	4.55

3.2.3.2 Grid Independence Study

In the previous section we evaluated the reliability of the 1/7th-model approach, and the results show that the 1/7th-model approach although over predicts the $1/2-\text{model}$ results, it still provides reasonable results in terms of boundary layer

properties. Therefore, a grid independence study has been conducted for the 1/7th-model approach for the test case with spires only. Four refinement levels have been used as shown in Figure 3.16 and Table 3.4. As one can observe from the results there is no significant difference as the grid gets finer. One should note in here that the grid size will change according to the test case considered. However, this assessment at least has provided an estimate of the minimum number of cells each test case requires. For instance, cases with spires only require at least 1.5 million cells, cases with roughness elements only require at least 3 million cells, and cases with spires and roughness elements require at least 4 million cells.

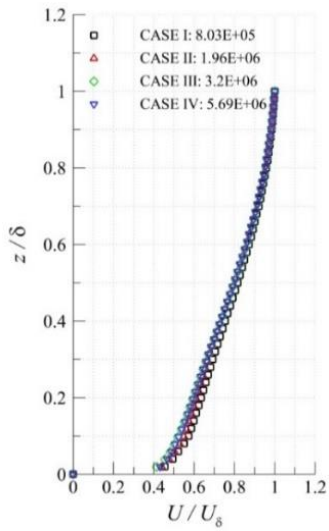

Figure 3.16 Grid independence study for 1/7th-model approach (spires only)

Table 3.4 Grid independence study for 1/7th-model approach (spires only)

Test Cases	CASE I	CASE II	CASE III	CASE IV
# of elements	8.03E+05	1.96E+06	3.20E+06	5.69E+06
α	0.26	0.26	0.26	0.26
$\delta\ (m)$	1.22	1.24	1.25	1.25
$\delta^*\ (m)$	0.25	0.26	0.28	0.28
$\theta\ (m)$	0.17	0.17	0.18	0.18
H	1.49	1.49	1.55	1.55

3.2.3.3 Empty Boundary Layer Wind Tunnel Test Section

Before we attempt to simulate the ABL inside RÜZGEM large-scale BLWT test section, analysis of the boundary layer within the wind tunnel empty test section is conducted for 2 different wind tunnel speeds (10 m/s & 20 m/s). Figure 3.17a and Table 3.5 presents a grid independence study for the empty test section. Results show that for 10 m/s the boundary layer thickness is around 0.277 m, and the power law is around 0.14. Table 3.6 shows the boundary layer properties for two different wind speeds. The results have been compared with the theoretical values of boundary layer thicknesses obtained from Schlighting [223] for flat plate boundary layer. As one can observe the boundary layer properties are comparable with the theoretical values; however, CFD results slightly over predict the theoretical values. This is mainly due to the 1/7th approach used in the CFD simulation, yet the results show that CFD is capable of predicting the boundary layer properties for the empty BLWT test section.

Table 3.5 Grid independence study for the empty BLWT test section

Test Cases	# of Elements	α	$\delta\ (m)$	$\delta^*\ (m)$	$\theta\ (m)$	H
CASE I	1.12E+05	0.11	0.407	0.028	0.023	1.217
CASE II	2.83E+05	0.12	0.326	0.028	0.023	1.217
CASE III	1.13E+06	0.13	0.310	0.031	0.025	1.240
CASE IV	2.07E+06	0.13	0.301	0.030	0.024	1.250
CASE V	3.84E+06	0.14	0.277	0.031	0.024	1.292
CASE VI	4.77E+06	0.14	0.277	0.030	0.024	1.25

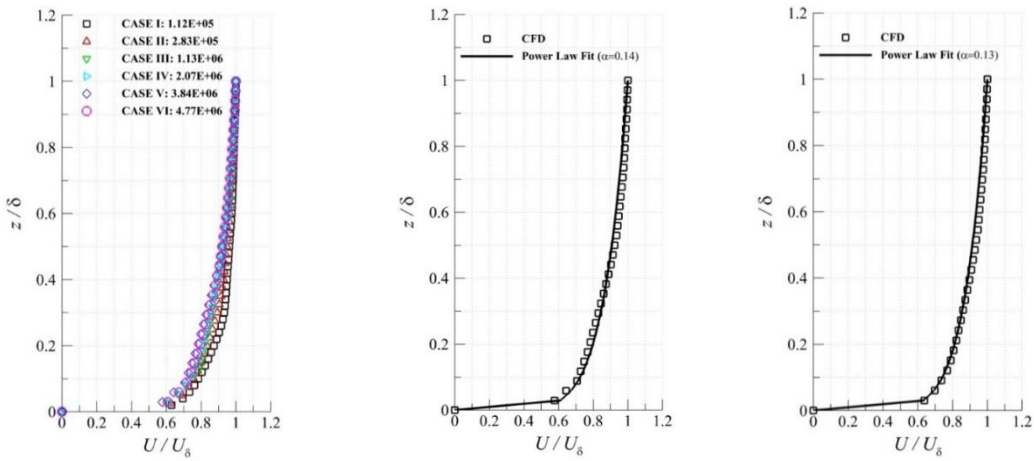

(a) (b) (c)

Figure 3.17 (a) Grid independent study for empty BLWT, (b) normalized velocity profile at 10 m/s, and (c) normalized velocity profile at 20 m/s.

Table 3.6 Comparison of boundary layer properties between the theoretical and CFD results for empty BLWT test section

Test Cases	$U_\infty = 10\ m/s$		$U_\infty = 20\ m/s$	
	Theoretical	CFD	Theoretical	CFD
α	0.14	0.14	0.14	0.14
$\delta\ (m)$	0.220	0.277	0.191	0.269
$\delta^*\ (m)$	0.027	0.031	0.024	0.026
$\theta\ (m)$	0.021	0.024	0.019	0.021
H	1.278	1.292	1.278	1.238

3.2.4 Effect of Spires and Roughness Elements

In this section we will present the effects of spires, roughness elements, and spires with roughness elements, in order to understand better the flow and boundary layer development within the wind tunnel test section as well as identify which combination of spires and roughness elements are adequate for the target terrain exposures to be used in the BLWT test section.

3.2.4.1 Effect of Spires

In this section we will investigate the effect of spire geometries for different terrain exposures. The Spires have been design according to Irwin's [182] approach as shown in Table 3.2. For each terrain exposure spire geometry will be different because the power law exponent is different. In this study, the number of spires, spire height and splitter size were kept the same, while the spire base width has changed according to the power law exponents of each terrain type. Table 3.7 summaries the spire geometries used for each terrain exposure. According to Irwin's approach, if power law exponent change the simulated boundary layer thickness will change accordingly, i.e. for the same number of spires and spire height, as the power law increases the boundary layer thickness will increase and the expected spire base width will also increase. The velocity used for the test cases is 10 m/s as measured from the inlet of the boundary layer test section. Moreover, the measurement location where the velocity profiles are extracted is 15 meters downstream of the test section inlet (i.e. centre of the turntable).

Table 3.7 Design parameters of spires for each terrain exposure (or category)

Terrain Exposure	α	N	$h\ (m)$	$\delta\ (m)$	$X_0\ (m)$	$b\ (m)$	$s\ (m)$	$w\ (m)^*$
A	0.4	12	1.17	1.01	7.0	0.19	0.58	0.29
B	0.25	12	1.17	0.95	7.0	0.15	0.58	0.29
C	0.15	12	1.17	0.90	7.0	0.11	0.58	0.29
D	0.10	12	1.17	0.88	7.0	0.09	0.58	0.29

$^*w=h/4$: splitter width

Figure 3.18 shows the normalized velocity profiles for different terrain exposures with the target power law profiles (*solid lines*) as well as the power law curve fits (*dashed lines*). As one can observe the velocity profiles for terrain exposure A and B under predicts the target power law profiles, on the other hand for terrain exposures C and D, the velocity profiles matches the target power law profiles. In terms of boundary layer thickness, the CFD results over predict the boundary layer

thicknesses obtained from design methodology. This is mainly due to the 1/7th approach used in the CFD methodology. These observations are reflected also on the boundary layer properties as shown in Table 3.8. This entails that in order to achieve the target power law profiles for terrain exposures A and B roughness elements are required. However, for terrain exposures C and D spires alone are sufficient to produce the target velocity profile.

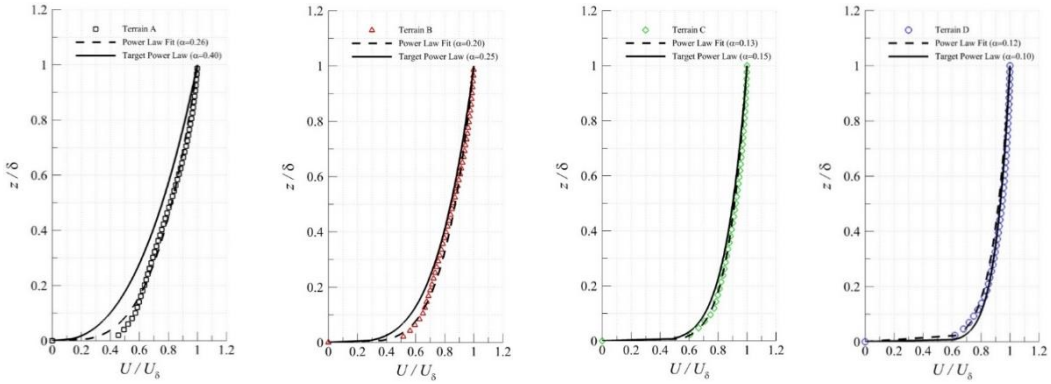

(a) (b) (c) (d)

Figure 3.18 Normalized velocity profiles for different terrain exposures: (a) Terrain Exposure A, (b) Terrain Exposure B, (c) Terrain Exposure C, and (d) Terrain Exposure D

Table 3.8 shows the boundary layer characteristics, as expected changing the spire's base width will change the boundary layer characteristics. For instance, as the spire's base width (b) increases the power law exponent, boundary layer thickness and other characteristics will increase as well. Note in Table 3.8 values in brackets represent the target power law exponent and boundary layer thickness for each terrain exposure based on Irwin's design approach.

Table 3.8 Summary of the atmospheric boundary layer properties

Test Cases	α	$\delta(m)$	$\delta^*(m)$	$\theta(m)$	H
Terrain Exposure A	0.26 (**0.4**)	1.22 (**1.01**)	0.25	0.17	1.49
Terrain Exposure B	0.20 (**0.25**)	1.16 (**0.95**)	0.19	0.14	1.38
Terrain Exposure C	0.13 (**0.15**)	1.05 (**0.90**)	0.11	0.09	1.26
Terrain Exposure D	0.12 (**0.10**)	1.03 (**0.88**)	0.10	0.08	1.24

Figure 3.19 presents the normalized velocity profiles and turbulent kinetic energy profiles extracted at 15 m downstream of the test section inlet for different terrain exposures. As expected terrain A which have largest spire width shows the highest velocity deficit in the velocity profile (i.e. highest shape factor, *H*), as well as the highest levels of turbulent kinetic energy, whereas terrain exposure D shows the least.

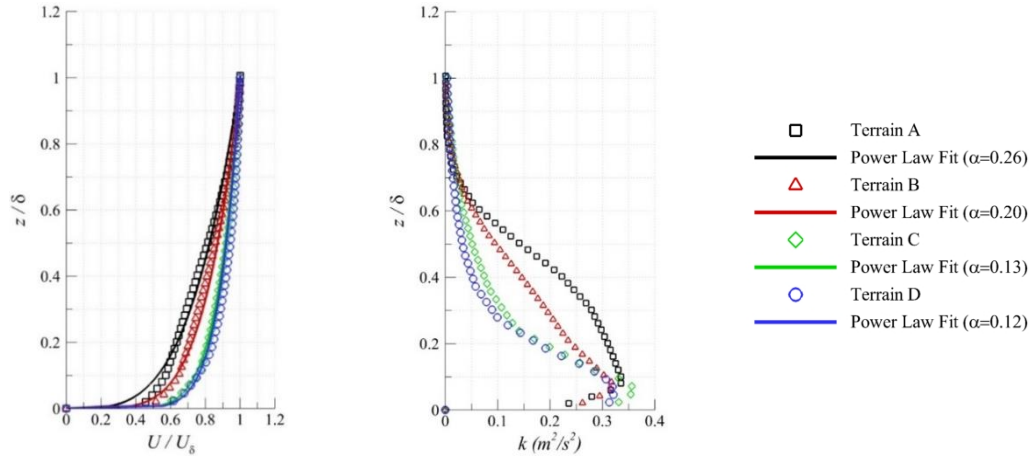

(a) (b)

Figure 3.19 (a) Normalized velocity profiles, and (b) turbulent kinetic energy profiles for different terrain exposures. Solid lines represent the power law curve fits

3.2.4.2 Effect of Roughness Element Height, Spacing and Layout

In the previous section we investigated the effects of the spire geometry on the boundary layer characteristics, and the results show that using spires alone especially for terrain exposures A and B will not achieve the desired target power law exponents. Therefore, as recommended roughness elements should also be included to further improve the velocity profile and achieve the target characteristics.

Roughness elements are one of the most fundamental passive devices used for ABL simulations inside the wind tunnel test section. Therefore, before combining both spires and roughness elements together, an initial assessment of the effect of

roughness elements on the characteristics of the boundary layer, velocity profiles and turbulent kinetic energy will be presented in this section. Test cases include the effect of roughness element height or size, roughness element spacing and roughness fetch layout.

Figure 3.20 shows 8 different cases of roughness element layouts distributed within the wind tunnel test section across a 7 m x 10 m roughness fetch. Each case includes the dimensions and type of layout as presented by the terminology followed in Figure 3.12 previously. In addition, the planar area density is also calculated for each test case. Planar area density represents the blockage imposed by the distribution of the roughness fetch on the flow development downstream. A high density roughness fetch causes more blockage and deficit in the velocity profiles and add more energy and turbulence to the flow field, thereby affecting the boundary layer characteristics. For instance, CASE IV has the highest density whereas CASE III has the lowest density.

Figure 3.21 shows the Normalized velocity profiles for the test cases considered together with power law curve fits in order to obtain the power law exponent and boundary layer characteristics as shown in Table 3.9. In general, one could observe that if roughness height, spacing or layout is changed the entire boundary layer characteristics will change as well. In addition, Figure 3.22 shows comparison between the test cases considered in terms of velocity and turbulent kinetic energy profiles.

This assessment of the effect of different roughness element height, spacing and layout, will help select which configuration to be use for a certain power law exponent and boundary layer thickness. For instance, if the target power law exponent is 0.4 (terrain A), *CASES V* and *CASE VIII* can be used, whereas *CASE III* and *CASE VI* can be used for terrain B and C respectively. However, using roughness elements alone might not be enough to achieve the target boundary layer thickness. Therefore, in the next section we will present the effect of combining spires with roughness elements on the boundary layer properties.

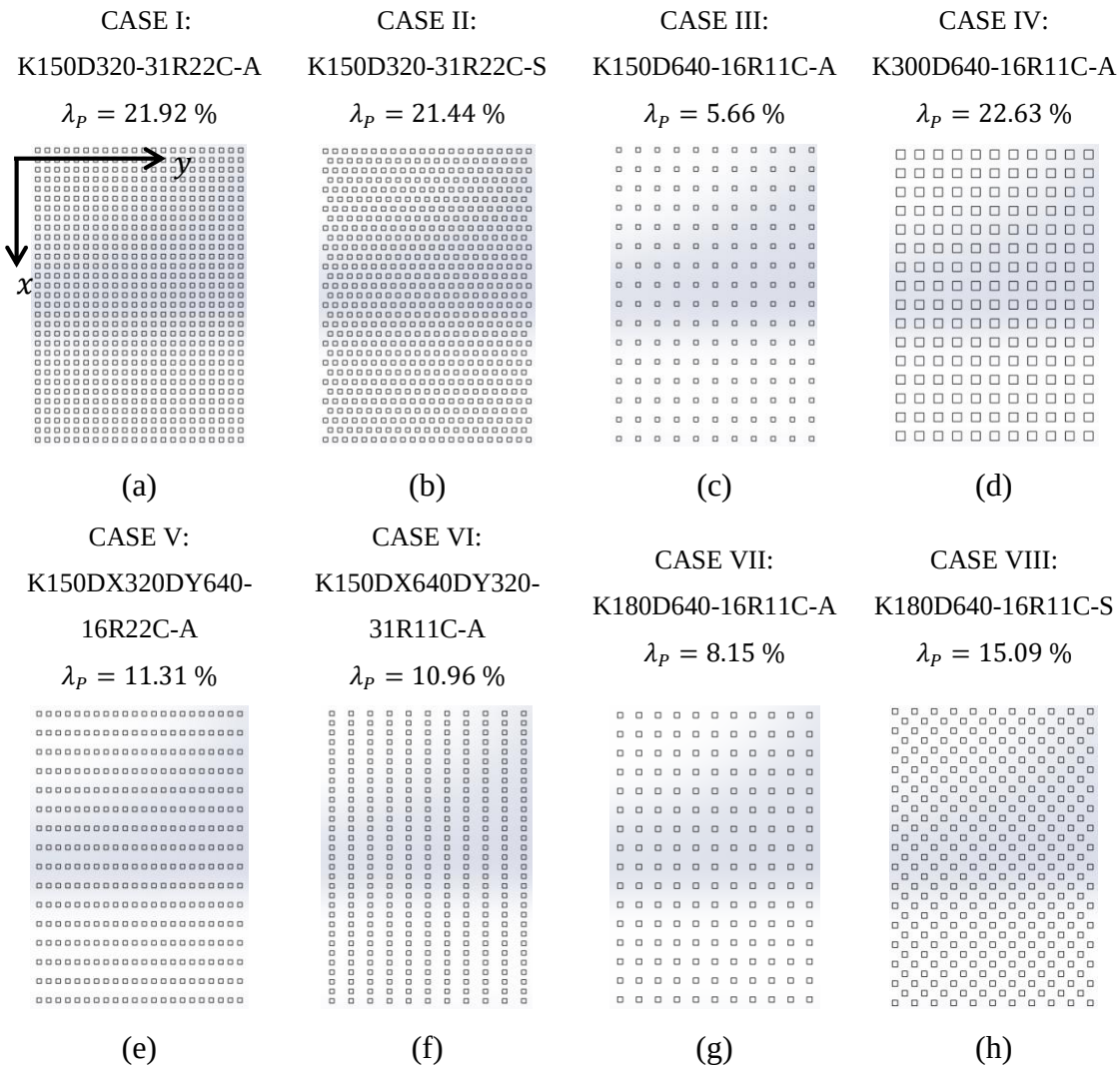

Figure 3.20 (a-h) Roughness element layouts and configurations. x-axis is along the wind direction, y-axis is along the transverse direction

CASE I:
K150D320-31R22C-A

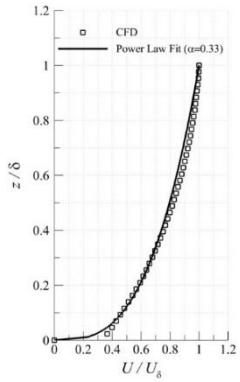

(a)

CASE II:
K150D320-31R22C-S

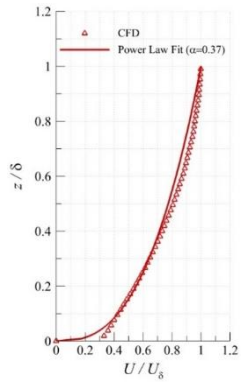

(b)

CASE III:
K150D640-16R11C-A

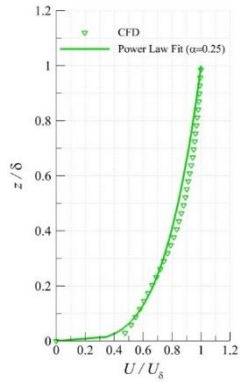

(c)

CASE IV:
K300D640-16R11C-A

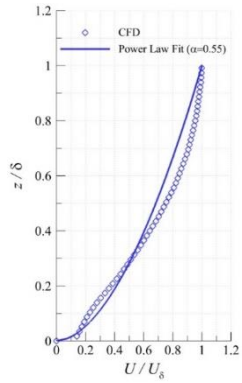

(d)

CASE V:
K150DX320DY640-16R22C-A

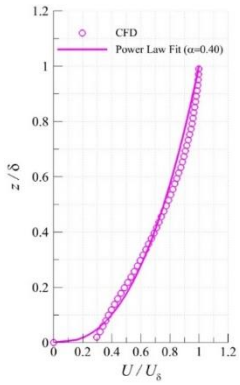

(e)

CASE VI:
K150DX640DY320-31R11C-A

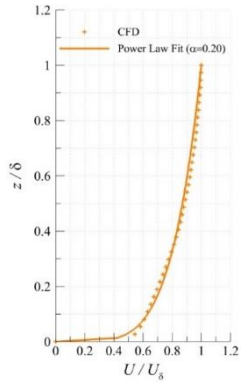

(f)

CASE VII:
K180D640-16R11C-A

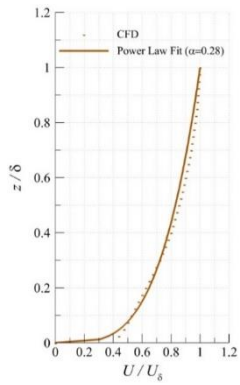

(g)

CASE VIII:
K180D640-16R11C-S

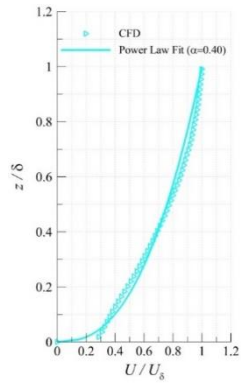

(h)

Figure 3.21 (a-h) Normalized velocity profiles for different roughness element layouts and configurations

Table 3.9 shows that boundary layer properties for the test cases considered. As one can observe:

- If the roughness element layout is changed (A to S), the boundary layer properties increase (*CASE I vs. CASE II & CASE VII vs. CASE VIII*).

- If roughness element spacing (D) is doubled with keeping roughness element size (K) and layout (A) the same, the boundary layer properties decreases (*CASE I vs. CASE III*).

- If roughness element size and spacing are doubled while keeping layout the same, the boundary layer properties increase (*CASE I vs. CASE IV*).

- If the spacing in the transverse direction is doubled compared to that along the wind direction, the boundary layer properties decreases (*CASE V vs. CASE VI*).

Table 3.9 Summary of atmospheric boundary layer properties for the cases of roughness elements

Properties	α	$\delta(m)$	$\delta^*(m)$	$\theta(m)$	H
CASE I: K150D320-31R22C-A	0.33	0.70	0.16	0.10	1.63
CASE II: K150D320-31R22C-S	0.37	0.86	0.21	0.12	1.71
CASE III: K150D640-16R11C-A	0.25	0.56	0.10	0.07	1.47
CASE IV: K300D640-16R11C-A	0.55	0.94	0.30	0.13	2.27
CASE V: K150DX320DY640-16R22C-A	0.40	0.82	0.22	0.12	1.82
CASE VI: K150DX640DY320-31R11C-A	0.20	0.60	0.09	0.07	1.38
CASE VII: K180D640-16R11C-A	0.28	0.65	0.13	0.08	1.52
CASE VIII: K180D640-16R11C-S	0.40	0.89	0.24	0.13	1.82

Figure 3.22 shows the velocity profiles as well as turbulent kinetic energy profiles for the test cases considered. As shown *CASE IV* results in the largest velocity deficit while *CASE VI* shows the least. In terms of turbulent kinetic energy *CASE V* produces the largest turbulence in the flow while *CASE VI* produces the least. This assessment is very critical when one uses both spires and roughness elements for ABL simulations. On one hand, the target boundary layer velocity profile and turbulence intensity profile should be met; however, this is challenging due to the reverse effects of the roughness elements. To elaborate, roughness elements increases the turbulence and wind shear in the flow field which might result in over estimating or not achieving the target ABL profiles. Therefore, care should be taken when simulating the ABL inside wind tunnels.

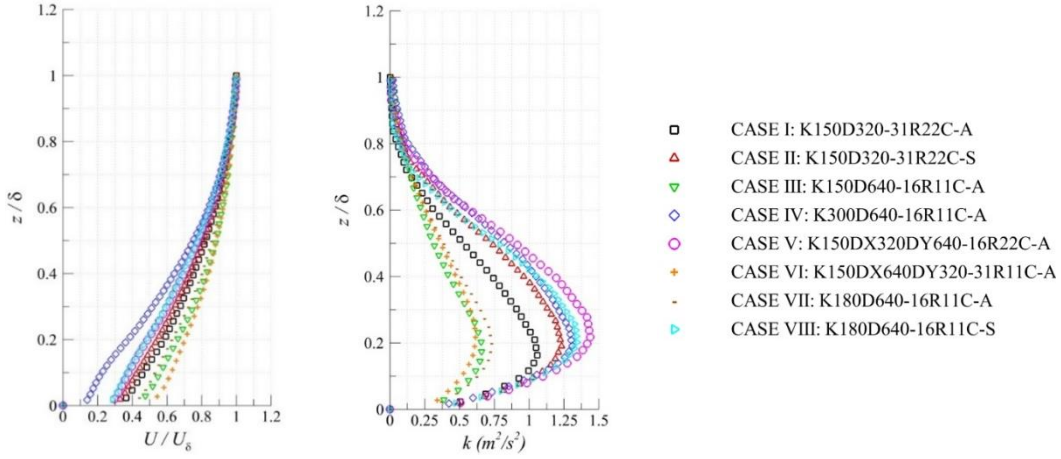

(a) (b)

Figure 3.22 (a) Normalized velocity profiles, and (b) turbulent kinetic energy profiles for different roughness element cases

3.2.4.3 Effect of Spires and Roughness Elements

In the previous sections we investigated the effects of spires and roughness elements separately. Results show that spires alone will not be sufficient to achieve the target power law especially for terrain exposures A and B. In addition, roughness elements play a major part in changing the boundary layer properties. Therefore, in this section we will investigate the effects of spires and roughness elements combined on the boundary layer characteristics and observe which test cases will be assigned for different terrain exposures especially A and B.

Figure 3.23 shows the Normalized velocity profiles for the test cases considered. Note here that *CASES I-VI* are used to achieve terrain exposure A, while *CASES VII* and *VIII* are used to achieve terrain exposure B. Table 3.10 shows the boundary layer properties for the test cases considered. As one can observe combining spires with roughness elements results in boundary layer properties increasing. For terrain exposure B (*CASES VII and VIII*) changing the layout shows no significant difference in the boundary layer properties. Whereas, for terrain exposures A, some cases under predicts (*CASE III*) the target power law while others over predicts it (*CASES I, IV & VI*). Only *CASES II and V* seems to achieve the target power law

profiles. Figure 3.24 shows the velocity and turbulent kinetic energy profiles for the test cases considered.

Table 3.10 Summary of the atmospheric boundary layer properties for the cases of spires with roughness elements

Terrain Exposure	Test Cases	α	$\delta\ (m)$	$\delta^*\ (m)$	$\theta\ (m)$	H
A	CASE I: 12S-K150D320-31R22C-A	0.45	1.45	0.44	0.22	1.94
	CASE II: 12S-K150D320-31R22C-S	0.40	1.39	0.39	0.21	1.84
	CASE III: 12S-K150D640-16R11C-A	0.35	1.32	0.34	0.19	1.72
	CASE IV: 12S-K300D640-16R11C-A	0.50	1.48	0.50	0.23	2.17
	CASE V: 12S-K180D640-16R11C-A	0.40	1.33	0.35	0.20	1.81
	CASE VI: 12S-K180D640-16R11C-S	0.45	1.43	0.43	0.22	1.97
B	CASE VII: 12S-K70D320-31R22C-A	0.27	1.25	0.24	0.16	1.54
	CASE VIII: 12S-K70D320-31R22C-S	0.27	1.24	0.24	0.16	1.54

CASE I:
12S-K150D320-
31R22C-A

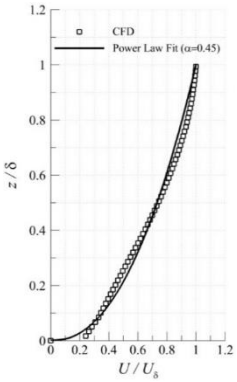

(a)

CASE II:
12S-K150D320-
31R22C-S

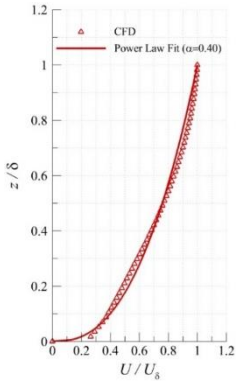

(b)

CASE III:
12S-K150D640-
16R11C-A

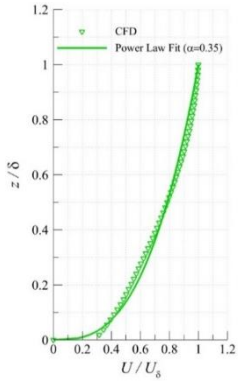

(c)

CASE IV:
12S-K300D640-
16R11C-A

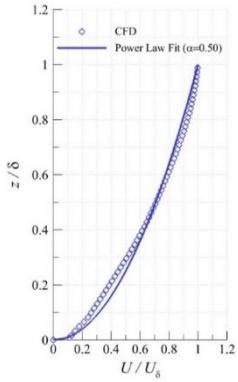

(d)

CASE V:
12S-K180D640-
16R11C-A

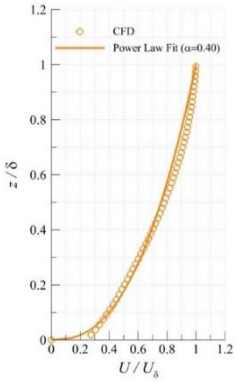

(e)

CASE VI:
12S-K180D640-
16R11C-S

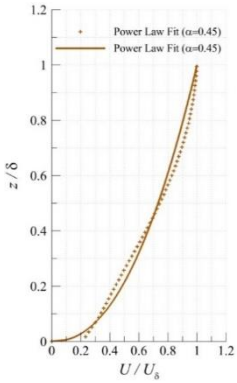

(f)

CASE VII:
12S-K70D320-
31R22C-A

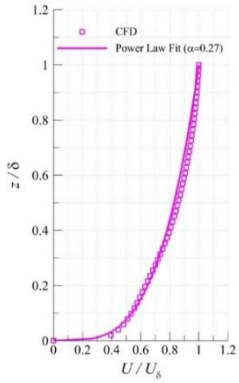

(g)

CASE VIII:
12S-K70D320-
31R22C-S

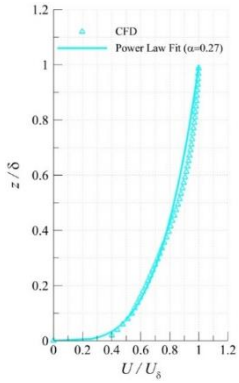

(g)

Figure 3.23 (a-h) Normalized velocity profiles for the cases of spires with roughness elements

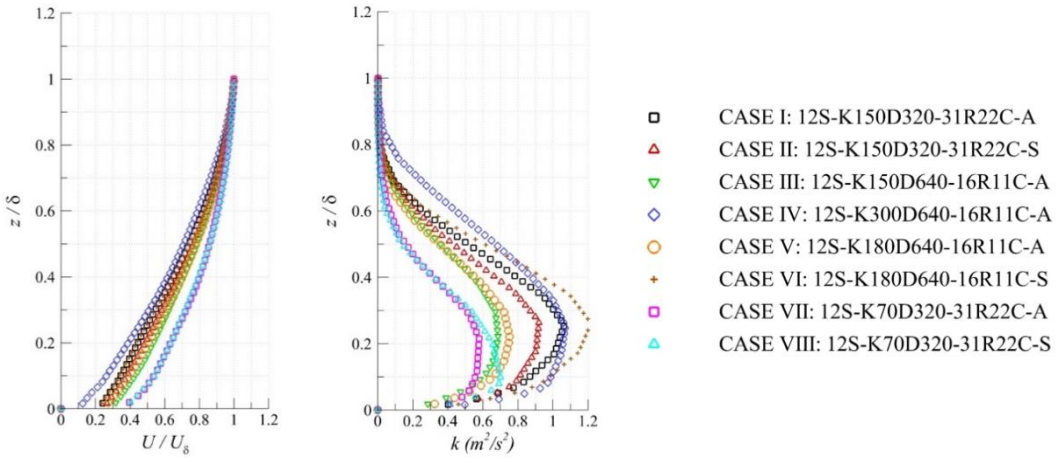

(a) (b)

Figure 3.24 (a) Normalized velocity profiles, and (b) turbulent kinetic energy profiles for different spires and roughness elements cases

3.2.4.4 Selection and Summary of Test Cases

In this section we summarize which cases are suitable for each terrain exposure. As shown in Table 3.11 and Figure 3.25, four cases are suitable for terrain exposure A, although their boundary layer thicknesses are different. While for terrain exposure B three cases are suitable. Terrain exposures C and D using spires alone is sufficient.

Table 3.11 Summary of the atmospheric boundary layer properties for each terrain exposure (or category)

	Test Cases	α	$\delta\ (m)$	$\delta^*\ (m)$	$\theta\ (m)$	H
Terrain Exposure A	Spires only	0.26	1.22	0.25	0.17	1.49
	K150DX320DY640-16R22C-A	0.40	0.82	0.22	0.12	1.82
	K180D640-16R11C-S	0.40	0.89	0.24	0.13	1.82
	12S-K150D320-31R22C-S	0.40	1.39	0.39	0.21	1.84
	12S-K180D640-16R11C-A	0.40	1.33	0.35	0.20	1.81
Terrain Exposure B	Spires only	0.20	1.16	0.19	0.14	1.38
	K150D640-16R11C-A	0.25	0.56	0.10	0.07	1.47
	12S-K70D320-31R22C-A	0.27	1.25	0.24	0.16	1.54
	12S-K70D320-31R22C-S	0.27	1.24	0.24	0.16	1.54
Terrain Exposure C	Spires only	0.13	1.03	0.11	0.09	1.26
Terrain Exposure D	Spires only	0.12	1.05	0.10	0.08	1.24

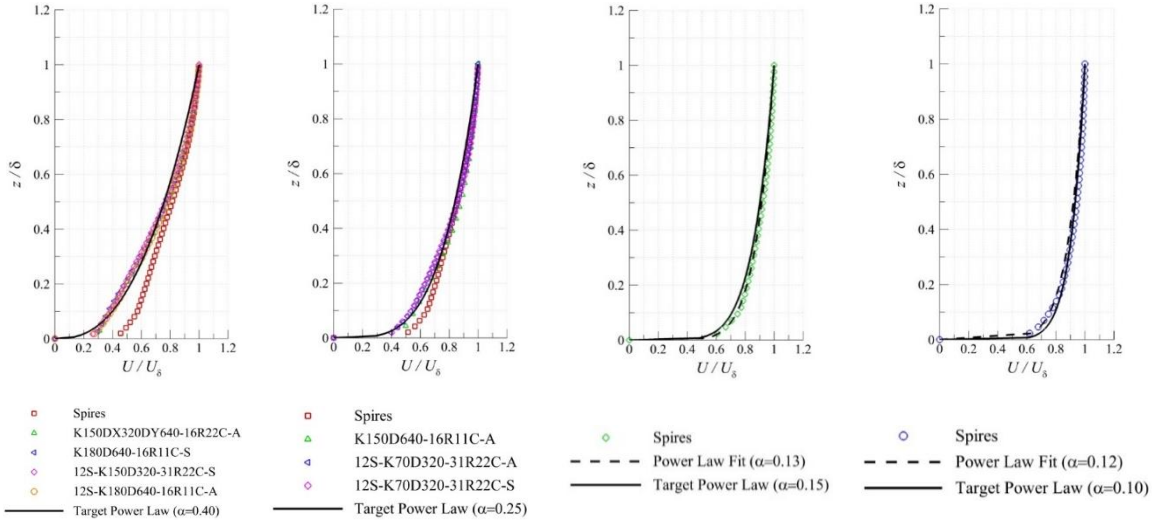

(a) (b) (c) (d)

Figure 3.25 Normalized velocity profiles: (a) Terrain exposure A, (b) Terrain exposure B, (c) Terrain exposure C, and (d) Terrain exposure D

3.3 RÜZGEM C3 Boundary Layer Wind Tunnel

In the previous section numerical simulations of the ABL inside RÜZGEM Large-Scale Boundary Layer wind tunnel were presented. However, due to the delay in the construction of the wind tunnel, no experimental data were presented. In order to complete this study another wind tunnel which is available in RÜZGEM Aerodynamics Laboratory will be utilized to continue the study. Inside this wind tunnel the ABL will be simulated using the spire-roughness element technique presented in the previous section and comparisons with numerical results will be conducted in order to validate the CFD approach.

3.3.1 Wind tunnel Facility

The wind tunnel used in this study is an open-return suction type boundary layer wind tunnel (RÜZGEM C3) of the Middle East Technical University (METU) Center for Wind Energy Research (RÜZGEM) as shown in Figure 3.26. The wind tunnel consists of a two-dimensional inlet contraction with a contraction ratio of 1: 5, and a

fully transparent test section with a cross-sectional area of $1 \times 1\ m^2$ and a length of $8\ m$. It is powered by a $45 - kW$ speed-controlled electrical motor, which drives a $1.2\ m$ diameter axial fan. A honeycomb and a screen are located upstream of the test section in order to ensure high flow quality inside the test section. Maximum velocity inside the test section is $25\ m/s$ and the average inlet turbulence intensity is about 1.0 %.

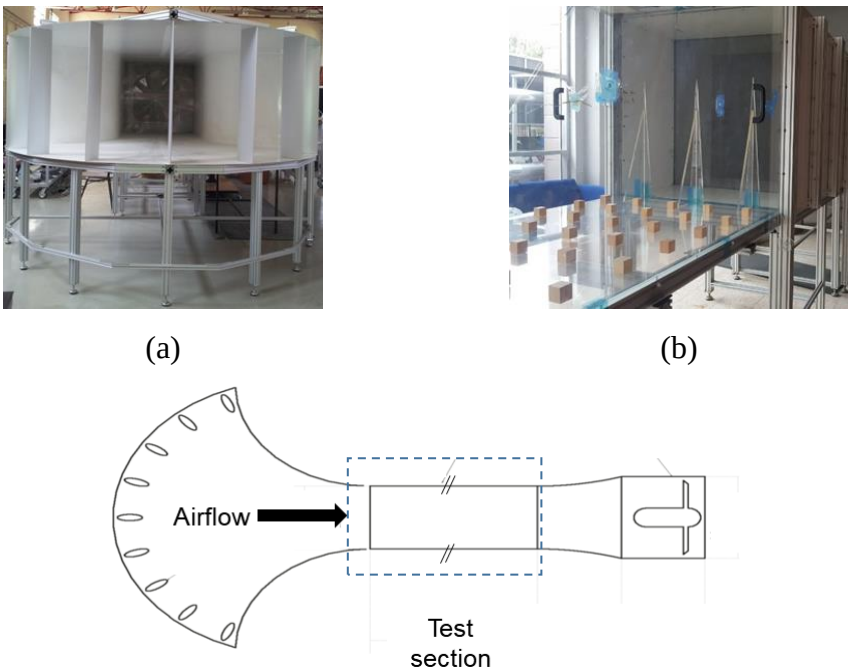

Figure 3.26 METUWIND C3 boundary layer wind tunnel: (a) inlet of the wind tunnel, (b) test section with spires and roughness elements, and (c) sketch of the wind tunnel

3.3.2 Experimental Characterization of the Wind Tunnel Facility

This section presents the experimental characterization of the wind tunnel facility. Flow quality at the inlet of the test section will be presented in terms of velocity and turbulence intensity profiles. Hotwire anemometry measurements are conducted at the inlet of the test section by traversing a single sensor hotwire vertically and

horizontally across the test section. Data are collected at a sampling rate of 10 kHz for 30 seconds duration. Measurements are conducted at 10 m/s wind speed.

Figure 3.27 shows the horizontal measurements conducted across the wind tunnel test section inlet in terms of streamwise velocity and turbulence intensity profiles. Two measurement test cases are conducted to check the reliability of the measurements. As one can observe from Figure 3.27a and b the velocity profiles show uniform velocity distribution across the test section inlet. However, there is a slight reduction in the velocity profile at the left hand side compared to the right hand side. Later it will be shown that the main reason for this is due to the 2-dimensional inlet contraction and blockage from walls due to small space in the laboratory. This problem is more pronounced on the turbulence intensity profiles as shown in Figure 3.27c. Although there is a uniform region between $0.3\ \text{m} \leq y \leq 0.7\ \text{m}$ with turbulence intensity levels of around 1%. Outside this region there are high turbulence intensity levels which persist downstream of the test section as will be shown later in this section. The main reason is due to the growing boundary layer on the side walls, which ultimately causing separation due to adverse pressure gradient caused by the 2D inlet contraction. This could potentially cause dramatic effects if one is interested in studying the wake characteristics of model wind turbines or porous discs. Therefore, for this reason and in order to carry out reliable study the inlet of wind tunnel will be replaced by designing a new 3-dimensional inlet contraction with a settling chamber as shown in Chapter 4.

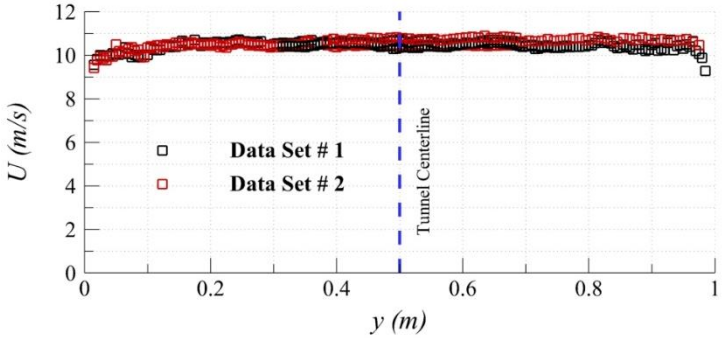

(a)

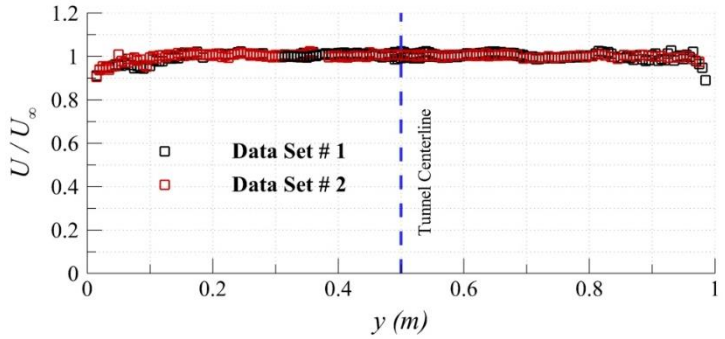

(b)

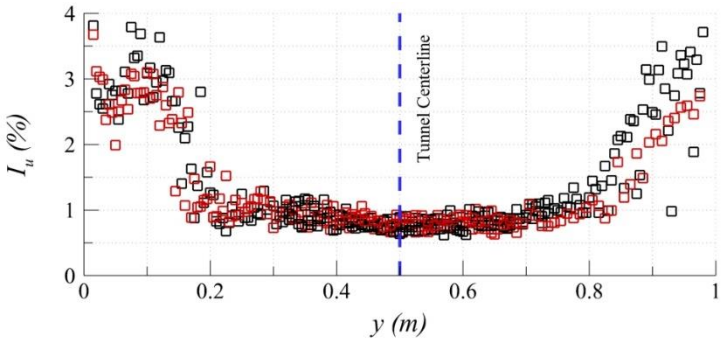

(c)

Figure 3.27 Horizontal measurements at the inlet of the test section: (a) streamwise velocity, (b) normalized streamwise velocity, (c) streamwise turbulence intensity. Dashed blue line marks the tunnel centerline

Figure 3.28 shows the vertical measurements conducted across the wind tunnel test section inlet. Across the vertical distance the flow shows good uniformity in terms of streamwise velocity profiles. On the other hand, the turbulence intensity profile shows higher turbulence levels near the walls compared to the centerline, this is

mainly due to the growing boundary on the bottom and top walls of the 2D inlet contraction.

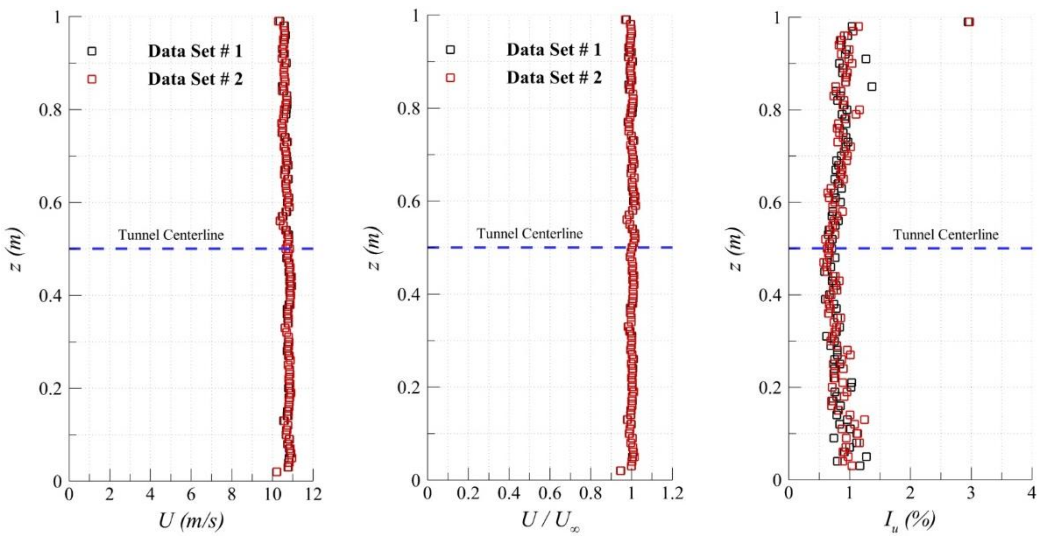

(a) (b) (c)

Figure 3.28 Vertical measurements at the inlet of the test section: (a) streamwise velocity, (b) normalized streamwise velocity, (c) streamwise turbulence intensity. Dashed blue line marks the tunnel centerline

3.3.3 Numerical Methodology

The CFD simulations of RÜZGEM C3 Boundary Layer Wind Tunnel test section have been conducted using the same numerical approach presented in section 3.1.2. Half-models have been considered in order to reduce the domain size and computational time with symmetry imposed as shown in Figure 3.29a for the wind tunnel. Figure 3.29 shows the computational domain with the boundary conditions as well as the unstructured hexahedral mesh for the spires with roughness elements case with a closed-up view of the boundary layer resolved around the spires and roughness elements.

The measured horizontal and vertical profiles shown previously in Figures 3.27 and 3.28 respectively have been used in the numerical simulation as inlet boundary conditions separately. To elaborate, since we are dealing with a 3-dimensional

geometry, the inlet boundary conditions will be interpolated across the entire plane of the test section. In addition, due to the non-uniformities in velocity and turbulence intensity profiles, and the ½-model approach used in the CFD simulations, the horizontal and vertical profiles will be tested separately. That is, the effects of vertical profile and horizontal profile will be tested separately in order to understand better how significant the problem will be on the downstream flow field and the reliability of the CFD approach.

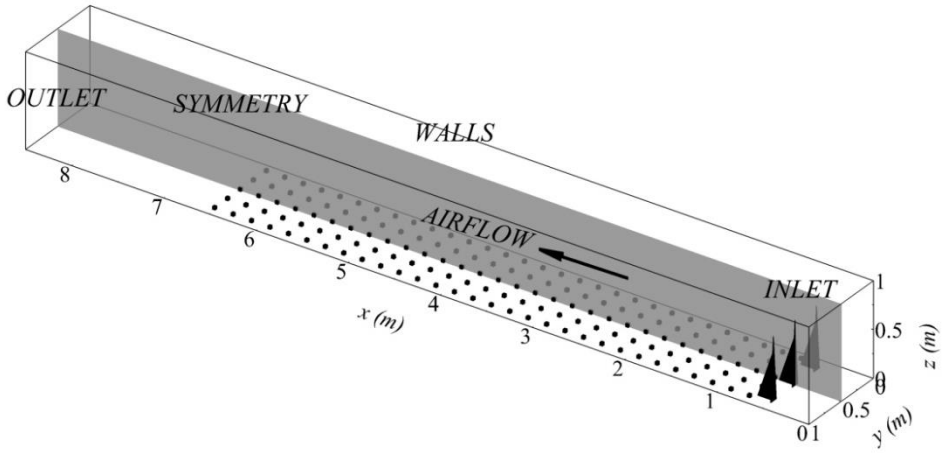

(a)

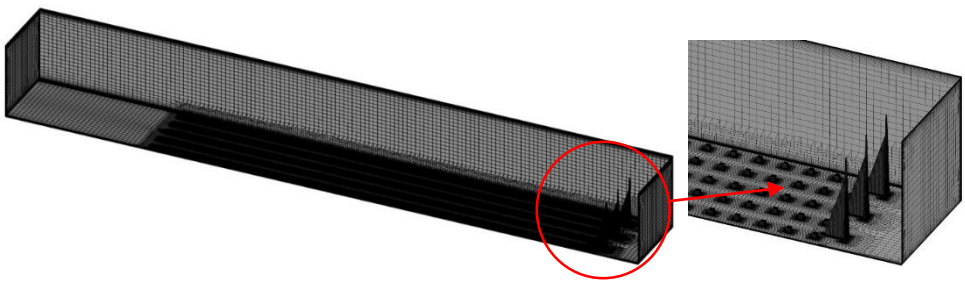

(b)

Figure 3.29 (a) Computational domain, (b) unstructured hexahedral mesh with close-up view of the mesh around the spires and roughness elements

3.3.4 Results of RÜZGEM C3 Boundary Layer Wind Tunnel

in this section we will present the comparisons between the numerical simulation and experimental results for three different test cases, namely the empty wind tunnel,

empty wind tunnel equipped with spires and the empty wind tunnel equipped with spires and roughness elements.

3.3.4.1 Empty Wind Tunnel

Figures 3.30 and 3.31 present the contours of the streamwise velocity and turbulent kinetic energy distributions in the empty wind tunnel along the x-z plane and x-y plane respectively. Velocity vectors were imposed on the velocity contour plots (Figures 3.30a and 3.31a) to show the development of the flow. As can be seen from the contour plots the flow shows typical distributions of streamwise velocity and turbulent kinetic energy. Uniform distribution of the velocity and turbulent kinetic energy is observed in the test section, as well as the growing boundary layer as one moves downstream from the inlet of the test section.

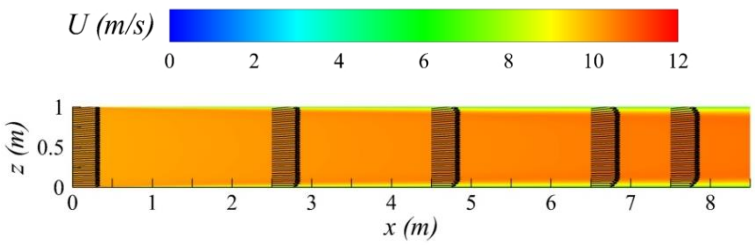

(a)

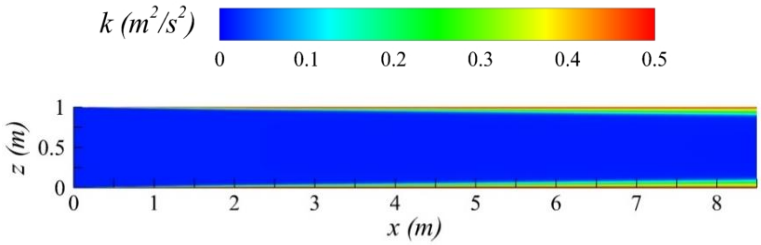

(b)

Figure 3.30 Contour plots of: (a) streamwise velocity, and (b) turbulent kinetic energy for the empty wind tunnel. Velocity profiles represented as vectors are shown at different streamwise positions

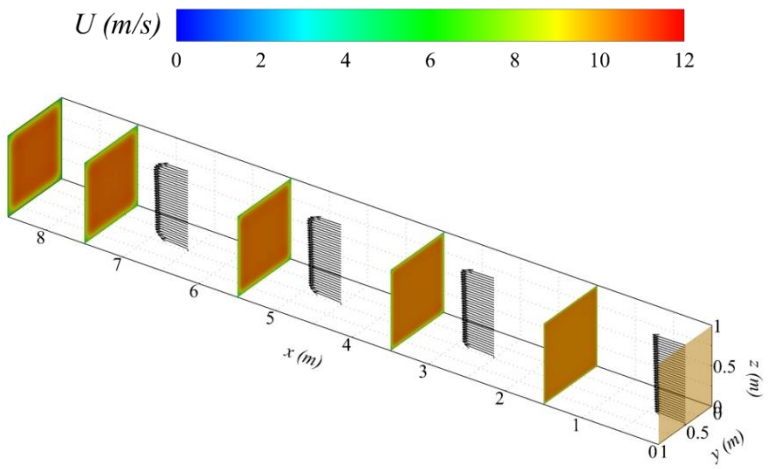

(a)

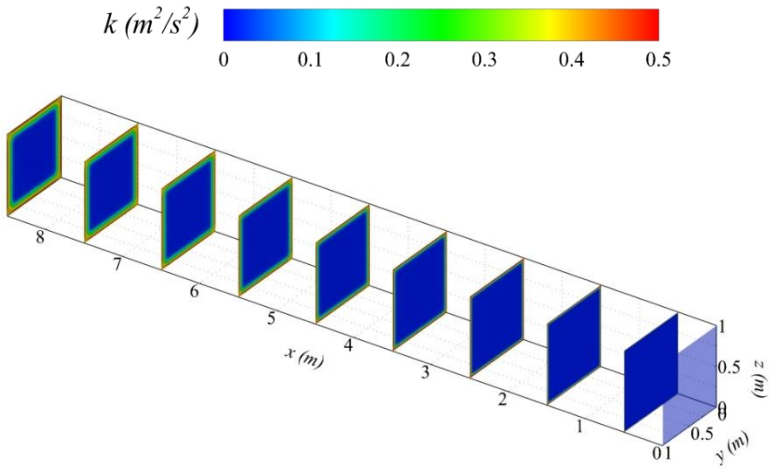

(b)

Figure 3.31 Contour plots of: (a) streamwise velocity, and (b) turbulent kinetic energy for the empty wind tunnel

Figures 3.32 and 3.33 show respectively the comparison between the experimental and numerical results across the horizontal and vertical distances at the inlet of the test section. One should keep in mind that two different types of inlet boundary conditions were used separately for comparisons (i.e. horizontal and vertical profiles). As mentioned previously, the horizontal profile shows non-uniformity in the streamwise velocity and turbulence intensity profiles unlike the vertical profiles. Therefore, we tested their effects separately as an inlet boundary condition. As expected both inlet boundary condition profiles show good match with the experimental data, since it is basically a curve fit of the measured data.

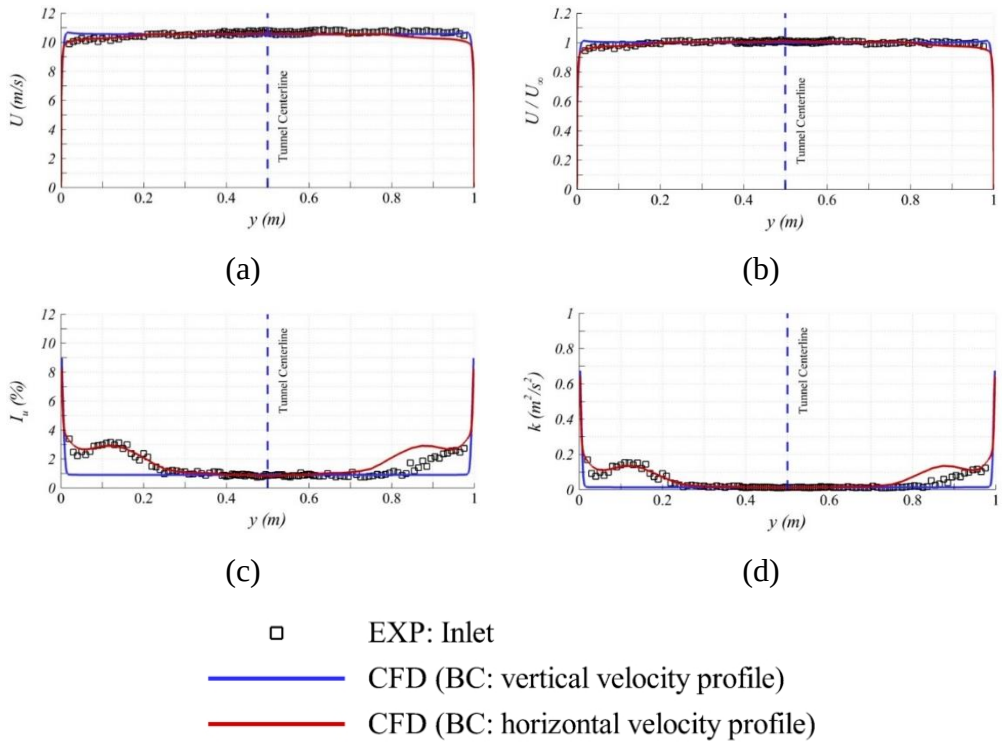

Figure 3.32 Horizontal profiles at the inlet of the test section: (a) streamwise velocity, (b) normalized streamwise velocity, (c) streamwise turbulence intensity, and (d) turbulent kinetic energy. Dashed blue line marks the tunnel centerline

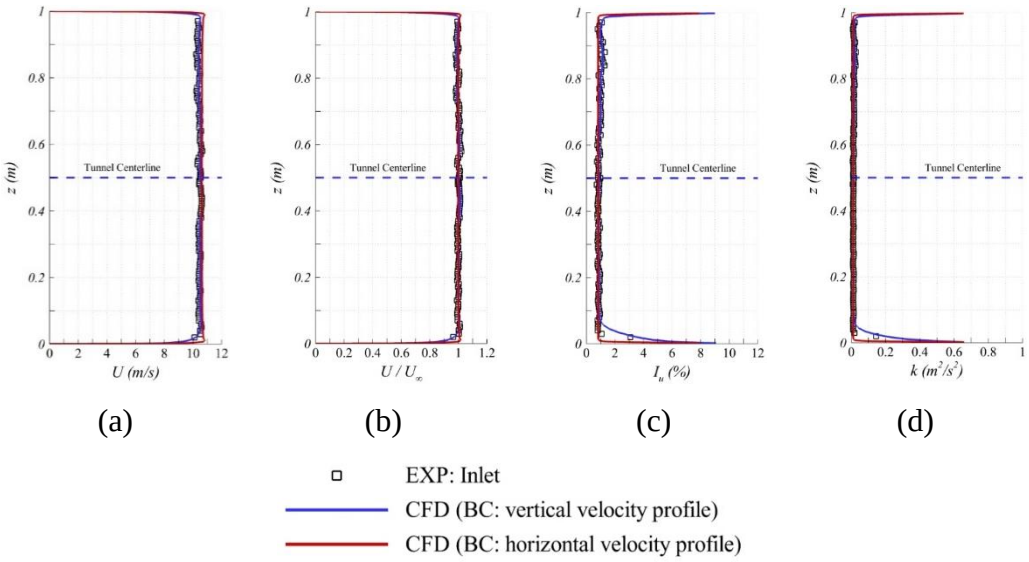

Figure 3.33 Vertical profiles at the inlet of the test section: (a) streamwise velocity, (b) normalized streamwise velocity, (c) streamwise turbulence intensity, and (d) turbulent kinetic energy. Dashed blue line marks the tunnel centerline

Based on the inlet boundary conditions used, comparisons with experimental data at 6 m and 7 m downstream of the test section inlet has been conducted in order to check the validity of the boundary conditions as well as assess the accuracy of the numerical simulation. In this respect, Figure 3.34 shows the horizontal profiles at 6 m downstream of the test section inlet. As one could observe, when the vertical profile is used as an inlet boundary condition better match between the experiments and numerical results is obtain for the streamwise velocity as shown in Figures 3.34a and b. Similarly, the turbulence intensity and turbulent kinetic energy profiles show good match except near the side walls where the numerical results under predict the experimental data if vertical profile is used and over predict it if the horizontal profile is used as an inlet boundary condition. Similar observations can be seen at 7 m downstream as shown in Figure 3.35. One could also observe, from Figures 3.34 and 3.35 that the problem associated with turbulence intensity at the inlet of the test section persists to downstream locations shown as a bump at the left hand side.

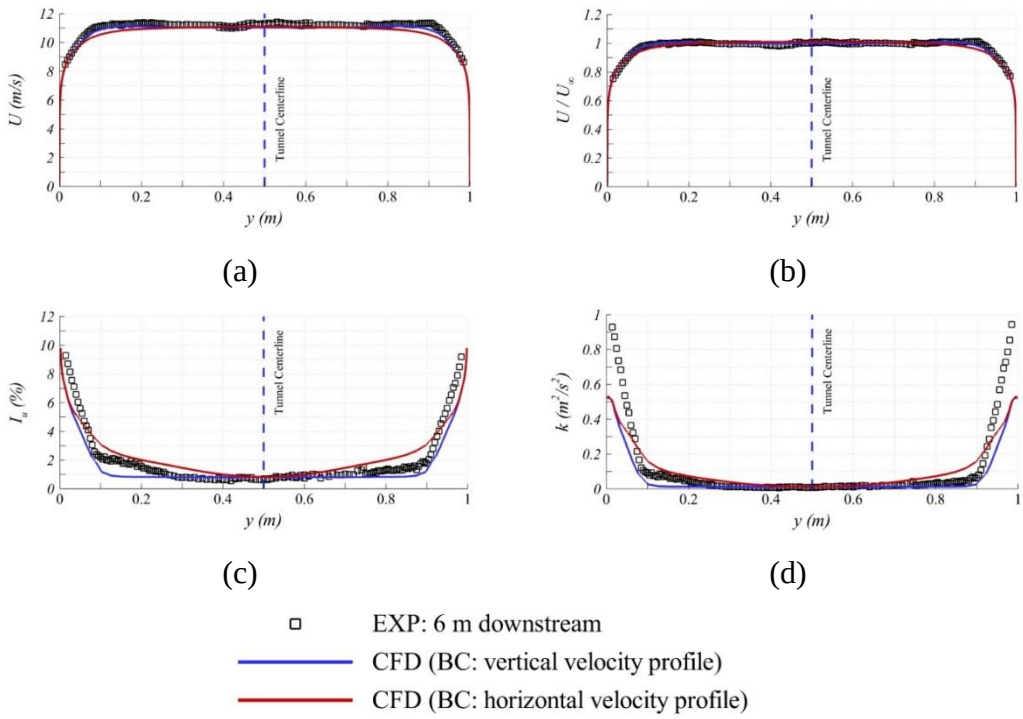

Figure 3.34 Horizontal profiles 6 m dowstream of the test section inlet: (a) streamwise velocity, (b) normalized streamwise velocity, (c) streamwise turbulence intensity, and (d) turbulent kinetic energy. Dashed blue line marks the tunnel centerline

Figure 3.36 shows comparisons between the measured data and numerical results along the vertical distance at 7 m downstream of the test section inlet. As can been from the results, the streamwise velocity distributions shown in Figure 3.36a and b shows good match between experiments and numerical results. On the other hand, the turbulence intensity and turbulent kinetic energy profiles show good match in the freestream flow outside the boundary layer. However, inside the boundary layer the numerical results under predict the measured data.

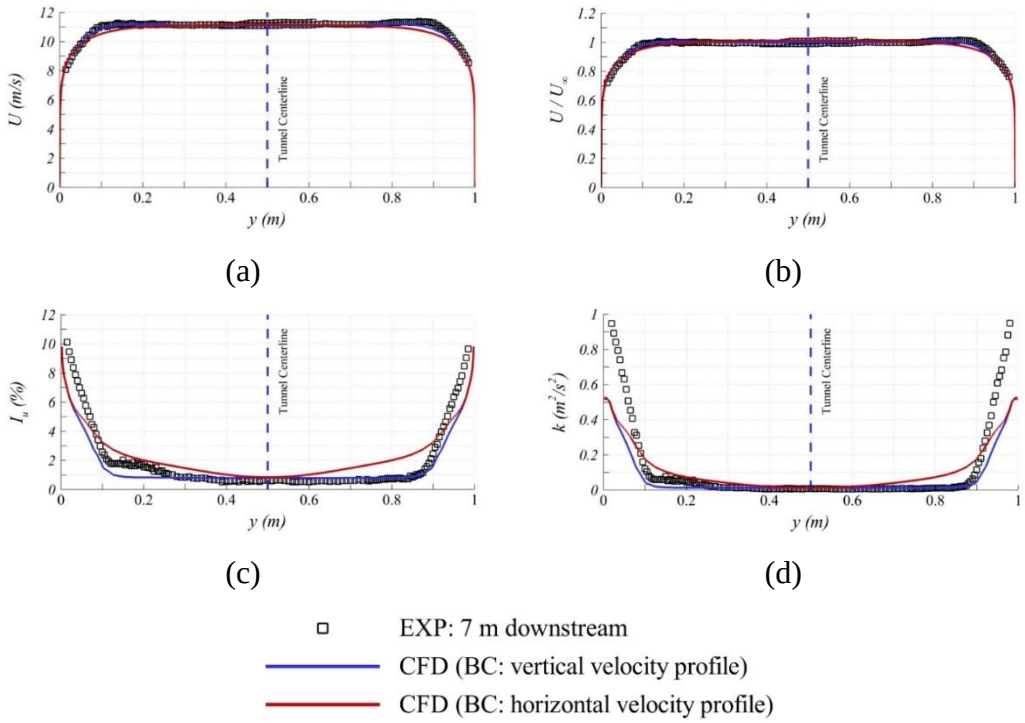

Figure 3.35 Horizontal profiles 7 m dowstream of the test section inlet: (a) streamwise velocity, (b) normalized streamwise velocity, (c) streamwise turbulence intensity, and (d) turbulent kinetic energy. Dashed blue line marks the tunnel centerline

Quantitative comparisons between the measured data and numerical results are presented in Table 3.12 in terms of boundary layer properties. Power law curve fits shows similar power law exponents and comparable boundary layer thicknesses. Figure 3.37a shows the normalized streamwise velocity with power law curve fit. The friction velocity and aerodynamic roughness height are obtained using the logarithmic law curve fit as shown in Figure 3.37b. However, the numerical results slightly under predict these values.

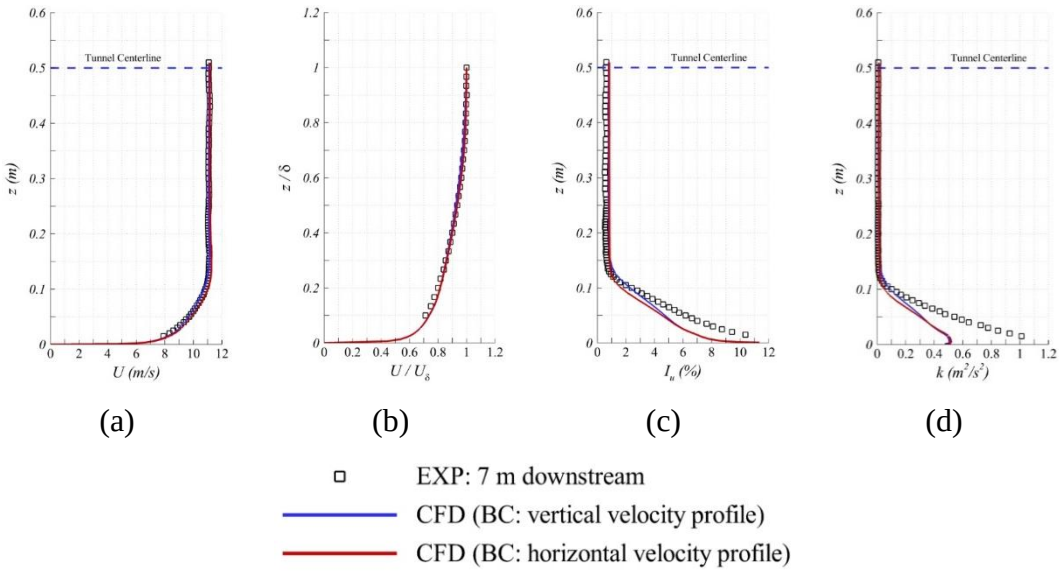

Figure 3.36 Vertical profiles 7 m dowstream of the test section inlet: (a) streamwise velocity, (b) normalized streamwise velocity, (c) streamwise turbulence intensity, and (d) turbulent kinetic energy. Dashed blue line marks the tunnel centerline

Table 3.12 Summary of atmospheric boundary layer properties for the empty wind tunnel

Properties	Experimental Results	CFD Results	Error (%)
α	0.13	0.13	0
$\delta\ (m)$	0.15	0.15	0
$\delta^*\ (m)$	0.017	0.016	5.88
$\theta\ (m)$	0.014	0.013	7.14
H	1.252	1.276	1.92
$u^*\ (m/s)$	0.557	0.471	15.44
$z_0\ (m)$	5.12E-05	1.38E-05	73
$U_e\ (m/s)$	11.110	11.112	0.018

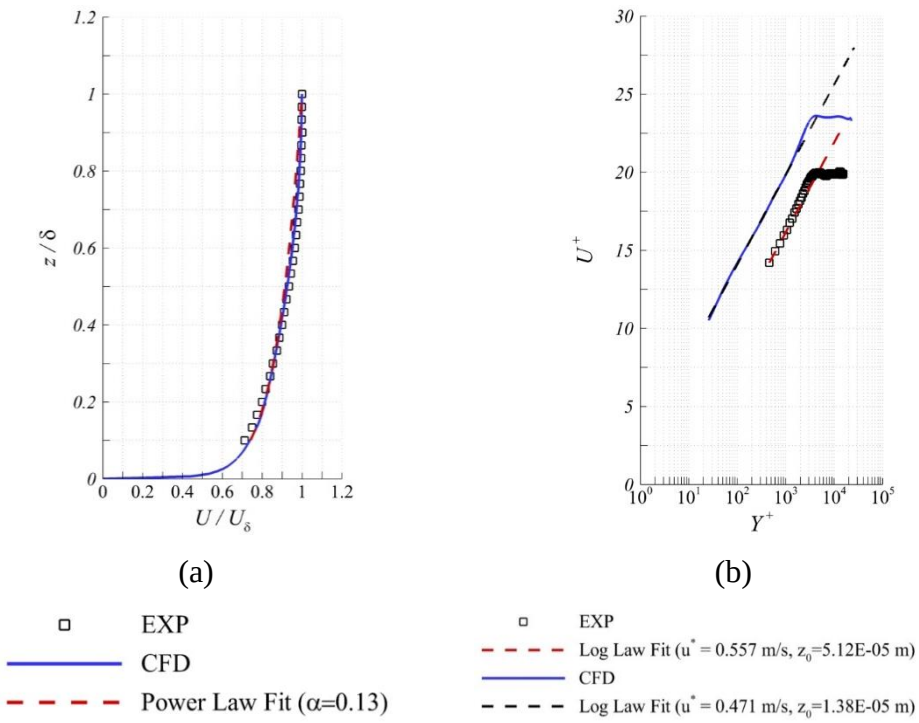

Figure 3.37 (a) streamwise velocity distribution with power law curve fit, and (b) log-law with logarithmic curve fit

3.3.4.2 Wind Tunnel Equipped with Spires

In this section we will present the experimental and numerical results for the empty wind tunnel equipped with spires test case. Three spires with a height of 0.67 m have been designed according to Irwin [182] design methodology and installed at the inlet of the test section in order to achieve a target power law exponent of 0.25 which corresponds to terrain exposure B. Table 3.13 summaries the design parameters of the spires and roughness elements (30 x 5 aligned).

Table 3.13 Design parameters of spires for terrain exposure B

Terrain Exposure	α	N	$h\ (m)$	$\delta\ (m)$	$X_0\ (m)$	$b\ (m)$	$s\ (m)$	$w\ (m)^*$	$D\ (m)$	$k\ (m)$
B	0.25	3	0.67	0.54	4.0	0.09	0.34	0.168	0.2	0.035

$w=h/4$: splitter width

Figures 3.38 and 3.39 present the contours of the streamwise velocity and turbulent kinetic energy distributions for the empty wind tunnel equipped with spires. As can be seen from the contour plots the effect of spires is significant associated. In the near wake the flow field is characterized with low momentum and high turbulent kinetic energy directly downstream of the spires. As one moves downstream the effect of spires reduces and the flow starts to recover to the freestream flow. Velocity vectors show the development of the boundary layer flow with downstream distance.

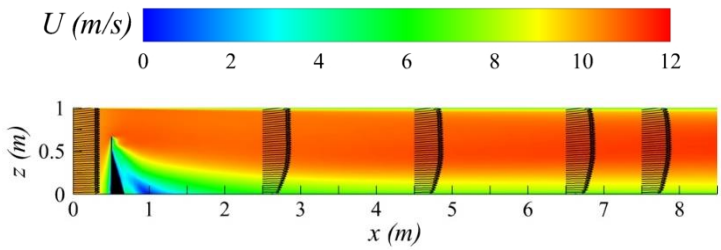

(a)

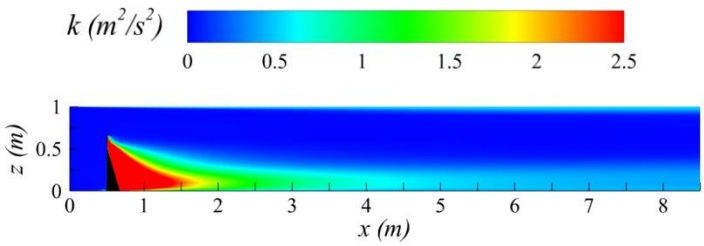

(b)

Figure 3.38 Contour plots of: (a) streamwise velocity, and (b) turbulent kinetic energy for the empty wind tunnel equipped with spires. Velocity profiles represented as vectors are shown at different streamwise positions

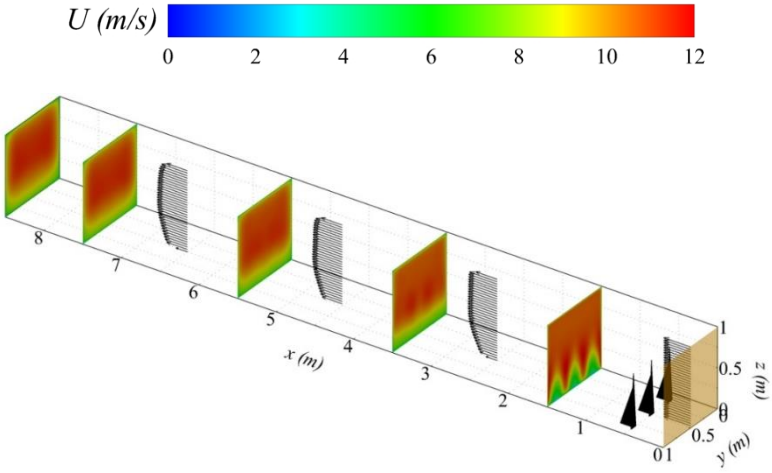

(a)

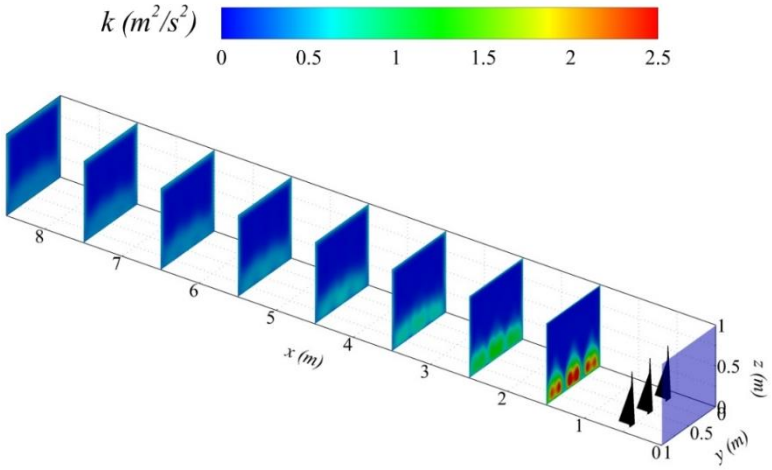

(b)

Figure 3.39 Contour plots of: (a) streamwise velocity, and (b) turbulent kinetic energy for the empty wind tunnel equipped with spires. Velocity profiles represented as vectors are shown at different streamwise positions

Figure 3.40 shows the horizontal profiles measured at 7 m downstream of the test section inlet. As one could observe, the effect of the spires on the velocity profiles is insignificant showing the wake has diffused downstream. On the other hand, the effects are still present on the turbulence intensity and turbulent kinetic energy. The numerical results show good match to the experimental data in terms of velocity profiles unlike the turbulence profiles where the numerical results under predict the experimental data.

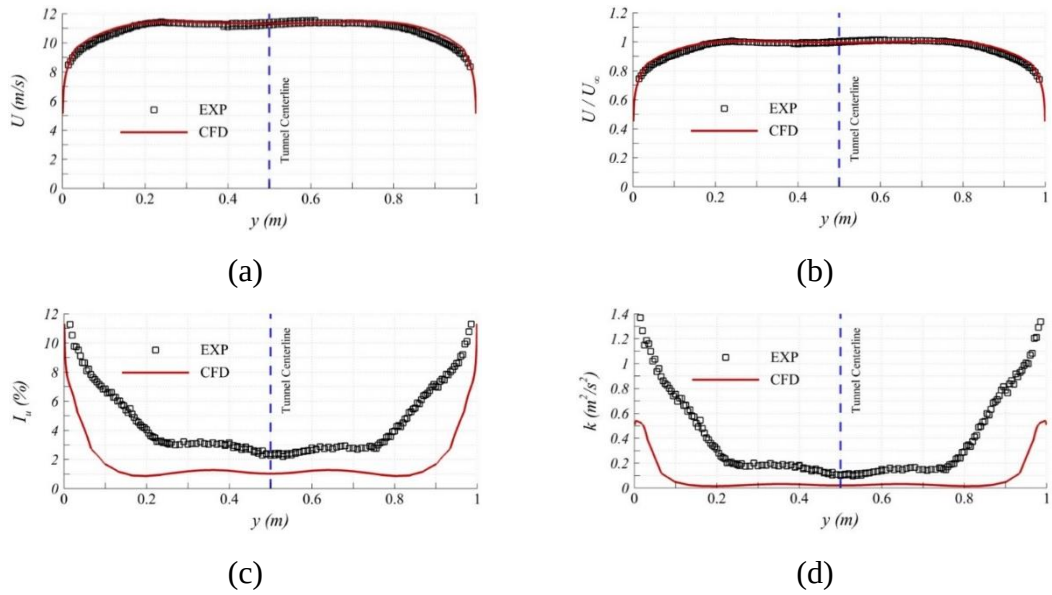

(a) (b)

(c) (d)

Figure 3.40 Horizontal profiles 7 m dowstream of the test section inlet: (a) streamwise velocity, (b) normalized streamwise velocity, (c) streamwise turbulence intensity, and (d) turbulent kinetic energy. Dashed blue line marks the tunnel centerline

Figure 3.41 shows the vertical profiles measured at 7 m downstream of the test section inlet. Similar observation can be seen in the velocity profiles where the numerical results show good match unlike the turbulence intensity and turbulent kinetic energy where it under predict the experimental data.

Quantitative comparisons between the measured data and numerical results are presented in Table 3.14 in terms of boundary layer properties for the case with spires. Power law curve fits show that the power law exponent is over predicted in the numerical results, however, comparable boundary layer thicknesses are obtained between the experiments and numerical results. Figure 3.42a shows the normalized streamwise velocity with power law curve fits. The friction velocity and aerodynamic roughness height are obtained using the logarithmic law curve fit as shown in Figure 3.42b. However, the numerical results slightly over predict these values.

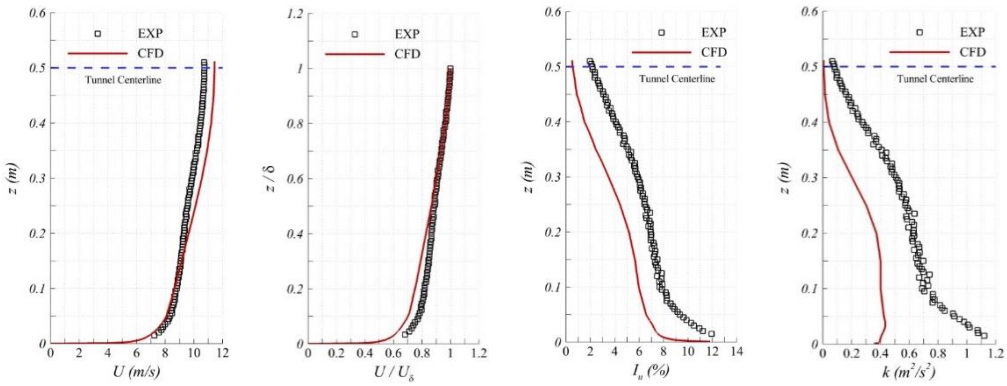

(a) (b) (c) (d)

Figure 3.41 Vertical profiles 7 m dowstream of the test section inlet: (a) streamwise velocity, (b) normalized streamwise velocity, (c) streamwise turbulence intensity, and (d) turbulent kinetic energy. Dashed blue line marks the tunnel centerline

Table 3.14 Summary of atmospheric boundary layer properties for the wind tunnel equipped with spires

Properties	Experimental Results	CFD Results	Error (%)
α	0.11	0.15	36.36
$\delta\ (m)$	0.445	0.436	2
$\delta^*\ (m)$	0.047	0.060	27.66
$\theta\ (m)$	0.036	0.047	30.56
H	1.214	1.286	5.93
$u^*\ (m/s)$	0.319	0.374	17.24
$z_0\ (m)$	1.72E-05	7.73E-05	-
$U_e\ (m/s)$	10.628	11.207	5.45

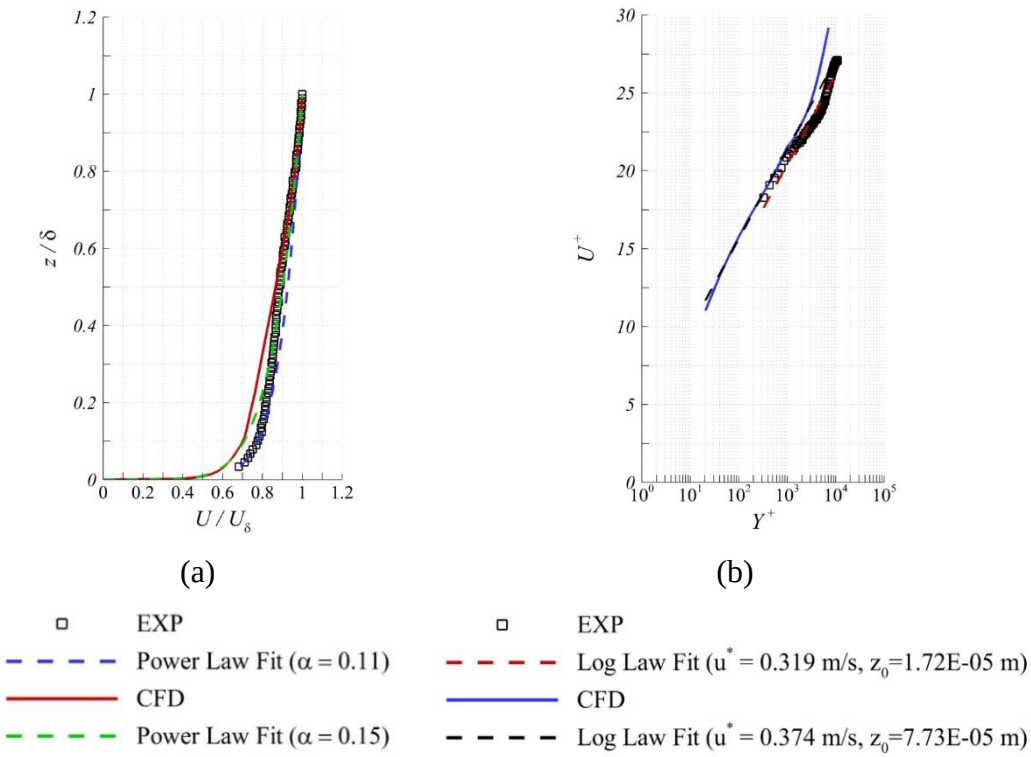

Figure 3.42 (a) streamwise velocity distribution with power law curve fit, and (b) log-law with logarithmic curve fit

3.3.4.3 Wind Tunnel Equipped with Spires and Roughness Elements

In this section we will present the experimental and numerical results for the empty wind tunnel equipped with spires and roughness elements. Three spires with a height of 0.67 m have been designed according to Irwin [182] design methodology and installed at the inlet of the test section in order to achieve a target power law exponent of 0.25 which corresponds to terrain exposure B. Additionally, a roughness fetch consisting of 200 roughness elements with a height of 35 mm and separation distance of 200 mm extends up to 6.5 m downstream of the test section inlet. The design parameters are summarized in Table 3.13 previously.

Figures 3.43 and 3.44 present the contours of the streamwise velocity and turbulent kinetic energy distributions for the empty wind tunnel equipped with spires and roughness elements. As can be seen from the contour plots the addition of roughness

elements is significant associated with it added momentum and high turbulent kinetic energy. As one moves downstream the effect of spires reduces and the flow starts to recover to the freestream flow. Velocity vectors show the development of the boundary layer flow with downstream distance.

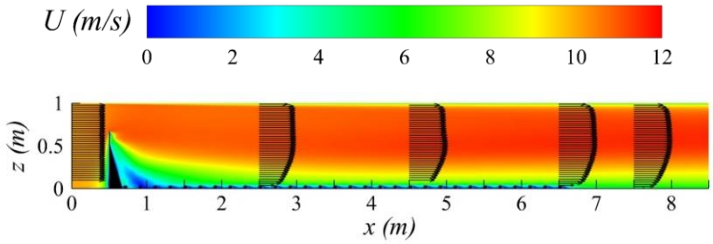

(a)

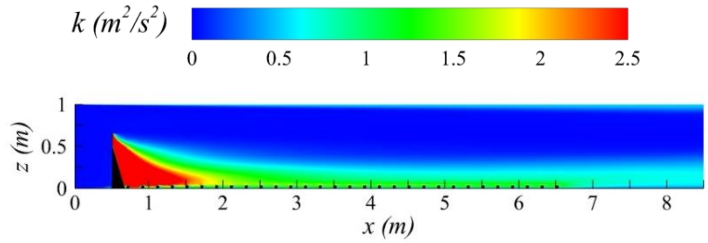

(b)

Figure 3.43 Contour plots of: (a) streamwise velocity, and (b) turbulent kinetic energy for the empty wind tunnel equipped with spires and roughness elements. Velocity profiles represented as vectors are shown at different streamwise positions

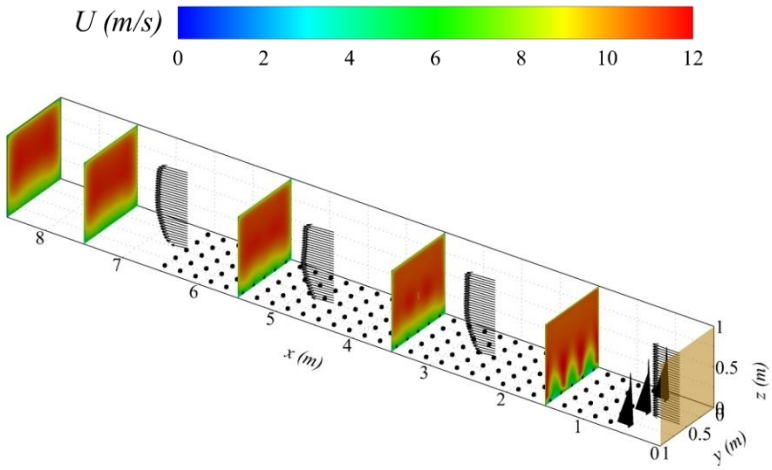

(a)

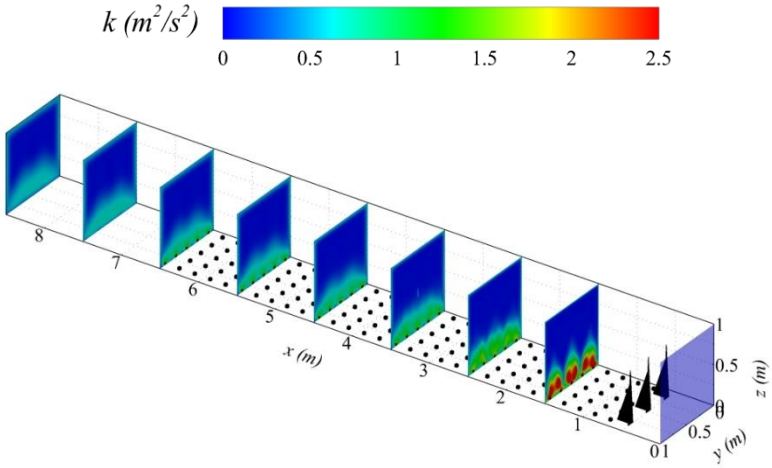

(b)

Figure 3.44 Contour plots of: (a) streamwise velocity, and (b) turbulent kinetic energy for the empty wind tunnel equipped with spires and roughness elements. Velocity profiles represented as vectors are shown at different streamwise positions

Figure 3.45 shows the vertical profiles measured at 7 m downstream of the test section inlet. Similar observation can be seen in the velocity profiles where the numerical results show good match unlike the turbulence intensity and turbulent kinetic energy where it under predict the experimental data.

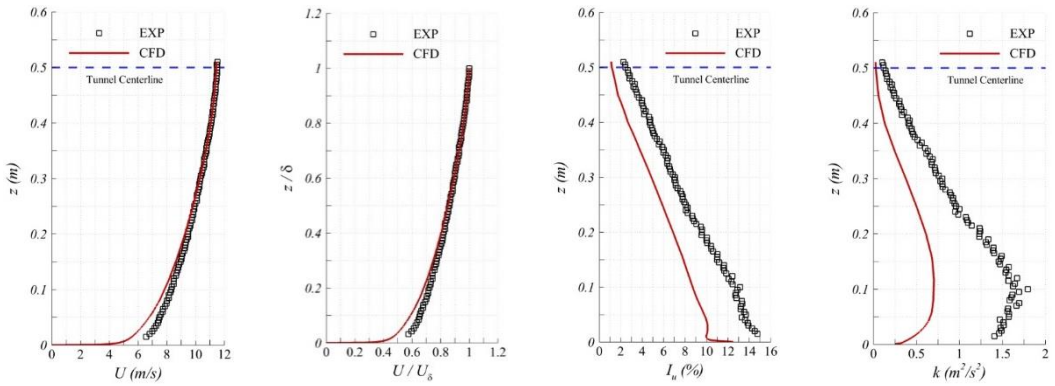

(a) (b) (c) (d)

Figure 3.45 Vertical profiles 7 m dowstream of the test section inlet: (a) streamwise velocity, (b) normalized streamwise velocity, (c) streamwise turbulence intensity, and (d) turbulent kinetic energy. Dashed blue line marks the tunnel centerline

Quantitative comparisons between the measured data and numerical results are presented in Table 3.15 in terms of boundary layer properties for the case with spires and roughness elements. Power law curve fits show that the power law exponent is over predicted in the numerical results, however, comparable boundary layer thicknesses are obtained between the experiments and numerical results. Figure 3.46a shows the normalized streamwise velocity with power law curve fits. The friction velocity and aerodynamic roughness height are also obtained using the logarithmic law curve fit as shown in Figure 3.46b. However, the numerical results slightly over predict those values.

The aim of this assessment is to check the validity of the numerical approach with experimental data, as well as check if the experimental results matches the properties of the ABL for terrain exposure B. One can see from the experimental results that the target power law exponent as well as the target boundary layer thickness are under predicted. This probably attributed to the distribution of roughness elements. That is more test cases in terms of roughness height and configuration need to be conducted to achieve the target properties.

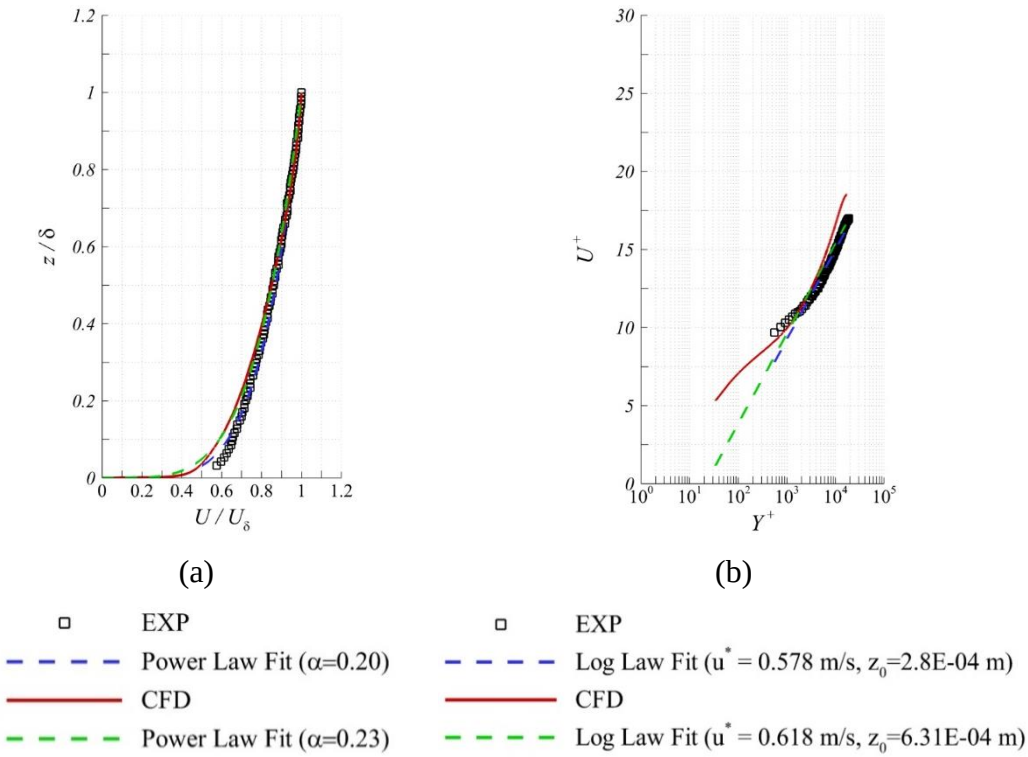

Figure 3.46 (a) streamwise velocity distribution with power law curve fit, and (b) log-law with logarithmic curve fit

Table 3.15 Summary of atmospheric boundary layer properties for the wind tunnel equipped with spires and roughness elements

Properties	Experimental Results	CFD Results	Error (%)
α	0.20	0.23	15
$\delta\ (m)$	0.470	0.476	1.28
$\delta^*\ (m)$	0.072	0.087	20.83
$\theta\ (m)$	0.053	0.061	15.10
H	1.358	1.444	6.33
$u^*\ (m/s)$	0.578	0.618	6.92
$z_0\ (m)$	2.8E-04	6.31E-04	-
$U_e\ (m/s)$	11.260	11.388	1.14
$u_{z_h}(m/s)$	7.025	6.325	9.96

Table 3.16 shows the aerodynamic roughness height normalized with the roughness element height compared with empirical relations obtained from literature. Aerodynamic roughness height is a critical parameter for ABL and terrain exposure selection. Correct estimation of this parameter is vital to represent the ABL and terrain characteristics. Several authors [224-229] attempted to quantify this parameter empirically based on wind tunnel measurements or field measurements. In here we compared the aerodynamic roughness height of the current study with empirical models proposed in the literature. As one could observe all the empirical models over predicts the experimental results.

Table 3.16 Comparison of aerodynamic roughness height with empirical formulas from literature

Aerodynamic Roughness Height	z_0/z_h
Experimental	2.43E-03
CFD	1.80E-03
$Lettau$ [224]	1.53E-02
$Theure$ [225]	4.65E-02
$Macdonal$ [226]	5.12E-02
$Kutzbac$ [227]	1.94E-0.2
$Raupac$ [228]	3.23E-02
$Bottem$ [229]	2.24E-02

3.3.4.4 Comparison with International Standards

This section presents the comparisons of the turbulence intensity profiles of the ABL for the case of spires and the case of spires with roughness elements against international standards from ASCE 7-16, ASCE 49-12 and EN1991-1-4-2005. Figure 3.47 shows the full scale comparison between the experimental results, CFD results as well as international standards. As one can observe both the experimental results as well as the numerical results underestimate the turbulence intensity of the international standards for terrain exposure B. Although, the velocity profiles match

well with the international standards for terrain exposure B, the turbulence intensity requires additional roughness elements to increase the turbulence in the ABL. However, cautious should be taken when trying to match the turbulence intensity levels by adding roughness elements which might result in higher power law exponent for the velocity profiles. Therefore, one should optimize which parameters are necessary to match.

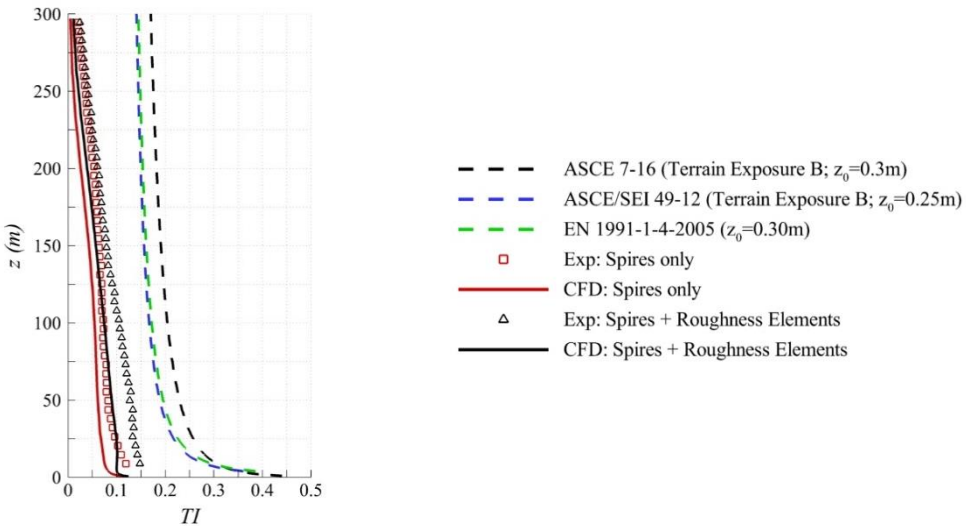

Figure 3.47 Comparison of the ABL turbulence intensity profiles at full scale with international standards

3.4 Upgrade of RÜZGEM C3 Boundary Layer Wind Tunnel

In the previous section we carried out an experimental as well as numerical simulation of RÜZGEM C3 boundary layer wind tunnel in order to generate an ABL inside the wind tunnel as well as validate the numerical approach. Results show that the numerical approach used in this study to simulate the ABL is valid when using the $1/2 - model$ approach. The numerical methodology seems to give acceptable results in terms of velocity profiles, however, it under predicts the turbulence intensity profiles. In addition, as mentioned during the previous section the wind tunnel seems to suffer from a non-uniform velocity and turbulence intensity distributions at the inlet of the test section and this non-uniformity persists to

downstream positions. The main reason is due to the two-dimensional inlet contraction.

In order to carry out reliable wake measurements downstream of the porous disc, the wind tunnel inlet design will be upgraded to a three-dimensional inlet contraction with a settling chamber and a bell-mouth in order to improve the flow quality. The new design of the wind tunnel is shown in Chapter 4, and Figures 3.47 and 3.48 shows comparison of the velocity and turbulence intensity profiles measured at the inlet of the test section along the horizontal and vertical directions between the old configuration and the new configuration of the wind tunnel.

As one could observe the new design of the inlet contraction has significantly improved the flow quality inside the test section of the wind tunnel. Uniform velocity distributions along the horizontal and vertical directions associated with uniform turbulence intensity distribution and lower levels of turbulence are clearly visible for new inlet design.

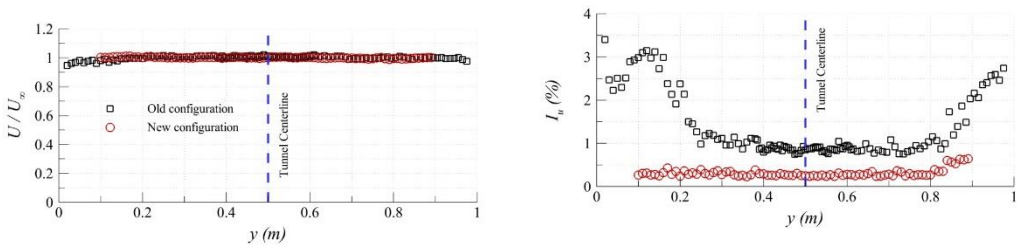

(a) (b)

Figure 3.48 Horizontal profiles of: (a) normalized streamwise velocity, and (b) streamwise turbulence intensity of the old and new configuration of the wind tunnel facility. Dashed blue line marks the tunnel centerline

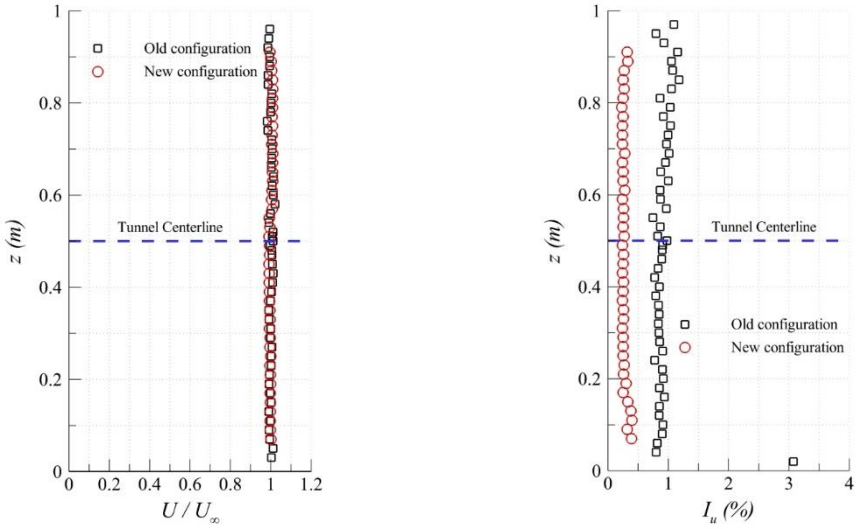

(a) (b)

Figure 3.49 Vertical profiles of: (a) normalized streamwise velocity, and (b) streamwise turbulence intensity of the old and new configuration of the wind tunnel facility. Dashed blue line marks the tunnel centerline

CHAPTER 4

POROUS DISC EXPERIMENTAL SETUP AND MEASUREMENT DETAILS

This chapter presents the experimental setup and measurements details conducted to investigate the effects of inflow boundary layer on the wake characteristics of a radially non-uniform porous disc.

4.1 Upgraded Wind Tunnel Facility

The experiments were performed in the open-return suction type boundary layer wind tunnel (RÜZGEM C3) of Middle East Technical University (METU) Center for Wind Energy Research (RÜZGEM) as shown in Figure 4.1. This wind tunnel facility is an upgrade of an older wind tunnel due to several problems occurring due to the 2D contraction of the wind tunnel. Modifications have been implemented by changing the entire inlet of the wind tunnel. The wind tunnel consists of a settling chamber section, a contraction with a contraction ratio of $1:5$, and a fully transparent test section with a cross-sectional area of $1 \times 1\ m^2$ and a length of $8\ m$. It is powered by a $45 - kW$ speed-controlled electrical motor, which drives a $1.2\ m$ diameter axial fan. The settling chamber includes a honeycomb and a screen in order to ensure high flow quality inside the test section. Maximum velocity inside the test section is $25\ m/s$ and the average inlet turbulence intensity is about $0.35\ \%$.

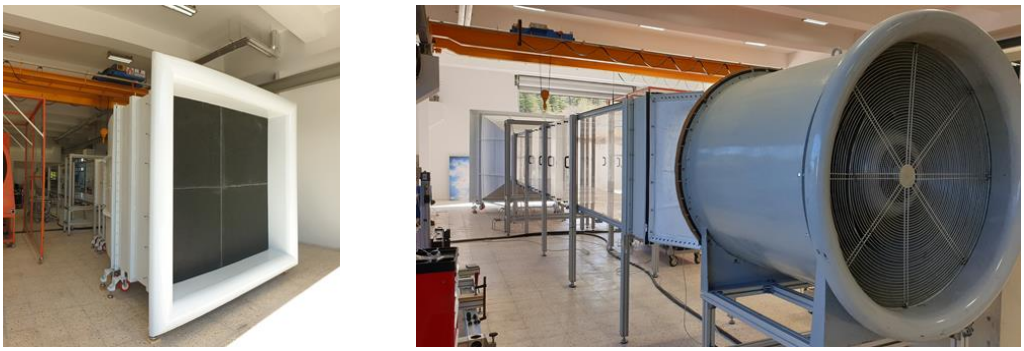

Figure 4.1 Open return boundary layer wind tunnel facility at Center for Wind Energy Research (RÜZGEM) at the Middle East Technical University (METU)

4.1.1 Wind Tunnel Control System

An in-house closed-loop wind tunnel control system developed in LABVIEW is used for the operation of the wind tunnel facility in three different modes. MODE 1 represents the manual operation of the wind tunnel based on fan speed (RPM). MODE 2 is conducted under a constant wind speed operation. Finally, constant Reynolds number operation is considered as MODE 3. Figure 4.2 shows a picture of the user interface for the operation and control of the wind tunnel facility.

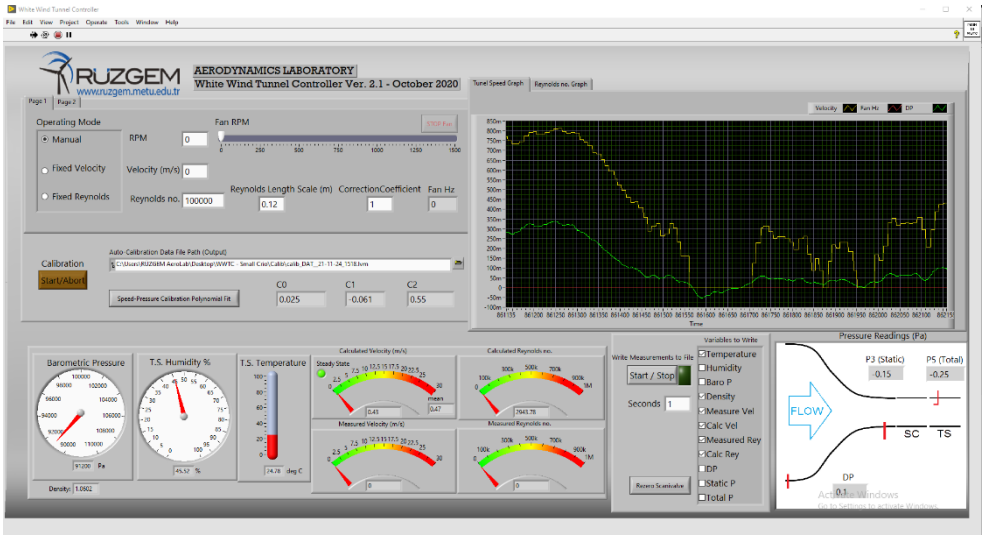

Figure 4.2 User interface of the closed-loop control system for the wind tunnel facility

The wind tunnel is instrumented with 8 static pressure tabs embedded on two locations on the surface of the contraction cone (referred to as position 1 and 2) as shown ın Figure 4.3. Static taps are drilled on four sides of the tunnel walls and are connected through manifolds. A pitot-static tube is mounted inside the front part of the test section in order to measure the static and total pressure of the flow as shown in Figure 4.3. The pitot-static pressure measurement is performed by a 16-channel differential pressure scanner from Scanivalve®. A differential pressure transmitter measures the pressure difference between section 1 and section 2 across the contraction cone as shown in Figure 4.3. A temperature/humidity sensor is situated inside the wind tunnel at the exit of the test section to measure the temperature and humidity of the airflow during the experiments. Atmospheric (Barometric) pressure is monitored by a sensor located outside the wind tunnel. The fan speed is adjusted using analog input speed reference node of the fan drive. The developed LabVIEW real-time application is used to acquire the measured data and adjust the fan rotating speed. This closed-loop control system takes into account the blockage effects due to models inserted in the test section (such as spires and roughness elements).

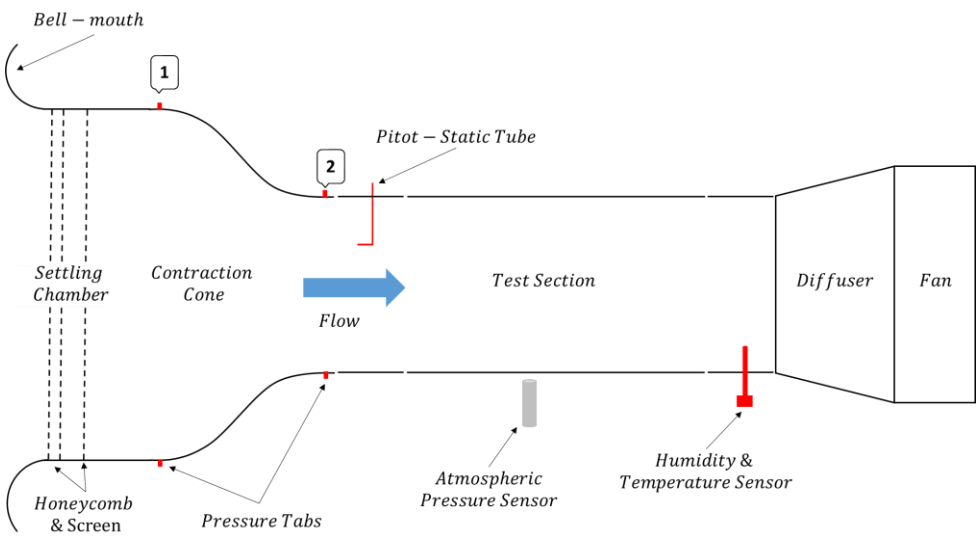

Figure 4.3 Sketch of the wind tunnel facility with the instruments and sensors locations for the closed-loop control system

The porous disc PIV measurements are conducted under constant Reynolds number operation (MODE 3). The Reynolds number is taken based on free stream velocity upstream of the disc and the disc diameter.

4.2 Porous Disc

The porous disc used in the experiments has a diameter of 120 mm, with radially non-uniform porosity. This non-uniform porosity is designed to match the induction and thrust coefficients of a small horizontal axis wind turbine that has the same diameter as the disc, as explained in Camp and Cal [157]. The porous disc has a thrust coefficient of 0.64 and an induction coefficient of 0.2. It was previously used as a part of a round-robin test campaign conducted by several different institutions [230].

This porous disc when compared with a full-scale wind turbine (assuming a wind turbine of 100-meter diameter) reveals that the wind turbine is scaled down about 830 times from a real-life length scale [115]. Cal et al. [115] claim that this ratio is approximately similar to the ratio of Reynolds numbers since the characteristic velocities in the wind tunnel and the fluid viscosity will be similar to those in field conditions. However, dynamic similarity will not be achieved when representing the detailed wind turbine and related interactions. Therefore, the focus will be on mean wake flow field, where Reynolds number effects are minimal.

The properties of the porous disc are given in Table 4.1 and its geometry is shown in Figure 4.4. The amount of blockage in the test section that is caused by the porous disc and the support is 1.15 %.

Table 4.1 Porous disc properties

Material	Plywood
Porosity	Non-uniform
Disc thickness	3.2 mm
Disc diameter	120 mm
Mast diameter	10 mm
Mast properties	Smooth shaft
Hub diameter	10.8 mm
Hub height	Not fixed
Blockage	1.15 %

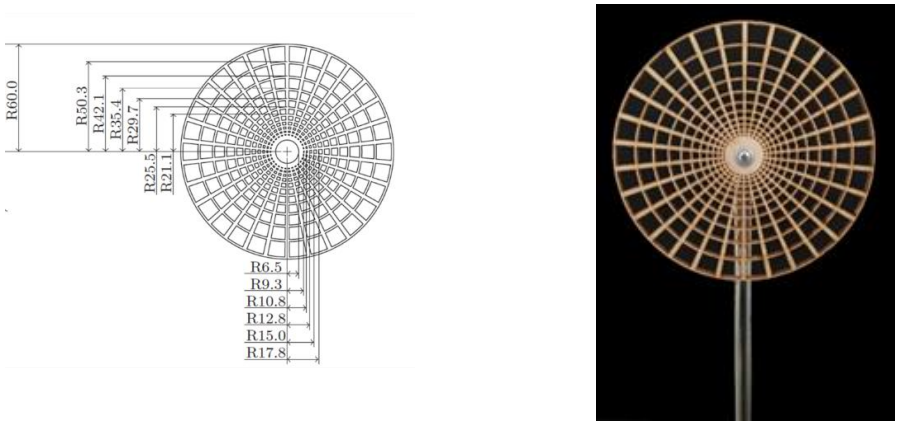

(a) (b)

Figure 4.4 (a) Schematic of the porous disc, 120 mm diameter and non-uniform porosity [230], (b) a picture of the porous disc used in the current experiments attached to the support

4.3 Boundary Layer Generation and Disc Inflow Conditions

A boundary layer velocity profile with a power law coefficient of 0.15 is obtained by placing three $0.67\,m$ high spires at the inlet of the test section. The spire geometries are designed by using the methodologies described by Irwin [182]. The generated boundary layer is representative of an onshore atmospheric boundary layer for a typical country side with flat terrain as indicated in Wind Energy Handbook by Burton et al. [167]. The porous disc is positioned $6\,m$ downstream of the inlet of the test section. A general sketch of the setup and relevant coordinate systems are presented in Figure 4.5. The (x', y', z') coordinate system is the local coordinate system that is fixed to the porous disc center and it is used as the reference for wake measurements while referring to different positions of the disc in the boundary layer. The (x, y, z) coordinate system is fixed at the bottom wall of the test section and it is used as the reference for the disc position in the test section.

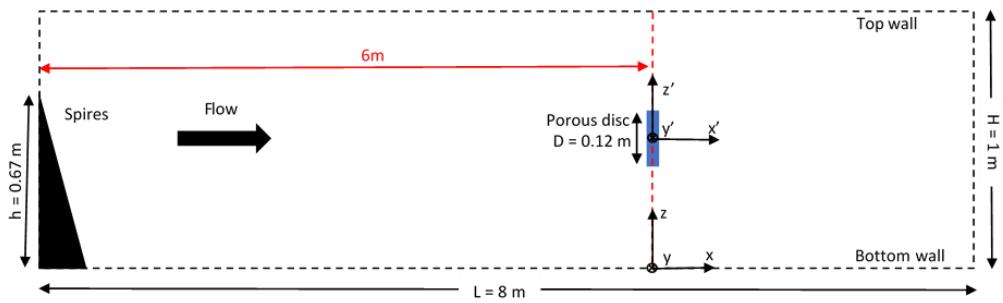

Figure 4.5 Schematic layout of the wind tunnel test section and porous disc measurement setup

Boundary layer measurements are performed for a disc Reynolds number of 102,000 based on the free-stream wind speed outside the boundary layer and the disc diameter. In order to obtain the inflow conditions, hot-wire anemometry measurements are conducted at two streamwise positions in the test section: the first one is about 1 m upstream of the disc at $(x/D = -8.5)$ with the disc present in the test section, and the second one at the disc position $(x/D = 0)$ without the disc. The boundary layer flow is measured by traversing a single sensor hotwire from bottom wall of the test section towards the top wall spanning a distance of 0.8 m $(z/D = 6.6)$. Data are collected at a sampling rate of 10 kHz for 30 $seconds$ for these measurements.

Figure 4.6 shows the variation of the mean streamwise velocity normalized with the free stream velocity (U_∞) and the streamwise turbulence intensity profiles for the generated boundary layer at both locations, together with a power law curve fit to the measured velocity profile with a power exponent of 0.15, which confirms that the desired velocity profile is obtained. The difference in velocity profiles between the two cases are marginal only with some minor differences in turbulence intensity below $z/D = 2$. The boundary layer thickness for both cases is estimated to be about 63 cm from the bottom wall through analysis of the velocity gradient profile in the wall normal direction after applying a running-average filter to the velocity profile with a window size of 7 data points. Based on this boundary layer thickness, other boundary layer parameters such as the displacement thickness, the momentum thickness and the shape factor are calculated also for both cases and the results are

listed in Table 4.2. The results reveal that the boundary layer profiles are identical, and the presence of the disc has minimal effect on the upstream boundary layer. It can be deduced that the boundary layer has reached a fully developed state since the velocity profiles at $x/D = -8.5$ and at $x/D = 0$ are basically identical, and there are only minor variations in turbulent kinetic energy levels around $z/\delta = 0.32$. In addition, the velocity and turbulence intensity profiles are representative of a neutral atmospheric boundary layer where thermal effects are not present as indicated in Wallace and Hobbs [231]. Therefore, this boundary layer profile is used as the inflow condition for the disc wake measurements.

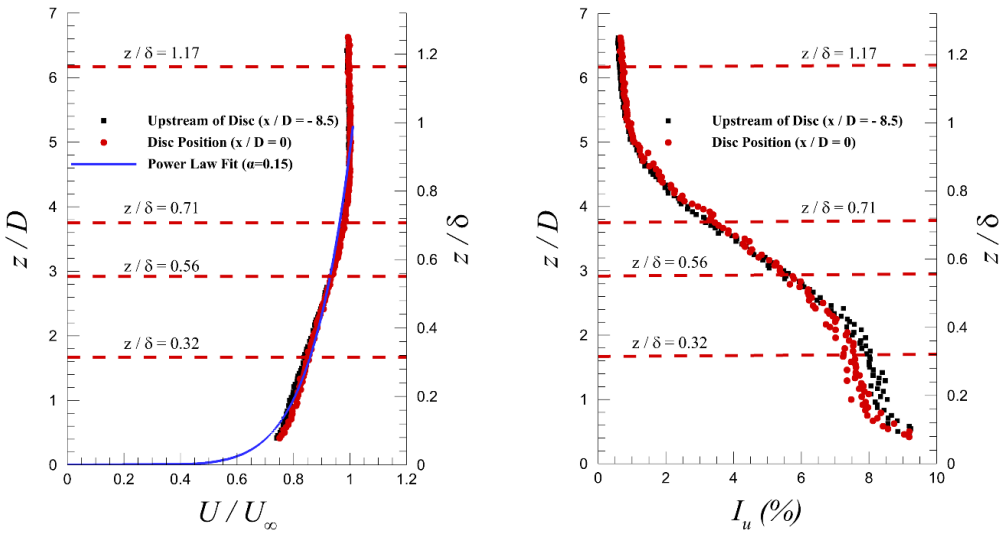

(a) (b)

Figure 4.6 Vertical profiles of: (a) normalized mean streamwise velocity, and (b) streamwise turbulence intensity. Dashed red lines mark the disc positions used during wake measurements

Table 4.2 Boundary layer properties at the streamwise positions of ($x/D = -8.5$) and ($x/D = 0$)

Boundary layer properties	α	$\delta\ (m)$	$\delta^*\ (m)$	$\theta\ (m)$	(δ^*/θ)
Upstream of disc position ($x/D = -8.5$)	0.15	0.63	0.054	0.045	1.20
Disc position ($x/D = 0$)	0.15	0.63	0.053	0.044	1.19

The boundary layer modeled inside the wind tunnel when compared to the real atmospheric boundary layer (the ABL thickness for flat terrains with 0.15 power-law exponent is expected to be around 274 m [169]), reveals that the ABL is scaled down by 435 times from real-life scale. The ratio of disc diameter to boundary layer thickness is about 0.2, however, the ratio of real wind turbine diameter to real ABL thickness is about 0.36. This reveals that the wind tunnel conditions are not scaled entirely when considering these ratios. Another criterion can be considered is the ratio between the hub height of the wind turbine to the boundary layer thickness, which it corresponds to 0.36 (assuming 100 m hub height) in full scale. In the wind tunnel measurements of the present study, the disc hub height is varied from 0.2 m to 0.74 m, resulting in a ratio between 0.32-1.17, this reveals that a real wind turbine can be scaled down without discrepancy in Reynolds number similarity.

4.4 Measurements Details

Based on the results of the inflow boundary layer profile shown in Figure 4.6, four positions are selected for the disc center (hub) placement to be used in wake measurements, i.e. $z/\delta = 1.17, 0.71, 0.56\ and\ 0.32$ as marked with red dashed lines in Figure 4.6. The corresponding z/D positions are also displayed on the figure. These positions are specifically selected to allow for assessing the effects of different inflow conditions on the porous disc wake. For the uniform inlet flow condition, the disc is positioned outside the boundary layer at $z/\delta = 1.17$ where the velocity and turbulence intensity gradients are minimal. On other selected locations, for example at $z/\delta = 0.71$ and $z/\delta = 0.56$, while there is an inflow velocity gradient for both cases that is significantly different from each other, the turbulence intensity gradient is similar. Comparing the cases for $z/\delta = 0.56$ and $z/\delta = 0.32$, these cases have similar velocity gradients across the disc while having significantly different turbulence intensity gradient in the inflow. The relevant conditions for the selected cases are listed in Table 4.3.

Table 4.3 Inflow conditions for porous disc wake measurements

z/D	6.17	3.75	2.92	1.67
z/δ	1.17	0.71	0.56	0.32
Re_D	1.02 x 10^5	9.65 x 10^4	9.22 x 10^4	8.26 x 10^4
U_{hub} (m/s)	14.9	14.21	13.47	11.48
U_{hub}/U_∞	1.0	0.97	0.92	0.83
I_{hub} (%)	0.6	3.2	5.5	8.0
velocity variation across the disk-top to bottom (m/s)	0.03	0.55	0.93	0.94
velocity gradient (s^{-1})	0.25	4.57	7.76	7.82
TI variation across the disk-top to bottom (%)	0.15	2.54	3.0	0.68
TI gradient (m^{-1})	0.01	0.21	0.25	0.06

As the disc is moved towards lower levels of the boundary layer, the freestream velocity at the z/δ location corresponding to the center of the disc (hub velocity) starts to get reduced and the disc effectively starts operating at lower average Reynolds numbers. When the disc is at the topmost position outside the boundary layer, i.e., at $z/\delta = 1.17$, the Reynolds number is about $102{,}586$. In the bottom most position, i.e., at $z/\delta = 0.32$, the Reynolds number goes down to $82{,}560$, based on the hub velocity and the disc diameter. Nevertheless, a strong Reynolds number dependency is not expected in this Reynolds number range. Based on the wake measurements of a small wind turbine that is of similar diameter as the disc considered in the present study, Chamorro et al. [232] indicated that main flow statistics such as mean velocity and turbulence intensity become independent of Reynolds number starting from approximately $Re = 93{,}000$. One can also observe from their results that there exists some relatively weak dependency from $Re = 50{,}000$ to $Re = 90{,}000$. To check the general Reynolds number dependency of the porous disc used in the current study, we have conducted thrust coefficient

measurements in a Reynolds number range from 50,000 to 120,000. The variation of the measured thrust coefficient with Reynolds number is presented in Figure 4.7. As is evident, the variation in thrust coefficient is marginal.

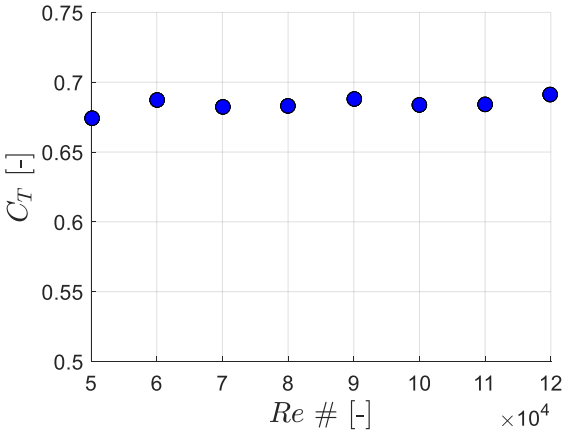

Figure 4.7 Thrust coefficient variation with Reynolds number for the porous disc

In addition to the fact that the Reynolds number gets reduced, the disc gets subjected to different levels of velocity and turbulence intensity gradients across its diameter as well as to progressively increasing levels of higher inflow turbulence intensity, as mentioned previously (see Table 4.3). In order to better focus mainly on the effects of the inflow gradients and turbulence intensity levels, the measured wake flow field distributions (as presented in the Results section of Chapter 5) are normalized by the corresponding hub velocity values at each z/δ location. The hub velocity to the free-stream velocity ratios are also listed in Table 4.3.

4.5 Particle Image Velocimetry

2D2C PIV measurements are carried out in the wake of the porous disc. Figure 4.8 shows the layout of the PIV measurement setup. The PIV system is composed of a Phantom v641 high speed camera with a Nikon-Nikkor 60 mm lens, a New Solo PIV Nd:YAG laser, a Dantec Dynamics timer box and Dynamic Studio data acquisition and analysis software. The laser and the camera as well as the optics are all attached on a three-axis traverse mechanism to allow easier measurement while

moving downstream of the disc. The light beam is emitted from the laser head along the lateral direction and directed upwards along the vertical direction using a mirror, then passes through a spherical and a cylindrical lens to be converted into a $2\ mm$ thick laser sheet. The illuminated plane is at the center of the test section, i.e., $x'z' - plane\ (y' = 0)$, as shown in Figure 4.8. The main objective in this study, as stated previously, is to focus on the effects of the inflow boundary layer on the wake development characteristics of an isolated disc with non-uniform porosity. For this reason, the disc support is not included in the flow field and the disc is supported from the sidewall of the wind tunnel.

The flow is seeded with fog of droplets with a mean diameter of $1\ \mu m$. Double-frame particle images are preprocessed using a low-pass filter technique in order to enhance the image quality and remove any background noise. Then, using a two-step adaptive-correlation analysis with the final interrogation window size of $32 \times 32\ pixels^2$ and 50 % overlap, a vector spacing of $2.0\ mm$ is obtained in the resulting vector maps. Time between the two laser pulses is defined as $80\ \mu s$. Figure 4.8 shows the experimental setup and Table 4.4 displays the experimental parameters used in the PIV measurements.

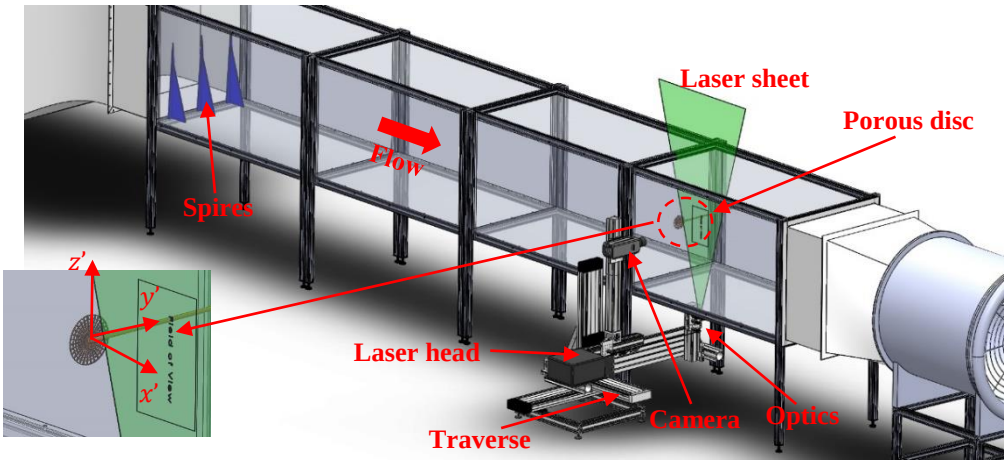

Figure 4.8 PIV measurement setup for porous disc wake measurements

The wake measurements are performed between $0.8 \leq x'/D \leq 7.5$ downstream of the porous disc by combining multiple PIV measurement windows as shown in

Figure 4.9. The solid blue rectangle shown in Figure 4.9 represents the porous disc with exaggerated thickness for clarity. The locations of the fields of view are represented in Figure 4.9, where each rectangular window represents an FOV in the $x' - z'\ plane$. The grey shaded area between the windows shows the overlap region between two adjacent FOVs, which is $0.33D$ for the first 4-windows that corresponds to around 20 vectors and $0.64D$ for the 5th window which corresponds to around 35 vectors. The larger overlap region in the last window is due to the limitation of the traverse system. The size of each field of view is $199 \times 321\ mm^2$ $(1.66D \times 2.67D)$ along the streamwise and vertical directions, respectively. The coordinate system is taken with respect to the disc hub center as shown in Figure 4.5 previously.

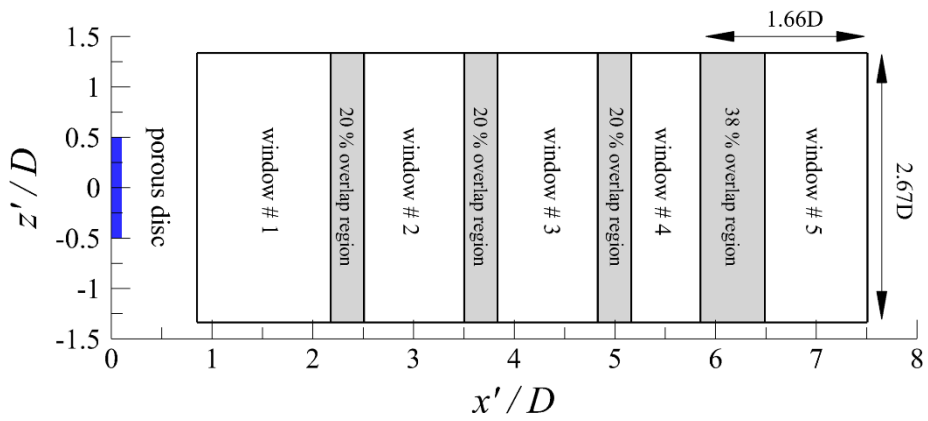

Figure 4.9 PIV measurement domain showing the windows with the overlap region and the field of view dimensions. The porous disc is marked as a solid blue rectangle and is located between: $-0.5 \leq z'/D \leq 0.5$

Table 4.4 2D2C-PIV experimental parameters

Seeding	Type	Fog
	Nominal diameter	$\approx 1\mu m$
	Seeding generator	Safex Fog generator
Laser Sheet	Laser type	Nd:YAG
	Manufacturer	New Wave Research
	Model	Solo 120XT
	Maximum Energy	$120\ mJ/pulse$

	Wavelength	$532\ nm$
	Thickness	$\approx 2\ mm$
Optics	Mirrors	Dielectric Mirror, $532\ nm$
	Spherical Lens	Plano-convex, $750mm\ FL$
	Cylindrical Lens	Plano-concave, $-12.4\ mm\ FL$
Camera	Sensor type	CMOS
	Sensor resolution	$2560 \times 1600\ pixel^2$
	Sensor size	$25.6 \times 16.0\ mm^2$
	Pixel pitch (size)	$10\ \mu m$
	Depth	$12\ bit$
	Max repetition rate	1400 fps @ Full resolution 2500 fps @ 1920×1080
	Internal memory buffer	$16\ GB$
Camera Lens	Manufacturer	Nikon
	Focal length	$60\ mm$
	f# (aperture)	2.8
Imaging	Image Magnification	0.08
	Field of View (FOV)	$199 \times 320.83\ mm^2$
	Camera-object distance	$600\ mm$
	Time between pulses (Δt)	$80\ \mu s$
	Recording rate	$10\ Hz$
PIV analysis	Pre-processing	Background intensity removal
	Correlation method	Adaptive-correlation
	Interrogation area (IA)	$128 \times 128\ to\ 32 \times 32\ pixel^2$
	Overlap between IAs	50 % overlap
	Post-processing	Universal outlier detection With a 3×3 kernel size
	Vector Spacing	$\approx 2.0\ mm$

4.6 Uncertainty Analysis

In the statistical analysis of the flow fields obtained with PIV, the convergence error influences the calculation of the flow field variables. It results from the calculation of statistical properties from a finite number of samples. In this study, $N = 1000$ statistically independent vector fields are taken in order to calculate the first and the second order moments of the flow. Under the assumptions that these samples follow a normal distribution and they are uncorrelated, the statistical uncertainty estimates of the mean flow, Reynolds stresses and turbulent kinetic energy are calculated with 95 % confidence level [233, 234]. The uncertainty estimates are then averaged over the complete flow field and the mean values are given in Table 4.5 for each case.

Table 4.5 The normalized mean statistical uncertainty estimates for the mean flow, Reynolds stresses and turbulent kinetic energy

Uncertainties	$z/\delta = 1.17$	$z/\delta = 0.71$	$z/\delta = 0.56$	$z/\delta = 0.32$
$(\Delta_U/U_{hub})_{mean} \times 100\ [-]$	0.53	0.60	0.65	0.74
$(\Delta_W/U_{hub})_{mean} \times 100\ [-]$	0.48	0.53	0.55	0.59
$\left(\Delta_{\overline{u'^2}}/U_{hub}^2\right)_{mean} \times 100\ [-]$	0.08	0.10	0.11	0.14
$\left(\Delta_{\overline{w'^2}}/U_{hub}^2\right)_{mean} \times 100\ [-]$	0.07	0.08	0.08	0.09
$\left(\Delta_{\overline{u'w'}}/U_{hub}^2\right)_{mean} \times 100\ [-]$	0.05	0.07	0.07	0.08
$\left(\Delta_k/U_{hub}^2\right)_{mean} \times 100\ [-]$	0.05	0.06	0.07	0.08

The above tabulated uncertainty values are essentially estimations of random errors due to statistical convergence under the assumption that the systematic errors in the PIV measurements, such as errors due to peak locking, calibration, particle time response, optical distortions, aberrations and hardware synchronization [235], are removed by correction or are negligible. On the other hand, in order to provide a rough uncertainty estimate for the PIV measurements, the so-called universal uncertainty constant of $0.1\ pixel$ [235] is considered, which yields an uncertainty value of $0.16\ m/s$ corresponding to the maximum value of $\Delta_{\mathrm{U,W}}/\mathrm{U}_{\mathrm{hub}} = 0.014$ for the $z\ /\ \delta = 1.17$ case.

It should be noted that the statistical uncertainty estimates for the second order moments of the flow are normalized with U_{hub}^2 since they are presented and analyzed in the same normalized form as shown in Chapter 5. For instance, the maximum values of k/U_{hub}^2 and $\overline{u'w'}/U_{hub}^2$ are roughly around 0.03 and 0.02, respectively (see Figure 5.4). Then, the reported uncertainty estimates correspond to 2.5 % - 3.5 % in average when compared to the maximum values of turbulent kinetic energy and Reynolds shear stress observed in the flow fields. In this respect, the reported uncertainty values for the second order moments of the flow should not be directly compared with those for the mean flow but should be interpreted in conjunction with their actual values in the flow fields.

CHAPTER 5

EFFECTS OF INFLOW WIND SHEAR AND TURBULENCE ON THE WAKE CHARACTERISTICS OF A RADIALLY NON-UNIFORM POROUS DISC

This chapter presents the results of an experimental investigation focusing on the effects of inflow boundary layer on the wake characteristics of a 0.12 m diameter porous disc with radially non-uniform porosity in terms of mean flow, turbulence and wake scaling. Two-dimensional two-component particle image velocimetry measurements within the wake are performed up to 7.5 diameters downstream as the disc is lowered deeper into a boundary layer that is representative of a neutral atmospheric boundary layer over a flat terrain. Results show that otherwise symmetrical wake velocity profiles that exist outside the boundary layer get skewed and sheared around the disc centerline in the boundary layer due to the inflow wind shear. The turbulent kinetic energy, its production and Reynolds shear stress levels in the wake get asymmetrical around the centerline of the disc such that the production of turbulent kinetic energy is observed to be higher above centerline. Due to the inflow shear, the wake centerline gets shifted downwards (i.e., towards the wind tunnel wall), which is in contrast to the observations on real wind turbine wakes in the literature where the wake actually lifts up. The asymmetrical and skewed velocity profiles both in the streamwise and cross-stream directions can be collapsed onto a single function by using proper wake scaling parameters based on the ratio of local strain to average strain within the velocity profile calculated separately for either side of the wake. Proper orthogonal decomposition on the wake velocity field shows coherent structures that are affected as the disc is immersed in the boundary layer as well as the main flow could be represented by the first few modes.

5.1 Effects on Mean Wake Flow Field

Figure 5.1 presents contours of normalized x-component of velocity (U) and normalized out-of-plane vorticity at different z/δ locations covering a streamwise extent up to $7.5\,D$ downstream of the disc. Here, x' and z' are local coordinates traveling with the disc, as defined previously in Figure 4.5. Starting with our baseline case, i.e., at $z/\delta = 1.17$ outside the boundary layer (Figure 5.1-1st row), fairly symmetric velocity and vorticity distributions around the centerline (the dashed black line marks the geometric center of the disc) are observed as expected. Symmetrical wake diffusion and the decay of the wake velocity deficit in the streamwise direction are also evident.

As moving towards lower z/δ positions within the boundary layer (i.e., following the contours from top to bottom), one can observe two main effects on the disc wake. First, the decay of the wake velocity deficit occurs much faster. For example, from the contour plots at $x'/D = 4$, wake velocity deficit at $z/\delta = 1.17$ (outside the boundary layer) is about 53 % higher than that at $z/\delta = 0.32$ (lowest position in the boundary layer, see Table 4.3). The wake velocity deficit progressively gets reduced at every x'/D as one moves deeper inside the boundary layer (more quantitative results will be shown later in the text). This effect is most probably due to increasing inflow turbulence intensity levels within the boundary layer at different hub heights causing increased mixing in the wake downstream of the disc. For instance, referring to Figure 4.6 (Chapter 4), the hub height turbulence intensity at $z/\delta = 1.17$ is about 0.6 %, whereas the one at $z/\delta = 0.32$ is about 8 %.

The second effect is that the wake centerline starts to deviate from the disc centerline, skewing down towards lower z'/D values, especially after $x'/D > 4$. The wake centerline shifting is represented by the solid grey line superimposed on the mean velocity contour plots in Figure 5.1-left. This skew becomes more evident as the mean velocity gradient becomes more pronounced at the inflow, for example at $z/\delta = 0.56$ and 0.32 (3rd and 4th rows in Figure 5.1, see Table 4.3). This is mainly due to the fact that the upper half of the wake ($z'/D > 0$) convects faster compared

to the lower half due to the inflow velocity gradient in the boundary layer, skewing the wake more towards below the centerline of the disc. The wake centerline presented in Figure 5.1-left was estimated by finding the minimum velocity at each streamwise location obtained from the PIV results. Due to variability of the measurement points, a polynomial curve fit to the points was applied showing the downward shifting of the wake centerline.

One should note that for wind turbines operating under inflow shear due to atmospheric boundary layer, opposite type of wake behavior was observed in general, i.e., the wake shifting upwards -not downwards- due to complex wake vorticity field and related interactions thereof. The lifting up of the wake of a wind turbine operating within ABL is mainly due to tip vortices getting closer to each other in the lower part of the wake due to lower convection velocities, which results in lifting up of the wake due to mutual interaction of these vortices. This phenomenon was first observed and explained by Sezer-Uzol and Uzol [236] and in more detail again by Sezer-Uzol and Uzol [237], confirmed through purely analytical models using vortex rings by Micallef et al. [238], drone based and LIDAR field measurements by Kocer et al. [239] and Zendehbad et al. [240], respectively. Although porous discs are commonly used in representing wind turbine wakes in wind tunnel studies, the wake response of porous discs to inflow shear is different compared to an actual wind turbine operating within ABL such that the wake centerline actually gets deflected downwards instead of upwards. This is because of the lack of tip vortex related dynamics downstream of a porous disc.

Non-dimensionalized vorticity distributions show that moving deeper in the boundary layer, the wake vorticity magnitudes get reduced due to higher inflow turbulence levels, and an asymmetry also starts to appear between the upper and lower halves of the disc wake due to the inflow wind shear. Reduction in vorticity magnitudes due to inflow boundary layer effects are also observed in previous studies such as Zhang et al. [120].

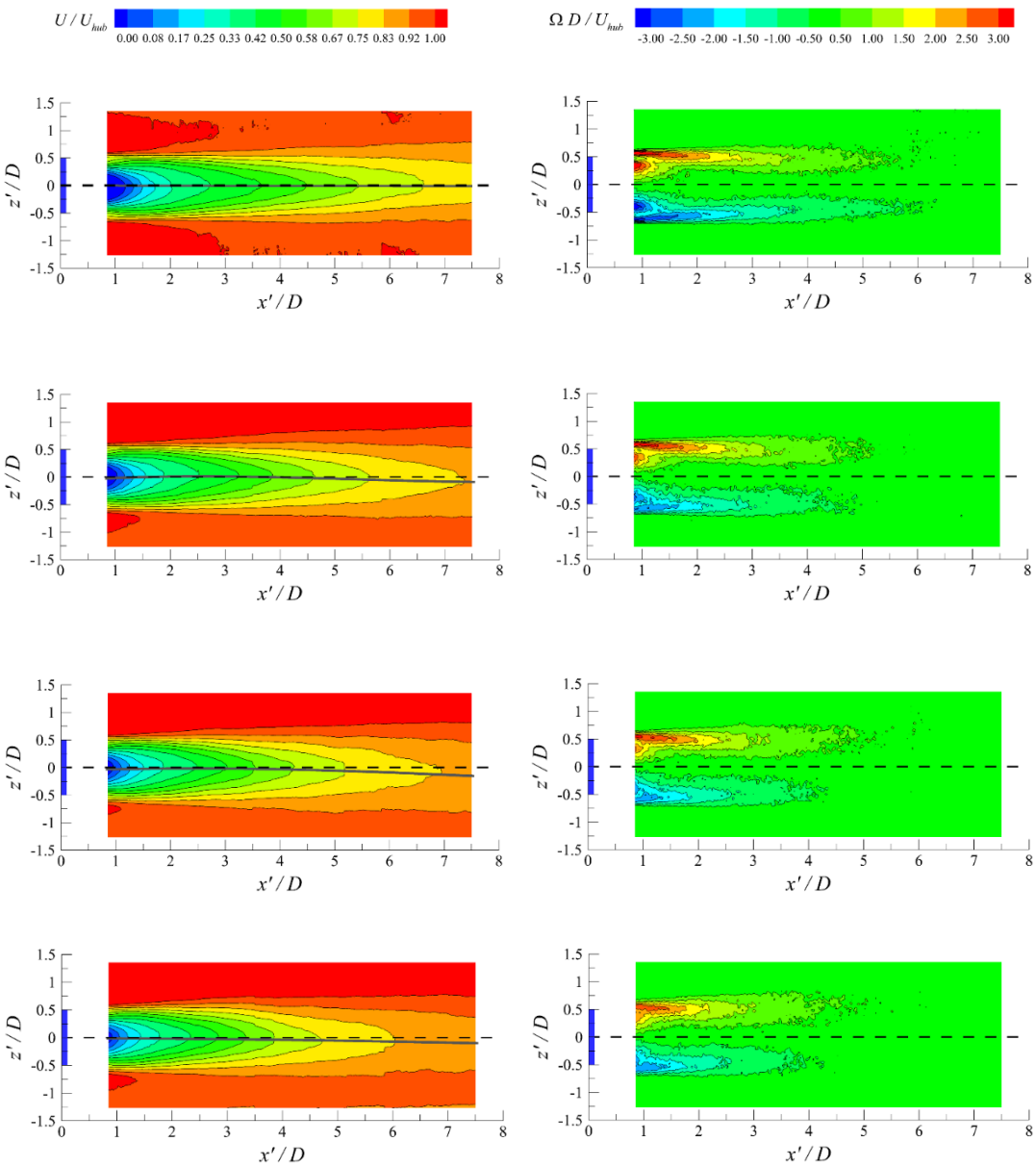

Figure 5.1 Mean streamwise velocity normalized with the velocity at hub height (left) and Normalized mean out-of-plane vorticity (right) at different disc positions. *1st row*: $z/\delta = 1.17$, *2nd row*: $z/\delta = 0.71$, *3rd row*: $z/\delta = 0.56$, *4th row*: $z/\delta = 0.32$. Porous disc is marked as a solid blue rectangle and is located between: $-0.5 \leq z'/D \leq 0.5$. The dashed black line passes through the center of the disc $z'/D = 0$. The solid grey line represents the wake centerline

Figure 5.2 shows the streamwise velocity distributions normalized by the hub velocity (U/U_{hub}) for all z/δ locations along the streamwise direction from $x'/D = 3$ to $x'/D = 7$ downstream of the disc. As one could observe, the impact of the inflow velocity gradients on the wake profiles within the boundary layer is clearly evident. The wake shapes on this plane get strained and become asymmetric as expected due to the non-uniform inflow compared to the case outside the boundary layer, i.e. at $z/\delta = 1.17$. In addition, as moving towards lower positions within the boundary layer the wake velocity profiles become more skewed due to higher velocity gradients, and the wake recovery is faster as the disc is subjected to higher turbulence intensity levels. The skewed wake shapes persist all the way downstream and they can still be depicted for example at $x'/D = 7$.

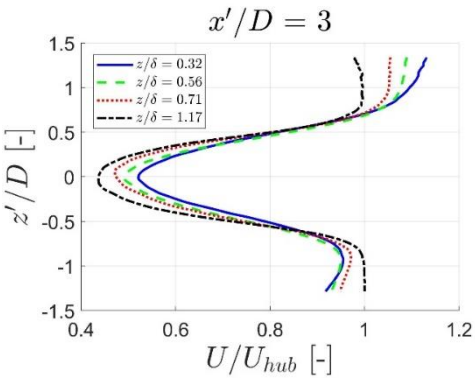

(a)

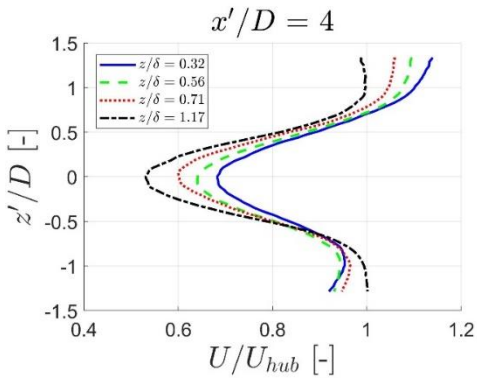

(b)

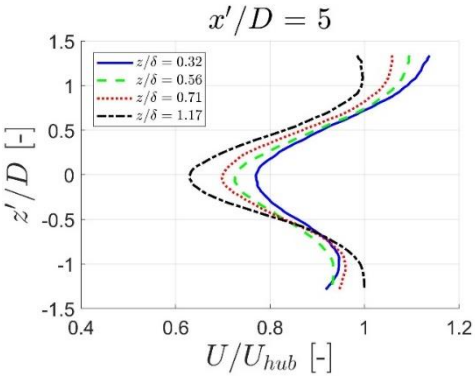

(c)

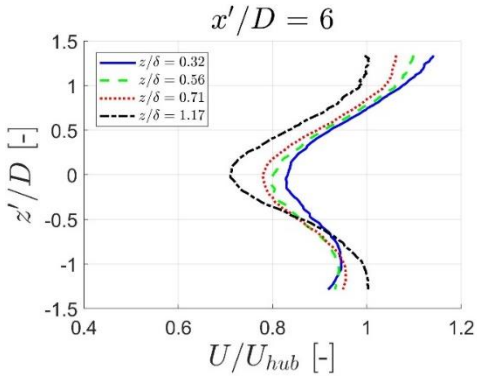

(d)

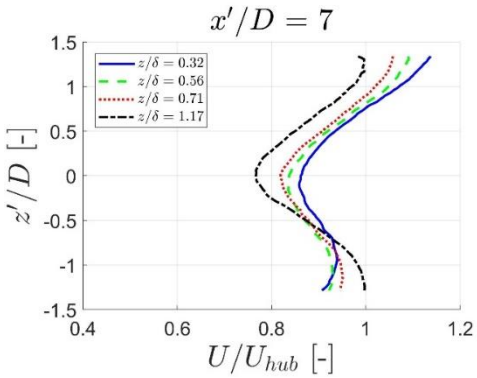

(e)

Figure 5.2 Normalized streamwise velocity distributions for all z/δ locations along the streamwise direction from (a-e): $x'/D = 3$ to $x'/D = 7$ downstream of the disc. Porous disc is located between: $-0.5 \leq z'/D \leq 0.5$

For these types of wake profiles that are subjected to basically non-uniform straining across the wake, it is generally difficult to depict a "freestream" condition to be used in the calculation of the wake velocity defect. At $z/\delta = 1.17$ (outside the boundary layer), the free stream condition is at $U/U_{hub} = 1$, as seen in Figure 5.2. At $z/\delta = 0.32$, on the other hand, there is a very skewed profile with different velocity levels outside the wake on either side of the wake. For this reason, in order to compare the wake velocity defect decay characteristics in a proper way, $(1 - U_{min}/U_{hub})$ variation in streamwise direction is presented in Figure 5.3, keeping in mind that U_{hub} is different for each case. It can be seen that in the regions for $x'/D < 2$ and for $x'/D > 3$, the velocity defect is always smaller (i.e., the minimum velocity is always higher) when the disc is inside the boundary layer. For example, at $x'/D = 4$ and at $x'/D = 7$, the wake velocity deficit at $z/\delta = 1.17$ (outside the boundary layer) is about 53 % and 70 % higher, respectively, than those at $z/\delta = 0.32$, indicating an enhanced level of mixing due to relatively high inflow turbulence levels when the disc is positioned within the boundary layer.

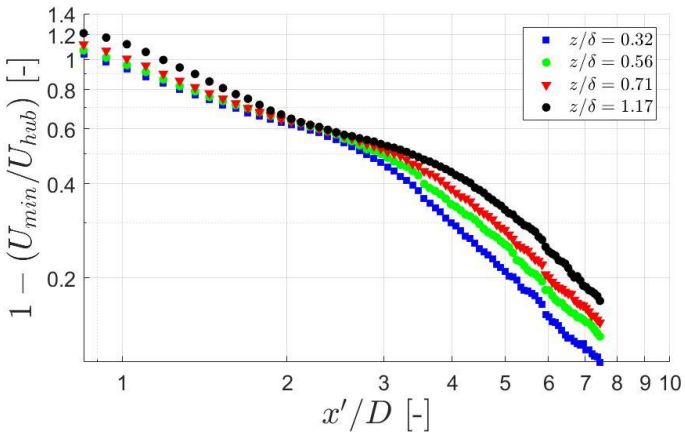

Figure 5.3 Velocity defect ($1\text{-}U_{min} / U_{hub}$) along the streamwise distance for the selected disc positions

5.2 Effects on Wake Turbulence

Figure 5.4 shows the turbulent kinetic energy and Reynolds shear stress distributions normalized by the square of the respective hub velocities in the wake of the porous

disc for four different z/δ positions. As one gets lower into the boundary layer, the asymmetry in turbulent kinetic energy distributions in cross-stream directions increases. Especially in the region $1.5 < x'/D < 5$, the upper half of the wake has significantly higher values compared to the lower part of the wake. This type of asymmetry was also observed in previous studies for the same porous disc [157]. The elevated turbulent kinetic energy region at the upper half also gets convected faster due to the inflow velocity gradient and results in an extended high turbulent kinetic energy region in the entire upper half of the wake compared to the lower part. This results in an upwards skew of the turbulent wake region away from the disc centerline, as can be seen by following the progressive contour plots from top to bottom in Figure 5.4. It is interesting to note that while the turbulence field is skewed upwards, the wake momentum field is slightly skewed downwards as previously shown in Figure 5.1.

The Reynolds shear stress contours show typical negative-positive type of distribution within the wake. The upper half is mostly negative as expected and the bottom half is positive. As the disc gets deeper into the boundary layer, the magnitude of the shear stress especially in the upper half of the wake gets larger creating an asymmetry in the shear stress distributions as well. The region between $1.5 < x'/D < 3.5$ has considerably higher shear stress level in magnitude at the upper half of the wake compared to the lower half. For example, at $x'/D = 2$ the levels are $30 - 50$ % higher in the upper half than those at the lower half. The shear stress distributions also show that the wake is in fact much wider and diffused more far downstream of the disc. For example, at $x'/D = 7$ and using the data on the contour boundaries the turbulent wake is calculated as about 37 % larger at $z/\delta = 0.32$ compared to the wake at $z/\delta = 1.17$. The upwards shift of the wake is also visible in the shear stress plots.

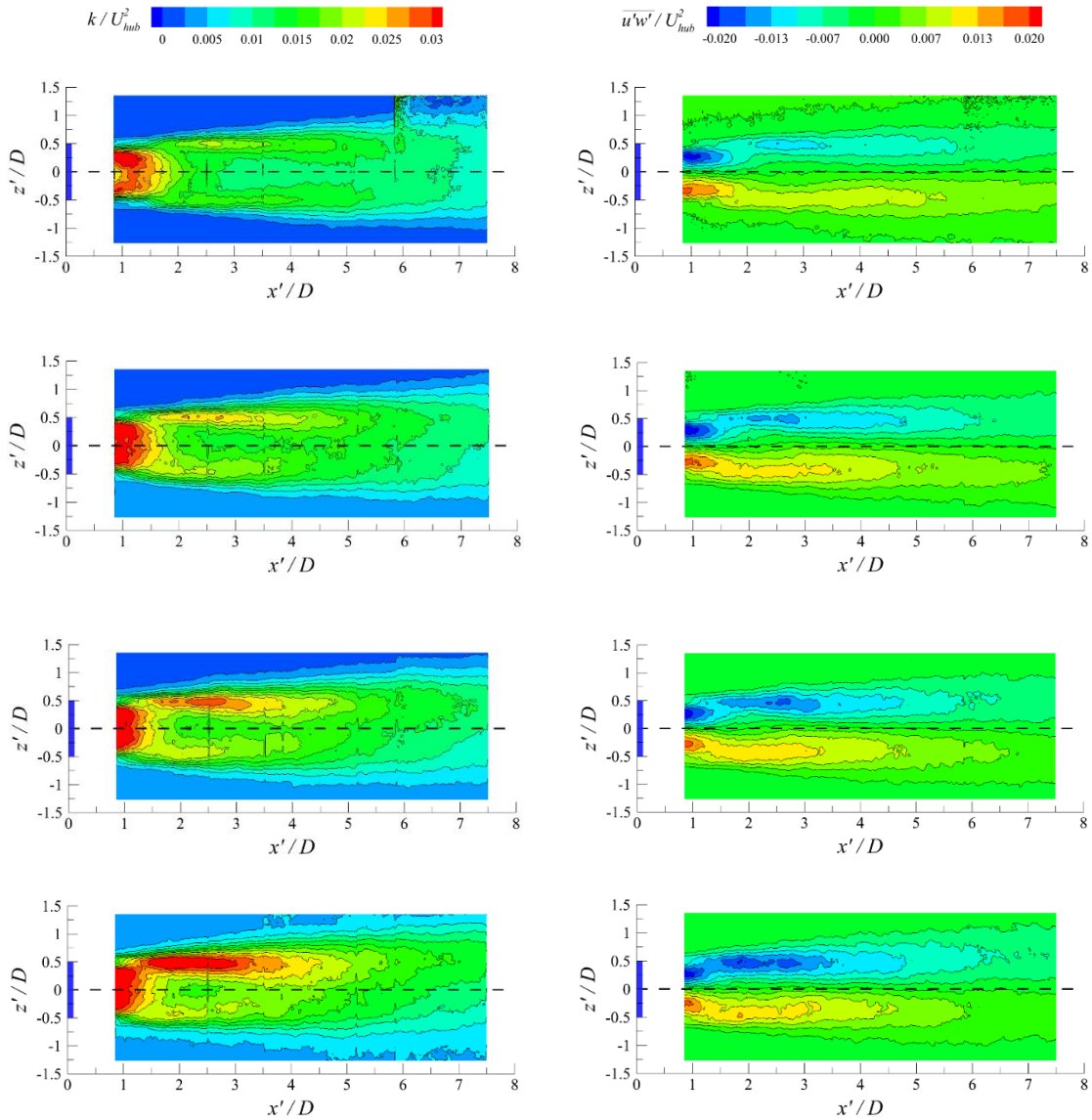

Figure 5.4 Mean turbulent kinetic energy normalized with the velocity at hub height (left), and mean Reynolds shear stress normalized with the velocity at hub height (right) at different disc positions. *1st row:* $z/\delta = 1.17$, *2nd row:* $z/\delta = 0.71$, *3rd row:* $z/\delta = 0.56$, *4th row:* $z/\delta = 0.32$. Porous disc is marked as a solid blue rectangle and is located between: $-0.5 \leq z'/D \leq 0.5$. The dashed black line passes through the center of the disc $z'/D = 0$

In order to better understand the asymmetry in the turbulent kinetic energy distributions, Figure 5.5 shows the distributions of the P_{12} component of the production of turbulent kinetic energy normalized by the diameter and the hub velocity. Using the 2D2C PIV data one can only calculate 4 terms out of the 6 terms of the production tensor and P_{12} is the dominant term among the four measured terms ($P_{12} = -\overline{u'w'}(dU/dz)$). Outside the boundary layer at $z/\delta = 1.17$, the main production zone is around $\pm 0.3 < z'/D < \pm 0.4$ along the centerline of the disc up to $x'/D = 1.4$ in the very near wake. This is followed by a production zone associated with the shear layers in the near wake more towards the tip of the disc around $z'/D = \pm 0.5$, covering a region about $1.5 < x'/D < 3$. The production then gradually gets reduced, which results in the gradual decay of turbulent kinetic energy after about $x'/D = 3$ as evident in Figure 5.4. Consistent with the turbulent kinetic energy distributions, P_{12} distributions become significantly asymmetric as one goes deeper inside the boundary layer. The production of turbulent kinetic energy gets much higher in the upper part of the wake compared to the lower part, which is in agreement with the increased levels of vorticity (Figure 5.1 - right) and Reynolds shear stress (Figure 5.4 - right) suggesting increased level of mean shear in the upper part of the wake. This mainly occurs in the near wake region but the strong asymmetry that is created extends well into the far wake beyond $x'/D = 3$. The increased velocity gradient on the upper half of the wake due to the skewed wake velocity profile shown in Figure 5.2 combined with the increased Reynolds stress levels in that region generates an increased production of turbulent kinetic energy at the upper half and contributes to the asymmetry of the wake.

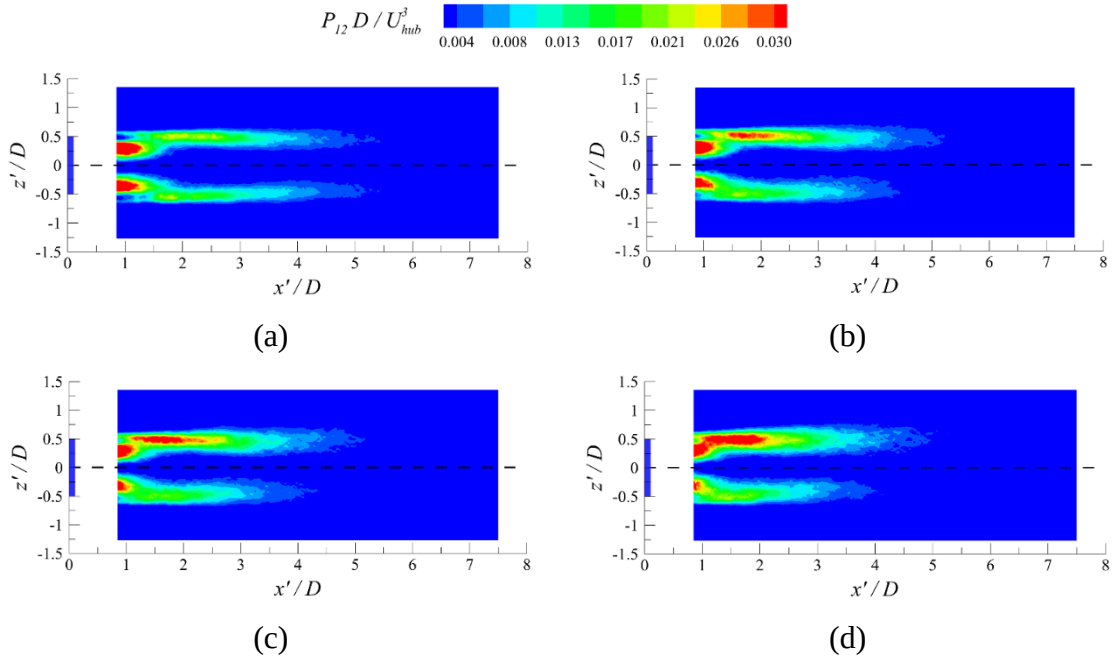

Figure 5.5 Production of turbulent kinetic energy (P_{12}) normalized with hub velocity and disc diameter at different disc positions. (a) $z/\delta = 1.17$, (b) $z/\delta = 0.71$, (c) $z/\delta = 0.56$, (d) $z/\delta = 0.32$. Porous disc is marked as a solid blue rectangle and is located between: $-0.5 \leq z'/D \leq 0.5$. The dashed black line passes through the center of the disc $z'/D = 0$

Figure 5.6 presents extracted turbulent kinetic energy profiles for all z/δ locations along the streamwise direction from $x'/D = 3$ and $x'/D = 7$ downstream of the disc. Outside the boundary layer at $z/\delta = 1.17$, fairly typical symmetrical double peak distribution can be seen at $z'/D = \pm 0.5$. The peak at the upper half progressively increases within the boundary layer and it is about 56 % higher at $z/\delta = 0.32$ than that at $z/\delta = 1.17$. The peak also slightly shifts downwards. The lower peak also increases but the peak level at $z/\delta = 0.32$ is only about 20 % higher than the peak at $z/\delta = 1.17$ especially at $x'/D = 3$ and $x'/D = 4$ respectively. Further downstream at $x'/D \geq 5$, the lower peak is almost indistinguishable and mixed out. The upper peak is still there and at $x'/D = 7$ the peak at $z/\delta = 0.32$ is still about 50 % higher than that at $z/\delta = 1.17$.

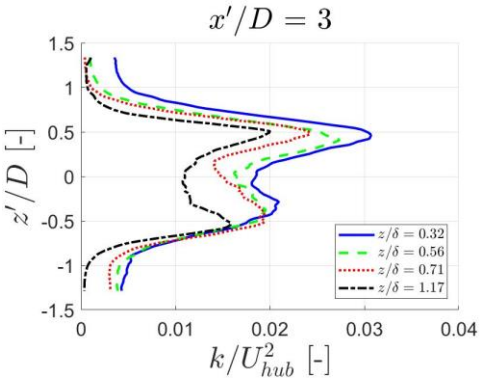

(a)

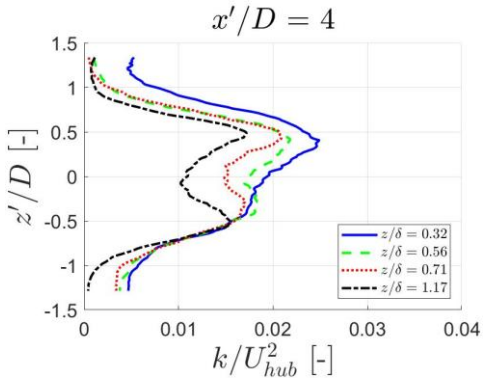

(b)

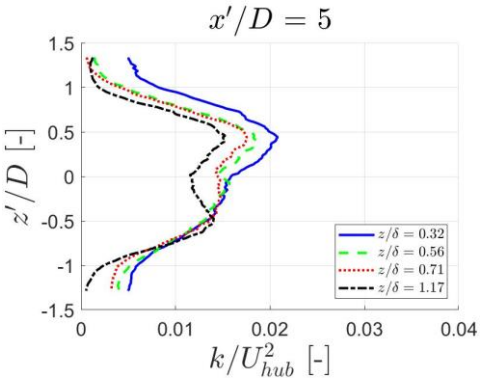

(c)

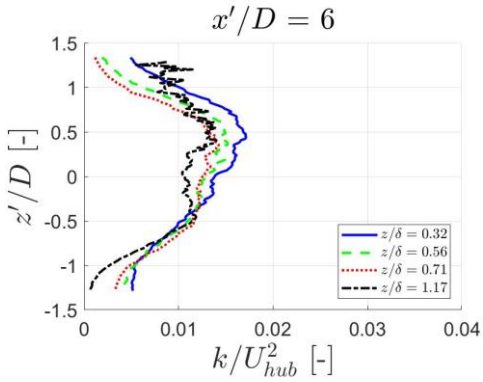

(d)

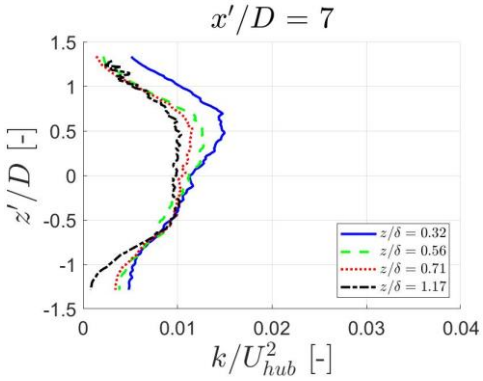

(e)

Figure 5.6 Normalized turbulent kinetic energy distributions for all z/δ locations along the streamwise direction from (a-e): $x'/D = 3$ to $x'/D = 7$ downstream of the disc. Porous disc is located between: $-0.5 \leq z'/D \leq 0.5$

In order to understand turbulent kinetic energy decay characteristics, k/U_{hub}^2 distributions are presented in Figure 5.7 along two horizontal lines at $z'/D = \pm 0.5$, showing the decay within the upper and lower halves of the wake in Figures 5.7a and b, respectively. In all cases, there is a production zone in which the turbulent kinetic energy keeps increasing up to a certain streamwise distance, typical of turbulent wakes. The streamwise location of the peak varies with the position of the disc in the boundary layer. In the upper half, the peak location moves upstream from around $x'/D = 2.6$ at $z/\delta = 1.17$ to $x'/D = 1.9$ at $z/\delta = 0.32$. In the lower half, all the peak locations within the boundary layer occur around $x'/D = 2$, whereas outside the boundary layer at $z/\delta = 1.17$, it is again around 2.6 similar to the upper half of the wake. After the peak location is reached, the turbulent kinetic energy starts to decay. Power law curve fits $(k/U_{hub}^2 = a \times (x'/D)^b)$ are made to the decay regions to investigate and compare the decay characteristics. It is known for homogeneous isotropic turbulence that the turbulent kinetic energy decay follows a power law with a power exponent in the range from -1.4 to 1 [241, 242]. The curve fit coefficients are listed separately for the upper and the lower halves of the wake in Table 5.1 for different disc positions within the boundary layer. As can be seen from Table 5.1, the decay exponent b does not vary in a wide range but mainly is limited within approximately $-0.8 > b > -1$, showing more variation in general in the upper half of the wake compared to the lower half, as also is evident from the plots in Figure 5.7.

Table 5.1 Power law fits for the decay of normalized turbulent kinetic energy of the upper and lower halves of the wake

Disc positions	Upper half			Lower half		
	a	b	R^2	a	b	R^2
$z/\delta = 1.17$	0.049	-0.793	0.951	0.058	-0.930	0.952
$z/\delta = 0.71$	0.079	-0.980	0.977	0.052	-0.877	0.973
$z/\delta = 0.56$	0.074	-0.905	0.975	0.056	-0.933	0.972
$z/\delta = 0.32$	0.080	-0.869	0.989	0.069	-1.048	0.979

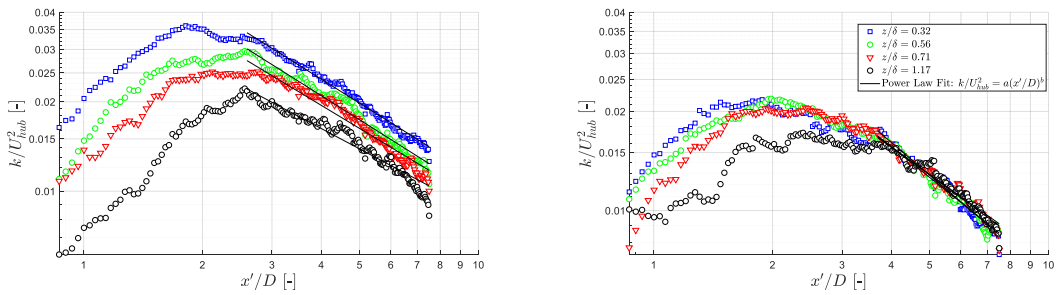

(a) (b)

Figure 5.7 Decay of normalized turbulent kinetic energy. (a) wake upper half, and (b) wake lower half along the streamwise distance for the selected disc positions. Solid black lines represent the power law fits (note that the legends are the same for both plots)

5.3 Wake Scaling Under the Effect of Inflow Shear

For typical turbulent symmetric wakes that are subjected to uniform external straining fields, standard wake scaling parameters are the velocity defect and the wake half-width [256]. However, the disc wake velocity profiles observed here (refer to Figure 5.2) are far from being symmetrical due to non-uniform external straining that the wake is subjected to because of the inflow velocity gradients created by the existence of the inflow boundary layer. In such asymmetric wakes, each side of the wake (i.e., the upper and the lower halves) have their own scales in general [257]. For these types of wake flows Chow et al. [258] proposed a new scaling methodology based on a parameter called β (Equation 5.4), which is the ratio of local shear strain (S_L) to average shear strain (S_A) within the wake as shown in equations 5.2 and 5.3 respectively.

As shown in previous studies [257-260], by looking at the local parameters that define the velocity profile in the form shown in Equation 5.1:

$$\frac{U_e(x') - U(x', z')}{U_e(x') - U_0(x')} = f(\eta)\,, \qquad \eta = \frac{z'}{\delta(x')} \qquad [5.1]$$

Where, x' is aligned with the center of the wake (i.e. downstream of the disc), z' is the relative distance from the wake center, U is the mean velocity in the x' direction, U_0 is the wake center velocity, U_e is the external flow velocity, and δ is the wake half-width, i.e. $U_e - U = 0.5(U_e - U_0)$ at $z' = \delta$ as shown in Figure 5.8. Figure 5.8 shows a schematic sketch of the wake scaling methodology and the definitions of the parameters involved.

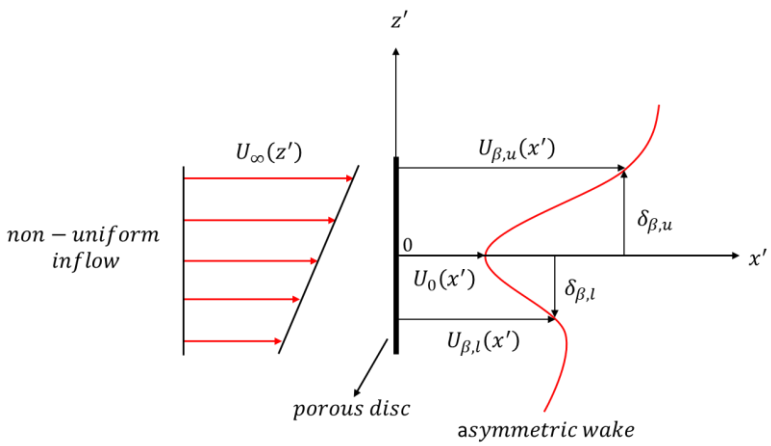

Figure 5.8 Wake scaling schematic and nomenclature

However, a unique U_e is difficult to define due to external non-uniformities, and therefore we cannot plot the data using the traditional scaling technique. Hence, instead, we define the width of the wake based on the distribution of strain [258].

The local shear strain, S_L, and the average shear strain, S_A, are defined as follows:

$$S_L = \frac{\partial U(x', z')}{\partial z'} = -\frac{U_e - U_0}{\delta} f'(\eta) \qquad [5.2]$$

$$S_A = \frac{U(x', z') - U_0(x')}{z'} = \frac{U_e - U_0}{z'} [1 - f(\eta)]\,, \qquad [5.3]$$

where, $f'(\eta) = df/d\eta$. Their ratio

$$\beta = \frac{S_L}{S_A} = \frac{\eta f'(\eta)}{1 - f(\eta)} \qquad [5.4]$$

is only a function of η, allowing us to use it instead of η as a parameter, to define the wake shape without having to define a velocity deficit.

Using this definition and selecting a certain value for β, one can define a length scale δ_β, which is the z' location within the wake at which β is equal to the selected value, and a velocity scale U_β, which is the velocity value at the position δ_β. These scales are found separately for the upper and lower halves of the wake and the wake halves are independently scaled using [258],

$$\frac{U_{\beta,i} - U(z')}{U_{\beta,i} - U_0} = f\left(\frac{z'}{\delta_{\beta,i}}\right), \qquad [5.5]$$

where the index i denotes to the upper or lower half of the wake.

Using this methodology with the β value of 0.5, the velocity profiles previously presented in Figure 5.2 are scaled and the results are shown in Figure 5.9 at different streamwise positions for different disc positions within the boundary layer. As is evident, the originally asymmetric wake velocity profiles at different z/δ positions within the boundary layer all collapse on to a single distribution at different streamwise locations.

The streamwise variation of asymmetric wake velocity profiles within the boundary layer at a certain z/δ position can also be scaled using the same methodology. Figure 5.10 presents the scaled wake velocity profiles at $z/\delta = 1.17, 0.71, 0.56$ & 0.32, for various streamwise positions from $x'/D = 3$ to $x'/D = 7$. It can be seen that the streamwise variation of the asymmetric profiles also collapse onto a single curve. Figure 5.11 summarizes the scaled velocity profiles for all distributions along the streamwise direction at every z/δ position.

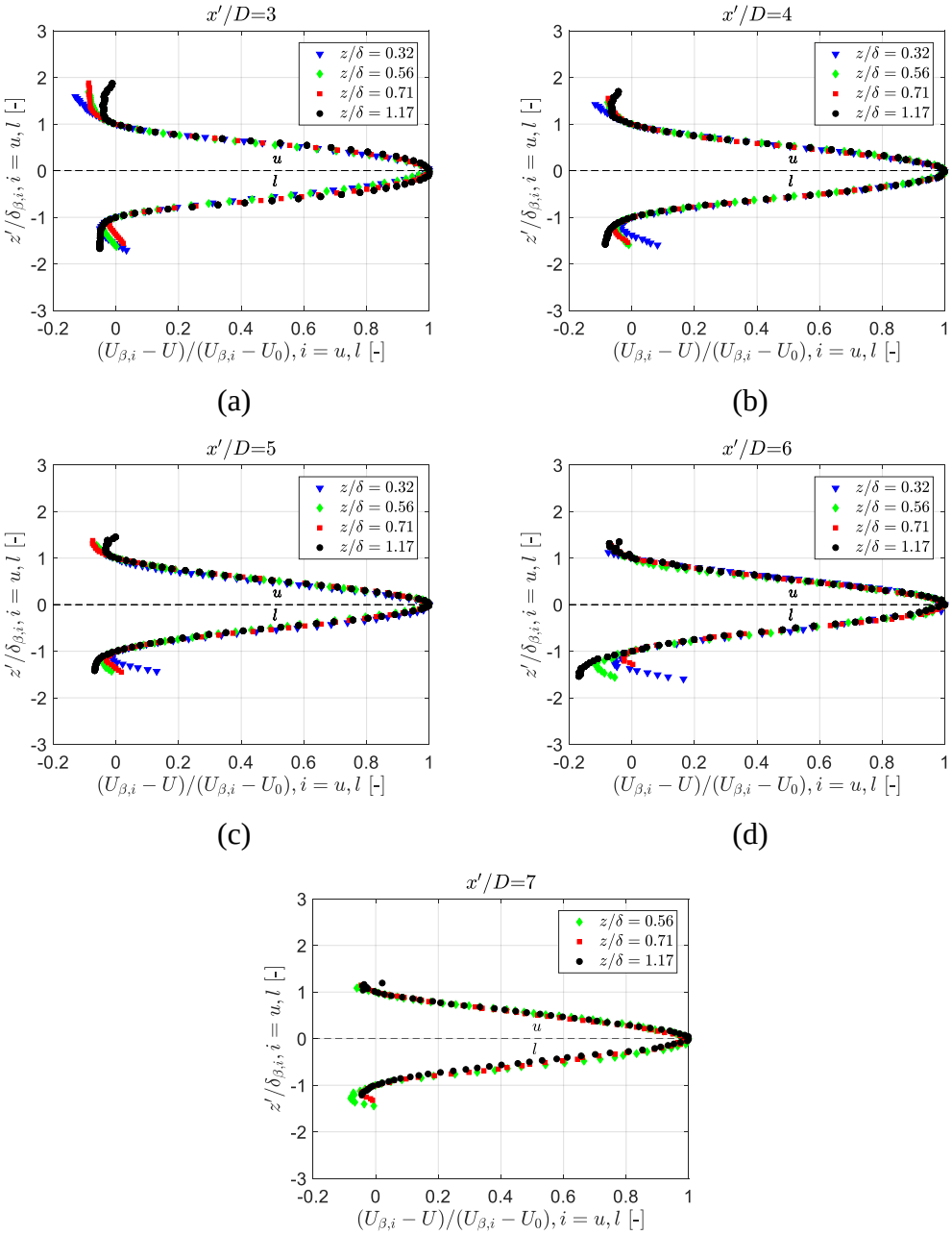

(a) (b) (c) (d) (e)

Figure 5.9 Scaled wake velocity profiles using $\beta = 0.5$ (as suggested by Chow et al. [258]) for the wake velocity profiles along the streamwise direction from (a-e): $x'/D = 3$ to $x'/D = 7$ downstream of the disc at different z/δ locations within the boundary layer (see Figure 5.2). Here *u* and *l* denote upper and lower halves of the wake, respectively

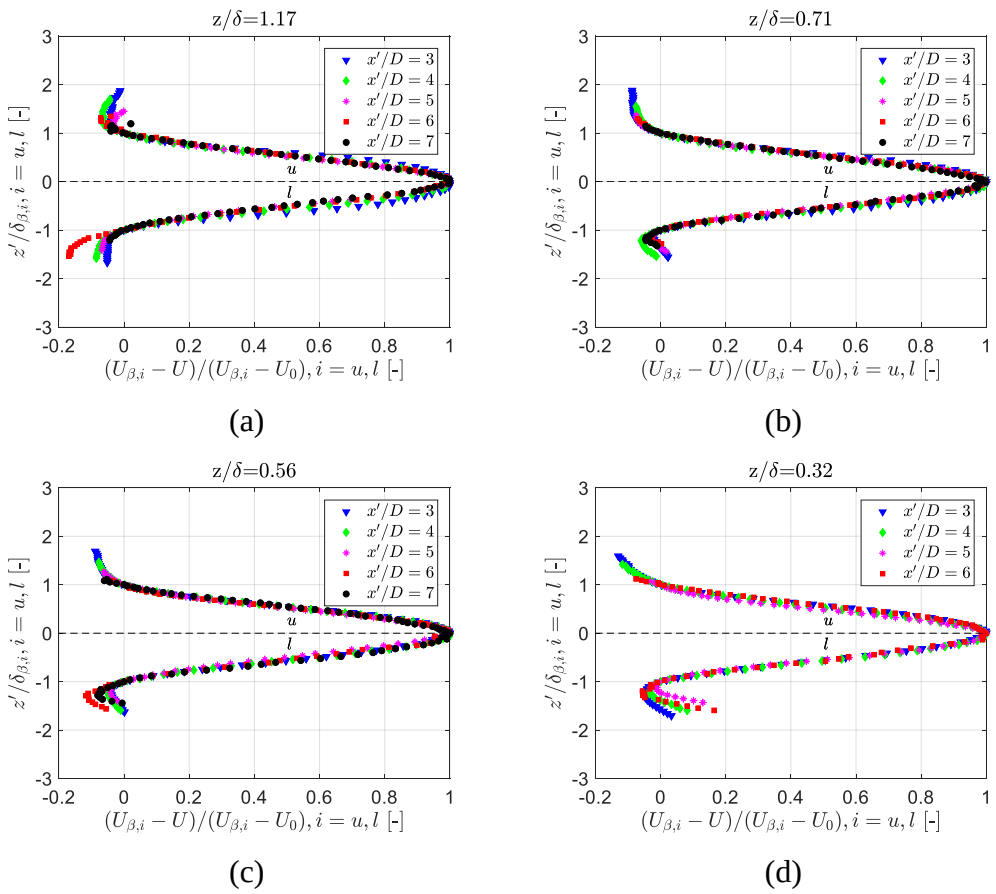

Figure 5.10 Scaled wake velocity profiles using $\beta = 0.5$ (as suggested by Chow et al. [258]) for the wake velocity profiles at different z/δ locations within the boundary layer along the streamwise direction from $x'/D = 3$ to $x'/D = 7$ downstream of the disc (see Figure 5.2). (a) at $z/\delta = 1.17$, (b) at $z/\delta = 0.71$, (c) at $z/\delta = 0.56$, and (d) at $z/\delta = 0.32$. Here u and l denote upper and lower halves of the wake, respectively

In order to do this scaling of the streamwise variations of the asymmetric wake velocity profiles as shown in Figure 5.11, it is required to know the streamwise variations of U_β and δ_β. These variations are presented in Figure 5.12a and b for $U_\beta - U_0$ and δ_β, respectively, from $x'/D = 3$ to $x'/D = 7$ for all z/δ locations. Coefficients of the power law curve fits are given in Table 5.2.

Regarding the streamwise distributions of $U_\beta - U_0$ presented in Figure 5.12a, all distributions for all z/δ locations except the far downstream part of the $z/\delta =$

0.32 case (where the vertical extent of the field of view is not sufficient to capture the complete wake) collapse on to a single curve for the upper half of the wake. On this side, the $U_\beta - U_0$ value decays with an exponent of $(x'/D)^{-1}$. On the lower side of the wake, differences are observed between the z/δ locations. The decay rate is higher at lower locations in the boundary layer, which is in agreement with the increased wake deficit decay observed at these locations (see Figure 5.3). The wake width as shown in Figure 5.12b, on the other hand, increases with an average exponent of $(x'/D)^{0.24}$ for all cases in the upper half. The increase rate of the wake width in the lower half shows a variation as a function of the position in the boundary layer with the maximum increase occurring at the highest location.

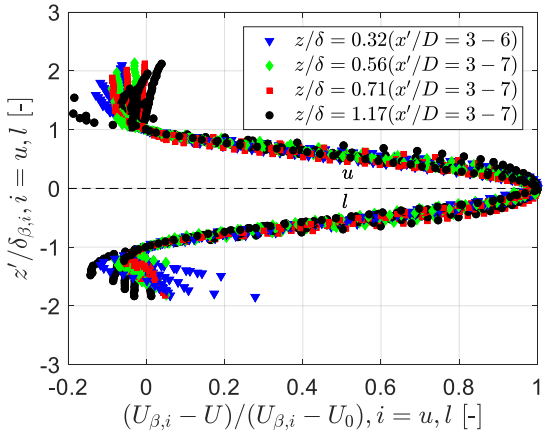

Figure 5.11 Scaled wake velocity profiles for all the wake velocity profiles at different z/δ locations within the boundary layer along the streamwise direction from $x'/D = 3$ to $x'/D = 7$ downstream of the disc. Here u and l denote upper and lower halves of the wake, respectively

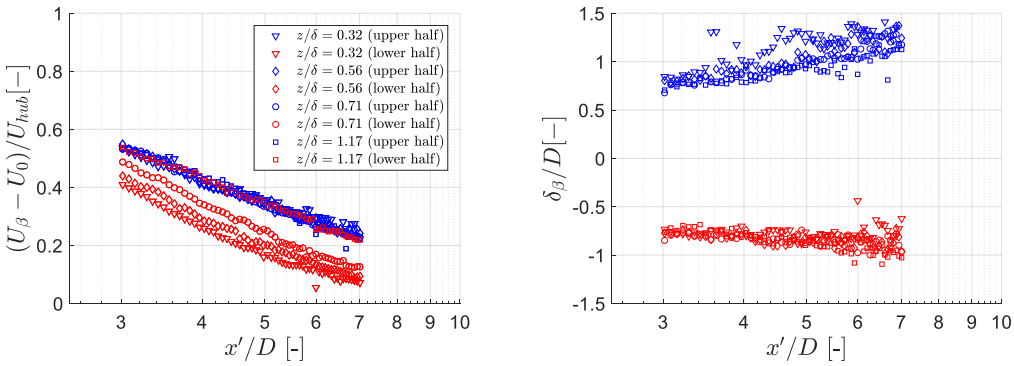

(a) (b)

Figure 5.12 Variations of: (a) $(U_\beta - U_0)/U_{hub}$, and (b) δ_β/D along the streamwise direction for the upper and lower halves of the wake for all z/δ locations (note that the legends are the same for both plots)

Table 5.2 Power law fit coefficients for the streamwise variations of the velocity scale (top) and length scale (bottom) distributions in the upper and lower halves of the wake for all z/δ locations

$(U_{\beta,i} - U_0/U_{hub}) = a \times (x'/D)^b$				
	Upper half		Lower half	
	a	b	a	b
$z/\delta = 0.32$	1.33	-0.83	3.74	-1.95
$z/\delta = 0.56$	1.60	-0.96	3.25	-1.75
$z/\delta = 0.71$	1.79	-1.05	2.93	-1.56
$z/\delta = 1.17$	1.80	-1.04	1.73	-1.02

$(\delta_\beta/D) = a \times (x'/D)^b$				
	Upper half		Lower half	
	a	b	a	b
$z/\delta = 0.32$	1.71	0.23	0.62	-0.10
$z/\delta = 0.56$	1.55	0.26	0.85	-0.39
$z/\delta = 0.71$	1.58	0.24	0.97	-0.46
$z/\delta = 1.17$	1.56	0.23	1.39	-0.71

The variation of the inlet flow conditions in terms of the velocity and the turbulence intensity profiles does not seem to generate any variation in the wake scaling parameters (i.e., $U_\beta - U_0$ and δ_β) defined for the upper half of the wake. In other words, a single power law equation can be defined for the calculation of $U_\beta - U_0$ and δ_β for the upper half of the wake regardless of the different inflow conditions. However, for the lower half of the wake, a trend is observed in the variation of these parameters as a function of the vertical position in the boundary layer such that the decay rate of the $U_\beta - U_0$ increases and the decay rate of the δ_β decreases as moving deeper in the boundary layer flow. As a result, using the distributions presented in Figures 5.9 to 5.12, one can in principle reconstruct any of the asymmetric wake velocity profiles at any streamwise position and at any z/δ location within the boundary layer, for this non-uniform porous disc.

5.4 Proper Orthogonal Decomposition

The proper orthogonal decomposition (POD) is a mathematical tool utilized to analyze the flow field structure of turbulent flows and quantitatively arrange these structures based on their contribution to the total kinetic energy [243, 244]. This method was first introduced by Lumley [245] and later by Sirovich who established the Snapshot POD which is more suitable for spatially dense but temporally sparse data [246]. When compared to other types of modal decompositions, the POD is capable of representing the maximum turbulence kinetic energy (TKE) of the flow using the least number of modes. The POD reorganizes the modes based on their energetic content, therefore, organized motions that represent little energy may not be important in the statistical sense but may be of dynamic significance and are restricted to high rank modes [247].

This technique has been used recently to analyze turbulent wakes downstream of wind turbines in order to understand their wake behavior and characteristics. For instance, Andersen et al. [248, 249] employed LES coupled with actuator line technique to model a wind farm using infinitely long row of turbines and employed POD to analyze the velocity field along the rotor plane. The results show the

meandering of the wake shed by upstream turbines. The spatial organization of the streamwise velocity component of low rank POD modes displayed the rotational symmetry which is typical of axisymmetric flows. VerHulst and Meneveau [250] simulated a large wind farm using LES and employed POD analysis to identify the most energetic flow structures. Their results show counter-rotating vortex pairs above the height of the wind turbines which accounted for the bulk of turbulent kinetic energy and were responsible for more than 14 % of the mean kinetic energy entrained. Bastine et al. [251] simulated a single wind turbine immersed in the ABL. POD analysis shows that only a few modes are necessary to capture the basic dynamical aspects of quantities that are relevant to a turbine in the wake flow. Hamilton et al. [252] applied POD analysis on wind tunnel measurements of aligned and staggered wind turbine arrays and found out that only 1 % of the total modes are needed to reconstruct the TKE production and the flux of TKE. Camp and Cal [253] performed POD on an array of model wind turbines and an equivalent array of porous discs. They found out that the structure of the wakes of wind turbines and porous discs are different in terms of the organization of turbulent kinetic energy. The first mode is similar spatially for the rotor and disc in both the near and far wake in the streamwise and vertical components unlike the cross-stream component. Aloui et al. [254] investigated the wake of a porous disc using PIV and performed POD in order to extract the main structure of the wake flow. They reported that the POD reveals the formation of alternating vortices in the shear zone located at the edges of the disc. Lignarolo et al. [255] conducted an experimental comparison using PIV between a model wind turbine and a porous disc and employed POD as a filter for separating the periodic fluctuations from the random fluctuations in the wake flow.

5.4.1 Theory

This section presents the theory and derivation of the snapshot proper orthogonal decomposition (SPOD) as formulated by Sirovich [246].

The fluctuating velocity in a flow $\boldsymbol{u}'(\boldsymbol{x}, t)$ is assumed to be approximated as a series of the form shown in Equation 5.6, where bold variables represent vectorial

quantities. Here $\boldsymbol{u}'$ is the velocity vector $\boldsymbol{U}$ minus its temporal mean $\bar{\boldsymbol{U}}$. $\boldsymbol{x}(x, y, z)$ is the position vector, $\boldsymbol{U}(U, V, W)$ is the velocity vector, and t represents time. The POD analysis is used to decompose the vector field $\boldsymbol{u}'(\boldsymbol{x}, t)$ into a set of deterministic spatial functions $\boldsymbol{\Phi}^{(n)}(\boldsymbol{x})$

$$\boldsymbol{u}'(\boldsymbol{x}, t) = \sum_{n=1}^{N} a_n(t)\, \boldsymbol{\Phi}^{(n)}(x)\,, \qquad [5.6]$$

where $a_n(t)$ is the time-dependent POD coefficient for mode n, $\boldsymbol{\phi}^{(n)}(\boldsymbol{x})$ is the spatial POD mode for mode n, and N is the number of snapshots. The fluctuating velocity measured over P spatial positions instantaneously and which is measured at N times is arranged into the matrix [247]:

$$\widehat{\boldsymbol{U}} = \frac{1}{N}\begin{bmatrix} u_1'^1 & u_1'^2 & \cdots & u_1'^N \\ \vdots & & \ddots & \vdots \\ u_P'^1 & u_P'^2 & \cdots & u_P'^N \end{bmatrix} \qquad [5.7]$$

The auto-covariance matrix, $\boldsymbol{C}$, can then be expressed from the product of $\widehat{\boldsymbol{U}}$ and its transpose as $\boldsymbol{C} = \widehat{\boldsymbol{U}}^T\widehat{\boldsymbol{U}}$. An eigenvalue problem involving $\boldsymbol{C}$ can be written as [247]:

$$\boldsymbol{C}\boldsymbol{A}_n = \lambda_n \boldsymbol{A}_n\,, \qquad [5.8]$$

where $\boldsymbol{A}_n$ is the eigenvector corresponding to the eigenvalue λ_n. Physically, the eigenvalues of the POD modes describe the turbulence kinetic energy represented by their respective modes. The eigenvalues of all N modes are ordered in magnitude such that [247]:

$$\lambda_1 > \lambda_2 > \cdots > \lambda_n\,, \qquad [5.9]$$

where λ_n is set to 0 during computation. From the results of the eigenvalue problem, the normalized POD modes can then be computed by projecting the snapshot basis into the eigenvalue space then normalizing which can be expressed as [247]:

$$\boldsymbol{\phi}^{(n)} = \frac{\widehat{\boldsymbol{U}}\boldsymbol{A}_n}{\left\|\widehat{\boldsymbol{U}}\boldsymbol{A}_n\right\|}, \qquad [5.10]$$

where $\| \cdots \|$ denotes the L_2-norm. Note that the set of eigenfunctions obtained herein are orthogonal in time rather than space. After concatenating the POD modes to form $\boldsymbol{\psi} = \left[\boldsymbol{\phi}^{(1)}\ \boldsymbol{\phi}^{(2)}\ \cdots\ \boldsymbol{\phi}^{(n)}\right]$, the POD coefficients can then be found using Equation 5.11 [247]:

$$\boldsymbol{a}_n = \boldsymbol{\psi}^{-1}\boldsymbol{u}'_n \qquad [5.11]$$

5.4.2 Snapshot Proper Orthogonal Decomposition

The analysis of the POD will be conducted in the near wake region of the porous disc, i.e., the first window of the flow field will be considered (refer to Figure 4.9 in Chapter 4). The size of this window is 1.66D x 2.67D (where D is the diameter of the disc). In here, each instantaneous PIV measurement is considered to be a snapshot of the flow field. An analysis is then performed on typically 1000 snapshots taken in the same plane. The mean velocity field can be considered the zeroth mode of the POD. The POD analysis is carried out by considering the streamwise velocity (U) and vertical velocity (W). Therefore, to create our snapshot matrix, we start by subtracting the time-averaged velocity field from each individual vector field. We obtain a dataset of $m \times n = 99 \times 199 = 15741$ fluctuating velocity fields, then reorder the dataset by concatenating each individual velocity field into one single $1 \times n$ row and we stack these rows onto each other. Since two velocity components are considered the resulting matrix is $15741 \times 2 = 31482$ fluctuating velocity fields.

In here four test cases will be considered based on the position of the disc within the boundary layer (i.e., $z/\delta = 1.17, 0.71, 0.56\ and\ 0.32$). Figure 5.13 shows the eigenvalues for the POD in each selected case. POD modes are sorted in terms of their TKE contribution as represented by their respective eigenvalues as shown in Figure 5.14 as well.

Figure 5.13 presents the eigenvalues for the snapshot POD in the near wake of the porous disc at different positions in the boundary layer. These eigenvalues are sorted based on their TKE contribution to the flow field.

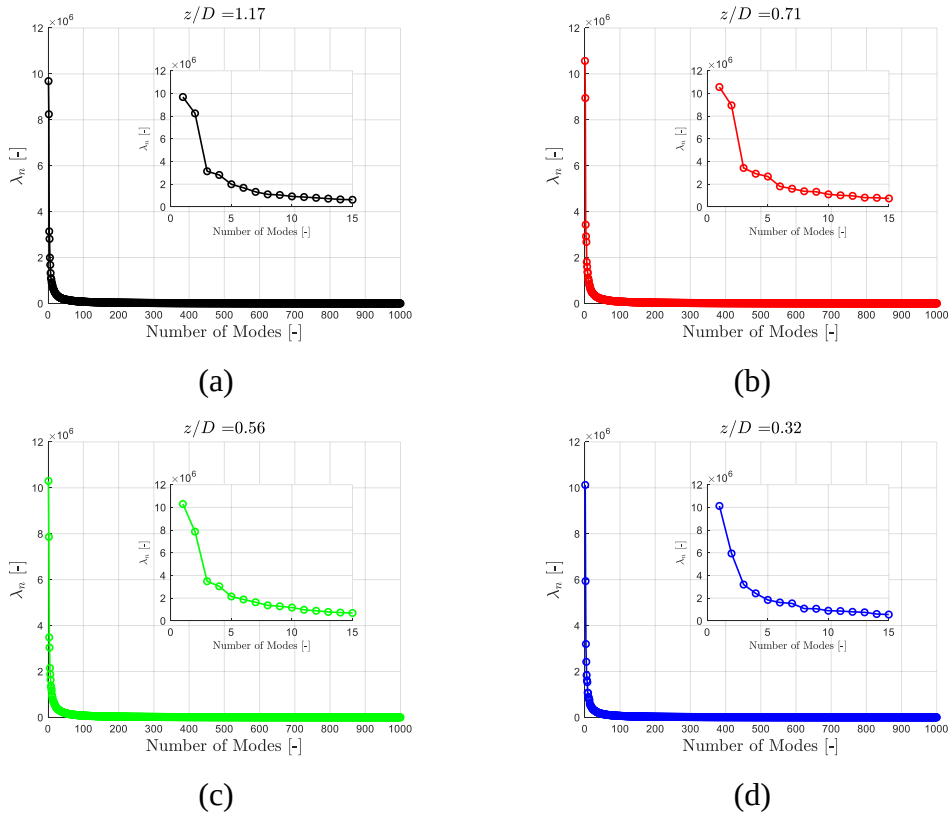

Figure 5.13 Eigenvalues for the snapshot POD in the near wake of the porous disc at different positions in the boundary layer. (a) $z/\delta = 1.17$, (b) $z/\delta = 0.71$, (c) $z/\delta = 0.56$, and (d) $z/\delta = 0.32$. Subgraphs shows only the first 15 modes

Figure 5.14 shows the percentage of TKE contribution from each eigenvalue in the near wake of the porous disc at different disc positions within the boundary layer. As one could observe the first mode contributes the most to the TKE and this contribution increases as we move deeper within the boundary layer. For instance, the first mode contributes to about 15 % of the total energy when the disc is outside the boundary layer (i.e., $z/\delta = 1.17$), on the other hand this contribution increases to around 17 % when the disc is at $z/\delta = 0.32$. This indicates that a large amount of the TKE is represented by the first mode. This increase is probably due to the wind shear as well as the increased levels of ambient turbulence intensity as the disc is

lowered deeper into the boundary layer. The second mode of the POD shows opposite behaviour as one goes deeper within the boundary the energy contribution of the second mode decreases. The third mode shows similar trend to mode 1 but with less energy contribution, on the other hand the fourth mode is similar in trend to mode two. The first 4 modes constitute on average around 36.93 % of the total energy for the case outside the boundary layer (i.e., $z/\delta = 1.17$), and around 37.17 % for the deepest position in the boundary layer (i.e., $z/\delta = 0.32$). Although, individual modes are different, their total energetic contribution is the same for all test cases. Therefore, looking at the first few modes is sufficient to identify dominant coherent motions. The higher order modes which contributes to less than 1 % of the total energy are neglected. Table 5.3 shows the percentage energy contribution of each mode for each selected position of the disc as well as the total energy contribution of the first 15 modes.

Table 5.3 Percentage of TKE contribution from each mode

z/δ	MODE 1	MODE 2	MODE 3	MODE 4	MODE 1 - 4	MODE 1 - 15
1.17	14.98 %	12.75 %	4.85 %	4.35 %	36.93 %	55.11 %
0.71	14.81 %	12.54 %	4.81 %	4.10 %	36.26 %	56.21 %
0.56	15.12 %	11.54 %	5.16 %	4.46 %	36.28 %	56.10 %
0.32	17.36 %	10.18 %	5.48 %	4.15 %	37.17 %	56.99 %

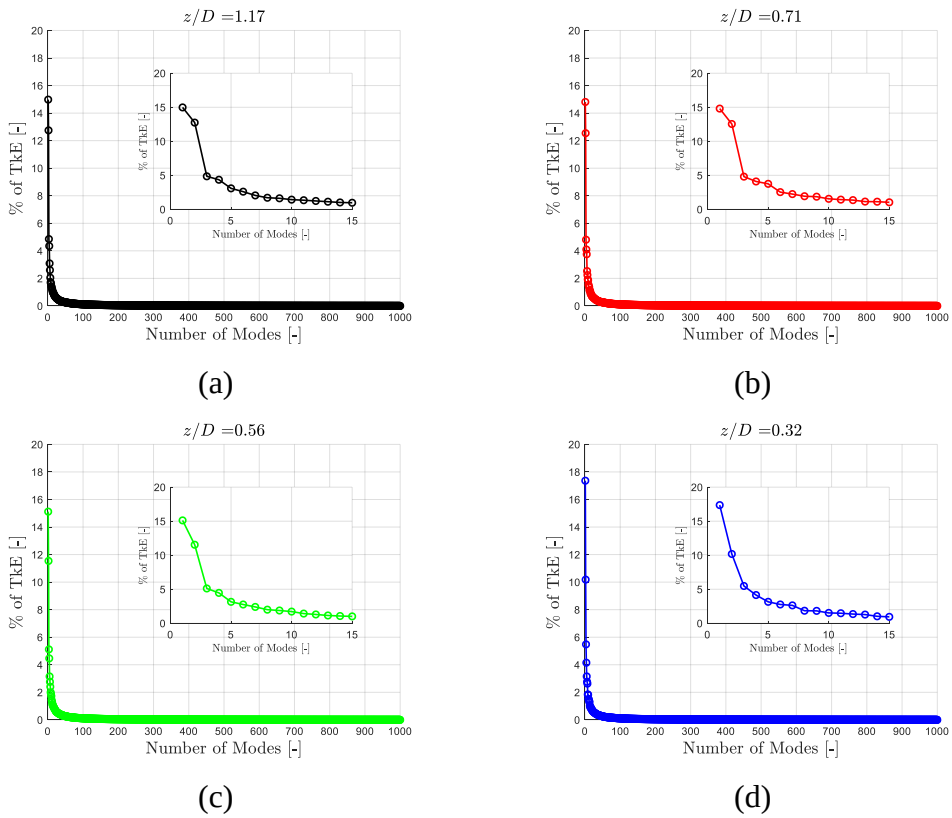

Figure 5.14 Percentage of TKE contribution from each eigenvalue in the near wake of the porous disc at different positions in the boundary layer. (a) $z/\delta = 1.17$, (b) $z/\delta = 0.71$, (c) $z/\delta = 0.56$, and (d) $z/\delta = 0.32$. Subgraphs shows only the first 15 modes

Figure 5.15 displays the streamwise and vertical components of the first spatial mode in the near wake of the porous disc at different disc positions in order to illustrated the differences in the flow features. For the case outside the boundary layer, i.e. $z/\delta = 1.17$ (1st row-left), the streamwise component of the first mode shows alternating flow structures (shown as red and blue patches) of opposite signs and different sizes. These patches are dominating the near wake region of the porous disc which represents a periodical (or alternating) motion of these coherent structures. The smaller structures occupy the region up to 1.25D downstream of the disc; however, the larger structures occupy a wider region and extend to beyond 2.5 downstream od the disc. As one moves deeper within the boundary layer (following the contours from top to bottom) these large structures occupy a wider area in the

flow field. For the case where the disc is at $z/\delta = 0.71$, these structures extend from 1.25D up to 2.5D downstream of the disc. The small structures diminishes significantly compared to the case outside the boundary layer (i.e. $z/\delta = 1.17$). At $z/\delta = 0.56\ and\ 0.32$, the smaller structures diminishes entirely and the large scale structures dominate the entire region downstream of the disc. Interestingly, one can observe as well the sign is reversed when the disc is at the deepest position, i.e., $z/\delta = 0.32$ (4th row-left). Similar interpretation can be deduced from the vertical component of the first spatial mode.

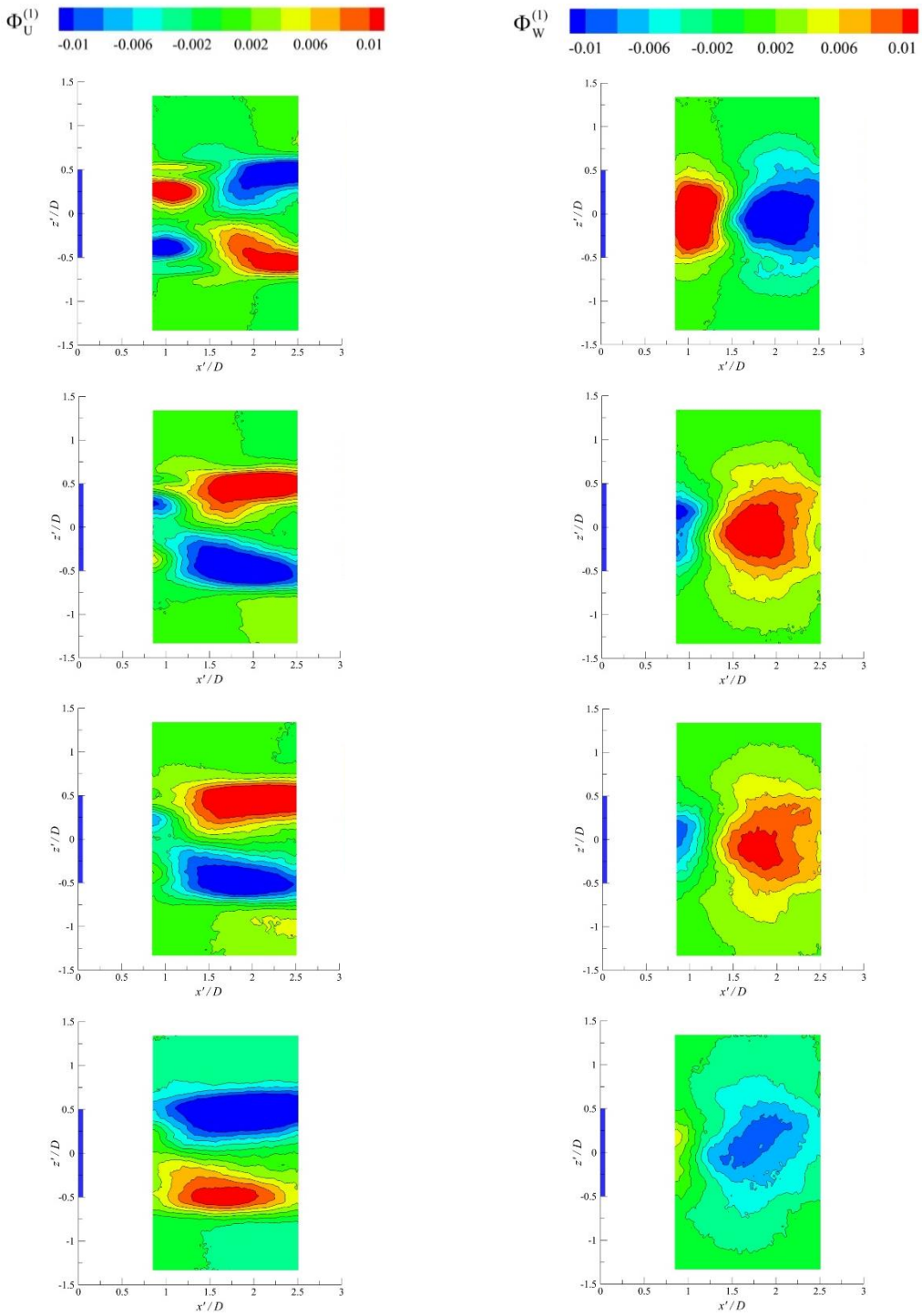

Figure 5.15 Components of the first spatial POD mode. Streamwise component $\phi_U^{(1)}$ (left), vertical component $\phi_W^{(1)}$ (right). *1st row:* $z/\delta = 1.17$, *2nd row*: $z/\delta = 0.71$, *3rd row*: $z/\delta = 0.56$, and *4th row:*$z/\delta = 0.32$. Porous disc is marked as a solid blue rectangle and is located between: $-0.5 \leq z'/D \leq 0.5$

Figure 5.16 displays the streamwise and vertical components of the second spatial mode in the near wake of the porous disc at different disc positions. One should note in here that the second mode contributes less to the total kinetic energy compared to the first mode. One could observe a trend as the mode index increases for all the cases considered. To elaborate, as the mode index increases there is a tendency towards smaller scale structures occupying the flow field downstream of the disc. For the case outside the boundary layer, i.e., $z/\delta = 1.17$ (1st row-left), the streamwise component of the second mode shows medium scale flow structures (shown as red and blue patches) of opposite signs occupy the region downstream of the disc. As one moves deeper within the boundary layer (following the contours from top to bottom) these regions diminish in size and are represented by multiple flow structures of alternating features. One can observe as well the sign is reversed when the disc is at $z/\delta = 0.56$ and $z/\delta = 0.32$. Similar interpretation can be deduced from the vertical component of the first spatial mode. In addition, as one moves towards lower positions in the boundary layer there is a sign of convective motion.

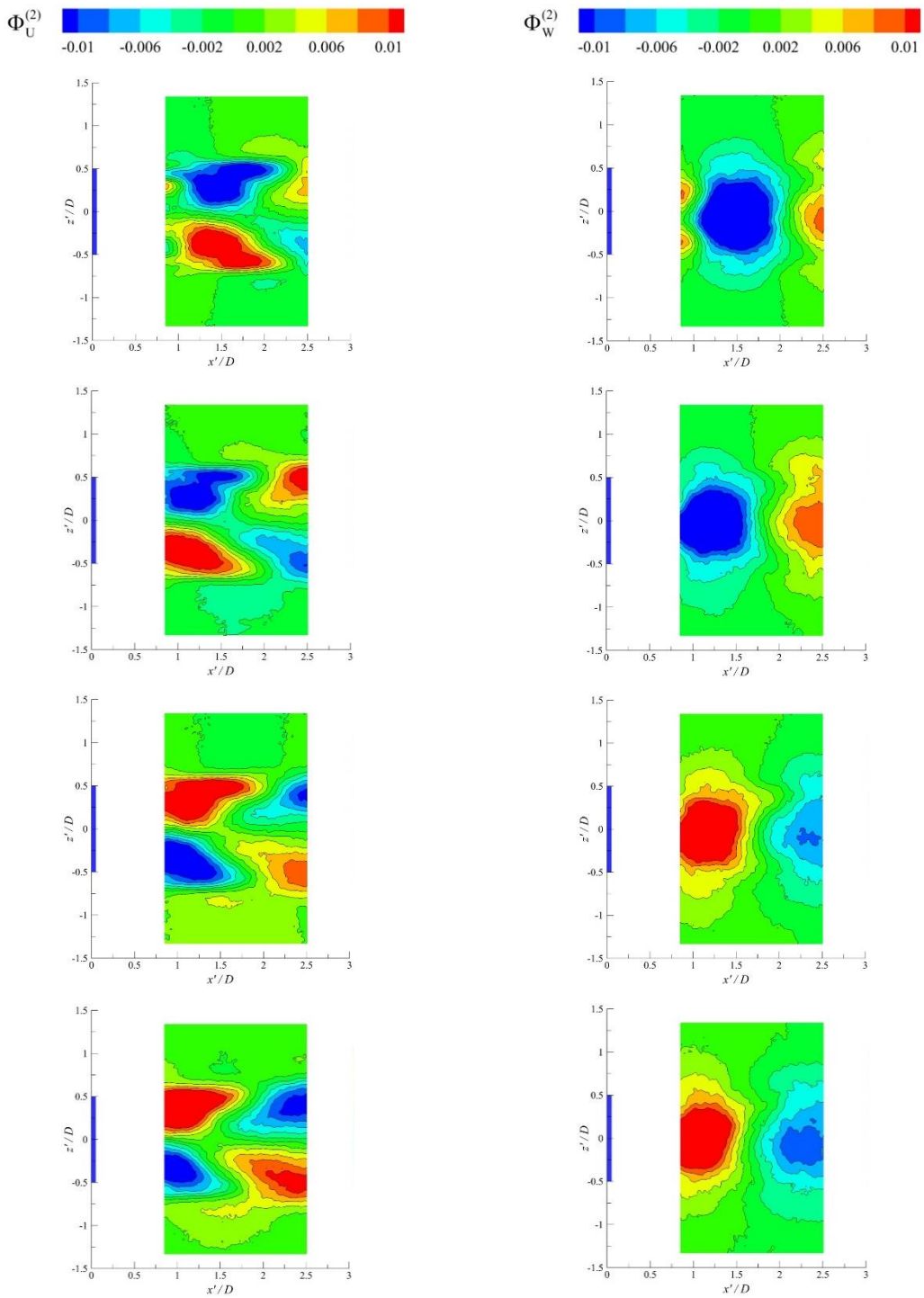

Figure 5.16 Components of the second spatial POD mode. Streamwise component $\phi_U^{(2)}$ (left), vertical component $\phi_W^{(2)}$ (right). *1st row:* $z/\delta = 1.17$, *2nd row*: $z/\delta = 0.71$, *3rd row*: $z/\delta = 0.56$, and *4th row:*$z/\delta = 0.32$. Porous disc is marked as a solid blue rectangle and is located between: $-0.5 \leq z'/D \leq 0.5$

Figure 5.17 and 5.18 display the streamwise and vertical components of the third and fourth spatial modes in the near wake of the porous disc at different disc positions. The flow features representing the third and fourth spatial modes show significantly different flow structures compared to the first and second modes for all the disc positions. Coherent structures are not visible and there seem to be a tendency towards chaotic behaviour, this could be a sign of deformation. In addition, these flow structures show no clear organization.

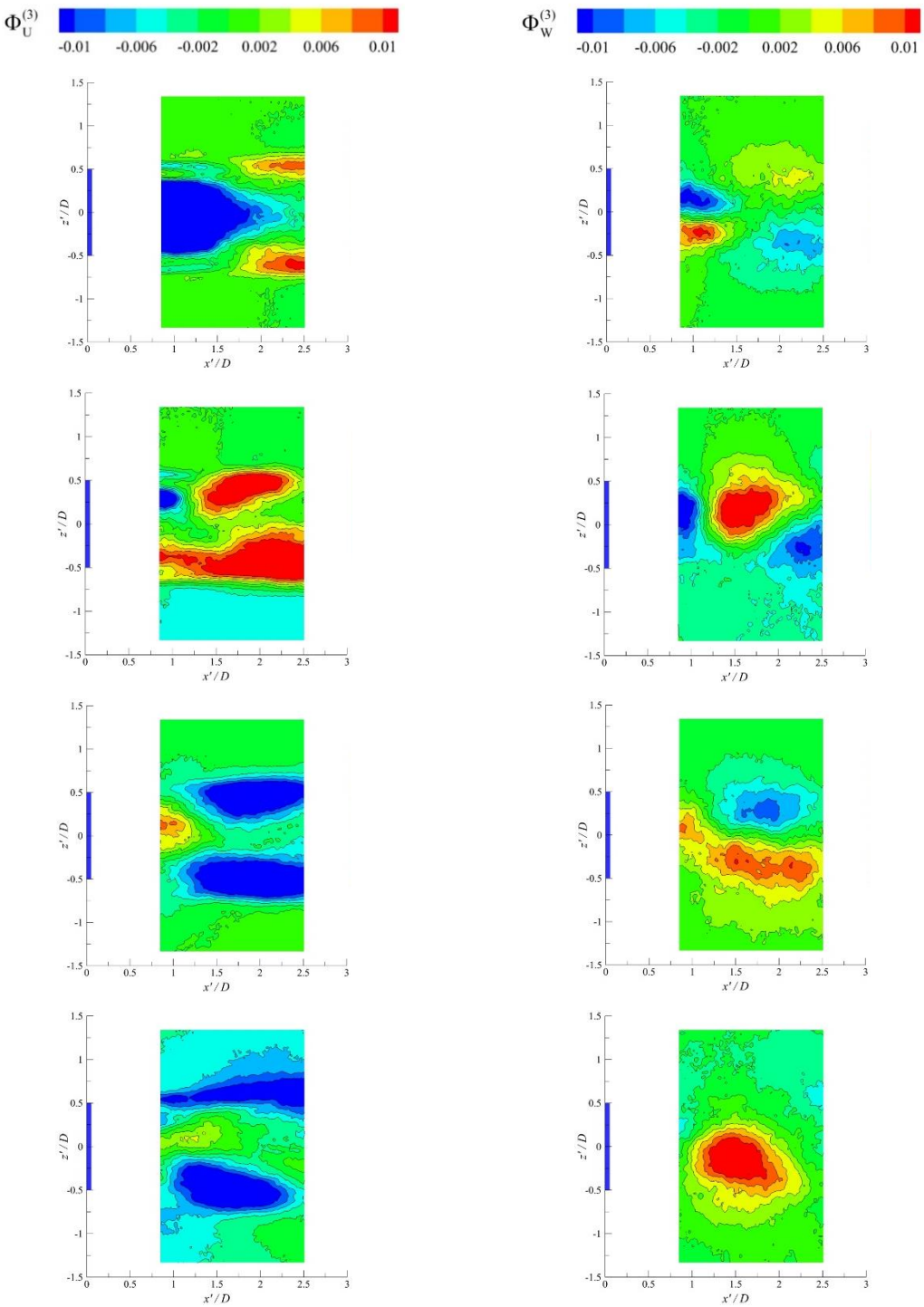

Figure 5.17 Components of the third spatial POD mode. Streamwise component $\phi_U^{(3)}$ (left), vertical component $\phi_W^{(3)}$ (right). *1st row:* $z/\delta = 1.17$, *2nd row*: $z/\delta = 0.71$, *3rd row*: $z/\delta = 0.56$, and *4th row:*$z/\delta = 0.32$. Porous disc is marked as a solid blue rectangle and is located between: $-0.5 \leq z'/D \leq 0.5$

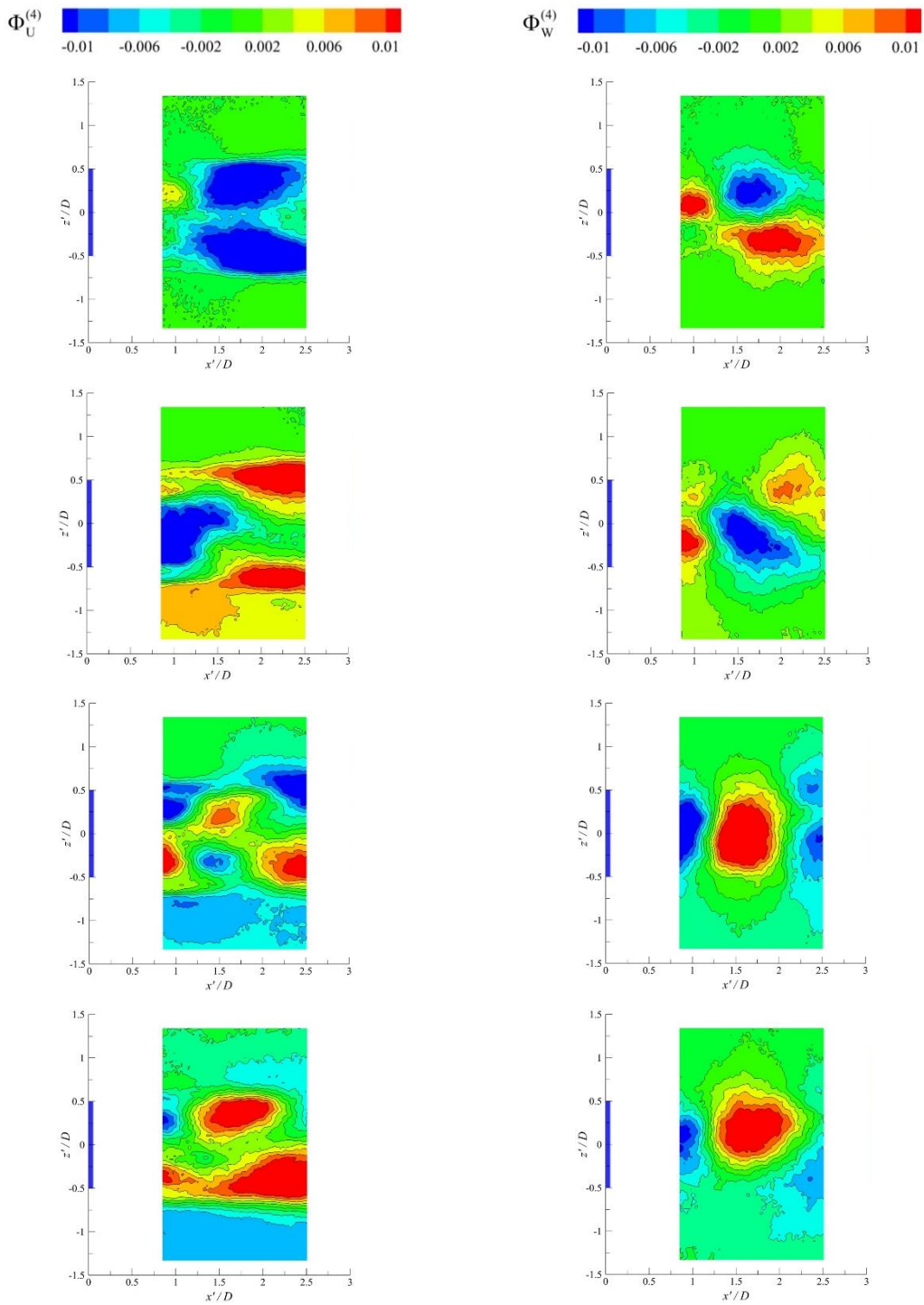

Figure 5.18 Components of the fourth spatial POD mode. Streamwise component $\phi_U^{(4)}$ (left), vertical component $\phi_W^{(4)}$ (right). *1st row:* $z/\delta = 1.17$, *2nd row*: $z/\delta = 0.71$, *3rd row*: $z/\delta = 0.56$, and *4th row:*$z/\delta = 0.32$. Porous disc is marked as a solid blue rectangle and is located between: $-0.5 \leq z'/D \leq 0.5$

CHAPTER 6

ON THE WAKE GROWTH RATE OF A POROUS DISC IMMERSED IN A BOUNDARY LAYER

This chapter presents comparisons between the wake velocity profiles of a porous disc with a radially non-uniform porosity against model predictions from Bastankhah and Porté-Agel wake model and Ishihara and Qian wake model as it is immersed in a boundary layer inflow. A method is proposed as an extension to the wake models to generate asymmetric wake velocity profiles. The comparison illustrates the deviation due to the wake growth rate and initial wake width estimation. The wake growth rate of the porous disc can be significantly higher than field turbines as well as those estimated through empirical relations suggested in the literature in the context of engineering wake models, particularly at low ambient turbulence conditions. This suggests caution in the use of porous discs to simulate wind turbine wakes and wind farms in wind tunnel studies. Results show that the when using the estimated wake growth rate and initial wake width of the porous disc, the wake models show better predictions overall for all the test cases considered.

6.1 Comparison of Wake Models Predictions with Porous Disc Data

This section presents the comparison between the porous disc wake velocity profiles at different streamwise positions with the predicted values from the wake models. In here, two Gaussian-based wake models are used, the Bastankhah and Porté-Agel [53] wake model with two wake growth rate definitions used in the literature formulated by Niyafar and Porté-Agel [264] and Fuertes et al. [265] (refer to Equations 6.1-6.4). The other model used for comparison is the one developed by Ishihara and Qian [64].

6.1.1 Wake Growth Rate and Initial Wake Width Models

The correct estimation of the wake growth rate is crucial for the analytical models to predict the wake velocity profiles of wind turbines accurately. Most of the available models use either a constant value as the wake growth rate parameter (k^*) or a simple empirical formula as a function of the ambient turbulence intensity [263] and the thrust coefficient in other models [64]. Studies [264, 265] have shown that the wake growth rate varies linearly with ambient turbulence intensity. Niyafar & Porté-Agel [264] used Large Eddy Simulations (LES) in order to estimate the variation of the wake growth rate with ambient turbulence intensity which is used together with the Bastankhah and Porté-Agel wake model [53]. They formulated an equation for the wake growth rate as shown in Equation 6.1, and reported that it is only valid for ambient turbulence intensity levels between 6.5% and 15%. In addition, for the initial wake width the following formula (Equation 6.2) is used from the original Bastankhah and Porté-Agel [53] wake model.

$$k^* = 0.383 I_{ambient} + 0.0037 \qquad [6.1]$$

$$\epsilon = 0.25\sqrt{\beta}, \qquad [6.2]$$

where $\beta = \frac{1}{2}\frac{1+\sqrt{1-C_T}}{\sqrt{1-C_T}}$.

Fuertes et al. [265], on the other hand, used field measurements to estimate the wake growth rate and came up with a relation between the wake growth rate parameter and ambient turbulence intensity as shown in Equation 6.3. They also proposed a relation for the initial wake width as a function of wake growth rate as shown in Equation 6.4.

$$k^* = 0.35 I_{ambient} \qquad [6.3]$$

$$\epsilon = -1.91 k^* + 0.34 \qquad [6.4]$$

Ishihara and Qian [64] proposed a relation for the wake growth rate and initial wake width as a function of ambient turbulence intensity and thrust coefficient presented in Equations 6.5 and 6.6 respectively.

$$k^* = 0.11 C_T^{1.07} I_{ambient}^{0.20} \quad [6.5]$$

$$\epsilon = 0.23 C_T^{-0.25} I_{ambient}^{0.17} \quad [6.6]$$

6.1.2 Modeling Wake Asymmetry

The wake velocity profiles obtained using any of the wake models in the literature, including the Bastankhah and Porté-Agel wake model [53] and Ishihara and Qian model [64] are basically generated on horizontal planes (i.e. parallel to the ground) downstream of the turbines. Therefore, these wakes are always symmetrical about the centerline of the wake. However, on the vertical planes downstream of a wind turbine or a porous disc, the wake velocity distribution becomes asymmetrical (or skewed) due to the presence of inflow wind shear. This asymmetry is created due to the fact that the top part of the wind turbine rotor is subjected to higher wind speeds compared to the bottom part of the rotor. In order to model these skewed wake conditions, here we propose a method to generate these asymmetric wakes on vertical planes downstream of a wind turbine rotor or a porous disc. Here we describe the methodology in three steps:

1) First, by using Equation 6.7 for the wake velocity deficit,

$$\frac{\Delta U}{U_\infty} = C(x') e^{-\frac{r^2}{2\sigma^2}} \Longrightarrow \Delta U = U_\infty C(x') e^{-\frac{r^2}{2\sigma^2}}, \quad [6.7]$$

where $C(x)$ and σ are the maximum normalized velocity deficit and wake width, which are constants at any streamwise position x'. r is the radial distance from the center of the wake along the z'- coordinate.

a) If U_∞ is constant (i.e. uniform inflow), the wake model will generate a symmetric wake as shown in Figure 6.1a.
b) If $U_\infty = U_\infty(r)$ (i.e. non-uniform inflow), the wake model will generate an asymmetric wake as shown in Figure 6.1b.

2) Based on the boundary layer inflow conditions shown in Figure 4.6 (Chapter 4) previously. A linearized variation of the inflow velocity is taken across the porous disc (or turbine rotor) when immersed within the boundary layer. This linearized variation is shown as follows in Equation 6.8:

$$U_{\infty}(r) = ar + b\,, \qquad [6.8]$$

where a and b are obtain from the inflow conditions as shown in Equation 6.9:

$$a = \frac{U_{top} - U_{bottom}}{D} = \frac{dU}{dr}$$

$$b = \frac{U_{top} + U_{bottom}}{2} = U_{hub} \qquad [6.9]$$

Here, U_{top} and U_{bottom} are the respective inflow velocities at the top and bottom edge of the porous disc (i.e. turbine rotor) and U_{hub} is the inflow velocity at the hub height. dU/dr is the velocity gradient across the rotor disc.

3) After obtaining the inflow velocity variation across the rotor, $U_{\infty}(r)$ is inserted into Equation 6.7 in order to obtain the asymmetric wake.

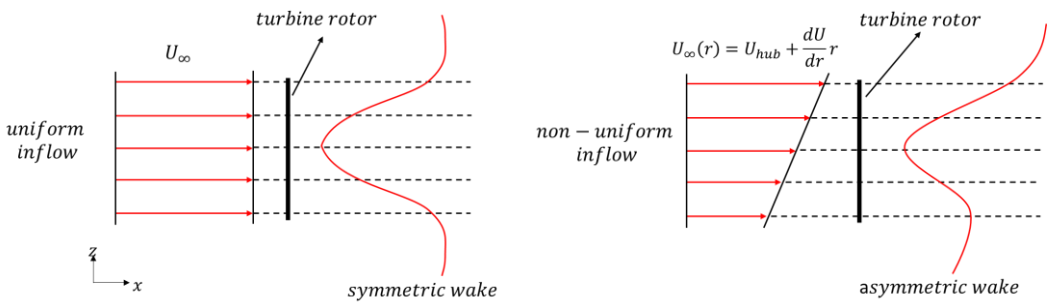

(a) (b)

Figure 6.1 Conceptual sketch showing the proposed methodology for generating asymmetric wake profiles: (a) symmetric wakes under uniform inflow, and (b) asymmetric wake under non-uniform inflow. The turbine rotor is represented as a solid black rectangle

6.1.3 Results

Therefore, using the original formulations of the wake models with Equations 6.1-6.4 with the Bastankhah and Porte-Agel wake model [53], and Equations 6.5 and 6.6 with the Ishihara and Qian wake model [64], Figures 6.2-6.5 present comparison between the experimental data of the porous disc with the predictions of the wake models along the streamwise direction at different positions of the disc in the boundary layer, i.e., $z/\delta = 1.17\,, 0.71, 0.56\ and\ 0.32$, respectively.

Starting with Figure 6.2 for the case outside the boundary layer, i.e., $z/\delta = 1.17$, where the wake is symmetric and the ambient turbulence intensity is low (see Table 6.1). The wake models fail to capture the velocity profiles correctly, although the Bastankhah and Porté-Agel wake model with the wake growth rate definition proposed by Fuertes et al. [265] seems to show better performance compared to the others especially at $x'/D = 4$ & 5. One can also observe that the wake models show a very slow growth rate in comparison with the porous disc data. One should note in here that the wake growth rate definition proposed by Niyafar and Porté-Agel [264] is valid for ambient turbulence intensity levels between 6.5% and 15%. This is probably why the wake model fails to predict the velocity profiles correctly. In addition, the wake width is underestimated in the Ishihara and Qian model as can be seen from the velocity profiles (see Table 1).

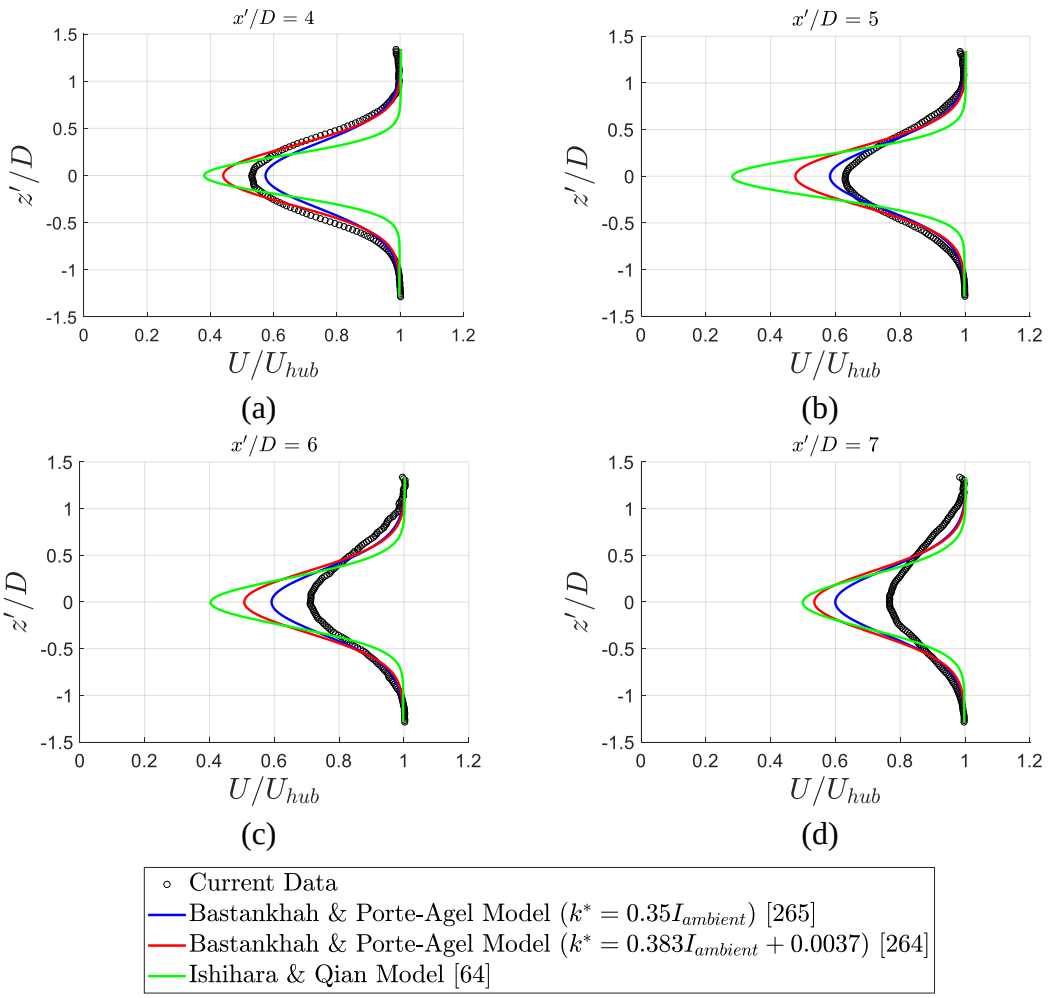

Figure 6.2 Comparison between the experimental data and the predictions of the wake models at $z/\delta = 1.17$ along the streamwise direction from (a-d): $x'/D = 4$ to $x'/D = 7$. Porous disc is located between: $-0.5 \leq z'/D \leq 0.5$

As the disc is immersed deeper within the boundary layer, Figure 6.3 shows the case where the disc at $z/\delta = 0.71$, one can observe that although the wake models can capture the asymmetry of the wake velocity profiles, they still fail to predict the values correctly especially at $x'/D = 4$ and $x'/D = 5$, on the other hand, at $x'/D = 6$ and $x'/D = 7$, the Bastankhah and Porté-Agel wake model shows better performance than the Ishihara and Qian model especially when using the wake growth formulation (see Equations 6.1 & 6.2) proposed by Niyafar and Porté-Agel [264]. Similar observations can be seen at $z/\delta = 0.56$ (see Figure 6.4) and

$z/\delta = 0.32$ (see Figure 6.5), although the predictions are slightly better due to increased inflow turbulence as one moves deeper within the boundary layer.

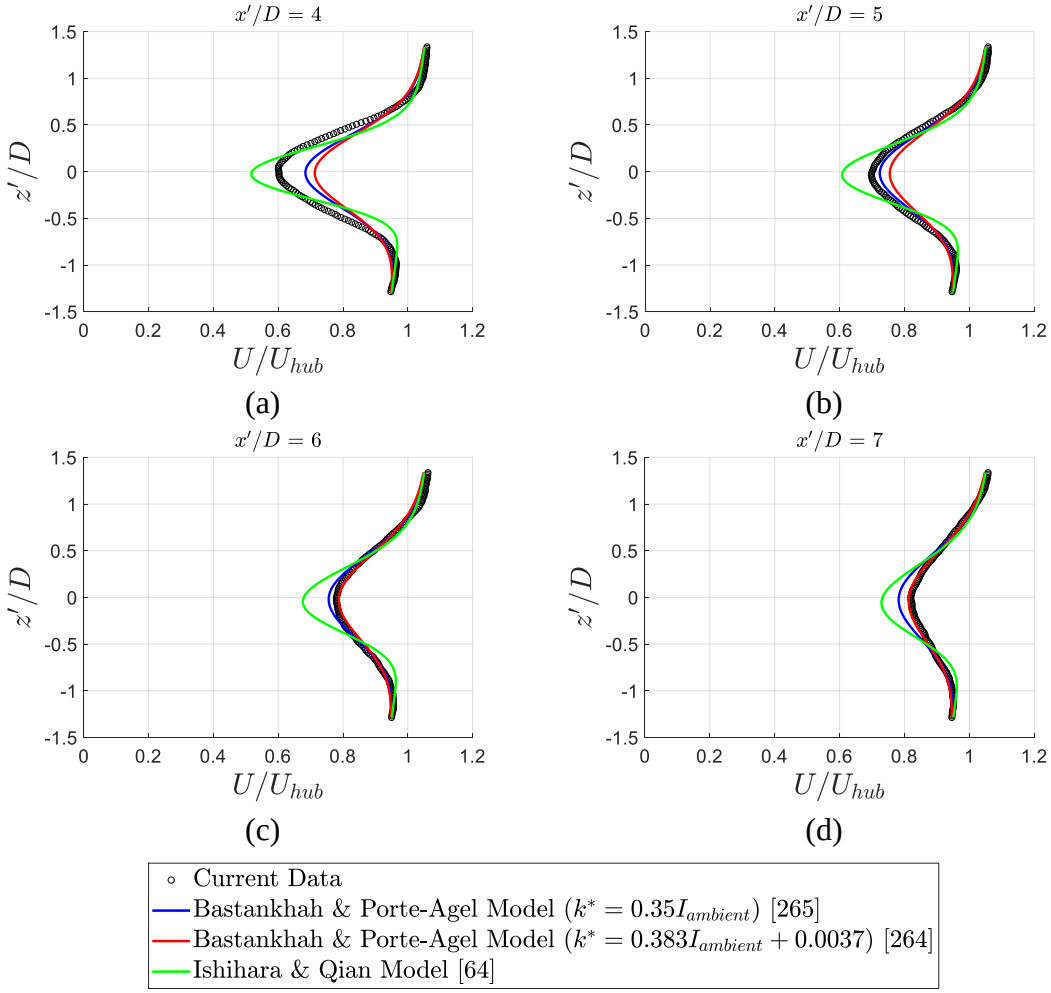

Figure 6.3 Comparison between the experimental data and the predictions of the wake models at $z/\delta = 0.71$ along the streamwise direction from (a-d): $x'/D = 4$ to $x'/D = 7$. Porous disc is located between: $-0.5 \leq z'/D \leq 0.5$

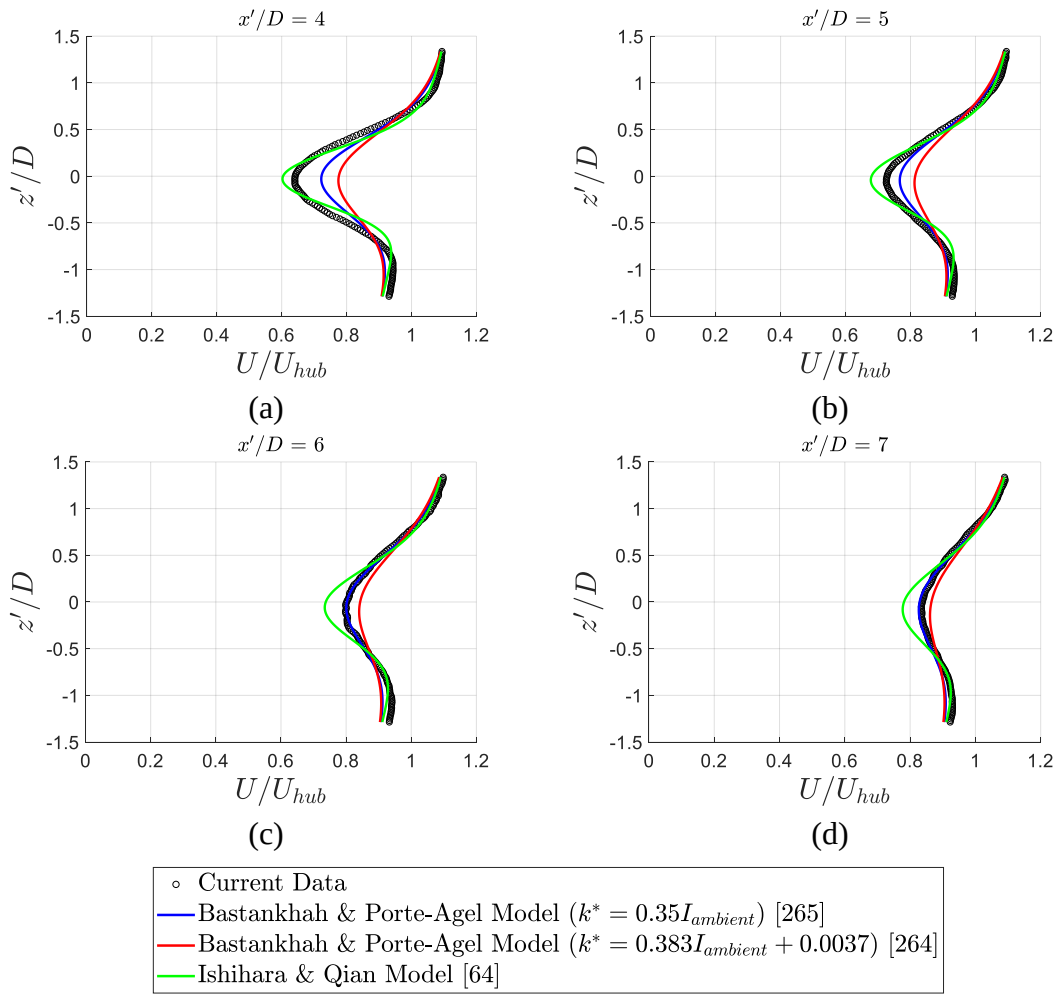

Figure 6.4 Comparison between the experimental data and the predictions of the wake models at $z/\delta = 0.56$ along the streamwise direction from (a-d): $x'/D = 4$ to $x'/D = 7$. Porous disc is located between: $-0.5 \leq z'/D \leq 0.5$

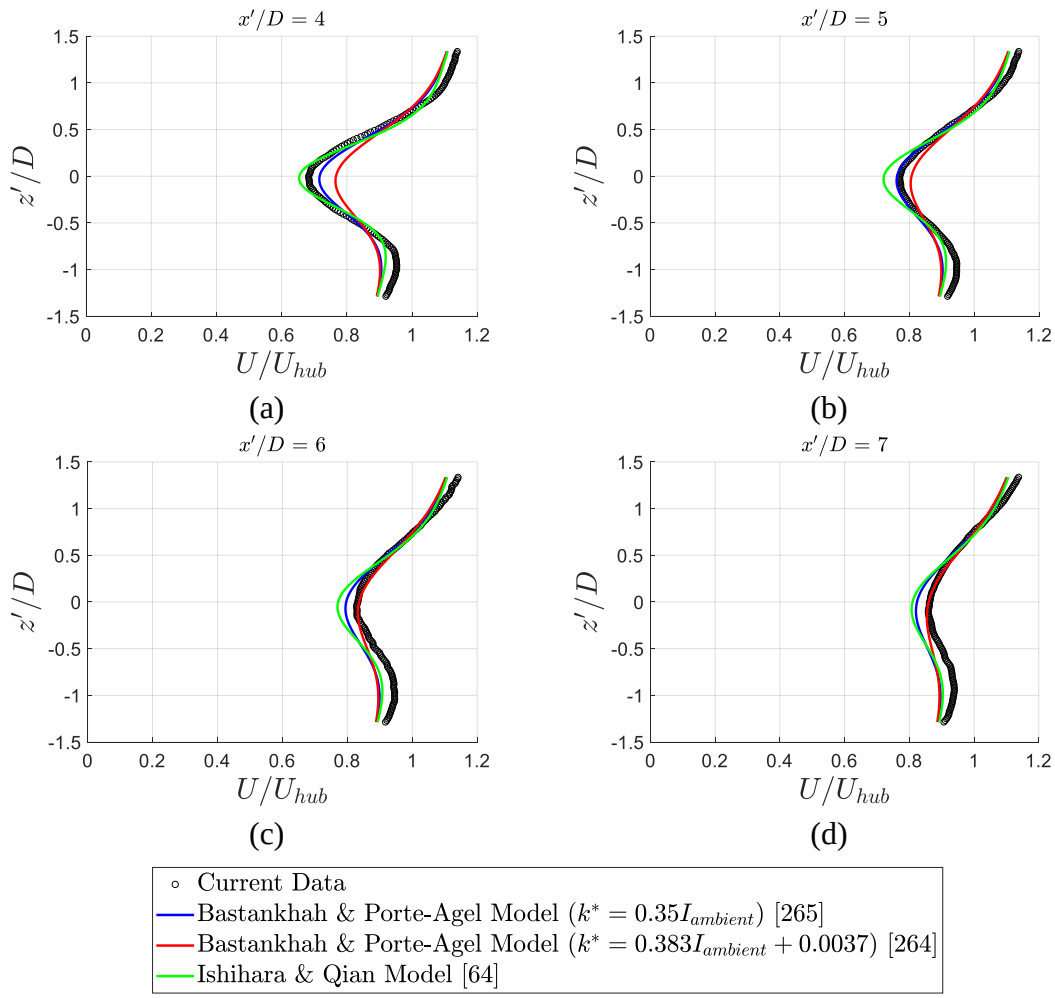

Figure 6.5 Comparison between the experimental data and the predictions of the wake models at $z/\delta = 0.32$ along the streamwise direction from (a-d): $x'/D = 4$ to $x'/D = 7$. Porous disc is located between: $-0.5 \leq z'/D \leq 0.5$.

These wake models which are effective in predicting wind turbine wakes especially for wind farm predictions and optimization [53, 64], seem to fail when compared to the porous disc especially at low ambient turbulence intensity levels. The wake models seem to generate very slow growth rate compared to the porous disc, this is probably due to the inherent differences between the porous disc and wind turbine, where the porous disc is considered as a turbulence generator. Studies have shown that at low ambient turbulence intensity the turbine (or porous disc) induced turbulence has a significant influence on the wake growth rate [263]. Others have reported that the wake growth rate is not only influenced by the ambient turbulence,

but also the shear-generated turbulence and the mechanical turbulence [55]. Therefore, in order to improve the predictions of these wake models, the correct wake growth rate and initial wake width will be estimated for the porous disc via velocity fields obtained through the PIV experiments as shown in the following section.

6.2 Porous Disc Wake Growth Rate

6.2.1 Estimation of Wake Growth Rate and Initial Wake Width

The comparison shown in section 6.1 between the porous disc experimental data and the predictions of the wake models, yields that the wake models fail to predict the porous disc wake velocity profiles correctly. The main reason is due to the deviation in the estimation of the wake growth rate and initial wake width. Hence, in order to improve the predictions of the wake models, the correct wake growth rate and initial wake width should be estimated for the porous disc.

Therefore, in this section, the wake growth rate and initial wake width parameters for the porous disc under different ambient turbulence intensity levels is directly calculated by use of the wake velocity fields obtained via PIV measurements. This is done by assuming a linear expansion for the wake represented by the following equation (Equation 6.10) as reported by Bastankhah and Porté-Agel [53] and Ishihara and Qian [64]:

$$\sigma/D = k^*(x'/D) + \epsilon \,, \qquad [6.10]$$

where σ is the standard deviation at every streamwise distance (x') for the velocity deficit profiles (usually considered as the wake width [64]) , k^* is the wake growth rate parameter and ϵ is the value of σ/D when x'/D approaches zero (i.e., initial wake width).

The wake width σ/D is calculated from the maximum velocity deficit using Equation 6.11:

$$\sigma/D = \sqrt{\frac{C_T}{8\left[1-\left(1-C(x'/D)\right)^2\right]}}, \qquad [6.11]$$

where $C(x'/D)$ represents the maximum normalized velocity deficit at each downstream location which occurs at the center of the wake, and C_T is the disc thrust coefficient.

One should note in here that the wake velocity profiles are asymmetric due to inflow velocity gradients as well as the wake centerline is shifting downwards as shown previously in Chapter 5. Therefore, in order to correctly estimate the wake growth rate from the porous disc PIV data and properly implement the above-mentioned method, the asymmetric velocity profiles are first normalized by subtracting the wake velocity profiles from the inflow boundary layer, which generates symmetric wake velocity profiles as shown in Figure 6.6.

As is evident in Figure 6.6 the wake velocity profiles are symmetric for all disc positions and at different streamwise positions. Consequently, the normalized wake deficit profiles are obtained using Equation 6.12.

$$\frac{\Delta U}{U_{hub}} = \frac{U_{hub} - U}{U_{hub}}, \qquad [6.12]$$

and the maximum normalized velocity deficit is obtained as follows:

$$C(x'/D) = \left(\frac{\Delta U}{U_{hub}}\right)_{max}, \qquad [6.13]$$

where ΔU is the wake velocity deficit, and U_{hub} is the velocity at hub height.

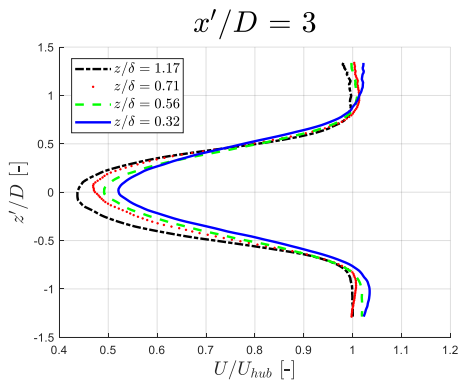

(a)

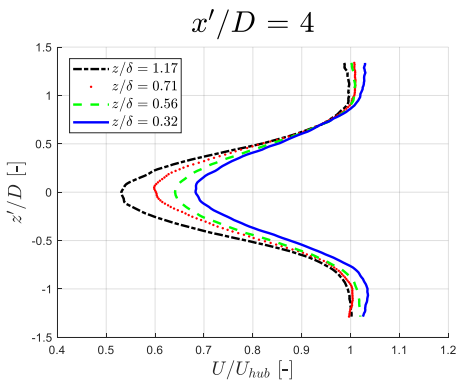

(b)

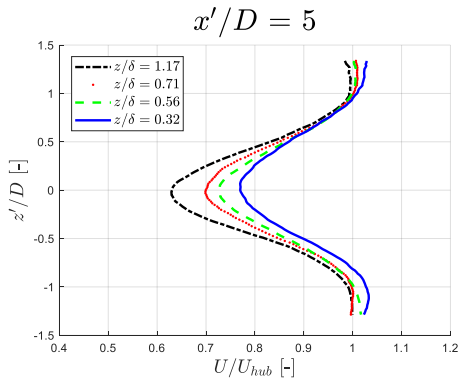

(c)

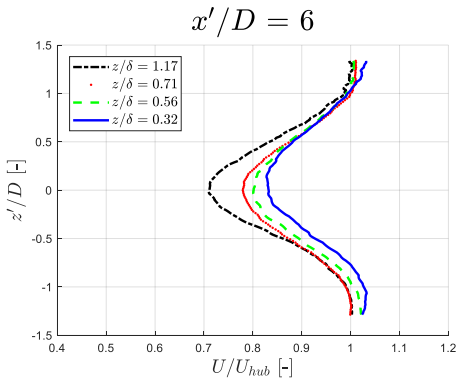

(d)

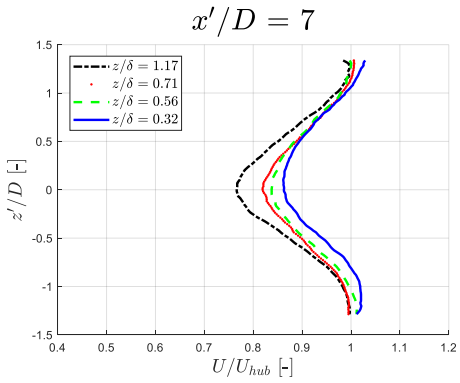

(e)

Figure 6.6 Normalized wake velocity profiles for all z/δ locations along the streamwise direction from (a-e): $x'/D = 3$ to $x'/D = 7$ downstream of the disc. Porous disc is located between: $-0.5 \leq z'/D \leq 0.5$

The variations of σ/D in the streamwise direction downstream of the porous disc are plotted in Figure 6.7 using Equation 6.11. In addition, linear curve fits are plotted

to estimate the wake growth rate, k^*, and initial wake width, ϵ, for the porous disc using Equation 6.10. The values of $k^*$and ϵ are obtained from Figure 6.7 and tabulated in Table 6.1 for different ambient turbulence intensities obtained at different positions in the boundary layer.

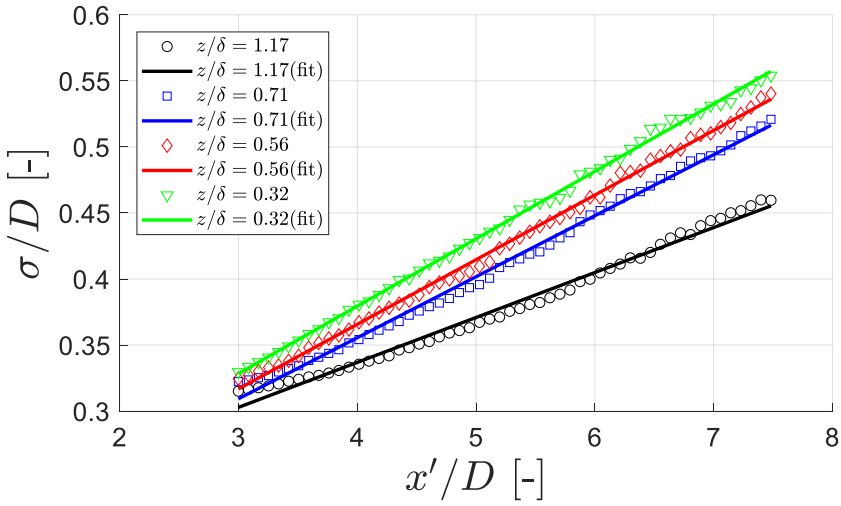

Figure 6.7 Variation of the normalized standard deviation (i.e. wake width) of the velocity deficit profiles for all z/δ locations along the streamwise direction with curve fits to obtain $k*$ and ϵ.

Table 6.1 $k^*$and ϵ for the selected boundary positions of the porous disc

z/δ	1.17	0.71	0.56	0.32
$I_{ambient}$ (%)	0.6	3.2	5.5	8.0
k^* (Current Study)	**0.034**	**0.046**	**0.049**	**0.051**
k^* (Niyafar & Porté-Agel [264])	0.006	0.016	0.025	0.034
k^* (Fuertes et al. [265])	0.002	0.011	0.019	0.028
k^* (Ishihara and Qian [64])	0.025	0.034	0.038	0.041
ϵ (Current Study)	**0.201**	**0.171**	**0.170**	**0.175**
ϵ (Niyafar & Porté-Agel [264])	0.289	0.289	0.289	0.289
ϵ (Fuertes et al. [265])	0.336	0.319	0.303	0.287
ϵ (Ishihara & Qian [64])	0.108	0.143	0.157	0.167

Figures 6.8 shows the variation of $k^*$and ϵ for the porous disc as well as the predicted values by the wake models. In addition, the wake growth rate for field measurements reported in Fuertes et al. [265] are also included for comparison. As shown in Table 1 and Figure 6.8 the wake growth rate values for the porous disc are generally higher than the predicted values of the equations proposed by Niyafar and Porté-Agel [264], Fuertes et al. [265], and Ishihara and Qian [64] respectively. It is observed that the wake growth rate trend for the porous disc data in general does not follow the linear variations as previously proposed by Niyafar & Porté-Agel [264] and Fuertes et al. [265], especially at low ambient turbulence intensity levels. At low ambient turbulence intensity levels, the k^* values are generally higher for porous discs than those for wind turbines. The wake growth rate predicted by Ishihara and Qian model although seems to give higher k^* values compared to other models, still under predicts the porous disc wake growth rate. The model also shows similar trend, indicating that the wake growth rate might not vary linearly with ambient turbulence intensity. On the other hand, the initial wake width variation shown in Figure 6.9 for the porous disc is over estimated by Niyafar and Porté-Agel [264], and Fuertes et al. [265] equations, and under estimated by Ishihara and Qian [64] especially at low ambient turbulence intensities. However, Ishihara and Qian model seems to give closer results for the initial wake width at higher ambient turbulence intensities as compared to the porous disc. Therefore, using the estimated values of k^* and ϵ for the porous disc directly instead of the equations presented in the wake models would improve the predictions significantly as shown in the next section.

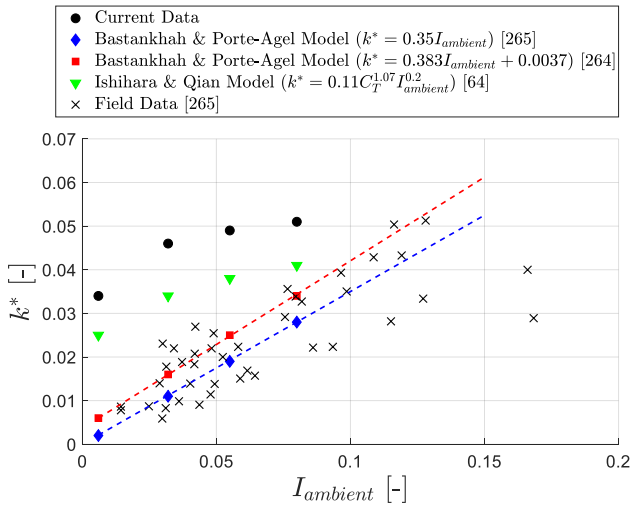

Figure 6.8 Variation of wake growth rate with ambient turbulence intensity for the porous disc as well as the values predicted by the wake models. Field data reported in Fuertes et al. [265] are included for comparison

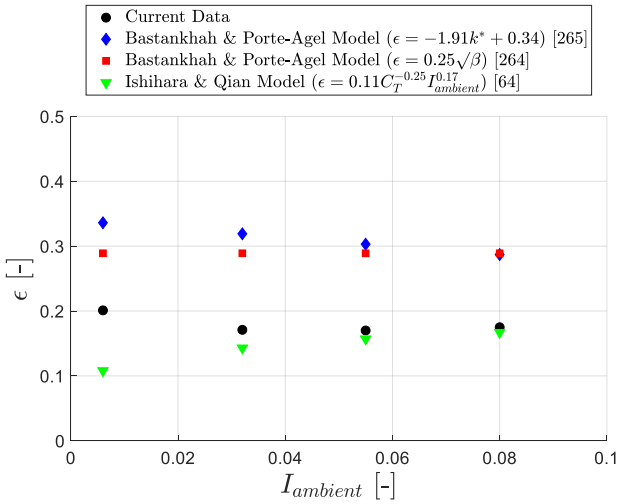

Figure 6.9 Variation of initial wake width with ambient turbulence intensity for the porous disc as well as the values predicted by the wake models.

6.3 Wake Turbulence and Disc Added Turbulence

Figure 6.10 presents the streamwise turbulence intensity contours at different z/δ locations covering a streamwise distance up to 7.5 D downstream of the disc. Here, x' and z' are the local coordinates traveling with the disc, as defined previously in

Figure 4.5 (Chapter 4). To begin with, fairly symmetrical turbulence intensity distributions are observed around the geometric centerline (the dashed black line marks the center of the disc, i.e., $z'/D = 0$) in the baseline case, i.e., at $z/\delta = 1.17$ outside the boundary layer (Figure 6.10a). As the disc is immersed within the boundary layer towards lower z/δ locations, one can observe the wake turbulence intensity fields get shifted or skewed upwards as one goes deeper within the boundary layer, with the upper half of the wake presenting higher turbulence intensity field. Similar observation can be seen previously in Figure 5.4 (Chapter 5).

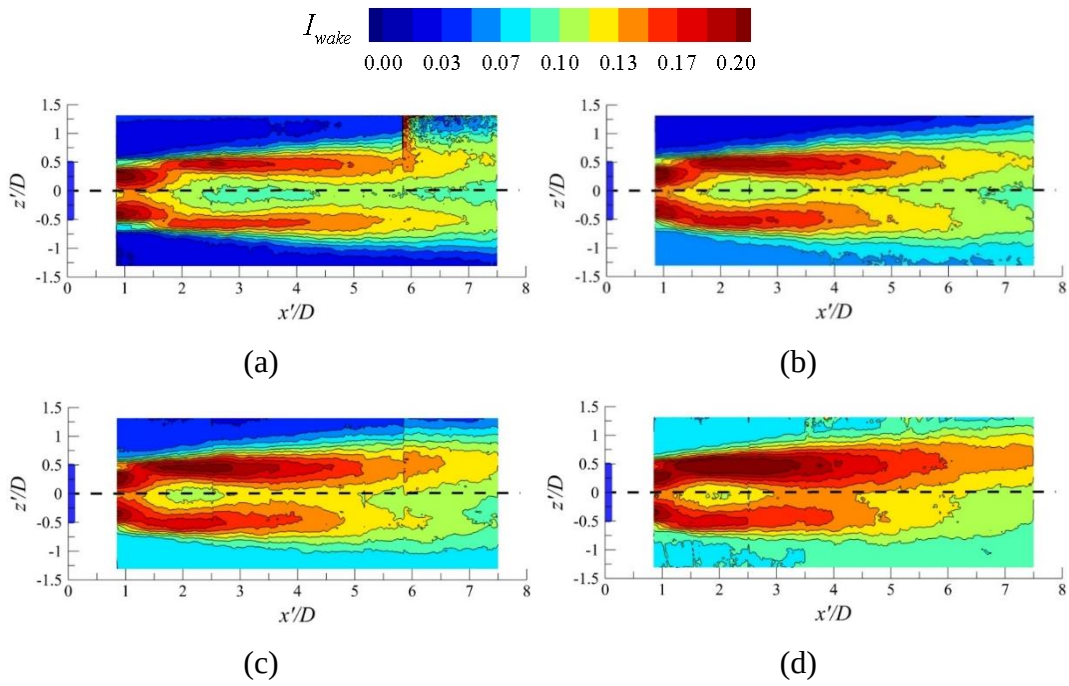

Figure 6.10 Streamwise turbulence intensity at different disc positions: (a) $z/\delta = 1.17$, (b) $z/\delta = 0.71$, (c) $z/\delta = 0.56$, and (d) $z/\delta = 0.32$. Porous disc is marked as a solid blue rectangle and is located between: $-0.5 \leq z'/D \leq 0.5$. The dashed black line represents the geometric centerline and passes through the center of the disc $z'/\mathrm{D} = 0$

Figure 6.11 displays the streamwise turbulence intensity distributions for all z/δ locations along the streamwise direction from $x'/D = 3$ to $x'/D = 7$ downstream of the disc. Outside the boundary at $z/\delta = 1.17$, typical fairly symmetrical double peak distribution can be seen respectively at $z'/D = \pm 0.5$. As one goes deeper

within the boundary layer asymmetrical distribution of the turbulence intensity in the wake starts to occur since the disc is exposed to a non-uniform inflow across its diameter. Furthermore, the magnitude of the peak at the upper half progressively increases within the boundary layer. Further downstream the upper peak persists until $x'/D = 7$, whereas the lower peak is almost indistinguishable and diffused. It was shown previously in Porté-Agel et al. [54] that under uniform inflow, I_{wake} has a double Gaussian distribution with the maximum values occurring at the edges of the wake. On the other hand, in boundary layer flows, the maximum value of the turbulence intensity usually occurs at the upper edge of the wake [54] which is consistent with the results in this study for porous discs.

Figure 6.12 presents the wake turbulence (I_{wake}) and disc added turbulence (I_{+}) variations with streamwise distance along the geometric centerline of the disc (i.e. $z'/D = 0$) for different z/δ positions. The disc added turbulence intensity is estimated using the formula given by Frandsen [261] as, $I_{+} = \sqrt{I_{wake}^2 - I_{ambient}^2}$, where I_{wake} is the streamwise turbulence intensity in the wake, and $I_{ambient}$ is the ambient (freestream) turbulence intensity.

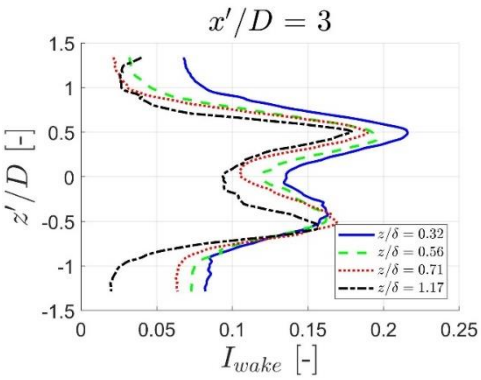

(a)

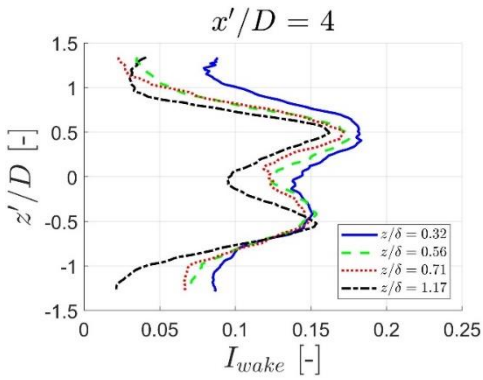

(b)

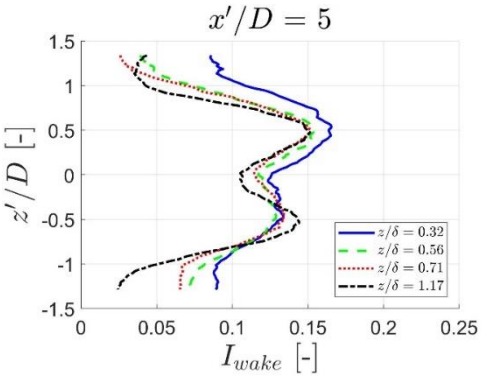

(c)

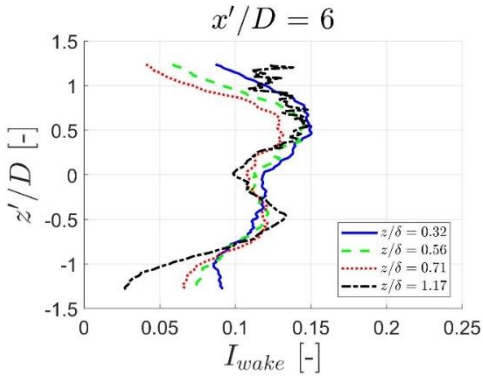

(d)

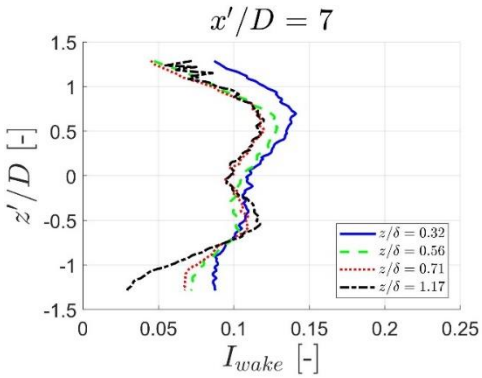

(e)

Figure 6.11 Turbulence intensity distributions for all z/δ locations along the streamwise direction from (a-e): $x'/D = 3$ to $x'/D = 7$ downstream of the disc. Porous disc is located between: $-0.5 \leq z'/D \leq 0.5$.

For the case outside the boundary layer (i.e. $z/\delta = 1.17$) where the ambient turbulence intensity is relatively low, the difference between the wake turbulence

and disc added turbulence is negligible for all positions in the streamwise direction. This indicates that the turbulence intensity in the wake is dominated by the disc-induced turbulence for the case of low ambient turbulence intensity. There is a peak just downstream of the disc (at around $x'/D = 1$) that is followed by a decay in both wake and disc-added turbulence intensity variations in the streamwise direction. It then remains almost constant beyond $x'/D = 3$ with a slight increase around $x'/D = 5$, which is most probably due to the merging of the two high turbulence intensity regions on either side of the wake. As one goes towards lower positions within the boundary layer, disparities start to occur between the wake turbulence and disc-added turbulence due to the progressively increasing freestream turbulence intensity levels. In relation to enhanced mixing and thus faster wake recovery for the cases within the boundary layer, interaction between the turbulence intensity patterns associated with the upper and lower shear layers takes place at a smaller streamwise distance to the disc, which can be inferred from Figure 6.10. This leads to the constant turbulence intensity regions narrowing down and secondary peak positions getting closer to the disc as one moves downwards in the boundary layer.

Figure 6.12 also shows that for the range of ambient turbulence intensity levels used in this study (i.e. $0.6\ \% \leq I_{ambient} \leq 8.0\ \%$) , the disc added turbulence is not very sensitive to changes in ambient turbulence intensity. This observation is consistent with recent porous disc experiments by Neunaber et al. [262]. To illustrate this point, the data presented in the study of Neunaber et al. [262] is used to produce Figure 6.13, which displays streamwise variations of the disc-added turbulence for different ambient (inflow) turbulence intensity levels in the range of $0.3\% \leq I_{ambient} \leq 10.3\%$. It is clear that the disc-added turbulence level is almost insensitive to the ambient turbulence intensity level in the given range. On the other hand, regarding model wind turbine rotors, generally a stronger influence of ambient turbulence is observed on now the “rotor-added turbulence”, which is also calculated by using the data presented by Neunaber et al. [262] and shown in Figure 6.13. Similar observations were also reported in the study of Polster [72], where the ambient turbulence intensity related variations in the wind turbine rotor wake start to diminish and the distributions start to converge on to each other after about $x'/D > 4$.

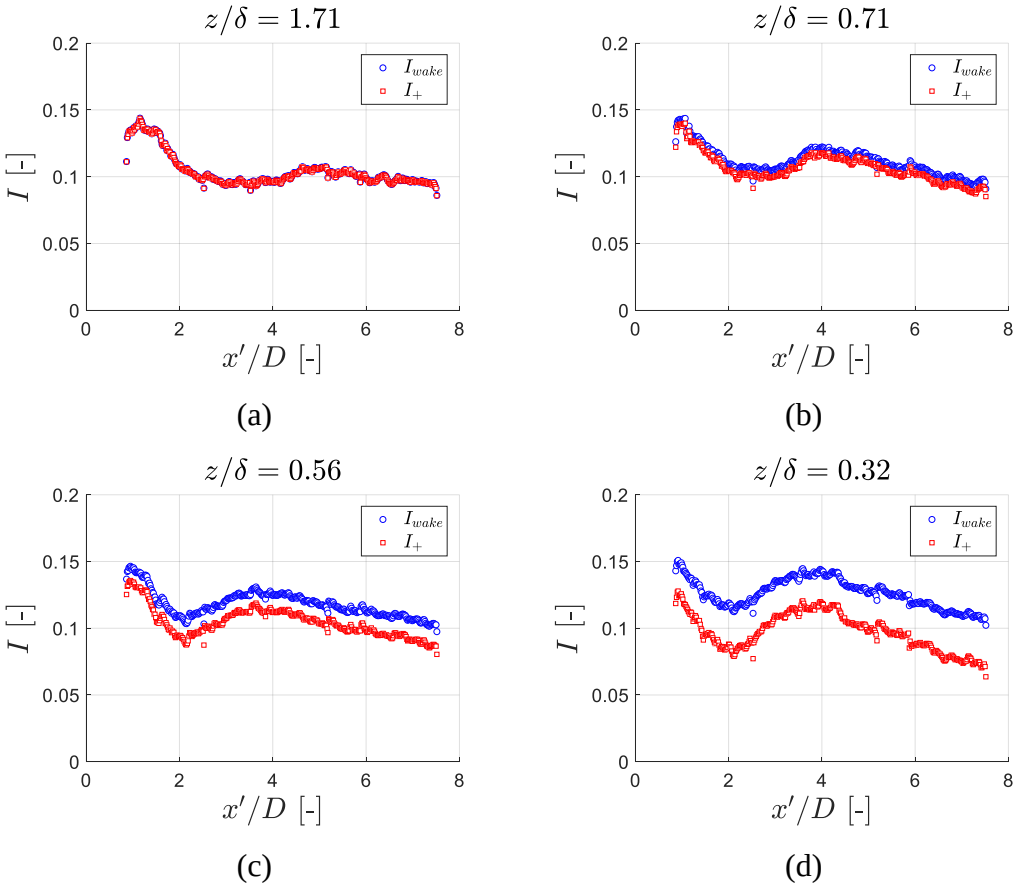

Figure 6.12 Wake turbulence intensity (I_{wake}) and disc added turbulence intensity (I_+) variations with streamwise distance along the geometric centerline of the disc (i.e. $z'/D = 0$) for different z/δ positions. (a) $z/\delta = 1.17$, (b) $z/\delta = 0.71$, (c) $z/\delta = 0.56$, and (d) $z/\delta = 0.32$

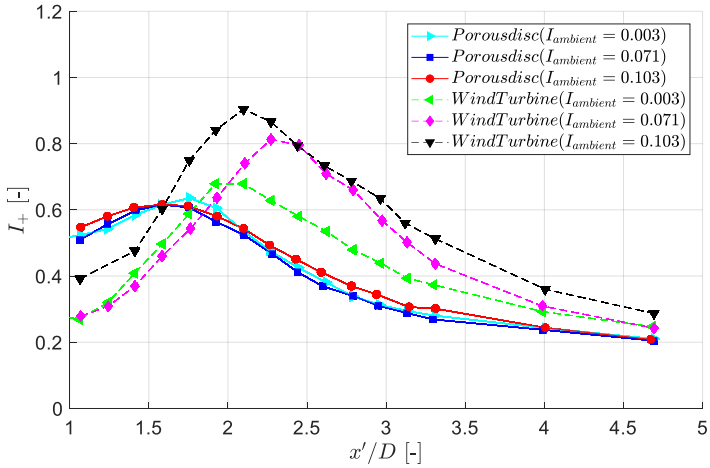

Figure 6.13 Rotor/Disc added turbulence intensity variations with streamwise distance along the centerline of the rotor/disc (i.e. $z'/D = 0$) at different ambient turbulence intensity levels for porous disc and model wind. This figure is prepared using the data presented in Neunaber et al. [262].

The differences observed in the disc/rotor added turbulence characteristics downstream of disc or wind turbine wakes under different ambient turbulence intensity levels have a significant influence in the spreading rates of these wakes, which is often modeled using a wake growth rate parameter in wake models in the literature. Many analytical models for the prediction of rotor added turbulence intensity have been proposed in the literature. In here comparison with the Crespo and Hernandez model [268] is conducted against the porous disc data. Crespo and Hernandez proposed the following formula (Equation 6.14):

$$I_{+,C\&H} = 0.73a^{0.8325} I_{ambient}^{0.0325} (x'/D)^{-0.32}, \qquad [6.14]$$

where a is the axial induction factor. This equation is valid in the range of $5 < x'/D < 15$, $0.07 < I_{ambient} < 0.14$, and $0.1 < a < 0.4$.

To check the validity of Equation 6.14, the disc-added turbulence variations obtained in this study are compared with the results of the model proposed by Crespo and Hernandez [268] in Figure 6.14. The model results show a reasonable agreement with the experimental data especially beyond $x'/D > 3$ downstream of the disc for all selected positions within the boundary layer. The validity of this model has also

been proven against LES of wind turbines as reported by Niyafar and Porté-Agel [264].

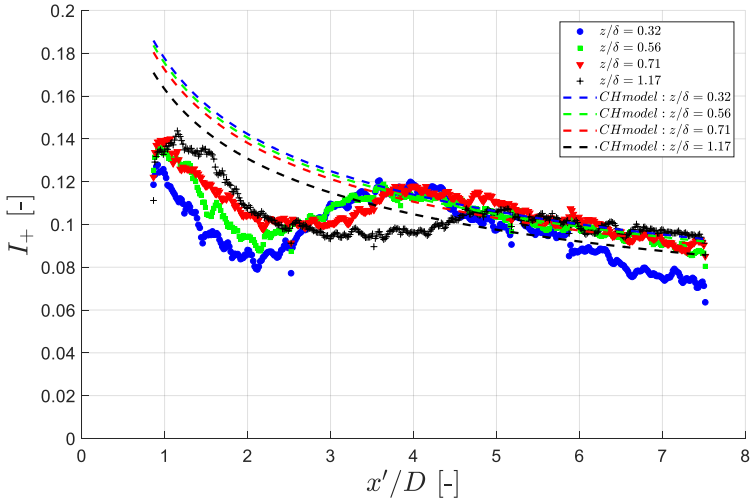

Figure 6.14 Comparison between the porous disc data of the current experiments and the Crespo and Hernandez model at different positions within the boundary layer.

6.4 Wake Model Predictions Based on the Estimated k^* and ϵ

Figure 6.15-6.18 presents comparisons between the porous disc data and the predictions of the wake models using the estimated k^* and ϵ at different disc positions in the boundary layer along the streamwise direction. For the case outside the boundary layer (i.e. $z/\delta = 1.17$) shown Figure 6.15, the prediction of the wake models improves significantly when using the correct k^* and ϵ values, especially for the Bastankhah and Porté-Agel wake model. On the other hand, the Ishihara and Qian model slightly over estimates the velocity values except at $x'/D = 7$ where the predictions match well with the experiments.

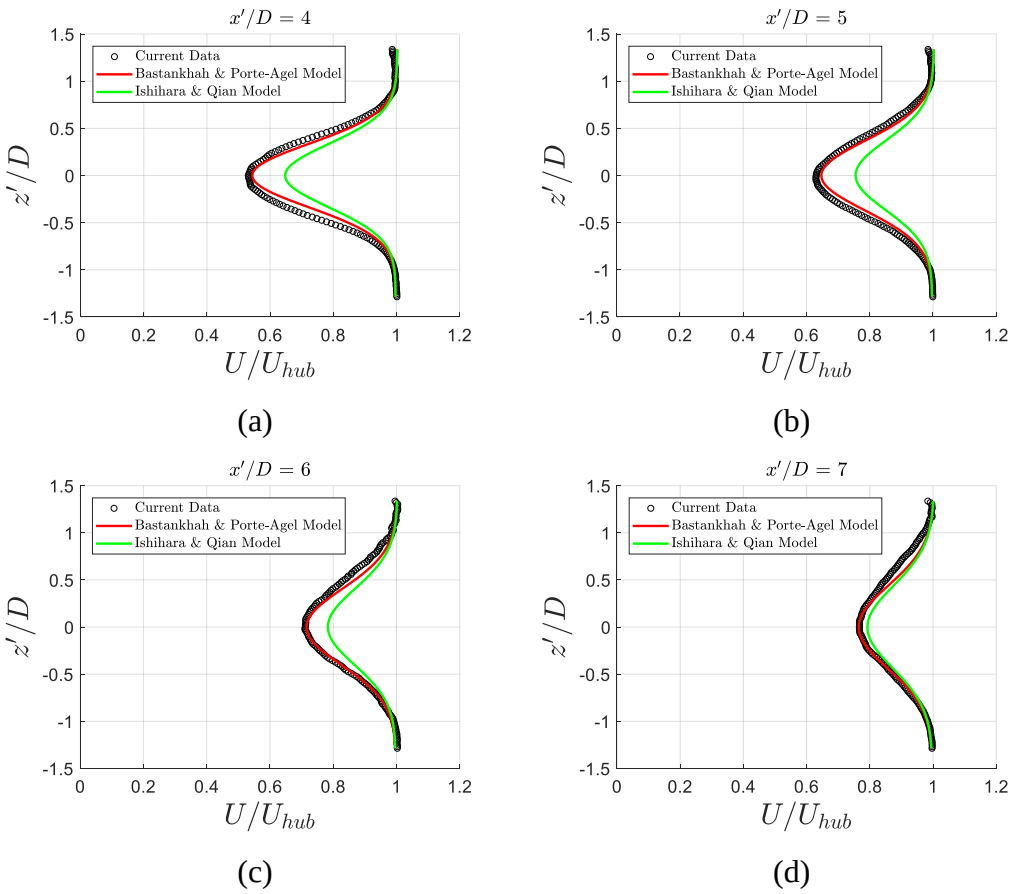

Figure 6.15 Comparison between the experimental data and the predictions of the wake models using the estimated k^* and ϵ at $z/\delta = 1.17$ along the streamwise direction from (a-d): $x'/D = 4$ to $x'/D = 7$. Porous disc is located between: $-0.5 \leq z'/D \leq 0.5$

As one moves deeper within the boundary layer, for instance at $z/\delta = 0.71$ (Figure 6.16), the wake models also show significant improvement in predicting the wake velocity profiles of the porous disc. At this position the ambient turbulence intensity is higher compared to the case outside the boundary layer, Ishihara and Qian wake model shows better match as the turbulence intensity increases especially at $x'/D = 6 \,\&\, 7$. The Bastankhah and Porté-Agel wake model shows good match at all streamwise positions. Similar observations can be seen at $z/\delta = 0.56$ and $z/\delta = 0.32$. One can also observe, as we move to lower positions the inflow turbulence intensity increases which results in improving the predictions of the Ishihara and Qian model significantly.

These results show that when using the correct wake growth rate and initial wake width the wake models predictions can improve significantly even at low ambient turbulence intensity levels. This suggests caution in the use of porous discs to simulate wind turbine wakes and wind farms in wind tunnel studies.

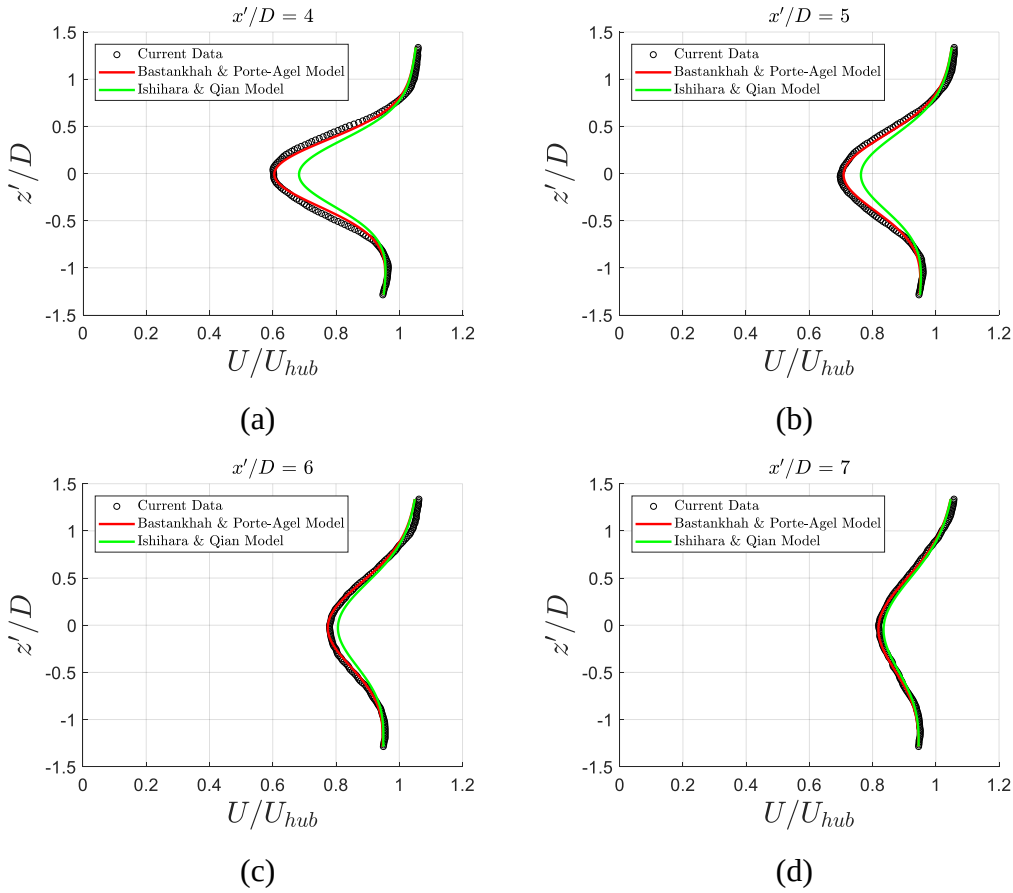

Figure 6.16 Comparison between the experimental data and the predictions of the wake models using the estimated k^* and ϵ at $z/\delta = 0.71$ along the streamwise direction from (a-d): $x'/D = 4$ to $x'/D = 7$. Porous disc is located between: $-0.5 \leq z'/D \leq 0.5$

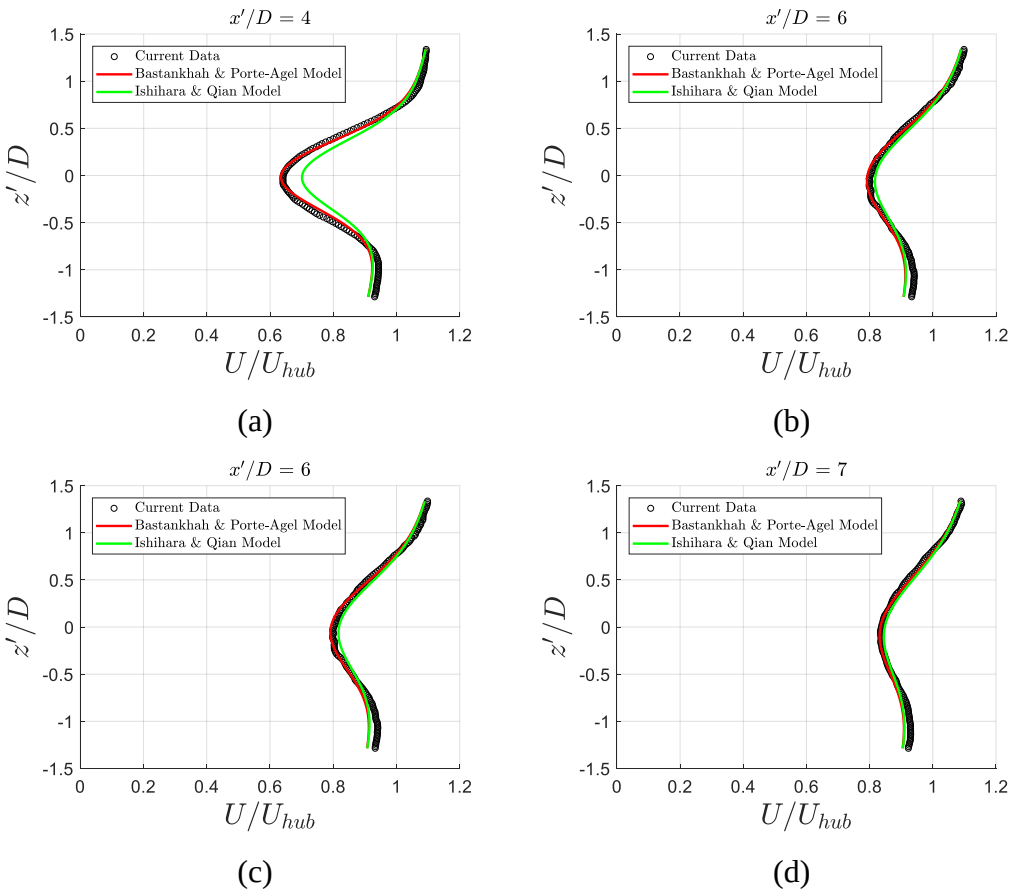

Figure 6.17 Comparison between the experimental data and the predictions of the wake models using the estimated k^* and ϵ at $z/\delta = 0.56$ along the streamwise direction from (a-d): $x'/D = 4$ to $x'/D = 7$. Porous disc is located between: $-0.5 \leq z'/D \leq 0.5$

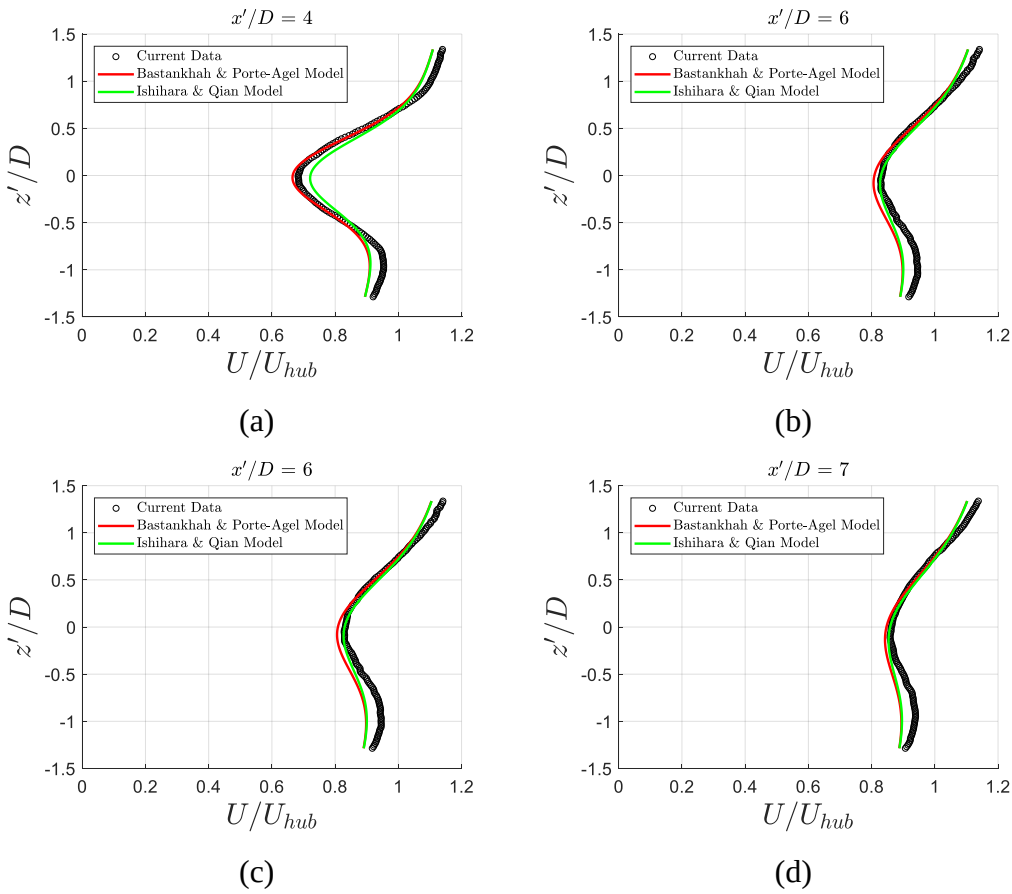

Figure 6.18 Comparison between the experimental data and the predictions of the wake models using the estimated k^* and ϵ at $z/\delta = 0.32$ along the streamwise direction from (a-d): $x'/D = 4$ to $x'/D = 7$. Porous disc is located between: $-0.5 \leq z'/D \leq 0.5$

6.5 Concluding Remarks

The wake velocity profiles of the porous disc with radially non-uniform porosity are compared against model predictions from Bastankhah and Porté-Agel wake model and Ishihara and Qian wake model as it is successively immersed in a boundary layer inflow. The comparison illustrates the deviations between the porous disc wake velocity fields and the predictions of the wake models due to different wake growth rate and initial wake width estimations. The results show that the wake spreading rates of porous discs are significantly different than field turbines as well as the ones predicted by the wake models.

CHAPTER 7

CONCLUSIONS AND FUTURE WORKS

Results of an experimental study, which aims to investigate the effects of inflow boundary layer on the wake characteristics, in terms of mean flow, turbulence, wake scaling, and proper orthogonal decomposition downstream of an isolated porous disc with radially non-uniform porosity, are presented. The generated boundary layer inside the wind tunnel is representative of a neutral atmospheric boundary layer over a flat terrain. 2D2C PIV measurements are performed for different inflow conditions in the wake of the porous disc covering a region up to 7.5 diameters downstream position. In addition, comparisons of the porous disc velocity fields against the predictions of two Gaussian-based analytical wake models are conducted to highlight the differences in the spreading rate characteristics in terms of the wake growth rate and initial wake width parameters.

The main conclusions are listed below:

- Results show that otherwise symmetrical wake velocity profiles that exist outside the boundary layer get skewed and sheared around the disc centerline in the boundary layer due to the inflow wind shear.
- The turbulent kinetic energy, its production and Reynolds shear stress levels get asymmetrical around the centerline of the disc. Due to higher mean velocity gradients on the upper half of the wake, which is due to the skewed mean velocity profiles, and high Reynolds shear stress levels at that location, increased production of turbulent kinetic energy is observed above the disc centerline.
- Due to the inflow shear, the wake centerline gets shifted downwards (i.e., towards the wind tunnel wall), opposite to the observations of real wind turbine wakes in the literature where the wake actually lifts up.

- The asymmetrical and skewed velocity profiles both in the streamwise and the cross-stream directions (i.e., along the boundary layer) can be collapsed onto a single function by using the proper wake scaling parameters based on the ratio of local strain to average strain in the velocity profile calculated separately for either side of the wake. The streamwise variations of these scaling parameters also collapse for different positions within the boundary layer, except for the velocity scale $U_\beta - U_0$ for the lower side of the wake, where the inflow dependent variations are observed.
- POD analysis reveals the differences in the flow structure when the disc is at different positions in the boundary layer. The turbulent kinetic energy contribution is the largest from the first mode. The first 15 modes constitute around 57% of the energy, which means the flow field can be reconstructed by focusing on the first few modes.
- The proposed method to generate asymmetric wake velocity profiles could be used as an extension to the wake models to predict the wakes of real wind turbines.
- The predictions of the wake models improve significantly when the estimated values of wake growth rate and initial wake width are used in the models instead of proposed equations especially at low ambient turbulence levels.
- The estimation of the wake growth rate shows that porous discs have generally higher wake growth rate than real wind turbines as well as the ones predicted by the wake models. The growth rate trend for the porous disc seems to follow an increasing variation that seems to be not linear with ambient turbulence intensity.

Future research will consider investigating the effects of ambient turbulence intensity without inflow shear on the wake growth rate variation of a porous disc and a model wind turbine of similar thrust coefficient to better quantify the growth rate in terms ambient turbulence, shear generated turbulence and mechanical turbulence.

REFERENCES

[1] Vermeer, L. J., Sorensen, J. N., and Crespo, A. 2003. Wind turbine wake aerodynamics. Progress in Aerospace Sciences, 39. 467-510. https://doi.org/10.1016/S0376-0421(03)00078-2.

[2] European Academy of Wind Energy, 2016. Long-term research challenges in wind energy-a research agenda by the European Academy of Wind Energy.

[3] Barthelmie, R. J., Courtney, M. S., Hojstrup, J., and Larsen, S. E. 1996. Meteorological aspects of offshore wind energy: observations from the Vindeby wind farm. Journal of Wind Engineering and Industrial Aerodynamics, 62. 191-211. https://doi.org/10.1016/S0167-6105(96)00077-3.

[4] Barthelmie, R. J., Hansen, O., Enevoldsen, K., Højstrup, J., Larsen, S., Frandsen, S., Pryor, S., Motta, M., and Sanderhoff, P. 2005. Ten years of meteorological measurements for offshore wind farms. Journal of Solar Energy Engineering, 127. 170-176. https://doi.org/10.1115/1.1850489.

[5] Barthelmie, R. J., Folkerts, L., Larsen, G. C., Rados, K., Pryor, S. C., Frandsen, S. T., Lange, B., and Schepers, G. 2006. Comparison of wake model simulations with offshore wind turbine wake profiles measured by Sodar. Journal of Atmospheric and Oceanic Technology, 23. 888-901. https://doi.org/10.1175/JTECH1886.1.

[6] Jensen, L. E., Mørch, C., Sørensen, P. B., and Svendsen, K. V. H. 2004. Wake measurements from the Horns Rev wind farm. European Wind Energy, 22-25 November, London, UK Proceedings CD.

[7] Christiansen, M. B., and Hasager, C. B. 2005. Wake effects of large offshore wind farms identified from satellite SAR. Remote Sensing of Environment, 98. 251-268. https://doi.org/10.1016/j.rse.2005.07.009.

[8] Hasager, C. B., Nielsen, M., Astrup, P., Barthelmie, R. J., Dellwik, E., Jensen, N. O., Jørgensen, B. H., Pryor, S. C., and Rathmann, O. 2005. Offshore wind

resource estimation from satellite SAR wind field maps. Wind Energy, 8. 403-419. https://doi.org/10.1002/we.150.

[9] Méchali, M., Barthelmie, R. J., Frandsen, S., Jensen, L., and Réthoré, P-E. 2006. Wake effects at Horns Rev and their influence on energy production. In Proceedings of the European Wind Energy Conference.

[10] Frandsen, S., Barthelmie, R., Pryor, S., Rathmann, O., Larsen, S., Højstrup, J., and Thøgersen, M. 2006. Analytical modelling of wind speed deficit in large offshore wind farms. Wind Energy, 9. 39-53. https://doi.org/10.1002/we.189.

[11] Barthelmie, R. J., Pryor, S. C., Frandsen, S. T., Hansen, K. S., Schepers, J. G., Rados, K., Schlez, W., Neubert, A., Jensen, L. E., and Neckelmann, S. 2010. Quantifying the impact of wind turbine wakes on power output at offshore wind farms. Journal of Atmospheric and Oceanic Technology, 27. 1302-1317. https://doi.org/10.1175/2010JTECHA1398.1.

[12] Barthelmie, R. J., Hansen, K. S., and Pryor, S. C. 2013. Meteorological controls on wind turbine wakes. Proceedings of the IEEE, 101. 1010-1019.

[13] Hansen, K. S., Barthelmie, R., Jensen, L. E., and Sommer, A. 2010. Power deficits due to wind turbine wakes at Horns Rev wind farm. The science of making torque from wind, 28-30 June, Heraklion, Greece.

[14] Hansen, K. S., Barthelmie, R. J., Jensen, L. E., and Sommer, A. 2012. The impact of turbulence intensity and atmospheric stability on power deficits due to wind turbine wakes at Horns Rev wind farm. Wind Energy, 15. 183-196. https://doi.org/10.1002/we.512.

[15] Bardal, L. M., Sætran, L. R., and Wangsnessa, E. 2015. Performance test of a 3MW wind turbine-effects of shear and turbulence. Energy Procedia, 80. 83-91. https://doi.org/10.1016/j.egypro.2015.11.410.

[16] Bardal, L. M., and Sætran, L. R. 2017. Influence of turbulence intensity on wind turbine power curves. Energy Procedia, 137. 553-558. https://doi.org/10.1016/j.egypro.2017.10.384.

[17] Stival, L. J. L., Guetter, A. K., and Andrade, F. O. 2017. The impact of wind shear and turbulence intensity on wind turbine power performance. ESPAÇO ENERGIA, issue 27.

[18] Sakagami, Y., Santos, P. A., Haas, R., Passos, J. C., and Taves, F. F. 2015. Effects of turbulence, wind shear, wind veer, and atmospheric stability on power performance a case study in Brazil. In Proceedings of the EWEA Annual Event.

[19] Wharton, S., and Lundquist, J. K. 2012. Atmospheric stability affects wind turbine power collection. Environmental Research Letters, 7. 014005. https://doi.org/10.1088/1748-9326/7/1/014005.

[20] Kumer, V-M., Reuder, J., and Oftedal Eikill, R. 2017. Characterization of turbulence in wind turbine wakes under different stability conditions from Static Doppler LiDAR Measurements. Remote Sensing, 9. 242. https://doi.org/10.3390/rs 9030242.

[21] Westerhellweg, A., Cañadillas, B., Kinder, F., and Neumann, T. 2012. Wake measurements at alpha ventus-dependency on stability and turbulence intensity. Journal of Physics: Conference Series, 555. 012106. https://doi.org/10.1088/1742-6596/555/1/012106.

[22] Barthelmie, R. J., Badger, J., Pryor, S. C., Hasager, C. B., Christiansen, M. B., and Jørgensen B. H. 2007. Offshore coastal wind speed gradients: issues for the design and development of large offshore windfarms. Wind Engineering, 31. 369-382. https://doi.org/10.1260/030952407784079762.

[23] Barthelmie, R. J., Frandsen, S. T., Nielsen, M. N., Pryor, S. C., Rethore, P.-E., and Jørgensen, H. E. 2007. Modelling and measurements of power losses and turbulence intensity in wind turbine wakes at Middelgrunden offshore wind farm. Wind Energy, 10. 517-528. https://doi.org/10.1002/we.238.

[24] Barthelmie, R. J., Frandsen, S. T., Rethore, P. -E., and Jensen, L. 2007. Analysis of atmospheric impacts on the development of wind turbine wakes at the Nysted wind farm. Proceeding of the European Offshore Wind Conference, Berlin, Germany, European Wind Energy Association, PO.36.

[25] Barthelmie, R. J., Hansen, K., Frandsen, S. T., Rathmann, O., Schepers, J. G., Schlez, W., Phillips, J., Rados, K., Zervos, A., Politis, E. S., and Chaviaropoulos P. K. 2009. Modelling and measuring flow and wind turbine wakes in large wind farms offshore. Wind Energy, 12. 431-444. https://doi.org/10.1002/we.348.

[26] Troen, I., and Petersen, E. L. 1989. European Wind Atlas. Risø National Laboratory: Roskilde, Denmark, 656.

[27] Mortensen, N. G., Heathfield, D. N., Myllerup, L., Landberg, L., and Rathmann, O. 2005. Wind atlas analysis and application program: WAsP 8 help facility.

[28] Frandsen, S. T., and Madsen, P. H. 2003. Spatially average of turbulence intensity inside large wind turbine arrays. In Offshore wind energy in Mediterranean and other European seas. Resources, technology, applications (OWEMES 2003), European Seminar, University of Naples, 10-12 April 2003, 97-106.

[29] Ainslie, J. F. 1988. Calculating the flow field in the wake of wind turbines. Journal of Wind Engineering and Industrial Aerodynamics, 27. 213-224. https://doi.org/10.1016/0167-6105(88)90037-2.

[30] Schepers, J. G. 2003. ENDOW. Validation and improvement of ECN's wake model. ECN-C-03-034, Netherlands.

[31] Crespo, A., Hernandez, J., Fraga, E., and Andreu, C. 1988. Experimental validation of the UPM computer code to calculate wind turbine wakes and comparison with other models. Journal of Wind Engineering and Industrial Aerodynamics, 27. 77-88. https://doi.org/10.1016/0167-6105(88)90025-6.

[32] Dekker, J. W. M., and Pierik, J. T. G. 1999. European wind turbine standards II. ECN Solar and Wind Energy, ECN-C–99-073, Petten, The Netherlands.

[33] Rados, K., Larsen, G., Barthelmie, R., Schelz, W., Lange, B., Schepers, G., Hegberg, T., and Magnusson, M. 2001. Comparison of wake models with data for offshore windfarms. Wind Engineering, 25. 271-280. https://doi.org/10.1260/030952401760177846.

[34] Magnusson, M., Rados, K. G., and Voutsinas, S. G. 1996. A study of the flow downstream of a wind turbine using measurements and simulations. Wind Engineering, 20. 389-403. https://www.jstor.org/stable/43749808.

[35] Riedel, V., and Neumann, T. 2007. RANS-modelling of wind flow through large offshore wind farm. European Wind Energy Conference and Exhibition, 7-10 May, Milan, Italy.

[36] Schlez, W., and Neubert, A. 2009. New developments in large wind farm modelling. European Wind Energy Conference and Exhibition.

[37] Frandsen, S. T., Jørgensen, H. E., Barthelmie, R. J., Rathmann, O., Badger, J., Hansen, K., Ott, S., Rethore, P.-E., Larsen, S. E., and Jensen, L. E. 2009. The making of a second-generation wind farm efficiency model complex. Wind Energy, 12. 445-458. https://doi.org/10.1002/we.351.

[38] Cleve, J., Greiner, M., Enevoldsen, P., Birkemose, B., and Jensen, L., 2009. Model-based analysis of wake-flow data in the Nysted offshore wind farm. Wind Energy, 12. 125-135. https://doi.org/10.1002/we.314.

[39] Jensen, N.O. 1983. A note on wind generator interaction. Technical Report Risø-M-2411, Risø National Laboratory, Roskilde, Denmark.

[40] Katic, I., Højstrup, J., Jensen, N. O. 1987. A simple model for cluster efficiency. In Palz, W., Sesto, E., editors, European Wind Energy Association (EWEC'86) Conference and Exhibition, 7-9 October, 1986, Rome, Italy, 1. 407-410.

[41] Emeis, S. 2010. A simple analytical wind park model considering atmospheric stability. Wind Energy, 13. 459-469. https://doi.org/10.1002/we.367.

[42] Emeis, S., and Frandsen, S. 1993. Reduction of horizontal wind speed in a boundary layer with obstacles. Boundary Layer Meteorology, 64. 297-305. https://doi.org/10.1007/BF00708968.

[43] Gaumond, M., Réthoré, P.-E., Bechmann, A., Ott, S., Larsen, G. C., Peña, A., and Hansen, K. S. 2012. Benchmarking of wind turbine wake models in large offshore windfarms. Poster session presented at The science of Making Torque from Wind, Oldenburg, Germany.

[44] Gaumond, M., Réthoré, P.-E., Ott, S., Peña, A., Bechmann, A., and Hansen, K.S. 2014. Evaluation of the wind direction uncertainty and its impact on wake modeling at the Horns Rev offshore wind farm. Wind Energy, 14. 1169-1178. https://doi.org/10.1002/we.1625.

[45] Crespo, A., Hernandez, J., and Frandsen, S. T. 1999. Survey of modelling methods for wind turbine wakes and wind farms. Wind Energy, 2. 1-24. https://doi.org/10.1002/(SICI)1099-1824(199901/03)2:1<1::AID WE16> 3.0.CO;2-7

[46] Barthelmie, R. J., and Jensen, L. E. 2010. Evaluation of wind farm efficiency and wind turbine wakes at the Nysted offshore wind farm. Wind Energy, 13. 576-586. https://doi.org/10.1002/we.408.

[47] Mortensen, N. G., Landberg, L., Troen, I., and Petersen, E. L. 1993. Getting started. Vol. 1, Wind Analysis and Application Program (WASP), User's Guide. Risø-I-666 (EN), Risoe National Laboratory, Roskilde, Denmark.

[48] Thøgersen, M.L. 2005. Wind PRO/PARK: introduction to wind turbine wake modelling and wake generated turbulence. Technical report, Niels Jernes Vej 10, DK- 9220 Aalborg, Denmark: EMD International A/S.

[49] Crasto, G., Gravdahl, A. R., Castellani, F., and Piccioni, E. 2012. Wake modeling with the actuator disc concept. Energy Procedia, 24. 385-392. https://doi.org/10.1016/j.egypro.2012.06.122.

[50] GH WindFarmer theory manual. Garrad Hassan and Partners Ltd., (2009).

[51] version 1.3 ed., Openwind theoretical basis and validation. AWS Truepower, LCC, (2010).

[52] Larsen, G. C. 1988. A simple wake calculation procedure. Tech note Risø-M-2760. Denmark: Risø National Laboratory.

[53] Bastankhah, M., and Porté-Agel, F. 2014. A new analytical model for wind-turbine wakes. Renewable Energy, 70. 116-123. https://doi.org/10.1016/j.renene.2014.01. 002.

[54] Porté-Agel, F., Bastankhah, M., and Shamsoddin, S. 2020. Wind-turbine and wind-farm flows: a review. Boundary-Layer Meteorology, 174. 1-59. https://doi.org/10.1007/s10546-019-00473-0.

[55] Chamorro, L. P., and Porté-Agel, F. 2009. A wind-tunnel investigation of wind-turbine wakes: boundary-layer turbulence effects. Boundary-Layer Meteorology, 132. 129-149. https://doi.org/10. 1007/s10546-009-9380-8.

[56] Chamorro, L. P., and Porté-Agel, F. 2010. Effects of thermal stability and incoming boundary-layer flow characteristics on wind-turbine wakes: a wind-tunnel study. Boundary-Layer Meteorology, 136. 515-533. https://doi.org/10.1007/s10546-010-9512-1.

[57] Markfort, C. D., Zhang, W., and Porté-Agel, F. 2012. Turbulent flow and scalar transport through and over aligned and staggered wind farms. Journal of Turbulence, 13. https://doi.org/10.1080/14685248.2012.709635.

[58] Zhang, W., Markfort, C. D., and Porté-Agel, F. 2013. Wind-turbine wakes in a convective boundary layer: a wind-tunnel study. Boundary-Layer Meteorology, 146. 161-179. https://doi.org/10. 1007/s10546-012-9751-4.

[59] Medici, D., and Alfredsson, P. H. 2006. Measurement on a wind turbine wake: 3D effects and bluff body vortex shedding. Wind Energy, 9. 219-236. https://doi.org/10.1002/we.156.

[60] Wu, Y. T., and Porté-Agel, F. 2012. Atmospheric turbulence effects on wind-turbine wakes: an LES study. Energies, 5. 5340-5362. https://doi.org/10.3390/en5125340.

[61] Nygaard, N., Jensen, L. E., Downey, R., and Méchali, M. 2013. Construction and validation of a new offshore wake model. In: ICOWES conference, Lyngby 26-37.

[62] Ishihara, T., Yamaguchi, A., and Fujino, Y. 2004. Development of a new wake model based on a wind tunnel experiment. Technical report, Global Wind, Technical Report, http://windeng. tu-tokyo. ac. jp/ishihara/-posters/2004_gwp_poster. pdf, (2004).

[63] Gao, X., Yang, H., and Lu, L. 2016. Optimization of wind turbine layout position in a wind farm using a newly-developed two-dimensional wake model. Applied Energy, 174. 192-200. https://doi.org/10.1016/j.apenergy.2016.04.098.

[64] Ishihara, T., and Qian, G. W. 2018. A new Gaussian-based analytical wake model for wind turbines considering ambient turbulence intensities and thrust coefficient effects. Journal of Wind Engineering and Industrial Aerodynamics, 177. 275-292. https://doi.org/10.1016/j.jweia. 2018.04.010.

[65] Tian, L., Zhu, W., Shen, W., Zhao, N., and Shen, Z. 2015. Development and validation of a new two-dimensional wake model for wind turbine wakes. Journal of Wind Engineering and Industrial Aerodynamics, 137. 90-99. https://doi.org/10.1016/j.jweia.2014.12.001.

[66] Zhang, Z., Huang, P., and Sun, H. 2020. A novel analytical wake model with a cosine-shaped velocity deficit. Energies, 13. 3353. https://doi.org/10.3390/en13133353.

[67] Sorensen, P., and Nielsen, T. 2006. Recalibrating wind turbine wake model parameters-validating the wake model performance for large offshore wind farms. In: European Wind Energy Association (EWEA) conference and exhibition.

[68] Shakoor, R., Hassan, M. Y., Raheem, A., and Wu, Y. K. 2016. Wake effect modeling: a review of wind farm layout optimization using Jensen's model. Renewable and Sustainable Energy Reviews, 58. 1048-1059. https://doi.org/10.1016/j.rser.2015.12.229.

[69] Göçmen, T., van der Laan, P., Réthoré, P. E., Diaz, A. P., Larsen, G. C., and Ott, S. 2016. Wind turbine wake models developed at the Technical University of Denmark: a review. Renewable and Sustainable Energy Reviews, 60. 752-769. https://doi.org/10.1016/j.rser.2016.01.113.

[70] Archer, C. L., Vasel-Be-Hagh, A., Yan, C., Wu, S., Pan, Y., Brodie, J.F., and Maguire, A. E. 2018. Review and evaluation of wake loss models for wind energy applications. Applied Energy, 226. 1187-1207. https://doi.org/10.1016/j.apenergy.2018.05.085.

[71] Renkema, D. J. 2007. Validation of wind turbine wake models. MSc. Thesis. TU Delft.

[72] Polster, M. F. 2017. Comprehensive comparison of analytical wind turbine wake models with wind tunnel measurements and wake model application on performance modelling of a downstream turbine. MSc. Thesis. NTNU.

[73] Stein, V. P., and Kaltenbach, H. J. 2018. Influence of ground roughness on the wake of a yawed wind turbine - a comparison of wind-tunnel measurements and model predictions. Journal of Physics: Conference Series, 1037.

[74] Campagnolo, F., Molder, A., Schreiber, J., and Bottasso, C. L. 2019. Comparison of analytical wake models with wind tunnel data. Journal of Physics: Conference Series, 1256.

[75] Amiri, H., Bay, A., Aysan, M. S., Yanık, T., Yazdanpanah, M., Yığılı, I., Yağmur, A. S., Kıray, O., Kıyıcı, F., Perçin, M., and Uzol, O. 2019.

Comparison of wake models with porous disc wake profile measurements. Wind Energy Science Conference, 17-20 June, UCC, Cork, Ireland.

[76] Jimenez, A., Crespo, A., Migoya, E., and Garcia, J. 2007. Advances in large-eddy simulation of a wind turbine wake Journal of Physics: Conference Series, 75. 012041.

[77] Jimenez, A., Crespo, A., Migoya, E., and Garcia, J. 2007. Large-eddy simulation of spectral coherence in a wind turbine wake. Environmental Research Letters, 3. 015004.

[78] Cabezon, D., Sanz, J., Marti, I., and Crespo, A. 2009. CFD modelling of the interaction between the surface boundary layer and rotor wake. In Proceeding of the European Wind Energy Conference, Marseille, France.

[79] Calaf, M., Meneveau, C., and Meyers, J. 2010. Large eddy simulation study of fully developed wind-turbine array boundary layers. Physics of Fluids, 22. 015110. https://doi.org/10.1063/1.3291077.

[80] Wu, Y. T., and Porté-Agel, F. 2011. Large-eddy simulation of wind-turbine wakes: evaluation of turbine parametrisations. Boundary-Layer Meteorology, 138. 345-366. https://doi.org/10.1007/s10546-010-9569-x.

[81] Olivares-Espinosa, H., Breton, S. -P., Nilsson, K., Masson, C., Dufresne, L., and Ivanell, S. 2018. Assessment of turbulence modelling in the wake of an actuator disk with a decaying turbulence inflow. Applied Sciences, 8. 1530. https://doi.org/10.3390/app8091530.

[82] Troldborg, N., Sorensen, J. N., and Mikkelsen, R. 2010. Numerical simulations of wake characteristics of a wind turbine in uniform inflow. Wind Energy, 13. 86-99. https://doi.org/10.1002/we.345.

[83] Martínez-Tossas, L. A., Churchfield, M. J., and Leonardi, S. 2015. Large eddy simulations of the flow past wind turbines: actuator line and disk modeling. Wind Energy, 18. 1047-1060. https://doi.org/10.1002/we.1747.

[84] Sørensen, J. N., Shen, W. Z., 2002. Numerical modeling of wind turbine wakes. Journal of Fluids Engineering, 124. 393-399. https://doi.org/10.1115/1.1471361.

[85] Sørensen, J. N., Mikkelsen, R. F., Henningson, D. S., Ivanell, S., Sarmast, S., and Andersen, S. J. 2015. Simulation of wind turbine wakes using the

actuator line technique. Philosophical Transactions of the Royal Society A, 373. 20140071. https://doi.org/10.1098/rsta.2014.0071.

[86] Porté-Agel, F., Wu, Y. T., Lu, H., and Conzemius, R. J. 2011. Large-eddy simulation of atmospheric boundary layer flow through wind turbines and wind farms. Journal of Wind Engineering and Industrial Aerodynamics, 99. 154-168. https://doi.org/10.1016/j.jweia.2011.01.011.

[87] Takanori, U. 2020. Effects of Inflow Shear on Wake Characteristics of Wind-Turbines over Flat Terrain. Energies, 13. 3745. https://doi.org/10.3390/en13143745.

[88] Sørensen, N. N., Michelsen, J. A., and Schreck, S. 2002. Navier–Stokes predictions of the NREL phase VI rotor in the NASA Ames 80 ft x 120 ft wind tunnel. Wind Energy, 5. 151-169. https://doi.org/10.1002/we.64.

[89] Bechmann, A., and Sørensen, N. N. 2009. CFD simulation of the MEXICO rotor wake. In European Wind Energy Conference and Exhibition, Marseille, France.

[90] Zhou, N., Chen, J., Adams, D. E., and Fleeter, S. 2015. Influence of inflow conditions on turbine loading and wake structures predicted by large eddy simulations using exact geometry. Wind Energy, 19. 803-824. https://doi.org/10.1002/we.1866.

[91] Sezer-Uzol, N., Gupta, A., and Long, L. N., 2007. 3-D time-accurate inviscid and viscous CFD simulations of wind turbine rotor flow fields. In Parallel CFD, International Conference on Parallel Computational Fluid Dynamics, Antalya, Turkey.

[92] Sanderse, B., Pijl, S. P. v. d., and Koren, B. 2011. Review of CFD for wind turbine wake aerodynamics. Wind Energy, 14. 799-819. https://doi.org/10.1002/we.458.

[93] Troldborg, N., Sørensen, J. N., and Mikkelsen, R. 2007. Actuator line simulation of wake of wind turbine operating in turbulent inflow. Journal of Physics: Conference Series, 75. 012063.

[94] Troldborg, N., Sørensen, J. N., Norkaer, J., Mikkelsen, R., and Flemming, R. 2009. Actuator line modeling of wind turbine wakes. DTU Report.

[95] Troldborg, N., Larsen, G. C., Madsen, H. A., Hansen, K. S., Sørensen, J. N., and Mikkelsen, R. 2011. Numerical simulations of wake interaction between two wind turbines at various inflow conditions. Wind Energy, 14. 859-876. https://doi.org/10.1002/we.433.

[96] Churchfield, M. J., Lee, S., Michalakes, J., and Moriarty, P. J. 2012. A numerical study of the effects of atmospheric and wake turbulence on wind turbine dynamics. Journal of Turbulence, 13. https://doi.org/10.1080/14685248.2012.668191.

[97] Wu, Y. T., and Porté-Agel, F. 2011. Large-eddy simulation of wind-turbine wakes: evaluation of turbine parametrisations. Boundary-Layer Meteorology, 138. 345-366. https://doi.org/10.1007/s10546-010-9569-x.

[98] Wu, Y. T., and Porté-Agel, F. 2012. Atmospheric turbulence effects on wind-turbine wakes: an LES study. Energies, 5. 5340-5362. https://doi.org/10.3390/en5125340.

[99] Porté-Agel, F., Lu, H., and Wu, Y-T. 2014. Interaction between large wind farms and the atmospheric boundary layer. Procedia IUTAM, 10. 307-318. https://doi.org/10.1016/j.piutam.2014.01.026.

[100] Wu, Y. T., and Porté-Agel, F. 2013. Modeling turbine wakes and power losses within the Horns Rev offshore wind farm using large-eddy simulation. EGU General Assembly, 7-12 April, Vienna, Austria, EGU2013-9626.

[101] Wu, Y. T., and Porté-Agel, F., 2014. Simulation of turbulent flow inside and above wind farms: model validation and layout effects. Boundary-Layer Meteorology, 146. 181-205. https://doi.org/10.1007/s10546-012-9757-y.

[102] Wu, Y. T., and Porté-Agel, F. 2014. Effects of wind direction and wind farm layout on turbine wakes and power losses in wind farms: an LES study. European Geosciences Union General Assembly, April 27 - May 02, Vienna, Austria.

[103] Lu, H., and Porté-Agel, F. 2011. Large-eddy simulation of a very large wind farm in a stable atmospheric boundary layer. Physics of Fluid, 23. 065101. https://doi.org/10.1063/1.3589857.

[104] Ivanell, S., Mikkelsen, R. F., Sørensen, J. N., Hansen, K. S., and Henningson, D. 2010. The impact of wind direction in atmospheric boundary layer on

interacting wakes at Horns Rev wind farm. The science of making torque from wind, 28-30 Jun, Heraklion, Greece, 407-426.

[105] Politis, E. S., Prospathopoulos, J., Cabezon, D., Hansen, K. S., Chaviaropoulos, P. K., and Barthelmie, R. J. 2012. Modeling wake effects in large wind farms in complex terrain: the problem, the methods and the issues. Wind Energy, 15. 161-182. https://doi.org/10.1002/we.481.

[106] Wang, J., Foley, S., Nanos, E. M., Yu, T., Campagnolo, F., Bottasso, C. L., Zanotti, A., and Croce, A. 2017. Numerical and experimental study of wake redirection techniques in a boundary layer wind tunnel. Journal of Physics: Conference Series, 854. 012048.

[107] Dörenkämper, M., Witha, B., Steinfeld, G., Heinemann, D., and Kühn, M. 2015. The impact of stable atmospheric boundary layers on wind-turbine wakes within offshore wind farms. Journal of Wind Engineering and Industrial Aerodynamics, 144. 146-153. https://doi.org/10.1016/j.jweia.2014.12.011.

[108] Schulz, C., Klein, L., Weihing, P., and Lutz, T. 2016. Investigations into the interaction of a wind turbine with atmospheric turbulence in complex terrain. Journal of Physics: Conference Series, 753. 0 32016.

[109] Sicot, C., Devinant, P., Laverne, T., Loyer, S., and Hureau, J. 2006. Experimental study of the effect of turbulence on horizontal axis wind turbine aerodynamics. Wind Energy, 9. 361-370. https://doi.org/10.1002/we.184.

[110] Chamorro, L. P., and Porté-Agel, F. 2009. A wind-tunnel investigation of wind-turbine wakes: boundary-layer turbulence effects. Boundary-Layer Meteorology, 132. 129-149. https://doi.org/10. 1007/s10546-009-9380-8.

[111] Chamorro, L. P., and Porté-Agel, F. 2010. Effects of thermal stability and incoming boundary-layer flow characteristics on wind-turbine wakes: a wind-tunnel study. Boundary-Layer Meteorology, 136. 515-533. https://doi.org/10.1007/s10546-010-9512-1.

[112] Zhang, W., Markfort, C. D., and Porté-Agel, F. 2013. Wind-turbine wakes in a convective boundary layer: a wind-tunnel study. Boundary-Layer Meteorology, 146. 161-179. https://doi.org/10. 1007/s10546-012-9751-4.

[113] Chamorro, L. P., and Porté-Agel, F. 2011. Turbulent flow inside and above a wind farm: a wind-tunnel study. Energies, 4. 1916-1936. https://doi.org/10.3390/en4111916.

[114] Chamorro, L., Arndt, R., and Sotiropoulos, F. 2011. Turbulent flow properties around a staggered wind farm. Boundary-Layer Meteorology, 141. 349-367. https://doi.org/10.1007/s10546-011-9649-6.

[115] Cal, R. B., Lebrón, J., Castillo, L., Kang, H. S., and Meneveau, C. 2010. Experimental study of the horizontally averaged flow structure in a model wind-turbine array boundary layer. Journal of Renewable and Sustainable Energy, 2. 013106. https://doi.org/10.1063/1.3289735.

[116] Maeda, T., Kamada, Y., Murata, J., Yonekura, S., Mizokoshi, T., and Kogaki, T. 2010. Effects of turbulence intensity on power output of wind turbine operating in wake. Renewable Energy Proceedings, 27 June - 2 July, Pacifico Yokohama, Yokohama, Japan.

[117] Maeda, T., Kamada, Y., Murata, J., Yonekura, S., Ito, T., Okawa, A., and Kogaki, T. 2011. Wind tunnel study on wind and turbulence intensity profiles in wind turbine wake. Journal of Thermal Science, 20. 127-132. https://doi.org/10.1007/s11630-011-0446-9.

[118] Mahmoodilari, M. 2012. The effect of turbulent flow on wind turbine loading and performance. PhD Thesis, University of Manchester.

[119] Hu, H., Yang, Z., and Sarkar, P. 2012. Dynamic wind loads and wake characteristics of a wind turbine model in an atmospheric boundary layer wind. Experiments in Fluids, 52. 1277-1294. https://doi.org/10.1007/s00348-011-1253-5.

[120] Zhang, W., Markfort, C. D., and Porté-Agel, F. 2012. Near-wake flow structure downwind of a wind turbine in a turbulent boundary layer. Experiments in Fluids, 52. 1219-1235. https://doi.org/10.1007/s00348-011-1250-8.

[121] Ozbay, A. 2012. Experimental investigations on the wake interferences of multiple wind turbines. MSc. Thesis, Iowa State University.

[122] Ozbay, A. 2014. An experimental investigation on wind turbine aeromechanics and wake interferences among multiple wind turbines. PhD Thesis, Iowa State University.

[123] Tian, W., Yuan, W., Ozbay, A., and Hu, H. 2013a. An experimental study on the performances of wind turbines over complex terrains. 51st AIAA Aerospace Sciences Meeting including the New Horizons Forum and Aerospace Exposition, 07-10 January, Grapevine (Dallas/Ft. Worth Region), Texas, AIAA-2013-0612. https://doi.org/10.2514/6.2013-612.

[124] Tian, W., Ozbay, A., Yuan, W., and Hu, H. 2013b. An experimental investigation on the performances of wind turbines sited over a hilly terrain. 31st AIAA Applied Aerodynamics Conference, 24-27 June, San Diago, CA, AIAA 2013-2804. https://doi.org/10.2514/6.2013-2804.

[125] Tian, W., Ozbay, A., and Hu, H. 2014. Effects of incoming surface wind conditions on the wake characteristics and dynamic wind loads acting on a wind turbine model. Physics of Fluids, 26. 125108. https://doi.org/10.1063/1.4904375.

[126] Mikkelsen, K., 2013. Effect of free stream turbulence on wind turbine performance. MSc. Thesis, NTNU University.

[127] Al-Abadi, A. 2014. Novel strategies for aerodynamic performance improvement of wind turbines in turbulent flow. Dr.-Ing., Der Technischen Fakultat der Friedrich-Alexander-Universitat Erlangen-Nurnberg.

[128] Al-Abadi, A., Kim, Y. J., Ertunc, O., and Delgado, A. 2016. Turbulence impact on wind turbines: experimental investigations on a wind turbine model. Journal of Physics: Conference Series, 753. 032046.

[129] Bastankhah, M. 2017. Interaction of atmospheric boundary layer flow with wind turbines: theoretical and experimental studies. PhD Thesis, EPFL.

[130] Bastankhah, M., and Porté-Agel, F. 2015. A wind tunnel investigation of wind turbine wakes in yawed conditions. Journal of Physics: Conference Series 625. 012014.

[131] Bastankhah, M., and Porté-Agel, F. 2017. A new miniature wind turbine for wind tunnel experiments. Part II: wake structure and flow dynamics. Energies, 10. 923. https://doi.org/10.3390/en10070923.

[132] Bastankhah, M., and Porté-Agel, F. 2017. Wind tunnel study of the wind turbine interaction with a boundary layer flow: upwind region, turbine

performance, and wake region. Physics of Fluids, 29. 065105. https://doi.org/10.1063/1.4984078.

[133] Bartl, J., and Sætran, L., 2017. Blind test comparison of the performance and wake flow between two in-line wind turbines exposed to different turbulent inflow conditions, Wind Energy Sciences, 2. 55-76. https://doi.org/10.5194/wes-2-55-2017.

[134] Bartl, J., Mühle, F., Schottler, J., Sætran, L., Peinke, J., Adaramola, M., and Hölling, M. 2018. Wind tunnel experiments on wind turbine wakes in yaw: effects of inflow turbulence and shear. Wind Energy Sciences, 3. 329-343. https://doi.org/10.5194/wes-3-329-2018.

[135] Schottler, J., Bartl, J., Mühle, F., Sætran, L., Peinke, J., and Hölling, M. 2018. Wind tunnel experiments on wind turbine wakes in yaw: redefining the wake width. Wind Energy Sciences, 3. 257-273. https://doi.org/10.5194/wes-3-257-2018.

[136] Jin, Y., Liu, H., Aggarwal, R., Singh, A., and Chamorro, L.P. 2016. Effects of freestream turbulence in a model wind turbine wake. Energies, 9. 830. https://doi.org/10.3390/en9100830.

[137] Coudou, N., Buckingham, S., and Beeck, J. 2017. Experimental study on the wind turbine wake meandering inside a scale model wind farm placed in an atmospheric boundary layer wind tunnel. Journal of Physics: Conference Series 854. 012008.

[138] Talavera, M., and Shu, F. 2017. Experimental study of turbulence influence on wind turbine performance. Renewable Energy, 109. 363-371. https://doi.org/10.1016/j.renene.2017.03.034.

[139] Swalwell, K. E., Sheridan, J., Melbourne, W. H. 2001. The effect of turbulence intensity on stall of the NACA 0021 aerofoil. 14th Australasian Fluid Mechanics Conference Adelaide University, 10-14 December, Adelaide, Australia.

[140] Devinant, P., Laverne, T., and Hureau, J. 2002. Experimental study of wind-turbine airfoil aerodynamics in high turbulence. Journal of Wind Engineering and Industrial Aerodynamics, 90. 689-707. https://doi.org/10.1016/S0167-6105(02)00162-9.

[141] Delnero, J. S., Marañon di Leo, J., Bacchi, F. A., Colman J., and Boldes, U. 2005. Experimental determination of the influence of turbulent scale on the lift and drag coefficients of low Reynolds number airfoils. Latin American Applied Research, 35.183-188.

[142] Sicot, C., Aubrun, S., Loyer, S., and Devinant, P. 2006. Unsteady characteristics of the static stall of an airfoil subjected to free-stream turbulence level up to 16%. Experiments in Fluids, 41. 641-648. https://doi.org/10.1007/s00348-006-0187-9.

[143] Watkins, S., Ravi, S., and Loxton, B. 2010. The effect of turbulence on the aerodynamics of low Reynolds number wings. Engineering Letters, 18, EL-18-3-09.

[144] Torres-Nieves, S., Maldonado, V., Castillo, L., Meneveau, C., and Kang, H. S. 2011. The role of large scales of turbulence in wind turbine blades at various angles of attack. 6th AIAA Theoretical Fluid Mechanics Conference, 27-30 June, Honolulu, Hawaii. https://doi.org/10.2514/6.2011-3613.

[145] Kamada, Y., Murata J., Maeda, T., Toki, T., and Tobuchi, A. 2011. Effects of turbulence intensity on dynamic characteristics of wind turbine airfoil. Journal of Fluid Science and Technology, 6. 333-341. https://doi.org/10.1299/jfst.6.333.

[146] Corten, G.P., Schaak, P., and Hegberg, T. 2004. Turbine interaction in large offshore wind farms wind tunnel measurements. ECN, Petten, ECN-C-04-048.

[147] Neff, D. E., Meroney, R. N., McCarthy, E., and Davis, E. 1990. Upstream and lateral wake effects on wind turbine performances. Journal of Wind Engineering and Industrial Aerodynamics, 36. 1405-1414. https://doi.org/10.1016/0167-6105(90)90136-Z.

[148] Vermeulen, P. E. J., and Builtjes, P. J. H. 1982. Turbulence measurements in simulated wind-turbine clusters. TNO Division of Technology for Society, 82-03003.

[149] Aubrun, S. 2005. Modelling wind turbine wakes with a porosity concept. Proceedings of the Euromech Colloqium 464b. Wind Energy, 265-270.

[150] Aubrun, S., Devinant, Ph., and Espana, G. 2007. Physical modelling of the far wake from wind turbines: application to wind turbine interactions. Proceedings of the European Wind Energy Conference. Milan, Italy.

[151] Aubrun, S., Espana, G., Loyer, S., Hayden, P., and Hancock, P.2012. Is the actuator disc concept sufficient to model the far-wake of a wind turbine? Progress in Turbulence and Wind Energy IV, SPPHY. 227-230.

[152] Aubrun, S., Loyer, S., Hancock, P. E., and Hayden, P. 2013. Wind turbine wake properties: comparison between a non-rotating simplified wind turbine model and a rotating model. Journal of Wind Engineering and Industrial Aerodynamics, 120. 1-8. https://doi.org/10.1016/j.jweia.2013.06.007.

[153] España, G., Aubrun, S., Loyer, S., and Devinant, P. 2011. Spatial study of the wake meandering using modelled wind turbines in a wind tunnel. Wind Energy, 14. 923-937. https://doi.org/10.1002/we.515.

[154] España, G., Aubrun, S., Loyer, S., and Devinant, P. 2012. Wind tunnel study of the wake meandering downstream of a modelled wind turbine as an effect of large-scale turbulent eddies. Journal of Wind Engineering and Industrial Aerodynamics, 101. 24-33. https://doi.org/10.1016/j.jweia.2011.10.011.

[155] Lignarolo, L. E. M., Ragni, D., Ferreira, C. J. S., and Bussel, G. J. W. v. 2014. Kinetic energy entrainment in wind turbine and actuator disc wakes-an experimental analysis. Journal of Physics: Conference Series, 524. 012163.

[156] Lignarolo, L. E. M., Ragni, D., Ferreira, C. J. S., and Bussel, G. J. W. v. 2016. Experimental comparison of a wind-turbine and of an actuator-disc near wake. Journal of Renewable and Sustainable Energy, 8. 023301. https://doi.org/10.1063/1.4941926.

[157] Camp, E. H., and Cal, R. B. 2016. Mean kinetic energy transport and event classification in a model wind turbine array versus an array of porous disks: energy budget and octant analysis. Phys. Rev. Fluids 1. 044404. https://doi.org/10.1103/PhysRevFluids.1.044404.

[158] Camp, E. H., and Cal, R. B. 2017. Low dimensional representations and anisotropy of a model wind turbine array versus an array of porous disks. International Conference on Future Technologies for Wind Energy, Boulder, Colorado, USA.

[159] Neunaber, I. 2019. Stochastic investigation of the evolution of small-scale turbulence in the wake of a wind turbine exposed to different inflow conditions. PhD Thesis, Carl von Ossietzky Universität Oldenburg. http://oops.uni-oldenburg.de/3852.

[160] Cuzzola, F., Leitl, B., and Schatzmann, M. 2010. Wind turbines in ABL-flow: a review on wind tunnel studies. Progress in Turbulence and Wind Energy IV: Proceedings of the iTi Conference, 239-242.

[161] Bossuyt, J. 2017. Study of wind farm ABL interaction based on wind tunnel experiments. PhD Thesis, KU Leuven.

[162] Helvig, S., Vinnes, M. K., Segalini, A., Worth, N. A., and Hearst, R. J. 2021. A comparison of lab-scale free rotating wind turbines and actuator disks. Journal of Wind Engineering and Industrial Aerodynamics, 209. 104485. https://doi.org/10.1016/j.jweia.2020.104485.

[163] Howland, M. F., Bossuyt, J., Martinez-Tossas, L. A., Meyers, J., and Meneveau, C. 2016. Wake structure in actuator disk models of wind turbines under uniform inflow conditions. Journal of Renewable and Sustainable Energy 8. 043301. https://doi.org/10.1063/1.4955091.

[164] Yu, W., Hong, V. W., Ferreira, C., and Kuik, G. A. M. v. 2017. Experimental analysis on the dynamic wake of an actuator disc undergoing transient loads. Experiments in Fluids, 58. 149. https://doi.org/10.1007/s00348-017-2432-9.

[165] Manwell, J. F., McGowan, J. G., and Rogers, A. L. 2009. Wind energy explained: theory, design and application. 2nd Edition, A John Wiley & Sons Ltd.

[166] Roisin, B. C. 2014. Environmental Fluid Mechanics. John Wiley & Sons, Inc.

[167] Burton, T., Sharpe, D., Jenkins, N., and Bossyanyi, E. 2001. Wind energy handbook. John Wiley & Sons.

[168] Counihan, J. 1975. Adiabatic atmospheric boundary layers: a review and analysis of data from the period 1880-1972. Atmospheric Environment, 9. 871-905. https://doi.org/10.1016/0004-6981(75)90088-8.

[169] ASCE-16. Minimum design loads and associated criteria for buildings and other structures. American Society of Civil Engineers.

[170] Garratt, J. R. 1992. The atmospheric boundary layer. Cambridge University Press, New York, NY.

[171] Cook, N. J. 1985. The designer's guide to wind loading of building structures. BRE, Garston, UK.

[172] Simiu E., and Scanlan, R. H. 1996. Wind effects on structures. John Wiley & Sons, Inc.

[173] Owen, P., and Zienkiewicz, H. 1957. The production of uniform shear flow in a wind tunnel. Journal of Fluid Mechanics, 2. 521-531. https://doi.org/10.1017/S0022112057000336.

[174] Armitt, J., and Counihan, J. 1967. The simulation of the atmospheric boundary layer in a wind tunnel. Atmospheric Environment, 2. 49-71. https://doi.org/10.1016/0004-6981(68)90019-X.

[175] Counihan, J. 1969a. A method of simulating a neutral atmospheric boundary layer in a wind tunnel. Paper No. 14, A.G.A.R.D. Conf: Proc. No. 48 The Aerodynamics of Atmospheric Shear Flow, Munich, Germany.

[176] Counihan, J. 1967. An improved method of simulating an atmospheric boundary layer in a wind tunnel. Atmospheric Environment, 3. 197-214. https://doi.org/10.1016/0004-6981(69)90008-0.

[177] Counihan, J. 1967. Further measurements in a simulated atmospheric boundary layer. Atmospheric Environment, 4. 259-275. https://doi.org/10.1016/0004-6981(70)90061-2.

[178] Counihan, J. 1967. Wind tunnel determination of the roughness length as a function of the fetch and the roughness density of three-dimensional roughness elements. Atmospheric Environment, 5. 637-642. https://doi.org/10.1016/0004-6981(71)90120-X.

[179] Counihan, J. 1967. Simulation of an adiabatic urban boundary layer in a wind tunnel. Atmospheric Environment, 7. 673-689. https://doi.org/10.1016/0004-6981(73)90150-9.

[180] Standen, N. M. 1972. A spire array for generating thick turbulent shear layers for natural wind simulation in wind tunnels. National Research Council Canada, Aeronautical Establishment, LTR-LA-94.

[181] Irwin, H.P.A.H. 1979. Design and use of spires for natural wind simulation. National Research Council Canada, Aeronautical Establishment, LTR-LA-233.

[182] Irwin H.P.A.H. 1981. The design of spires for wind simulation. Journal of Wind Engineering and Industrial Aerodynamics, 7. 361-366. https://doi.org/10.1016/0167-6105(81)90058-1.

[183] Peterka I. A., and Cermak, J. E. 1974. Simulation of atmospheric flows in short wind tunnel test sections. Fluid Mechanics Program Research Report, Colorado State University.

[184] Cook, N. J. 1973. On simulating the lower third of the urban adiabatic boundary layer in a wind tunnel. Atmospheric Environment, 7. 691-705. https://doi.org/10.1016/0004-6981(73)90151-0.

[185] Cook, N. J. 1975. A boundary-layer wind tunnel for building aerodynamics. Journal of Wind Engineering and Industrial Aerodynamics, 1. 3-12. https://doi.org/10.1016/0167-6105(75)90003-3.

[186] Cook, N. J. 1978. Wind-tunnel simulation of the adiabatic atmospheric boundary layer by roughness, barrier and mixing device methods. Journal of Wind Engineering and Industrial Aerodynamics, 3. 157-176. https://doi.org/10.1016/0167-6105(78)90007-7.

[187] Raine, J. K. 1974. Simulation of a neutrally stable rural atmospheric boundary layer in a wind tunnel. 5th Australasian conference on Hydraulics and Fluid Mechanics.

[188] Tieleman, T., and Reinhold, A. 1978. On the wind-tunnel simulation of the atmospheric surface layer for the study of wind loads on low-rise buildings. Journal of Wind Engineering and Industrial Aerodynamics, 3. 21-38. https://doi.org/10.1016/0167-6105(78)90026-0.

[189] Farell, C., and Iyengar, A. K. S. 1999. Experiments on the wind tunnel simulation of atmospheric boundary layers. Journal of Wind Engineering and Industrial Aerodynamics, 79. 11-35. https://doi.org/10.1016/S0167-6105(98)00117-2.

[190] Phillips, J. C., Thomas, N. H., Perkins, R. J., and Miller, P. C. 1999. Wind tunnel velocity profiles generated by differently-spaced flat plates. Journal of Wind Engineering and Industrial Aerodynamics, 80. 253-262.

[191] Wittwer, A. R., and Moller, S. V. 2000. Characteristics of the low-speed wind tunnel of the UNNE. Journal of Wind Engineering and Industrial Aerodynamics, 84. 307-320. https://doi.org/10.1016/S0167-6105(99)00110-5.

[192] Burton, W. V. 2001. Wind tunnel simulation of an atmospheric boundary layer. MSc. Thesis, Texas Tech University.

[193] Balendra, T., Shah, D. A., Tey, K. L., and Kong, S. K. 2002. Evaluation of flow characteristics in the NUS-HDB wind Tunnel. Journal of Wind Engineering and Industrial Aerodynamics, 90. 675-688. https://doi.org/10.1016/S0167-6105(01)00223-9.

[194] Lopes, M. F. P., Gomes M. G., and Ferreira, J. G. 2008. Simulation of atmospheric boundary layer for model testing in a short wind tunnel. Experimental Techniques, 32. 36-43. https://doi.org/10.1111/j.1747-1567.2007.00293.x.

. [195] Jones, E. C. 2008. Experimental simulation of atmospheric boundary layers and extreme gust events. MSc. Thesis, Iowa State University.

[196] Kozmar, H. 2008. Influence of spacing between buildings on wind characteristics above rural and suburban areas. Wind and Structures, 11. 413-426. https://doi.org/10.12989/WAS.2008.11.5.413.

[197] Kozmar, H. 2009. Natural wind simulation in the TUM boundary layer wind tunnel. EACWE 5, Florence, Italy.

[198] Kozmar, H. 2010. Scale effects in wind tunnel modeling of an urban atmospheric boundary layer. Theoretical and Applied Climatology, 100. 153-162. https://doi.org/10.1007/s00704-009-0156-3.

[199] Kozmar, H. 2010. An alternative approach to experimental simulation of wind characteristics in urban environments. Procedia Environmental Sciences, 4. 43-50. https://doi.org/10.1016/j.proenv.2011.03.006.

[200] Kozmar, H. 2011. Wind tunnel simulations of the suburban ABL and comparison with international standards. Wind and Structures, 14. 15-34. https://doi.org/10.12989/was.2011.14.1.015.

[201] Kozmar, H. 2011, Truncated vortex generators for part-depth wind-tunnel simulations of the atmospheric boundary layer flow. Journal of Wind Engineering and Industrial Aerodynamics, 99. 130-136. https://doi.org/10.1016/j.jweia.2010.11.001.

[202] Shojaee, S. M. N., Kayısoglu, B., Uzol, O., and Kurc, O. 2009. Design and analysis of passive devices for ABL simulations in a short aeronautical wind tunnel. 5th Ankara International Aerospace Conference, 17-19 August, Ankara, Turkey.

[203] Shojaee, S. M. N., Uzol, O., and Kurc, O. 2014. Atmospheric boundary layer simulation in a short wind tunnel. International Journal of Environmental Science and Technology, 11. 59-68.

[204] Marinho, L. P., Avelar, A. C., Fisch, G., Roballo, S. T, Souza, L.F., Gielow, R., and Da Mota Girardi, R. 2009. Studies using wind tunnel to simulate the ABL at the Alcantara space center. Journal of Aerospace Technology and Management.

[205] Al-Nehari, H. A., Abdel-Rahman, A. K., Nassib, A. M., and Shafey, H. M. 2010. Design and construction of a wind tunnel for environmental flow studies. Journal of Engineering Sciences, 38. 177-193.

[206] Al-Nehari, H. A., Abdel-Rahman, A. K., and Shafey, H. M. 2010. Characterization of a low-speed wind tunnel simulating urban atmospheres. Journal of Engineering Sciences, 38. 509-532.

[207] Varshney, K. 2012. Tailoring wind properties by various passive roughness elements in a boundary-layer wind tunnel. Journal of Thermal Sciences, 21. 336-341. https://doi.org/10.1007/s11630-012-0552-3.

[208] Avelar, A. C., Brasileiro, F. L. C., Marto, A. G., Marciotto, E. R., Fisch, G., and Faria, A. F. 2012. Wind tunnel simulation of the atmospheric boundary layer for study of the wind pattern at the Alcantara space center. Journal of Aerospace Technology and Management, 4. 463-473.

[209] Pires, L. B. M., de Paula, I. B., Fisch, G., Gielow, R., and da Mota Girardi, R. 2013. Simulations of the atmospheric boundary layer in a wind tunnel with short test section. Journal of Aerospace Technology and Management, 5. 305-314. http://dx.doi.org/10.5028/jatm.v5i3.190.

[210] Bai, Y. 2015. A new wind tunnel setup and evaluation of flow characteristics with and without passive devices. MSc. Thesis, University of Windsor.

[211] Hobson-Dupont, M. 2015. The development of a small scale wind tunnel simulating the atmospheric boundary layer. MSc. Thesis, San José State University.

[212] Hohman, T. C., Van Buren, T., Martinelli, L., and Smits, A. J. 2015. Generating an artificially thickened BL to simulate the neutral atmospheric boundary layer. Journal of Wind Engineering and Industrial Aerodynamics, 145. 1-16.

[213] Aldin Bin Za'aba, K., Asrar, W., and Al Dheeb, M. 2016. Generation of atmospheric boundary layer in the IIUM low speed wind tunnel. IOP Conference Series: Materials Science and Engineering, 184. 012008.

[214] De Paepe, W., Pindado, S., Bram, S., and Contino, F. 2016. Simplified elements for wind tunnel measurements with type-III-terrain atmospheric boundary layer. Measurement, 91. 590-600. https://doi.org/10.1016/j.measurement.2016.05.078.

[215] Kuznetsov, S., Ribičić, M., Pospíšil, S., Plut, M., Trush, A., and Kozmar, H. 2017. Flow and turbulence control in a boundary layer wind tunnel using passive hardware devices. Experimental Techniques, 41. 643-661. https://doi.org/10.1007/s40799-017-0196-z.

[216] Song, P. 2017. Simulation of atmospheric boundary layer in an open-loop wind tunnel using spire-roughness-element technique. MSc. Thesis, University of Windsor.

[217] Numeca CFD FINE/OPEN Theory Guide, 2010.

[218] Menter, F. R. 1994. Two-equation eddy-viscosity turbulence models for engineering applications. AIAAJ Journal, 32. 1598-1605. https://doi.org/10.2514/3.12149.

[219] Choi, Y.-H., and Merkle, C. L. 1993. The application of preconditioning in viscous flows. Journal of Computational Physics, 105. 207-223. https://doi.org/10.1006/jcph.1993.1069.

[220] Yassen, Y. El-S., and Abdelhamed, A. S. 2015. CFD modeling of the atmospheric boundary layer in short test section wind tunnel. American Journal of Aerospace Engineering, Special Issue: Hands-on Learning Technique for Multidisciplinary Engineering Education, 2. 38-46.

[221] Amerio, L. 2014. Numerical and experimental analysis of peak pressure loads on rectangular building. PhD Thesis, Politecnico Milano.

[222] Grimmond, C. S. B., and oke, T. R. 1999. Aerodynamic properties of urban areas derived from analysis of surface form. Journal of Applied Meteorology and Climatology, 38. 1261-1292. https://doi.org/10.1175/1520-0450(1999)038<1262:APOUAD>2.0.CO;2.

[223] Schlighting H. 1979. Boundary layer theory. 7th edition, Mcgraw-Hill Series in Mechanical Engineering.

[224] Lettau, H. 1969. Note on aerodynamic roughness-parameter estimation on the basis of roughness-element description. Journal of Applied Meteorology and Climatology, 8. 828-832. https://doi.org/10.1175/1520-0450(1969)008<0828:NOARPE>2.0.CO;2.

[225] Theurer, W. 1993. Dispersion of near ground emissions in complex building arrangements. PhD Thesis, IHW University of Karlsruhe, Germany.

[226] Macdonald, R., Griffiths, R., and Hall, D. 1998. An improved method for the estimation of surface roughness of obstacle arrays. Atmospheric Environment, 32. 1857-1864. https://doi.org/10.1016/S1352-2310(97)00403-2.

[227] Kutzbach, J. 1961. Investigations of the modifications of wind profiles by artificially controlled surface roughness. MSc. Thesis, University of Wisconsin, Madison.

[228] Raupach, M. R. 1994. Simplified expressions for vegetation roughness length and zero-plane displacement as functions of canopy height and area index. Boundary-Layer Meteorology, 71. 211-216. https://doi.org/10.1007/BF00709229.

[229] Bottema, M. 1995c. Parameterization of aerodynamic roughness parameters in relation with air pollutant removal efficiency of streets. WIT Transactions on Ecology and the Environment, Air Pollution Engineering and Management, 10. 235-242.

[230] Aubrun, S., Bastankhah, M., Cal, R. B., Conan, B., Hearst, R. J., Hoek, D., Hölling, M., Huang, M., Hur, C., Karlsen, B., Neunaber, I., Obligado, M., Peinke, J., Percin, M., Saetran, L., Schito, P., Schliffke, B., Sims-Williams, D., Uzol, O., Vinnes, M. K., and Zasso, A. 2019. Round-robin tests of porous disc models. Journal of Physics: Conference Series, 1256. 012004.

[231] Wallace, J. M., and Hobbs, P. V. 2006. Atmospheric science: an introductory survey. Academic Press, Cambridge.

[232] Chamorro, L. P., Arndt, R. E. A., and Sotiropoulos, F. 2012. Reynolds number dependence of turbulence statistics in the wake of wind turbines. Wind Energy, 15. 733-742. https://doi.org/10.1002/we.501.

[233] Benedict, L., and Gould, R. 1996. Towards better uncertainty estimates for turbulence statistics. Experiments in Fluids, 22. 129-136. https://doi.org/10.1007/s003480050030.

[234] Sciacchitano, A., and Wieneke, B. 2016. PIV uncertainty propagation. Measurement Science and Technology, 27. 084006.

[235] Sciacchitano, A. 2019. Uncertainty quantification in particle image velocimetry. Measurement Science and Technology, 30. 092001.

[236] Sezer-Uzol, N., and Uzol, O. 2009. Effect of steady and transient wind shear on the wake structure and performance of a horizontal axis wind turbine rotor. Proceedings of 47th AIAA Aerospace Sciences Meeting, 5-8 Jan, Orlando World Center Marriott, Orlando, Florida.

[237] Sezer-Uzol, N., and Uzol, O. 2013. Effect of steady and transient wind shear on the wake structure and performance of a horizontal axis wind turbine rotor. Wind Energy, 16. 1-17. https://doi.org/10.1002/we.514.

[238] Micallef, D., Ferreira, C. S., Sant, T., and van Bussel, G. 2010. An analytical model of wake deflection due to shear flow. 3rd EWEA Conference - Torque 2010: The Science of making Torque from Wind, 28-30 June, Heraklion, Crete, Greece.

[239] Kocer, G., Chokani, N., and Abhari, R. S. 2012. Wake structure of a 2MW wind turbine measured using an instrumented UAV. 50th AIAA Aerospace Sciences Meeting including the New Horizons Forum and Aerospace Exposition, AIAA 2012-0231, 09-12 January, Nashville, Tennessee. https://doi.org/10.2514/6.2012-231.

[240] Zendehbad, M., Chokani, N., and Abhari, R., S. 2016. Volumetric three-dimensional wind measurement using a single mobile-based LiDAR. Journal of Solar Energy Engineering, 138. 011003. https://doi.org/10.1115/1.4031946.

[241] Gad-El-Hak, M., and Corrsin, S. 1974. Measurements of the nearly isotropic turbulence behind a uniform jet grid. Journal of Fluid Mechanics, 62. 115-143.

[242] Mohamed, M. S., and Larue, J. C. 1990. The decay power law in grid-generated turbulence. Journal of Fluid Mechanics, 219. 195-214. https://doi.org/10.1017/S0022112090002919.

[243] Berkooz, G., Holmes, P., and Lumley, J. L. 1993. The proper orthogonal decomposition in the analysis of turbulent flows. Annual review of fluid mechanics, 25(1):539–575, 1993.

[244] Holmes, P., Lumley, J. L., Berkooz, G., and Rowley, C. W. 2012. Turbulence, coherent structures, dynamical systems and symmetry. Cambridge University Press, Cambridge, 2nd edition. https://doi.org/10.1017/CBO9780511622700.

[245] Lumley, J. L. 1967. The structure of inhomogeneous turbulent flows. In: Yaglom, A.M. and Tartarsky, V.I., Eds., Atmospheric Turbulence and Radio Wave Propagation, 166-177.

[246] Sirovich, L. 1987. Turbulence and the dynamics of coherent structures. Part I: coherent structures. Quarterly of Applied Mathematics, 45. 561-571. http://www.jstor.org/stable/43637457.

[247] Camp, E. H. 2018. Wind energy and wind-energy-inspired turbulent wakes: modulation of structures, mechanisms and flow regimes. PhD Thesis, Portland State University.

[248] Andersen, S. J., Sørensen, J. N., and Mikkelsen, R., 2013. Simulation of the inherent turbulence and wake interaction inside an infinitely long row of wind

turbines. Journal of Turbulence, 14. 1-24, 2013. https://doi.org/10.1080/14685248.2013.796085.

[249] Andersen, S. J., Sørensen, J. N., and Mikkelsen, R. 2014. Reduced order model of the inherent turbulence of wind turbine wakes inside an infinitely long row of turbines. Journal of Physics: Conference Series, 555. 012005.

[250] VerHulst C., and Meneveau, C. 2014. Large eddy simulation study of the kinetic energy entrainment by energetic turbulent flow structures in large wind farms. Physics of Fluids, 26. 025113. https://doi.org/10.1063/1.4865755.

[251] Bastine, D., Witha, B., Wächter, M., and Peinke, J. 2015. Towards a simplified dynamic wake model using POD analysis. Energies, 8. 895-920. https://doi.org/10.3390/en8020895.

[252] Hamilton, N., Tutkun, M., and Cal, R. B. 2016. Low-order representations of the canonical wind turbine array boundary layer via double proper orthogonal decomposition. Physics of Fluids, 28. 025103. https://doi.org/10.1063/1.4940659.

[253] Camp, E. H., and Cal, R. B. 2019. Low-dimensional representations and anisotropy of model rotor versus porous disk wind turbine arrays. Physical Review Fluids, 4. 024610. https://doi.org/10.1103/PhysRevFluids.4.024610.

[254] Aloui, F., Kardous, M., Cheker, R., and Ben Nasrallah, S. 2013. Study of the wake induced by a porous disc. 21éme Congrés Français de Mécanique. Bordeaux, 26 au 30 aout.

[255] Lignarolo, L. E. M., Ragni, D., Simão Ferreira, C. J., and van Bussel, G. J. W. 2015. Turbulent mixing in wind turbine and actuator disc wakes: an experimental analysis. AIAA SciTech, 33rd Wind Energy Symposium, 5-9 January, Kissimmee, Florida. https://doi.org/10.2514/6.2015-0223.

[256] Pope, S. B. 2000. Turbulent flows. 1st ed. Cambridge University press, Cambridge.

[257] Thomas, F. O., and Liu, X. 2004. An experimental investigation of symmetric and asymmetric turbulent wake development in pressure gradient. Physics of Fluids, 16. 1725. https://doi.org/10.1063/1.1687410.

[258] Chow, Y-C., Uzol, O., Katz, J., and Meneveau, C. 2005. Decomposition of the spatially filtered and ensemble averaged kinetic energy, the associated fluxes and scaling trends in a rotor wake. Physics of Fluids, 17. 085102. https://doi.org/10.1063/1.1990206.

[259] Moser, R. D., Rogers, M. M., and Ewing, D. W. 1998. Self-similarity of time evolving plane wakes. Journal of Fluid Mechanics, 367. 255-289. https://doi.org/10.1017/S0022112098001426.

[260] Wygnanski, I., Champagne, F., and Marasli, B. 1986. On the large-scale structure in two-dimensional, small-deficit, turbulent wakes. Journal of Fluid Mechanics, 168. 31-71. https://doi.org/10.1017/S0022112086000289.

[261] Frandsen, S. T. 2007. Turbulence and turbulence-generated structural loading in wind turbine clusters. PhD Thesis, Risø National Laboratory, DTU.

[262] Neunaber, I., Holling, M., Whale, J., and Peinke, J. 2021. Comparison of the turbulence in the wakes of an actuator disc and a model wind turbine by higher order statistics: A wind tunnel study. Renewable Energy 179. 1650-1662. https://doi.org/10.1016/j.renene.2021.08.002.

[263] Cheng, W. C., and Porté-Agel, F. 2018. A simple physically-based model for wind-turbine wake growth in a turbulent boundary layer. Boundary-Layer Meteorology, 169. 1-10. https://doi.org/10.1007/s10546-018-0366-2.

[264] Niayifar, A., and Porté-Agel, F. 2015. A new analytical model for wind farm power prediction. Journal of Physics: Conf. Series, 625.

[265] Fuertes, F. C., Markfort, C. D., and Porté-Agel, F. 2018. Wind turbine wake characterization with nacelle-mounted wind LIDARS for analytical wake model validation. Remote Sensing, 10. 668. https://doi.org/10.3390/rs10050668.

[266] Theunissen, R., Housley, P., Allen, C. B., and Carey, C. 2015. Experimental verification of computational predictions in power generation variation with layout of offshore wind farms. Wind Energy, 18. 1739-1757. https://ui.adsabs.harvard.edu/abs/2015WiEn...18.1739T.

[267] Teng, J., and Markfort, C. D. 2020. A calibration procedure for an analytical wake model using wind farm operational data. Energies, 13. https://doi.org/10.3390/en13143537.

[268] Crespo, A., and Hernandez, J. 1996. Turbulence characteristics in wind-turbine wakes. Journal of Wind Engineering and Industrial Aerodynamics, 61. 71-85. https://doi.org/10.1016/0167-6105(95)00033-X.

CURRICULUM VITAE

PERSONAL INFORMATION

Surname, Name: Abdulrahim, Anas

EDUCATION

Degree	Institution	Year of Graduation
MS	METU Aerospace Engineering	2014
BS	METU Aerospace Engineering	2011
High School	Nazih El Bizri High School, Lebanon	2006

WORK EXPERIENCE

Year	Place	Enrollment
2020-Present	ODTÜ RÜZGEM	Scientific Project Expert
2015-2020	University of Turkish Aeronautical Association	Lecturer
2012-2020	ODTÜ RÜZGEM	Aerodynamics Lab Assistant
2011-2015	ODTÜ RÜZGEM	Project Assistant

FOREIGN LANGUAGES

Arabic (native), Advanced English, Intermediate Turkish

PUBLICATIONS

1. Abdulrahim, A., Akpolat, M.T., Hassanein, A., Perçin, M., Uzol, O., 2022, "On the Wake Growth Rate of a Porous Disc Immersed in a Boundary Layer", Energies Special Issue: Fast-Running Engineering Models of Wind Farm Flows (*under review*).
2. Abdulrahim, A., Akpolat, M.T., Hassanein, A., Perçin, M., Uzol, O., 2021, "Effects of Inflow Boundary Layer on the Wake of a Radially Non-Uniform Porous Disc", Journal of Renewable and Sustainable Energy Special Issue: Wind Tunnel Research, Dynamics, and Scaling for Wind Energy.

3. Abdulrahim, A., Anik, E., Ostovan, Y., Uzol, O., 2016, “Effects of Tip Injection on the Performance and Near Wake Characteristics of a Model Wind Turbine Rotor”, Renewable Energy Vol. 88 p73-82.
4. Öztürk, B., Hassanein, A., Abdulrahim, A., Perçin, M., Uzol, O., 2022, “Effects of Freestream Turbulence on the Wake Growth Rate of a Model Wind Turbine and a Porous Disc”, The Science of Making Torque from Wind, TU Delft, Netherland, June 1-3, 2022.
5. Akpolat, M.T., Abdulrahim, A., Hassanein, A., Perçin, M., Uzol, O., 2021, “Experimental Characterization of Micro Vortex Generators in Low-Speed Flows”, 11th Ankara International Aerospace Conference, Middle East Technical University (METU), Ankara, Turkey, September 8-10, 2021.
6. Abdulrahim, A., Akpolat, M.T., Perçin, M., Uzol, O., 2021, “Comparison of Analytical Wake Model Predictions with Experimental Data for a Non-Uniform Porous Disc for Uniform and Non-Uniform Inflow Conditions”, Wind Energy Science Conference (WESC), Leibniz University, Hannover, Germany, May 25-28, 2021.
7. Erol, B., Karabakla, E., Abdulrahim, A., Perçin, M., Uzol, O., 2021, “Effects of Wind Tunnel Blockage and Turbulence intensity on the Performance of a Small Wind Turbine: An In-House Round Robin Study”, Wind Energy Science Conference (WESC), Leibniz University, Hannover, Germany, May 25-28, 2021.
8. Abdulrahim, A., Elfarra, M., Uzol, O., 2019, “A Numerical Assessment of Atmospheric Boundary Layer Simulation Inside Two Different Boundary Layer Wind Tunnels”, 10th Ankara International Aerospace Conference, Middle East Technical University (METU), Ankara, Turkey, September 18-20, 2019.
9. Anik, E., Abdulrahim, A., Uzol, O., 2016, “Effects of Mie Vanes and Tip Injection on the Performance and Wake Characteristics of HAWT”, 34th ASME Wind Energy Symposium, AIAA SciTech2016, California, USA, 4-8 January 2016.
10. Anik, E., Abdulrahim, A., Uzol, O., 2015, “2D-PIV Investigation of the Effects of Tip Injection on the Tip Flow Characteristics of a Model HAWT”, 11th EAWE PhD Seminar, Stuttgart, Germany, 23-25 September 2015.

11. Ostovan, Y., Anik, E., Abdulrahim, A., Uzol, O., 2015, “Experimental Investigation of the Effects of Tip Injection on the Performance of Two Interacting Wind Turbine”, Large Wind-Power Plants: Interaction, Control and Integration (Windfarms2015), Leuven, Belgium, 8-10 July.
12. Abdulrahim, A., Anik E., Uzol, O., 2015, “Effects of Tip Injection and Mie Vanes on the Performance of a Model Wind Turbine Rotor”, NAWEA 2015 Symposium, North American Wind Energy Academy, Blacksburg, Virginia USA, 9-11 June 2015.
13. Abdulrahim, A., Anik E., Uzol, O., 2015, “Experimental Investigation of the Wake Flow Field of a Model Wind Turbine Rotor with Tip Injection”, 33rd ASME Wind Energy Symposium, AIAA SciTech2015, Florida, USA, 5-9 January 2015.
14. Abdulrahim, A., Anik, E., Ostovan, Y., Uzol, O., 2014, “Effects of Tip-Injection on the Flow Downstream of a Model Wind Turbine Rotor Blade Tip”, 10th EAWE PhD Seminar on Wind Energy in Europe, 28-31 October 2014, Orléans France.
15. Anık, E., Abdulrahim, A., Ostovan, Y., Mercan, B., Uzol, O., 2014, “Active control of the tip vortex: an experimental investigation on the performance characteristics of a model turbine”, The Science of Making Torque from Wind, Technical University of Denmark (DTU), Copenhagen, Denmark, June 18-20, 2014.
16. Abdulrahim, A., Kaya, H., Uzol, O., Kurc, O., 2013, “Discrete Vortex Simulations of a Generic Bridge Cross-section and Comparisons with Time-Resolved Particle Image Velocimetry Data”, Proceedings of 12th Americas Conference on Wind Engineering (12ACWE), Seattle, Washington, USA, June 16-20, 2013.
17. Abdi, I.A., Abdulrahim, A., Haser, S., Uzol, O., Kurc, O., 2012, “Experimental and Numerical Investigation of Wind Effects on Long Span Bridge Decks”, Proceedings of 10th International Congress on Advances in Civil Engineering, Ankara, Turkey, September 2012.
18. Erol, B., Karabakla, E., Abdulrahim, A., Perçin, M., Uzol, O., 2021,” Rüzgar Tüneli Testlerinde Blokaj Seviyesinin Küçük Ölçekli Bir Rüzgar Türbininin

Performansi Üzerindeki Etkisi" Mühendis ve Makina Dergisi Yazar Bilgileri (*under review*)

19. Erol, B., Karabakla, E., Abdulrahim, A., Perçin, M., Uzol, O., 2021, "Rüzgar Tüneli Testlerinde Blokaj Seviyesinin Küçük Ölçekli Bir Rüzgar Türbininin Performansi Üzerindeki Etkisi", 6th İzmir Rüzgar Sempozyumu, İzmir, Turkey, Eylül 23-24, 2021.
20. Ostovan, Y., Mutlu, T., Onay, O.K., Khalilov, J., Kutkan, H., Cete, A.R., Mercan, B., Abdulrahim, A., Uzol, O., Ozdede, S., 2012, "Açik ve Açik Jet Odali Rüzgar Tünellerinin Tasarimi, Üretimi ve Karakterizasyon Sonuçlari", IV. Ulusal Havacilik Ve Uzay Konferansi 12-14 Eylül 2012, Hava Harp Okulu, İstanbul, UHUK-2012-1210.